University of Melbourne

Doctoral Thesis

Phenomenology of Particle Dark Matter

by
Rebecca Kate Leane
ORCID: 0000-0002-1287-8780

A thesis submitted in fulfillment of the requirements for the degree of Doctor of Philosophy

in the

School of Physics
Faculty of Science
University of Melbourne

May 5, 2017

Declaration of Authorship

I, Rebecca Kate Leane, declare that this thesis:

- comprises only my own original work, except where indicated in the preface,
- was done wholly while in candidature;
- gives due acknowledgement in the text to all other materials consulted;
- and is fewer than 100,000 words in length, exclusive of Tables, Figures, Bibliographies, or Appendices.

Signed:

Date:

"I was just so interested in what I was doing I could hardly wait to get up in the morning and get at it. One of my friends said I was a child, because only children can't wait to get up in the morning to get at what they want to do."

– Barbara McClintock (Nobel Prize in Medicine)

Abstract

The fundamental nature of dark matter (DM) remains unknown. In this thesis, we explore new ways to probe properties of particle DM across different phenomenological settings.

In the first part of this thesis, we overview evidence, candidates and searches for DM.

In the second part of this thesis, we focus on model building and signals for DM searches at the Large Hadron Collider (LHC). Specifically, in Chapter 2, the use of effective field theories (EFTs) for DM at the LHC is explored. We show that many widely used EFTs are not gauge invariant, and how, in the context of the mono-W signal, their use can lead to unphysical signals at the LHC. To avoid such issues, the next iteration of a minimal DM framework, called simplified models, are considered. We discuss use of such models at the LHC in Chapter 3, and show that in the context of a renormalizable gauge-invariant theory, any isospin violating effects in mono-W signals cannot be large. In Chapter 4, we discuss an alternative search strategy to mono-X searches at the LHC — in the case that DM does not couple directly to hadrons, the mono-X signature does not exist, and instead a leptophilic DM signature can be probed. We focus on the prospects for leptophilic DM with a spin-1 mediator at the LHC, and discuss constraints from other experiments.

In the third part of this thesis, we turn to astrophysical signals of DM. In Chapter 5, we show that a consequence of enforcing gauge invariance in simplified DM models provides a new dominant s-wave DM annihilation process for indirect detection searches, and set limits on the annihilation cross section from Pass 8 observations of the Fermi Gamma-ray Space Telescope. In Chapter 6, we demonstrate the impact of mass generation for simplified models, finding that the relic density and indirect detection constraints, along with the DM interaction types, are strongly dictated by the mass generation mechanism chosen. In Chapter 7, we show that the multi-mediator approach advocated in the previous two chapters can also lead to a new dominant signal, in the form of dark initial state radiation. Finally in Chapter 8, we look to the Sun to find that if DM annihilates to long-lived mediators, the gamma rays and neutrinos produced can be strongly probed by gamma-ray telescopes and observatories Fermi-LAT, HAWC, and LHAASO, as well as neutrino telescopes IceCube and KM3Net. Interestingly, these telescopes can provide the strongest probe of the DM spin dependent scattering cross section, outperforming standard high-energy solar neutrino searches and direct detection experiments by several orders of magnitude.

Publications

The following is a chronological list of journal publications completed during this PhD candidature:

1. N. F. Bell, Y. Cai, **R. K. Leane*** and A. D. Medina, "Leptophilic dark matter with Z' interactions", Phys. Rev. D 90, no. 3, 035027 (2014) [arXiv:1407.3001 [hep-ph]].

2. N. F. Bell, Y. Cai, J. B. Dent, **R. K. Leane*** and T. J. Weiler, "Dark matter at the LHC: Effective field theories and gauge invariance", Phys. Rev. D92, no. 5 053008 (2015) [arXiv:1503.07874 [hep-ph]].

3. N. F. Bell, Y. Cai and **R. K. Leane***, "Mono-W Dark Matter Signals at the LHC: Simplified Model Analysis", JCAP 01 (2016) 051 [arXiv:1512.00476 [hep-ph]].

4. N. F. Bell, Y. Cai and **R. K. Leane***, "Dark Forces in the Sky: Signals from Z' and the Dark Higgs", JCAP 08 (2016) 001 [arXiv:1605.09382 [hep-ph]].

5. N. F. Bell, Y. Cai and **R. K. Leane***, "Impact of Mass Generation for Simplified Dark Matter Models", JCAP 01 (2017) 039 [arXiv:1610.03063 [hep-ph]].

6. **R. K. Leane**, K. C.Y. Ng, J. F. Beacom, "Powerful Solar Signatures of Long-Lived Dark Mediators" [arXiv:1703.04629 [astro-ph.HE]].

7. N. F. Bell, Y. Cai, J. B. Dent, **R. K. Leane*** and T. J. Weiler, "Enhancing Dark Matter Annihilation Rates with Dark Bremsstrahlung" [arXiv:1705.01105 [hep-ph]].

*Author list is alphabetical, as per convention in particle physics.

Acknowledgements

My time as a PhD student has been one I will always treasure. For that, I have many people to thank.

Firstly, I thank my supervisor, Nicole Bell. I could not have been more lucky to have such a sharp, discerning and understanding person as my mentor during my PhD. I have learnt so much from you, not just about physics, but also all the little things that are important along the way. You have supported many things I wanted to do during my PhD candidature, allowing me flexibility, while holding a high standard for work. I am deeply grateful.

To my advisory panel, Ray Volkas and Andrew Melatos (and informally, also Matt Dolan), thank you for providing me with invaluable gifts of perspective and support.

To my collaborators, John Beacom, Yi Cai, James Dent, Anibal Medina, Kenny Ng, and Tom Weiler, it has been a pleasure working with and learning from you.

A highlight during my PhD has been the numerous adventures abroad. To Tom Weiler, thank you for hosting my stay in Nashville, and for your extensive generosity and support. To John Beacom, thank you for inviting me to work with you at Ohio State after our brief initial meeting, and opening many doors. I am deeply grateful for your ongoing support and mentorship. To the graduate students and postdocs I have met abroad at conferences and summer schools, thank you for your gifts of friendship. I already look back at many of our adventures fondly.

I was very fortunate to be a member of CoEPP during my PhD, which has provided significant resources, both financial (particularly for travel (and many servings of Thursday morning cake and tea)), as well as a supportive work environment. I thank all the staff and students in CoEPP, as well as the School of Physics at the University of Melbourne, for making my time here so enjoyable.

Finally, to my family, thank you for your ongoing unconditional love, support, and understanding. I would not be where I am today without you.

Contents

Declaration of Authorship **iii**

Abstract **vii**

Publications **ix**

Acknowledgements **xi**

List of Figures **xx**

List of Tables **xxi**

List of Abbreviations **xxiii**

Preface **xxvii**

I Dark Matter and the Universe **1**

1 Introduction **3**

1.1 Astrophysical Evidence for Dark Matter 3

1.1.1 First Observation in Galaxies 3

1.1.2 Galactic Rotation Curves 4

1.1.3 Gravitational Lensing and Merger Events 4

1.2 Cosmological Evidence for Dark Matter 6

1.2.1 Cosmological Parameters 6

1.2.2 CMB, BAO, BBN and Supernovae 8

1.2.3 Large Scale Structure 12

1.3 Theories and Candidates 15

1.3.1 Adding to the Standard Model 15

1.3.2 Theories for Dark Matter 17

1.3.3 Weakly Interacting Massive Particles and Thermal Freezeout 20

1.4 Searches for Particle Dark Matter 22

1.4.1 Interpreting Searches Within a Minimal Theory Framework 22

1.4.2 Collider Searches 24

1.4.3 Direct Detection Searches 25

1.4.4 Indirect Detection Searches 28

Gamma-ray Signals 28

Positron and Neutrino Signals 31

II Dark Matter at the Large Hadron Collider 33

2 Effective Field Theories and Gauge Invariance 37
2.1 Introduction 37
2.2 EFT operators and gauge invariance 38
2.2.1 Scalar operator 38
2.2.2 Vector operator: 39
2.3 Mono-W and $SU(2)_L$ invariance 39
2.4 Renormalizable models and EFTs 42
2.5 Conclusion 45

3 Mono-W Simplified Models and Gauge Invariance 47
3.1 Introduction 47
3.2 Simplified Models for the Mono-W 48
3.2.1 t-channel Colored Scalar Mediator 48
3.2.2 s-channel Z' Mediator 49
3.3 LHC Constraints and Reach 50
3.3.1 Mono lepton channel 50
3.3.2 Mono fat jet channel 52
3.3.3 Results 53
3.4 $SU(2)$ Breaking Effects and Enhancements from W_L Production . . 55
3.4.1 Isospin Violation in the t-channel Model 56
Cross Section Enhancement from W_L Contribution 57
$SU(2)$ Breaking and the M_T Spectrum 58
3.4.2 Isospin Violating Effects in s-channel Models 58
3.5 Conclusion 59

4 Leptophilic Dark Matter with Z' Interactions 61
4.1 Introduction 61
4.2 Leptophilic Model 63
4.3 Dark Matter Relic Density 64
4.4 Constraints from $(g-2)_\ell$, LEP and other searches 65
4.5 LHC Phenomenology 66
4.5.1 Z' Decay to Leptons 68
Four Electron Final State: $m_{Z'} < m_Z$ 69
Four Muon Final State: $m_{Z'} < m_Z$ 69
Four Muon Final State: $m_{Z'} > m_Z$ 72
4.5.2 Z' Decay to Dark Matter 78
4.6 Discussion 78
4.7 Conclusions 79

III Dark Matter in the Sky **81**

5 Dark Forces in the Sky: Signals from Z' and the Dark Higgs **85**
5.1 Introduction . . . 85
5.2 Model Setup . . . 88
5.3 Dark Matter Annihilation Processes for Indirect Detection . . . 90
5.3.1 Annihilation Cross Sections . . . 90
5.3.2 Decay Widths of the Dark Higgs and Z' . . . 92
5.4 γ-ray Energy Spectra . . . 94
5.5 Annihilation Limits from Dwarf Spheriodal Galaxies and AMS-02 . 95
5.6 Other Model Constraints . . . 98
5.6.1 Collider and Direct Detection Constraints . . . 98
5.6.2 BBN and CMB Constraints . . . 98
5.6.3 Unitarity . . . 98
5.7 Summary . . . 99

6 Impact of Mass Generation for Simplified Dark Matter Models **101**
6.1 Introduction . . . 101
6.2 Mass Generation for Spin-1 Simplified Models . . . 103
6.3 Scenario I: Bare DM Mass and Z' Mass from Stueckelberg Mechanism 104
6.3.1 Model . . . 104
6.3.2 Cross Sections . . . 106
6.3.3 Relic Density . . . 106
6.4 Scenario II: DM Mass and Z' Mass both from Dark Higgs Mechanism 107
6.4.1 Model . . . 107
6.4.2 Cross Sections . . . 109
6.4.3 Relic Density . . . 111
6.5 Scenario III: DM Mass from Dark Higgs Mechanism, Z' Mass from Stueckelberg Mechanism . . . 113
6.5.1 Model . . . 113
6.5.2 Cross Sections . . . 114
6.5.3 Relic Density . . . 114
6.6 Scenario IV: Bare DM Mass, Z' Mass from Dark Higgs Mechanism . 117
6.6.1 Model . . . 118
6.6.2 Cross Sections . . . 118
6.6.3 Relic Density . . . 118
6.7 Indirect Detection Phenomenology . . . 121
6.8 Discussion and Summary . . . 122

7 Enhancing Dark Matter Annihilation Rates with Dark Bremsstrahlung **125**
7.1 Introduction . . . 125
7.2 Overview of Fermionic Dark Matter Annhilation . . . 127
7.2.1 Direct annihilation to SM particles . . . 127

7.2.2 Direct annihilation to dark mediators . . . 127
7.3 Dark Initial State Radiation . . . 128
7.4 Lifting Helicity Suppression in $A \otimes A$ Interactions . . . 130
7.4.1 Helicity suppressed $\overline{\chi}\chi \to \overline{f}f$ . . . 131
7.4.2 Dark vector ISR, $\overline{\chi}\chi \to \overline{f}fZ'$ . . . 131
7.4.3 Competition with $\chi\chi \to Z'Z'$ . . . 132
7.5 Lifting p-wave suppression in $S \otimes S$ interactions . . . 132
7.5.1 p-wave suppressed $\chi\chi \to \overline{f}f$ . . . 134
7.5.2 Dark pseudoscalar ISR, $\chi\chi \to ff\phi$ . . . 134
7.5.3 Competition with $\chi\chi \to \phi\phi\phi$ . . . 135
7.6 Conclusion . . . 136

8 Powerful Solar Signatures of Long-Lived Dark Mediators 139
8.1 Introduction . . . 139
8.2 Dark Matter Solar Capture and Annihilation . . . 141
8.3 Long-Lived Dark Mediator Scenario . . . 142
8.3.1 Opportunities and Framework . . . 142
8.3.2 Annihilation Rate . . . 143
8.3.3 Branching Fractions . . . 143
8.3.4 Energy Spectra . . . 143
8.3.5 Optimal Signal Conditions . . . 145
8.4 High-Energy Solar Gamma Rays . . . 146
8.4.1 Procedure . . . 147
8.4.2 Discussion of Results . . . 147
8.5 High-Energy Solar Neutrinos . . . 150
8.5.1 Procedure . . . 151
8.5.2 Discussion of Results . . . 154
8.6 Model Interpretation of Results . . . 156
8.6.1 Dark Vector or Axial-Vector . . . 156
8.6.2 Fundamental Dark Scalar or Pseudoscalar . . . 156
8.6.3 Multi-Mediator Scenarios . . . 157
8.6.4 General Considerations . . . 158
8.7 Other constraints . . . 158
8.8 Conclusions . . . 159

9 Conclusion 163

A Full cross sections 165
A.1 Cross Sections . . . 165

Bibliography 167

List of Figures

1.1 Rotational velocity vs. radius measurements for spiral galaxies . . . 5
1.2 Optical and x-ray image of the Bullet Cluster overlaid with mass contours from measurements of weak gravitational lensing 7
1.3 Combined likelihood map using CMB, BAO and the Union SNe Ia Set, for the matter $\Omega_m = \Omega_b + \Omega_\chi$ and energy Ω_Λ content of the universe 10
1.4 Theoretical abundances of isotopes (curves) and baryonic densities as predicted by BBN, overlaid with experimental measurements (boxes) of light elements 11
1.5 Temperature power spectrum of the CMB from the nine year WMAP analysis, South Pole Telescope data, Atacama Cosmology Telescope data 12
1.6 Measurements of density fluctuations vs. length scale across independent studies, compared with Λ_{CDM} predictions 13
1.7 Large scale structure from the Millennium Simulation, and from large scale observations including the Coma Cluster, the CfA2 'Great Wall', the Sloan Great Wall, and 2dFGRS 14
1.8 Dark matter candidates as a function of their mass scale 19
1.9 Departure of comoving number density from thermal equilibrium at freezeout for increasing annihilation cross section as a function of dark matter mass m over equilibrium temperature T 21
1.10 EFT contact interaction. 22
1.11 Benchmark simplified models for DM searches: s-channel spin-1 mediator, s-channel spin-0, and t-channnel colored scalar 24
1.12 Diagram for "mono-X" searches at the LHC 25
1.13 Current LHC limits from ATLAS on Dirac DM with spin-1 mediator 26
1.14 Summary of limits and sensitivity to DM-nucleon spin-independent scattering cross section at current and upcoming direct detection experiments 28
1.15 Gamma-ray spectral shapes for various DM annihilation processes 30
1.16 DM annihilation to $b\bar{b}$ limit from Fermi-LAT Pass 8 data on dwarf spheroidal galaxies 30
1.17 Positron excess flux reported by AMS-02 31
1.18 Limits on the DM-proton spin-dependent scattering cross section from direct detection experiments and neutrino telescopes 32

2.1 Contributions to the mono-W process in the effective field theory framework . . . 40
2.2 Total parton-level cross sections as a function of energy for mono-W isospin violating EFT, for $\Lambda = 600$ GeV and particular choices of ξ. . 43

3.1 Contributions to the mono-W process in a t-channel colored scalar model . . . 49
3.2 Contributions to the mono-W process in an s-channel Z' model . . 49
3.3 M_T distribution for $m_{\eta_u} = m_{\eta_d} = 200$ GeV, $g = 1$, $m_\chi = 10, 500, 1000$ GeV in the t-channel model . . . 51
3.4 Parameter space and exclusions for the t-channel colored scalar model . . . 53
3.5 Parameter space and exclusions for the s-channel Z' model . . . 54
3.6 Ratio of the hadron level cross sections for the mono-W process to the mono-jet process at 14 TeV, in a renormalizable t-channel scalar model with isospin violation . . . 57
3.7 M_T distribution for $m_{\eta_u} = 220$ GeV, $g = 1$, $m_\chi = 200$ GeV in the t-channel model with isospin violation . . . 58
3.8 Contributions to the mono-W process in the Z-Z' mixing model . . 59

4.1 Loop-suppressed direct detection signal for leptophilic dark matter. 62
4.2 DM annihilation processes, which determine the relic density at freezeout. . . . 65
4.3 Production of a leptophilic Z' at a hadron collider . . . 67
4.4 Z' production cross section at the 14 TeV LHC, via the process $pp \to \ell^+\ell^- Z'$ . . . 67
4.5 Invariant mass for four muons and transverse momentum p_T for leading in p_T muon for $pp \to 4\mu$ in the SM and Z' model . . . 70
4.6 Invariant mass for first and second leading muons in p_T and third and fourth leading muons in p_T for $pp \to 4\mu$ in the SM and Z' model 71
4.7 Invariant mass for first and second leading muons in p_T and transverse momentum p_T for p_T leading muon both before cuts, for $pp \to 4\mu$ in the SM and Z' model . . . 73
4.8 Invariant mass of third and fourth leading in p_T muons before cuts and after cuts, for $pp \to 4\mu$ in the SM and Z' model . . . 74
4.9 Parameter space for g_μ vs. $m_{Z'}$ in the leptophilic model, with $g_\chi = g_\mu$ 75
4.10 Parameter space for g_μ vs. $m_{Z'}$ in the leptophilic model, with $g_\chi = 4g_\mu$ and $g_\chi = 8g_\mu$ . . . 76
4.11 Parameter space for g_e vs. $m_{Z'}$ with $g_\chi = g_e$, and g_τ vs. $m_{Z'}$ with $g_\chi = g_\tau$, in the leptophilic model . . . 77

5.1 Spin-1 simplified model annihilation processes . . . 87
5.2 Spin-0 simplified model annihilation processes . . . 87

5.3 Annihilation diagrams for the s-wave processes $\chi\chi \to sZ'$ 91
5.4 Annihilation diagrams for the s-wave processes $\chi\chi \to Z'Z'$ 92
5.5 Relative cross section sizes for the two dominant s-wave diagrams, $\chi\chi \to sZ'$ and $\chi\chi \to Z'Z'$ 93
5.6 Comparison of gamma ray spectra for DM annihilation into sZ' vs. $Z'Z'$, and gamma-ray spectra for DM annihilation with various DM masses 95
5.7 95% confidence limits (C.L.) on the DM annihilation cross section from Fermi data on 15 dwarf spheroidal galaxies 97

6.1 DM relic density contours as a function of DM mass and dark gauge coupling in scenario I 106
6.2 Relative cross sections for the two dominant s-wave annihilation processes in scenario II, $\chi\overline{\chi} \to sZ'$ and $\chi\overline{\chi} \to Z'Z'$ 110
6.3 DM relic density contours in scenario II, as a function of m_χ and g_χ, for various choices of the dark Higgs and Z' mass 112
6.4 Cross section for the two dominant s-wave annihilation processes of scenario III, $\chi\overline{\chi} \to sZ'$ and $\chi\overline{\chi} \to Z'Z'$ 115
6.5 Relic density contours for scenario III, as a function of m_χ and g_χ . 116
6.6 DM annihilation to two dark Higgs bosons, $\chi\overline{\chi} \to ss$ 117
6.7 Relative cross section for the two dominant s-wave annihilation processes in scenario IV, $\chi\overline{\chi} \to sZ'$ and $\chi\overline{\chi} \to Z'Z'$ 119
6.8 DM relic density contours for scenario IV as a function of m_χ and g_χ 120
6.9 95% confidence limits (C.L.) on the DM annihilation cross section for sZ' and $Z'Z'$ processes from Fermi Pass 8 data on 15 dwarf spheroidal galaxies 123

7.1 Dark vector and dark scalar ISR diagrams 128
7.3 s-wave process for DM annihilation to dark vectors 132
7.2 Comparison of s-wave cross sections for dark vector ISR process and 2-body $Z'Z'$, for $m_{Z'}$ and Λ 133
7.4 s-wave process for DM annihilation to pseudoscalars. 135
7.5 Comparison of s-wave cross sections for pseudoscalar ISR process and 3-body $\phi\phi\phi$ process for $m_\phi = 0$ and $\Lambda = 1000$ GeV 135

8.1 Long-lived vs short-lived mediator scenarios from DM annihilation in the Sun 140
8.2 Impact of varying mediator mass on gamma-ray and neutrino spectra 144
8.3 Probability of gamma rays from the mediator surviving and reaching a detector at Earth, for varying mediator properties 145
8.4 Estimates of presently allowed gamma-ray spectra from solar observations by Fermi-LAT 148

8.5 Optimal sensitivity for DM scattering cross sections from current and future solar gamma-ray observations, for DM in the Sun annihilating to pairs of long-lived mediators 149
8.6 Neutrino flux from DM annihilating in the Sun to long-lived mediators with $Y \to 2\tau$, compared with cases for short-lived mediators in the center of the Sun with $\chi\chi \to \tau\bar{\tau}$ 153
8.7 The muon spectrum (entering + starting) for a gigaton neutrino detector with 317 days of exposure 154
8.8 Constraints and sensitivities for the spin-dependent DM scattering cross section from neutrinos 155

List of Tables

4.1 Lorentz structure of the leptophilic Z' couplings 64

6.1 The spectrum of DM annihilation scenarios to spin-1 or spin-0 mediators with distinct phenomenology once mass generation is specified 105

7.1 Suppression factors for DM annihilation to two different mediators M_1 and M_2, which have varying Lorentz structures 128
7.2 Suppression factors for DM annihilation with varying Lorentz structures: vector (V), axial-vector (A), scalar (S) or pseudoscalar (P) . . 129

List of Abbreviations

AMS	**A**lpha **M**agnetic **S**pectrometer
ATLAS	**A** **T**oroidal **L**HC **A**pparatu**S**
BAO	**B**aryonic **A**coustic **O**scillation
BAU	**B**aryon **A**symmetry of the **U**niverse
BBN	**B**ig **B**ang **N**ucleosynthesis
BSM	**B**eyond the **S**tandard **M**odel
C.L.	**C**onfidence **L**evel
CMB	**C**osmic **M**icrowave **B**ackground
CMS	**C**ompact **M**uon **S**olenoid
DARWIN	**Dar**k matter **Wi**mp search with liquid xeno**N**
DES	**D**ark **E**nergy **S**urvey
DM	**D**ark **M**atter
dSphs	**D**warf **Sph**eriodial Galaxie**S**
EFT	**E**ffective **F**ield **T**heory
EM	Electro**m**agnetism
EW	Electro**w**eak
FLRW	**F**riedmann-**L**emaître-**R**obertson-**W**alker
FSR	**F**inal **S**tate **R**adiation
H.c.	**H**ermitian **C**onjugate
HAWC	**H**igh **A**ltitude **W**ater **C**herenkov (Observatory)
ISR	**I**nitial **S**tate **R**adiation
LAT	**L**arge **A**rea **T**elescope
LEP	**L**arge **E**lectron-**P**ositron (Collider)
LHAASO	**L**arge **H**igh **A**ltitude **A**ir-**C**herenkov **O**bservatory
LHC	**L**arge **H**adron **C**ollider
LSND	**L**iquid **S**cintillator **N**eutrino **D**etector
LUX	**L**arge **U**nderground **X**enon (Experiment)
NFW	**N**avarro-**F**renk-**W**hite
NLO	**N**ext-to-**L**eading-**O**rder
Panda-X	**P**article **and** **A**strophysical **X**enon (Detector)
PDFs	**P**arton **D**istribution **F**unction**s**
SD	**S**pin-**D**ependent
SI	**S**pin-**I**ndependent
SM	**S**tandard **M**odel (of Particle Physics)
Super-K	**S**uper-**K**amiokande

SUSY	**Su**per**sy**mmetry
UV	**U**ltra**v**iolet
vev	**V**acuum **E**xpectation **V**alue
VIB	**V**irtual **I**nternal **B**remstrahlung
WIMP	**W**eakly **I**nteracting **M**assive **P**article
WMAP	**W**ilkinson **M**icrowave **A**nisotropy **P**robe

For Reenie.

Preface

This thesis comprises nine chapters based on original work, including publications or preprints (Chapter 7 is based on a paper currently in final preparation).

Part I (Chapter 1) features an original introduction and literature review of dark matter.

Part II features publications on dark matter signals at the LHC. In each of the papers in this part of the thesis, I performed all calculations, made all plots and figures, and prepared the first draft of each paper. Chapter 2 is based on a collaborative work with Nicole Bell, Yi Cai, James Dent and Tom Weiler. Chapter 3 is based on a collaborative work with Nicole Bell and Yi Cai, and Chapter 4 is collaborative work with Nicole Bell, Yi Cai and Anibal Medina.

Part III features publications on signals of dark matter in the sky. Chapter 5 features my own original ideas, developed in consultation with Nicole Bell and Yi Cai. I performed all calculations, made all plots and figures, and wrote the draft. Chapter 6 is an extension of the ideas in the previous chapter, where I performed all calculations and made all plots, except for the relic density which was done by Yi Cai. Chapter 7 is based on a collaborative work developed with Nicole Bell, Yi Cai, James Dent and Tom Weiler, where I performed all calculations, made all plots and figures, and prepared the draft. Chapter 8 is based on a collaborative work developed with Kenny Ng and John Beacom, where I performed all calculations, made all plots and figures, except for Section 8.5, which was done by Kenny Ng. The writing in Chapter 8 was a collaborative effort which I led, apart from Section 8.5, which was predominately written by Kenny Ng.

Chapter 9 is an original conclusion based on the above work.

This work was supported in part by the Australian Research Council, Tom Weiler's DOE grant DESC-0010504, and John Beacom's NSF grant PHY-1404311.

Part I

Dark Matter and the Universe

Chapter 1

Introduction

EVERYTHING we can see and feel makes up five percent of the energy-matter content of the universe. What makes up the rest remains one of the most exciting unsolved mysteries of modern physics. In this chapter, we overview the current status of answers to questions such as: what is ninety-five percent of the universe, and how do we know its there? What do we know about it? What could it be?

Without knowing their fundamental nature, we call these ubiquitous substances, "dark energy" and "dark matter". The former is a repulsive energy, causing the universe to expand at an increasing rate. The latter is an attractive matter, acting as a cosmic glue throughout the universe. Together, both these dark substances have intricately affected the evolution and development of our universe, shaping it into what we observe today.

In this thesis, we will focus on the unknown, elusive matter substance, dark matter. In the first section of this chapter, examples of evidence for dark matter from astrophysical observations are presented. In the second section, examples of evidence from cosmological observations are presented. In the third section, we outline theories which can explain the fundamental nature of dark matter, with a focus on particle dark matter, and finally in the fourth section of this chapter we discuss how particle dark matter may be found; through measurements of its annihilation, scattering and production cross sections.

1.1 Astrophysical Evidence for Dark Matter

1.1.1 First Observation in Galaxies

Dark matter first revealed itself, unexpected, through strange behaviour of galaxy clusters and their constituents. The existence of dark matter was first posited by 20th Century astronomers Kelvin [1] (1906), Opik [2] (1915), Kapteyn [3] (1922), Jeans [4] (1922), Lindblad [5] (1926) and Oort [6] (1932), to potentially explain discrepancies in the expected total density of matter near the Sun or in the Milky Way [7]. In 1931, Edwin Hubble and Milton Humason had published results on the redshifts of galaxies [8]. A Swiss astronomer, Fritz Zwicky, was perplexed by the results — there seemed to be some curious behaviour in a particular galaxy

cluster, the Coma Cluster. Particularly, the rotational velocities of the galaxies were unexpectedly high. He related the kinetic energy of the cluster to its gravitational potential via the virial theorem, finding that apparently, most of the mass of the cluster was mysteriously *missing*. There had to be something else, something non-luminous, hiding within the cluster. In his 1933 work [9], he concluded,

> *If this would be confirmed, we would get the surprising result that dark matter is present in much greater amount than luminous matter.*

Later, it turned out that Zwicky had overestimated the amount of dark matter by a few orders of magnitude, but his qualitative result stood: something dark and unknown exists in the universe and is much more abundant than visible matter. Since discovery of Zwicky's *dunkle kalte Materie* (cold dark matter), evidence in support of his hypothesis has accumulated across several length scales.

1.1.2 Galactic Rotation Curves

By the 1970s, striking evidence for dark matter began to increasingly appear at the galactic scale. From Newtonian dynamics, it is expected that any object in orbit at an increasing radius r around a galaxy of mass $M(r)$ should have decreasing rotational velocity $v(r)$ proportional to $1/\sqrt{r}$, arising from the known relation

$$v(r) = \sqrt{\frac{G_N M(r)}{r}}, \tag{1.1}$$

where G_N is Newton's constant. However, across observations of hundreds of galaxies [10], instead of decreasing with increasing r, the rotational velocity hardly changes across the galaxy, remaining approximately flat[1].

This behaviour can be explained if there is a hidden dark component present in the galaxy. Specifically, it is posited that a dark halo permeates not just the galactic disk of visible matter, but also extends out further than the visible component. This can exactly reproduce the observed galactic behaviour [12], as shown in Fig. 1.1.

1.1.3 Gravitational Lensing and Merger Events

As described by General Relativity, the more massive the astrophysical object, the greater it will distort the fabric of space-time, affecting nearby geodesics of light. So, the amount in which light travelling from some background source has been bent around a foreground (lensing) object, allows the mass of the lensing object to be measured. Depending on the mass of the foreground object, different grades of gravitational lensing are realised: the background object may appear temporarily brighter due to a transient lensing object (microlensing), there can be

[1]This behaviour had also been observed as early as 1939 in the Andromeda Galaxy [11], but the link with DM had not been readily made.

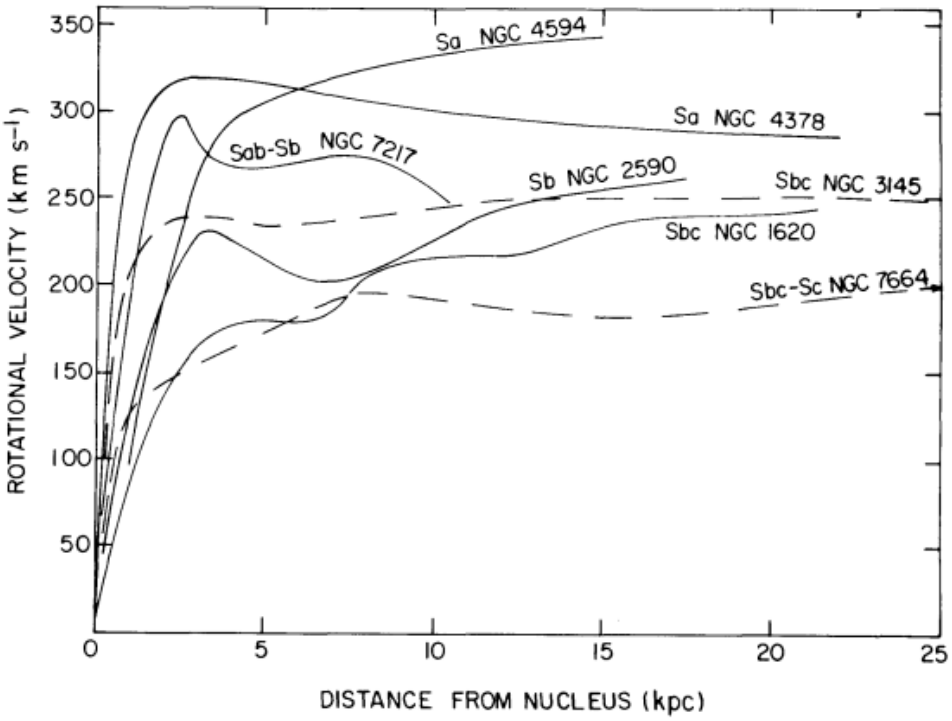

FIGURE 1.1: Rotational velocity vs. radius measurements for spiral galaxies. [12]

some distortion of the background object (weak lensing), or muliple copies of the background object can even appear, including Einstein rings (strong lensing) [13]. By comparing the mass of a lensing object with its own luminosity, it is perennially shown that there is a significant non-visible component to many astrophysical objects.

In 2006, gravitational lensing was famously used in a merger event of galaxies in the Bullet Cluster (1E 0657-558), to make a striking observation about the *nature* of DM [14]. In the merger event shown in Fig. 1.2, galaxies are observed to be colliding. Collisions of visible matter, mostly comprising highly interactive gas, are predicted to produce significant amounts of X-rays. While this is indeed observed as shown in Fig. 1.2, what is most interesting is that when the mass density measurements from weak gravitational lensing are overlaid, as shown by the green contours, the mass density does not align with the visible mass of the cluster. Instead, the strongest gravitational potential is *completely displaced* from the visible matter. Of course, gravitational sources are not expected to exist in the absence of matter. The conclusion is that there exists a *weakly interacting* matter which has passed through the bulk of the matter, barely slowed by the collision, unlike the hot gas emitted by the colliding visible matter which follows behind. This weakly interacting matter explains the excess gravitational potential, and provides the dominant mass contribution to the cluster. This is believed to be

dark matter[2].

Similar behaviour was soon seen in other merger events [17, 18]. However, conflicting evidence also soon appeared in the "Train Wreck Cluster" (Abell 520). It was reported that the gravitational potential was centered on the core of the merger, indicating a significant self-interaction cross-section [19] which is difficult to reconcile with a standard WIMP. Later, the weak gravitational lensing analysis of Abell 520 was reexamined, and it was concluded that Abell was indeed consistent with predictions of collisionless dark matter, as confirmed now in many merger events [20].

1.2 Cosmological Evidence for Dark Matter

Dark matter has played a significant role in cosmology and the evolution of the universe. In this section, we outline cosmological evidence in support of dark matter, starting first with cosmological parameter values for the dark and visible sectors.

1.2.1 Cosmological Parameters

Through many observations, the universe has been revealed to exhibit extraordinary isotropy and homogeneity. The space-time metric used to encapsulate such features, the Friedmann-Lemaître-Robertson-Walker (FLRW) metric, is a maximally symmetric three dimensional space embedded in a four dimensional space-time [21],

$$ds^2 = dt^2 - a^2(t)\left(\frac{dr^2}{1-kr^2} + r^2(d\theta^2 + sin^2\theta d\phi^2)\right), \tag{1.2}$$

where $a(t)$ is the cosmological scale factor and k is the three-space curvature constant, which can be any of $-1, 0$ or $+1$. Matter in the universe is described by the energy-momentum tensor $T^{\mu\nu}$, which in terms of this metric is written as

$$T^{\mu\nu} = pg^{\mu\nu} + (p+\rho)u^\mu u^\nu, \tag{1.3}$$

where p is the isotropic pressure, $g^{\mu\nu}$ is the metric tensor, ρ is the energy density and u^μ is the velocity vector. Space-time, described by the FLRW metric, is warped in the presence of matter, described by the energy-momentum tensor. These are

[2]Note that an objection to the DM interpretation is that the evidence for new physics only exists through gravitational effects. As such, a suggestion is that the issue is with description of gravity, rather than a need for DM [15]. However, this is strongly disputed through evidence of merger events; even modification of gravitational laws predict gravitational potential should be centered on the observed mass, but this is not what is seen. Furthermore, features of the CMB such as the power spectrum, and measurements from BBN, cannot be explained without a new, non-baryonic type of matter.

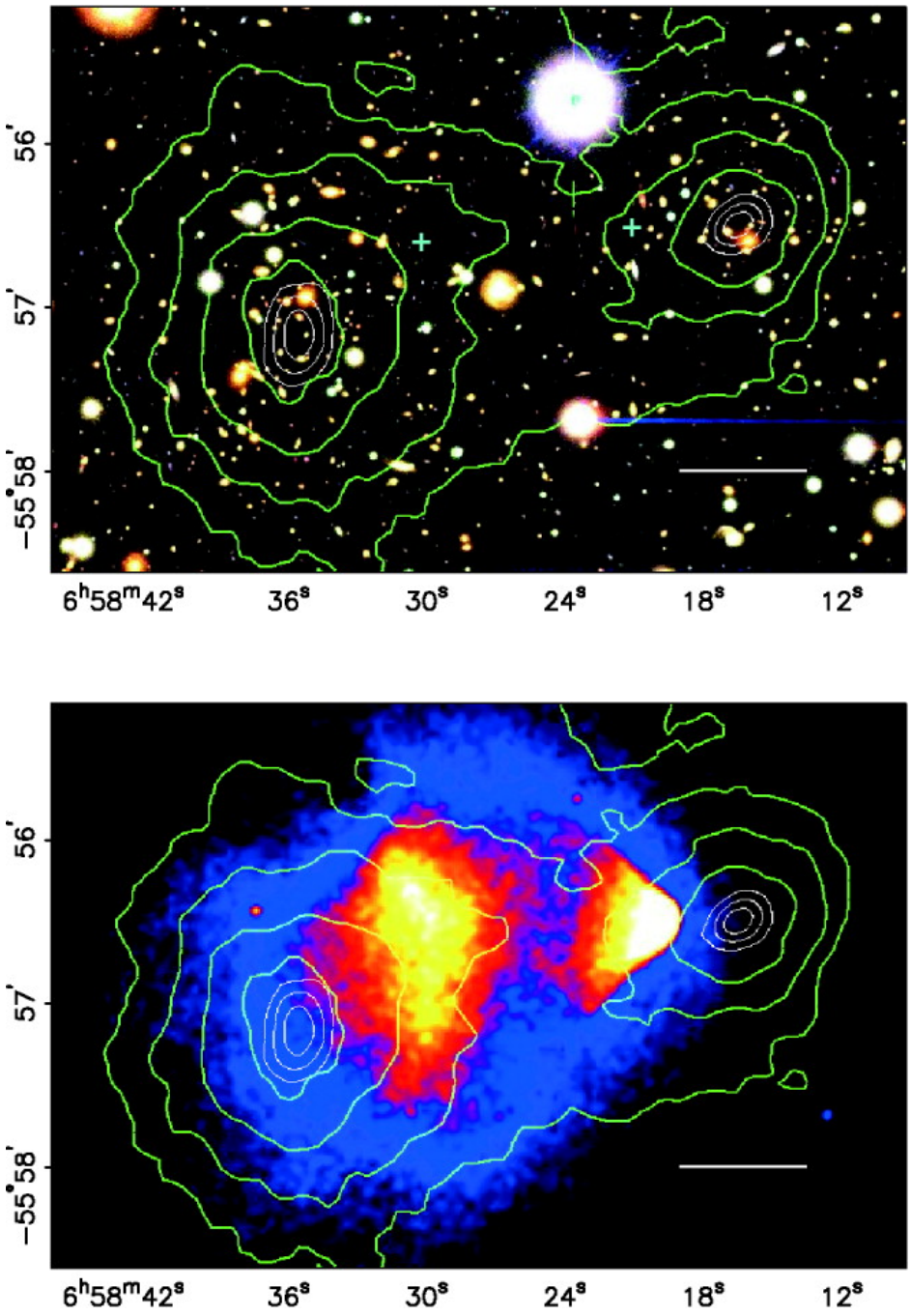

FIGURE 1.2: **Top:** Optical image of the Bullet Cluster from the Hubble Space Telescope, with the green lines showing mass density contours as determined by weak gravitational lensing. [14] **Bottom:** X-ray image from the Chandra telescope [16], with the hot glowing gas showing the interactions from visible matter. The gravitational potential is displaced from the bulk of the visible matter. [14]

united in the Einstein field equations,

$$R_{\mu\nu} - \frac{1}{2} g_{\mu\nu} R - \Lambda g_{\mu\nu} = 8\pi G_N T^{\mu\nu}, \tag{1.4}$$

where R and $R_{\mu\nu}$ are the Ricci scalar and tensor respectively. Λ is the cosmological constant, which drives the accelerated expansion of space-time. The zero-zero component of these equations gives the Friedmann equation,

$$\left(\frac{\dot{a}(t)}{a(t)}\right)^2 = \frac{8\pi G_N \rho}{3} - \frac{k}{a(t)^2} + \frac{\Lambda}{3}. \tag{1.5}$$

The ratio of $\dot{a}(t)$ to $a(t)$ is defined as the Hubble parameter H,

$$H(t) \equiv \frac{\dot{a}(t)}{a(t)}, \tag{1.6}$$

which is related to the critical energy density of the universe, ρ_c, by

$$\rho_c \equiv \frac{3H^2}{8\pi G_N}, \tag{1.7}$$

where a flat universe is assumed ($k = 0$, $\rho = \rho_c$) as per current observations. Therefore, the contribution of any particular species, Ω_i, to the total energy-matter budget of the universe can be determined by the ratio of the observed cosmological density of the particular species ρ_i to the total critical density of the universe,

$$\Omega_i \equiv \frac{\rho_i}{\rho_c}. \tag{1.8}$$

The total energy-matter budget of the universe is shared between matter, Ω_{m}, radiation, Ω_{rad}, and the repulsive energy driving accelerated expansion, Ω_Λ, called "dark energy", such that

$$\Omega_{\mathrm{universe}} = \Omega_{\mathrm{m}} + \Omega_\Lambda + \Omega_{\mathrm{rad}}, \tag{1.9}$$

where Ω_{rad} only made a non-negligible contribution in the early universe. In the universe today, effectively only matter and dark energy contribute. To determine the relative amounts of matter and dark energy today several key observations are combined, as discussed in the following subsection.

1.2.2 CMB, BAO, BBN and Supernovae

In 1998 it was first observed that the universe is expanding at an increasing rate [22]. Precise measurements of the acceleration of this rate can be found using a class of astrophysical objects called "standard candles". Objects in this class, such as type-1a supernovae (SNe Ia) and variable stars, have a known absolute luminosity. Therefore, their redshift can be used to determine the rate in which they are accelerating away. Similarly, and independently, objects called "standard

rulers" can be used to determine changes in expansion rate, as standard rulers have known physical lengths over cosmic time. A key example are Baryonic Acoustic Oscillations (BAO). BAO are acoustic waves produced in a battle between interactions of matter and gravity within the anisotropic primordial plasma, leading to baryonic shells of a known physical length (the sound horizon) [23]. Measurements of the sound horizon at the time of recombination from the cosmic microwave background (CMB) can be compared to measurements in the universe today, independently revealing the expansion rate of the universe.

A large scale study was performed using hundreds of SNe Ia, called the "union set", to determine properties of the universe consistent with the currently observed expansion rate, and this can be combined with data on BAO and the CMB, to determine the energy-matter content of the universe. The intersection of this data, as shown in Fig. 1.3, shows each of these measurements are in agreement on the energy-matter content of the universe. Most recently, the contributions from matter Ω_m and energy Ω_Λ are measured as [24]

$$\Omega_m = 0.308 \pm 0.012, \quad \Omega_\Lambda = 0.728 + 0.015 - 0.016. \tag{1.10}$$

Finally, the matter content of the universe is shared between baryonic matter, Ω_b, and dark matter Ω_χ,

$$\Omega_m = \Omega_b + \Omega_\chi. \tag{1.11}$$

The precise breakdown of these components can be determined by examining Big Bang Nucleosynthesis (BBN) and CMB data of the early universe. In the early universe, photons were in thermal equilibrium with the primordial electron proton plasma. After the Big Bang, the universe continually cooled, and after 380,000 years this eventually allowed stable neutral atoms to form. This made the plasma transparent to photons, causing the photons to decouple, such that they are mostly only affected by redshift due to increasing scale factor $a(t)$, resulting almost in a black body spectrum with $T \sim 2.73$ K. While the photon distribution was homogeneous, BAO led to anisotropies in the CMB, which are seen in the angular power spectrum of the CMB. The acoustic peaks are highly sensitive to the dark and visible content in the early universe. This has been measured by the Wilkinson Microwave Anisotropy Probe (WMAP), as shown in Fig. 1.5.

BBN describes the origin and production of light nuclei and their isotopes (Deuterium, Helium and Lithium) in the early universe [26], which is tightly correlated with the initial baryon density. The predicted baryon density by BBN can then be compared with the observed abundances of these isotopes in the universe today. Fig. 1.4 shows the theoretical and experimental abundances of isotopes and baryon densities from BBN, overlaid with measurements of the baryon density from the CMB.

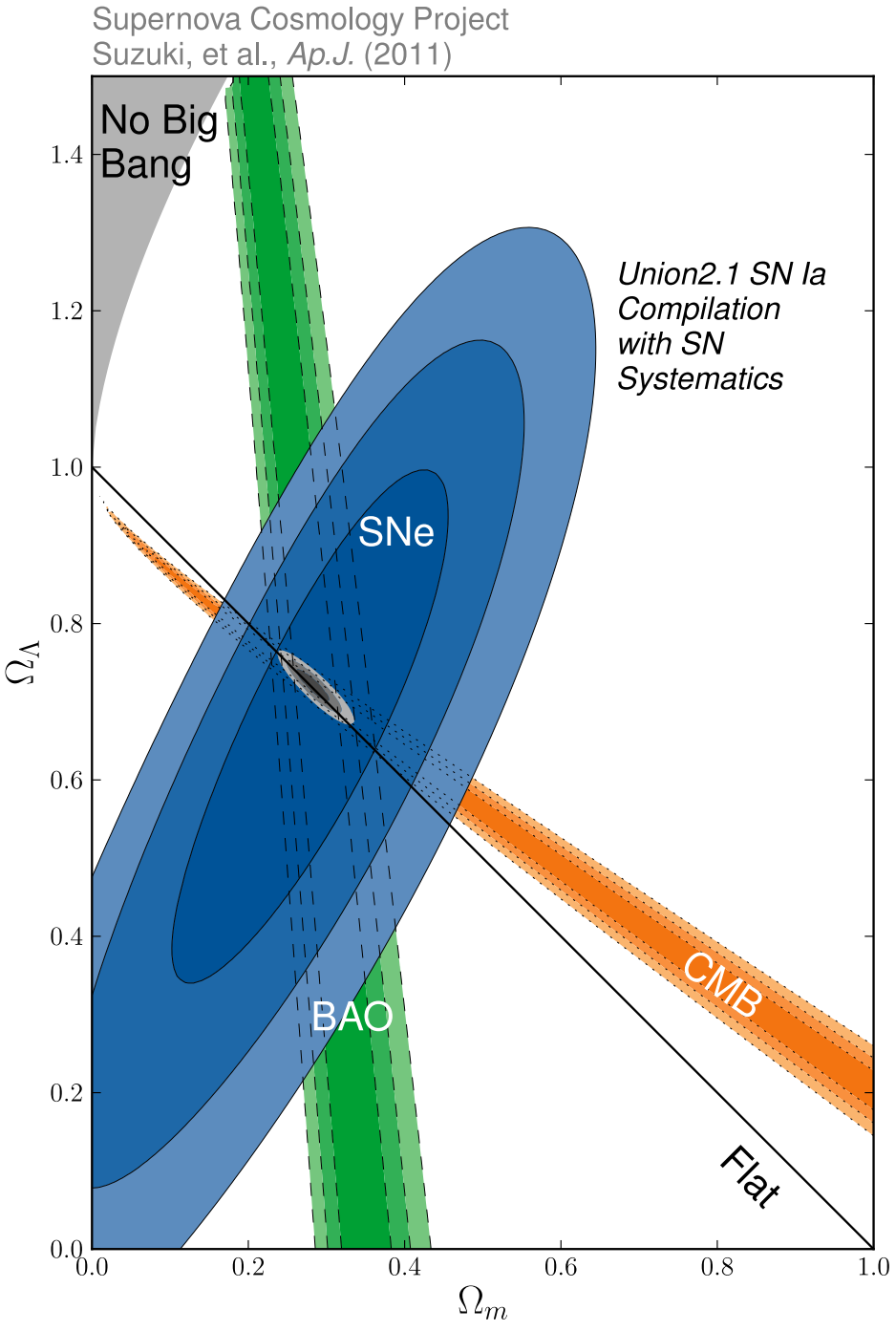

FIGURE 1.3: Combined likelihood map using CMB, BAO and the Union SNe Ia Set, for the matter $\Omega_m = \Omega_b + \Omega_\chi$ and energy Ω_Λ content of the universe. [25]

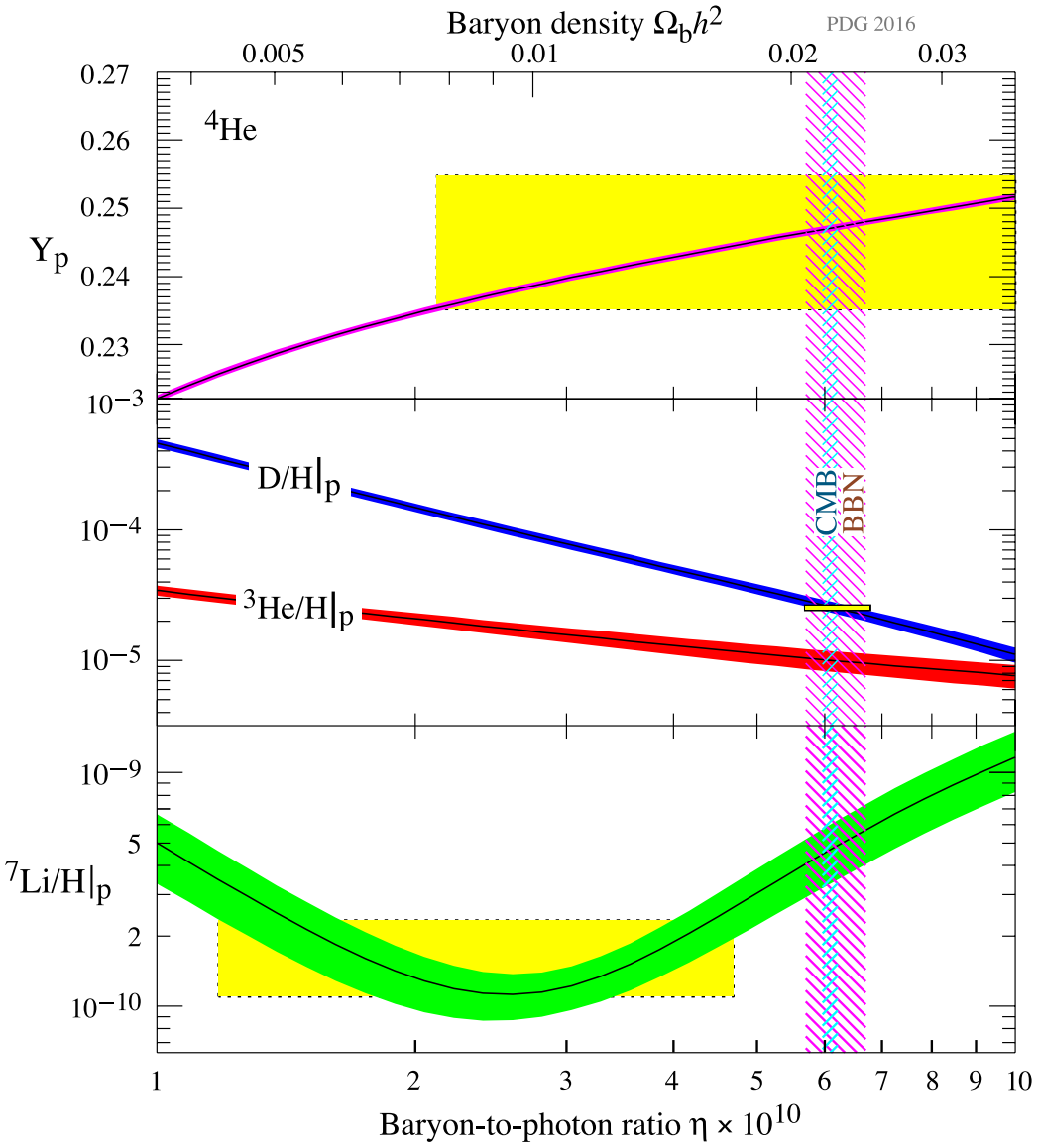

FIGURE 1.4: Theoretical abundances of isotopes (curves) and baryonic densities as predicted by BBN, overlaid with experimental measurements (boxes) of light elements at 2.75σ. The vertical bands are the baryon density determined from CMB data and the BBN concordance range. [26, 27]

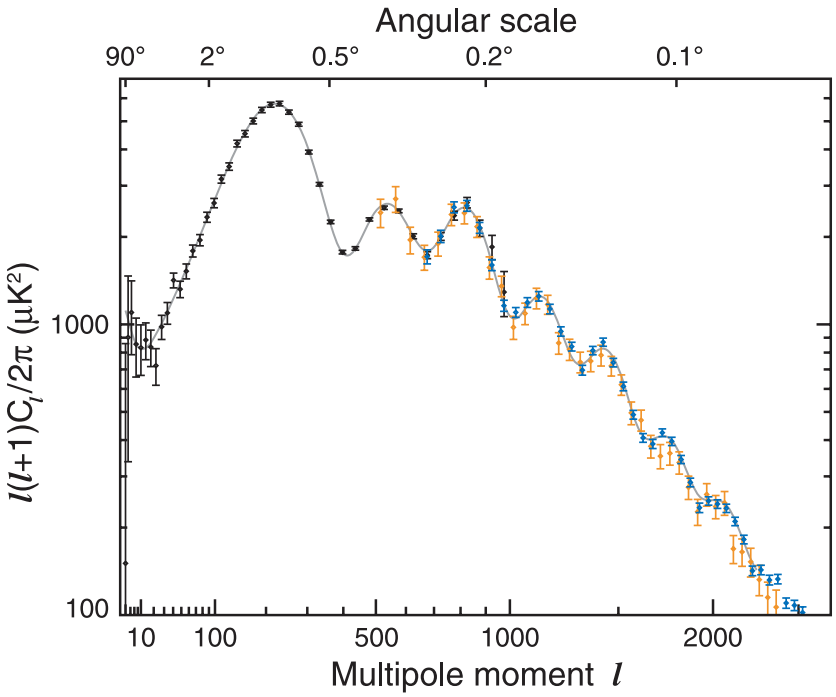

FIGURE 1.5: Temperature power spectrum of the CMB from the nine year WMAP analysis (black), South Pole Telescope (SPT) data (blue) [28], Atacama Cosmology Telescope (ACT) data (orange) [29]. The theoretical prediction by the Λ_{CDM} model (gray) matches perfectly with observation. [30]

Most recently, the total amount of baryonic and dark matter in the universe is determined to be [24]

$$\Omega_b h^2 = 0.02255 \pm 0.00016, \Omega_\chi h^2 = 0.1198 \pm 0.0015. \tag{1.12}$$

This reveals that dark matter is five times more abundant than the visible, baryonic matter in the universe.

1.2.3 Large Scale Structure

The Standard Cosmological Model, Λ_{CDM}, has been extremely successful, with predictions matching experimental measurements across many observations. It assumes a flat universe described by General Relativity which began with the Big Bang, cold (non-relativistic) dark matter and accelerated expansion of the universe driven by dark energy. In Λ_{CDM}, as the universe expands with increasing scale radius a, the Hubble parameter satisfying Eq. (1.6) can be expressed as [32]

$$H = H_0 \sqrt{a^{-3}\,\Omega_{\mathrm{m}} + a^{-4}\,\Omega_{\mathrm{rad}} + \Omega_\Lambda}, \tag{1.13}$$

where H_0 is the present-day Hubble constant. The energy density of the early universe was dominated by radiation, which scales proportionally to a^{-4}. This eventually became sub-dominant to the energy density of matter, which scales

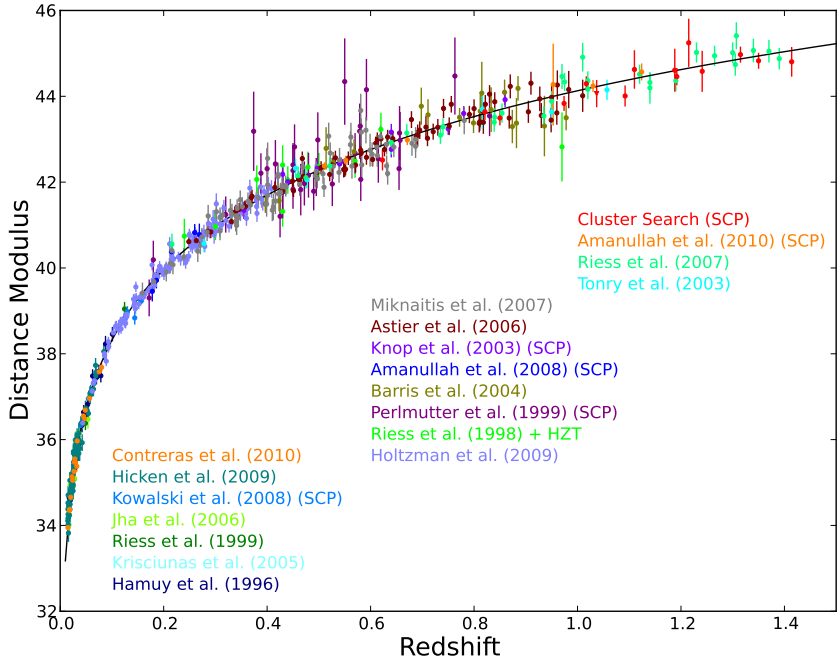

FIGURE 1.6: Measurements of density fluctuations vs. length scale across independent studies, as listed. The theoretical prediction by the Λ_{CDM} model is shown as the black line, and matches observations. [25]

proportionally to a^{-3}. In the matter dominated universe, relics of the small anisotropies of the early universe from cosmological perturbations grew into the large scale filaments and galaxy structures we observe today, highly sensitive to the presence of both dark and visible sectors. In Fig. 1.6, we show the measured density fluctuations of the universe across varying length scale. Indeed, the observations from many independent studies match the predictions of Λ_{CDM}.

Analytically, intricately describing this complex evolution to compare to observations is effectively impossible. Instead, semi-analytic techniques are used incorporating N-body simulations to compare theoretical predictions with today's observations. The Millennium Simulations [33–35] are the most complex of their kind, with the most recent run simulating 6720^3 particles in a cube with sides 13 billion light years long [35]. Such a simulation is shown in Fig. 1.7, and is further independent evidence for dark matter.

The structures observed require dark matter to be either cold (non-relativistic) or at most partially warm (semi-relativistic) at the time of structure and galaxy formation [36]. Hot (relativistic) dark matter wipes out density perturbations at small scales, such that the observed small-scale structure would not be possible. Interestingly, while structure observations match N-body simulations for Λ_{CDM} / cold dark matter at large scales, they do not for the DM density profiles of galaxies, especially in their centres. Here, N-body simulations predict a cuspy galactic centre, while observations report low density cores. Furthermore, simulations for cold dark matter overproduce the observed number of satelites of the Milky Way

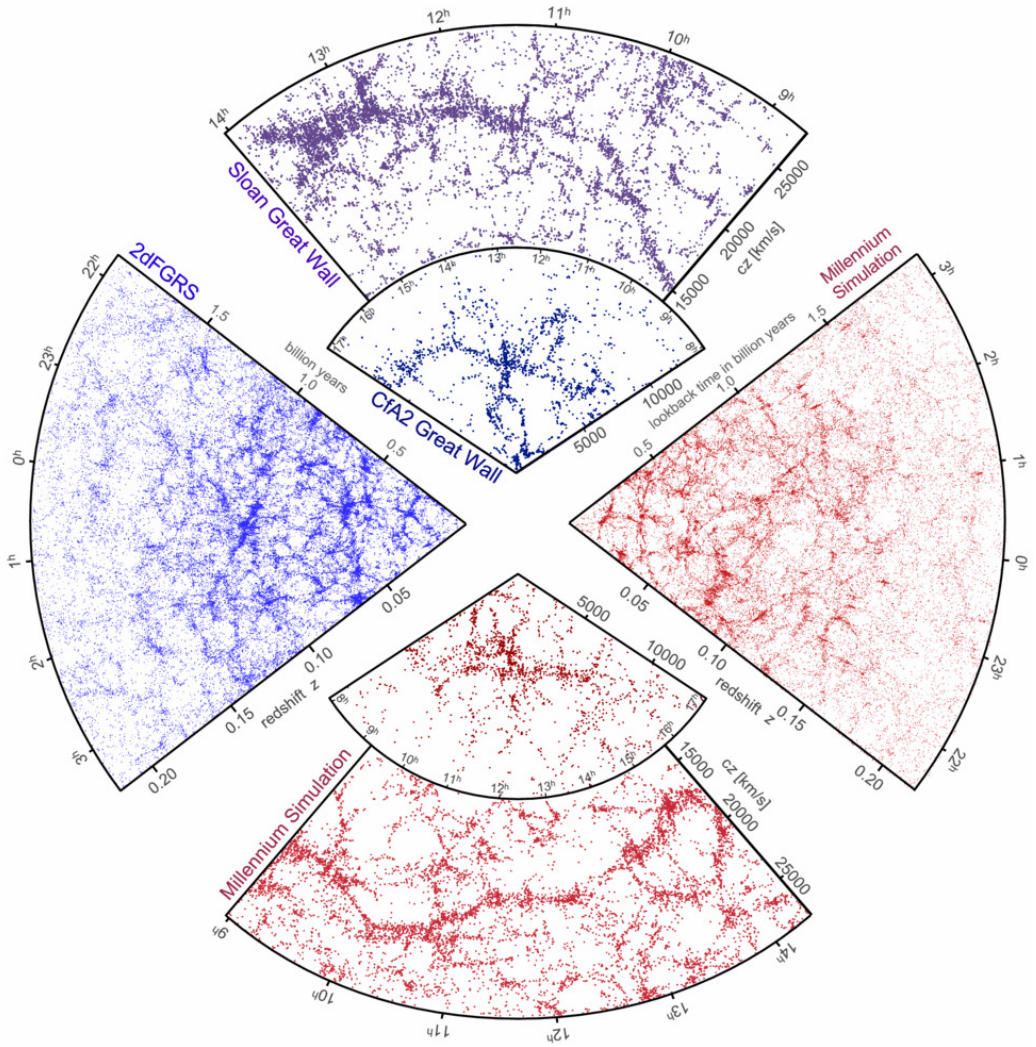

FIGURE 1.7: Large scale structure from the Millennium Simulation (red), and from large scale observations (blue) including the Coma Cluster, the CfA2 'Great Wall', the Sloan Great Wall, and 2dFGRS. [31]

(the "missing satelite" problem) [37]. For warm dark matter, the tension between theory and observation at the galactic core is ameliorated, but then an insufficient number of galactic satellites are predicted. These remain open issues for dark matter theories, but may be explained by DM self-interactions, or alternatively insufficiently incorporating galactic baryonic effects into simulations [38, 39].

1.3 Theories and Candidates

In this section, we first discuss the Standard Model of Particle Physics, which while missing a viable dark matter candidate, will provide a theoretical foundation on which to build DM models. We then outline theories which can describe dark matter, with a focus on WIMPs, then discuss their detection prospects through collider, direct and indirect searches.

1.3.1 Adding to the Standard Model

The Standard Model (SM) of Particle Physics is the reigning theory describing the particle content of the universe, unifying our knowledge of quantum mechanics and special relativity. It is the accumulation of decades of bottom-up approaches to matching theory with physical observations. To date, it has been extremely successful, with its predictions confirmed to high experimental precision through numerous experiments.

The unbroken local symmetry group of the SM is $SU(3)_c \otimes SU(2)_W \otimes U(1)_Y$, where $SU(3)$ gauge interactions (QCD) describe the strong interactions, and $SU(2)_W \otimes U(1)_Y$ describes electroweak (EW) interactions. The number of gauge degrees of freedom is paralleled by the number of generators of the Lie algebra of the symmetry group — there are a total of 12 gauge degrees of freedom shared by the gauge bosons of each group, g, W, B respectively. However, W and Z bosons are observed to be massive, and with only two degrees of freedom in the unbroken phase, from two transverse polarization states,

$$\epsilon^{\mu}_{\pm} = \frac{1}{\sqrt{2}}(0, 1, \pm i, 0), \tag{1.14}$$

these gauge bosons cannot be massive (here the motion is in the $\hat{z}$ direction). Three degrees of freedom are required for a boson to be massive, as by spanning a 3-basis it is no longer possible to boost into a frame where all existing polarizations are parallel (i.e. by Lorentz invariance the boson must be massive in all frames). The third degree of freedom for a massive gauge boson comes from longitudinal polarizations,

$$\epsilon^{\mu}_{0} = \frac{1}{M}(p, 0, 0, E), \tag{1.15}$$

which is parallel to the momentum direction.

In the SM, the mechanism to break the electroweak symmetry and provide fundamental masses was first posited in 1964, called the Higgs mechanism [40–42]. In the Higgs mechanism, a complex scalar doublet charged under $SU(2)_L$,

$$\Phi \equiv \begin{pmatrix} \phi^+ \\ \phi^0 = \frac{1}{\sqrt{2}}(H + v_{\mathrm{EW}} + i\Im\phi^0) \end{pmatrix}, \tag{1.16}$$

obtains a vacuum expectation value (vev) to spontaneously break the electroweak (EW) gauge group of the SM, $SU(2)_W \otimes U(1)_Y$, down to $U(1)_{EM}$. The Goldstone modes associated with the symmetry breaking (extra degrees of freedom provided by the Higgs field), $\phi^\pm$ and $\Im\phi^0$ become the longitudinal modes of the $W^\pm$ and Z bosons respectively. As the gauge bosons have gained an additional degree of freedom, with a total of three, they are massive. According to the Goldstone Boson Equivalence theorem, the origin of these longitudinal modes is recovered in the high energy limit, where the Goldstone boson from spontaneous symmetry breaking is equivalent to the longitudinal mode in Eq 1.15. The photon, γ, mediates EM interactions, and remains massless under the unbroken $U(1)_{EM}$. Finally, what remains is the real neutral scalar, $1/\sqrt{2}(H + v_{\mathrm{EW}})$, which is the Higgs boson, experimentally discovered as the final piece of the SM, leaving the SM a physically self- consistent theory[3].

The fundamental matter content of the SM, fermions, are described in classes; leptons and quarks, each with three increasingly massive copies of the same gauge interaction structure: electrons (e) muons (μ) and taus (τ), and up (u) charm (c) top (t), down (d) strange (s) bottom (b) quarks.

The left handed (L) spinor components of $U(1)_{EM}$ charged leptons $\ell_L = e_L, \mu_L, \tau_L$ are related to the $U(1)_{EM}$ neutral leptons of the same flavour, $\nu_L = \nu_{eL}, \nu_{\mu L}, \nu_{\tau L}$, by an $SU(2)_L$ transformation, and only the charged leptons have right handed (R) spinor components, which are singlets under $SU(2)_L$:

$$L \equiv \begin{pmatrix} \nu_L \\ \ell_L \end{pmatrix} \sim (1, 2, -1/2), \quad \ell_R \sim (1, 2, -1). \tag{1.17}$$

The other type of fundamental fermions in the SM, quarks, are also charged under $SU(3)$ color,

$$Q \equiv \begin{pmatrix} u_L \\ d_L \end{pmatrix} \sim (3, 2, -1/6), \qquad \begin{matrix} u_R \sim (3, 1, 2/3), \\ d_R \sim (3, 1, -1/3). \end{matrix} \tag{1.18}$$

Without introduction of the Higgs field, any mass terms for SM fermions break the SM gauge symmetry. Once the SM Higgs is included, the quarks and charged

[3]Furthermore, without the Higgs, scattering of longitudinal W bosons in the process $W_L^+W_L^- \to W_L^+W_L^-$ grows like $\sqrt{s}/m_W$, violating unitarity at high energies. An internal Higgs exchange contribution to $W_L^+W_L^-$ removes these violations, taming the bad high energy behaviour and making the SM a physically consistent theory.

leptons obtain mass through the $SU(2)$ invariant Yukawa interaction

$$\lambda_{i,j}\overline{\psi_L^i}\Phi\psi_R^j + h.c., \tag{1.19}$$

where $\lambda_{i,j}$ encapsulates coupling strength and therefore masses for each fermion, related to the Higgs vev.

Despite the perennial success of the SM, it cannot account for all observed physical phenomena. The introduction of the Higgs field, while solving the problem of origin of fundamental mass, triggers a new problem of naturalness, as the contributions to the Higgs mass from quartic self-interactions require an excessively fine-tuned cancellation with the bare Higgs mass, to produce the physically observed Higgs mass.

In addition, the fundamental force of gravity, as separately described by General Relativity, cannot be incorporated to the SM. This is because the Poincaré symmetry of the SM gauge group requires Minkowski (flat) spacetime; warped spacetime in the presence of matter, as predicted by General Relativity, destroys the underlying symmetry structure of the SM.

Importantly, facing the topic of this thesis, the SM fails to offer a DM candidate. Its closest candidates, the three families of electrically neutral neutrinos, were promising candidates in the past [43, 44], but have been shown to be too light and thus relativistic [45] to reproduce the observed behaviour of DM. Among other reasons, these failures motivate building and studies of Beyond the Standard Model (BSM) theories. To describe the particle nature of DM in this thesis, we will borrow building blocks and concepts from SM theory, but must in general go beyond to accurately capture features of the observed universe.

1.3.2 Theories for Dark Matter

There exist a plethora of BSM models in the literature, many with their own distinct DM candidates. These candidates are varied in their nature, in their type and in their predictions. For example, DM can have a mass m_χ ranging from $10^{-31} < m_\chi < 10^{48}$ GeV, spanning 80 orders of magnitude [46, 47].

To match the DM observations described in the previous section, there are some minimal requirements of DM candidates. These are that the candidate or candidates within the theory are:

- **About five times more abundant than baryonic matter:** Measurements from BBN, BAO, CMB, and Supernovae provide ratios as per Eq. (1.12). BBN, CMB and large scale structure data reveal DM cannot be predominantly baryonic matter, including MACHOs (Massive astrophysical compact halo objects) [48] (this is also independently confirmed by weak gravitational lensing [49]).

- **Stable, or have lifetime greater than age of universe:** DM needs to exist long enough to continually produce the observed phenomena. In many theories, this is due to DM being charged under a discrete global symmetry forbidding its decay.

- **Gravitationally interacting:** Evidence presented in the previous section demonstrates DM must have gravitational interactions.

- **Either neutral or very lightly charged under EM:** The upper bound of EM charge q_{DM} for millicharged DM is $|q_{\rm DM}| \lesssim 10^{-14}|e|m_{\rm DM}/{\rm GeV}$, arising from limits of magnetic fields in galaxy clusters [50].

- **Mostly dissipationless:** Dark haloes do not allow for large amounts of cooling via radiation. However, a small fraction could be allowed via dark radiation, in scenarios where more than one dark structure is present, such as double disk DM [51, 52]. Alternatively, if DM is dissipative, energy injection is required from other substantial heat sources such as supernovae [53] to reconcile observations of galaxy structures.

- **Either self-interacting or non-self-interacting:** The upper limit on DM self interactions is $\sigma_{\rm DM-DM}/m_{\rm DM} \lesssim 1.8\,{\rm barn/GeV}$, arising from observations of the Bullet cluster [54, 55]. DM self-interactions may solve many problems of galactic structure [36]. Further, the non-observation of dark acoustic oscillations impose that an upper limit of five percent of DM may interact strongly with dark radiation [56].

- **Mostly either cold (non-relativistic) or warm (semi-relativistic):** Dark matter cannot be hot (relativistic) due to observations of small-scale structure. If the free-streaming length of DM is much larger than small (galactic) scales, density perturbations are wiped out, in tension with observations.

Some popular DM candidates satisfying these conditions are shown in Fig. 1.8 as a function of their mass scale. These include Fuzzy DM [46], Ultra-light scalars [57], Dark Photon Condensates [58], the QCD axion [59, 60], sterile neutrinos [61–64], Gravitino [65], Strongly Interacting Massive Particles (SIMPs) [66], Asymmetric DM [67], Weakly Interacting Massive Particles (WIMPs) [21], Topological Defects [68], WIMPZILLAs [69], and Primordial Black Holes [47]. The motivations behind these models, like their candidates, are greatly varied. These range from linking the origin of baryonic asymmetry in the visible sector, with an asymmetry in the dark sector, such as in Asymmetric DM, to a residual DM candidate from solving the strong CP problem of the SM, such as the QCD axion.

While the motivation behind many BSM theories is to solve many missing observational predictions of the SM, some BSM theories designed to solve issues in the SM naturally provide a DM candidate as a byproduct. Many of these DM candidates just happen to naturally emerge around the weak scale, pointing

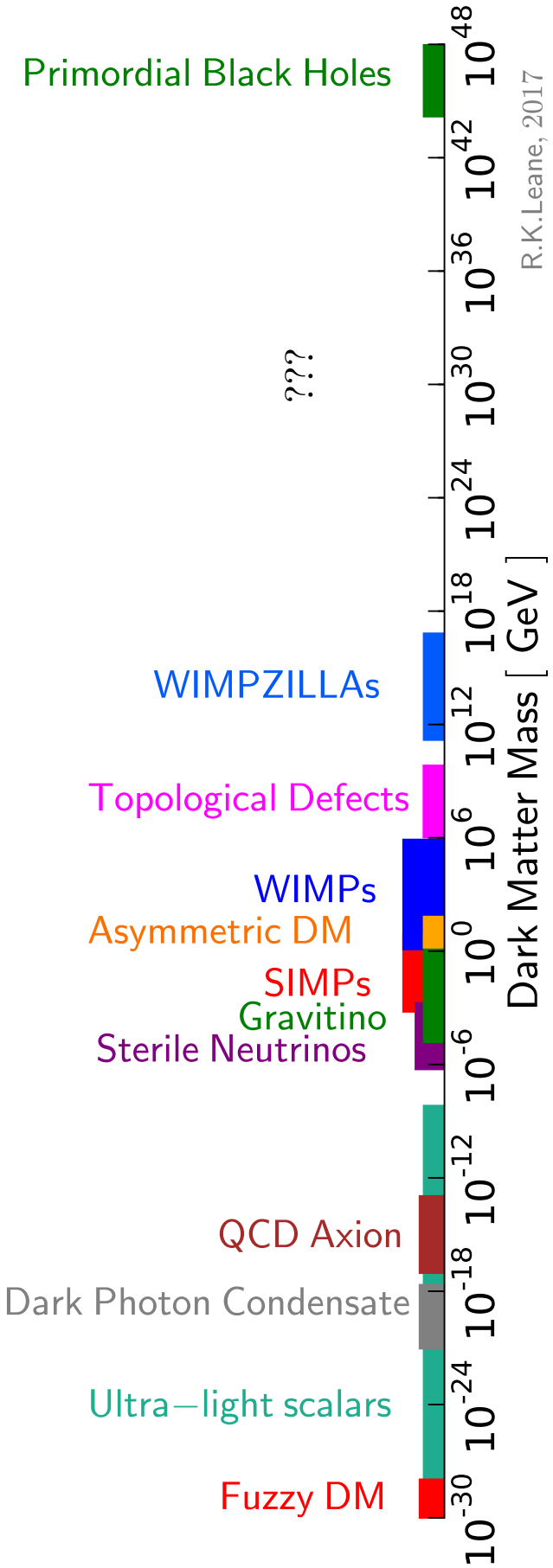

FIGURE 1.8: Dark matter candidates as a function of their mass scale.

towards an appealing WIMP DM candidate from both a particle physics and astrophysics perspective. WIMPs also offer realistic detection prospects, as they produce signals in the energy range of many experiments. For these reasons, we now focus our attention of WIMP DM candidates.

1.3.3 Weakly Interacting Massive Particles and Thermal Freezeout

WIMPs are nicely motivated, as a class of particles with the properties outlined above, as well as a weak scale interaction cross section which naturally produces the right amount of dark matter in the universe today. For thermal WIMPs, this is achieved with DM in thermal and chemical equilibrium with SM particles in the early universe. As the universe expands, DM particles become increasingly separated, and particle-antiparticle annihilation to SM particles can no longer occur on a large scale. DM then "freezes out", and what is left is a relic density of DM particles, scattered throughout the universe, which should match that of Eq. (1.12). This means that the larger (smaller) the annihilation cross section, the lower (higher) the relic density.

Specifically, the evolution of the number density of DM particles, n_χ, throughout the expanding universe is described by the Boltzmann equation

$$\frac{dn_\chi}{dt} = -\langle\sigma v\rangle(n_\chi^2 - n_{\chi,eq}^2) - 3Hn_\chi, \tag{1.20}$$

where H is the Hubble parameter related to the critical density ρ_c as per Eq. (1.7), and n_χ the equilibrium number density for non-relativistic DM defined as

$$n_{\chi,eq} = g\left(\frac{m_{\rm DM}T}{2\pi}\right)^{3/2}\exp\left(\frac{-m_{\rm DM}}{T}\right), \tag{1.21}$$

with g as the number of DM internal degrees of freedom. The Boltzmann equation can be rewritten in terms of the comoving number density, $Y = n_\chi/s$, as a function of $x = m_\chi/T$,

$$\frac{dY}{dx} = \frac{1}{3H}\frac{ds}{dx}\langle\sigma v\rangle(Y^2 - Y_{eq}^2), \tag{1.22}$$

where the total entropy density s for radiation as function of the temperature of the thermal bath T is

$$s = h_{\rm eff}(T)\frac{2\pi}{45}T^3. \tag{1.23}$$

Therefore combining with Eq. (1.7) the Boltzmann equation is

$$\frac{dY}{dx} = -\sqrt{\frac{\pi g_*}{45G_N}}\frac{m_{\rm DM}}{x^2}\langle\sigma v\rangle(Y^2 - Y_{eq}^2), \tag{1.24}$$

where $g_* \approx 100$ is the number of degrees of freedom at freeze-out. Approximating the number density today, n_0 as $Y_{t\to\infty}s_0$ (where s_0 is the entropy density today),

the freeze out point occurs when [21]

$$Y_{\infty}^{-1} = \sqrt{\frac{\pi g_*}{45}} M_{\text{Planck}}(a + 6b/x)x^{-2}, \tag{1.25}$$

where a and b are respectively contain the leading s and p-wave contributions to the DM annihilation cross section (see Eq. 1.38). To describe the relic density in terms of the critical energy density, we use the relation

$$\Omega_{\chi} = \frac{\rho_{\chi}}{\rho_c} = \frac{s_0 Y_0 m_{\chi}}{\rho_c}, \tag{1.26}$$

to arrive at the relic density of DM,

$$\Omega_{DM}h^2 \approx \frac{1.07 \times 10^9 \text{GeV}^{-1}}{M_{\text{Planck}}} \frac{x_{\text{F}}}{\sqrt{g_*}} \frac{1}{a + 3b/x_F}, \tag{1.27}$$

where the freeze-out temperature T_F is included in $x_F \equiv m_{\chi}/T_F$, where usually $x_F \approx 20$. This is shown in Fig. 1.9.

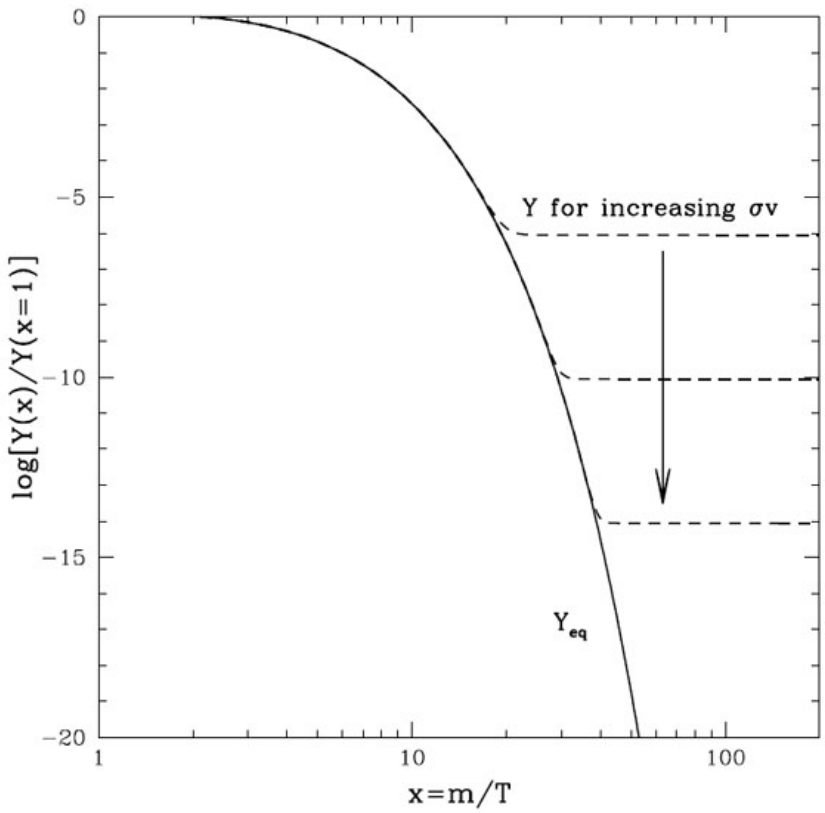

FIGURE 1.9: Departure of comoving number density from thermal equilibrium (solid) at freezeout (dashed line) for increasing annihilation cross section as a function of dark matter mass m over equilibrium temperature T. [70]

The relic density is predominantly given by the s-wave contribution, which is

$$\Omega_\chi h^2 \approx 0.12 \times \frac{2.2 \times 10^{-26} \text{cm}^3/\text{s}}{\langle \sigma v \rangle} \qquad \text{(Majorana)} \tag{1.28}$$

$$\Omega_\chi h^2 \approx 0.12 \times \frac{4.4 \times 10^{-26} \text{cm}^3/\text{s}}{\langle \sigma v \rangle} \qquad \text{(Dirac)} \tag{1.29}$$

Therefore, to produce the observed relic density of Eq. (1.12), the thermal relic annihilation cross section of DM is $\langle \sigma v \rangle \approx 2.2(4.4) \times 10^{26} \text{cm}^3/\text{s}$ for Majorana (Dirac) DM[4]. Strikingly, this is exactly at the weak scale, and this coincidence is refered to as the "WIMP miracle". Coupled with the theory motivation, this strongly motivates DM candidates with weak scale masses and interaction strengths, exactly in the range of experimental sensitivity. We now discuss the experimental prospects for WIMP searches in the next section.

1.4 Searches for Particle Dark Matter

1.4.1 Interpreting Searches Within a Minimal Theory Framework

It has been shown in the previous sections that there exist many DM theories each with distinct DM candidates. As we still have no information as to which theory is correct, it is desirable to interpret experimental results in a model independent manner where possible. Furthermore, to maximise the discovery potential or limits for SM across different DM searches, namely at collider (subsection 1.4.2), direct detection (subsection 1.4.3), and indirect detection (subsection 1.4.4) experiments, complementarity of these experiments should be considered. If a potential DM signal is found or excluded at a particular experiment, it can be cross checked at other experiments for consistency. Furthermore, depending on the model, some searches are better probes of different properties of DM. Exploiting complementarity of these searches in this way allows a larger overview of the currently allowed properties of DM, and provides an faster way forward for discovery.

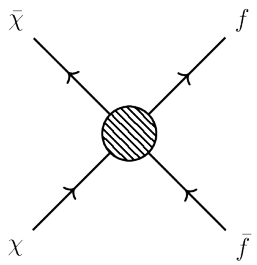

FIGURE 1.10: EFT contact interaction.

As many dark matter experiments came online, this model independent approach was first taken in the context of effective field theories (EFTs) [71, 72]. EFTs

[4]The factor of two accounts for the fact that Majorana DM is self-conjugate, and comparably Dirac DM is distinct to its antiparticle and consequently has an extra degree of freedom.

are a low-energy approximation to a complete high-energy theory, rendering themselves relatively model independent as this in the low energy limit, multiple high-energy theories may share the same behaviour. For example, in some complete theory, there may be a mediating force between the dark and visible sectors, with mass M. In the case that the momentum transfer p of the process is much smaller than the mediator mass, the interaction between fermionic DM χ and SM fermions f can be approximated at the lowest order by the effective operator[5],

$$\mathcal{L}_{\text{eff}} = \frac{1}{\Lambda^2}(\overline{\chi}\Gamma^{\mu}\chi)(\overline{f}\Gamma_{\mu}f), \tag{1.30}$$

where Γ_{μ} are the Lorentz structures and $\Lambda = M/\sqrt{g_{\chi}q_f}$ is the cutoff scale for validity, with M the mass of the heavy mediating state which has been integrated out (which holds provided $\Lambda \gg p$), and g_{χ} and q_f are the couplings of the mediator to DM and SM fermions respectively. This framework is powerful because the higher dimensional theory (in the appropriate limit) is reduced to a lower, two-dimensional parameter space, which is exactly the same across all DM processes and experiments. So, despite different experiments probing different types of DM interactions, EFTs allow for limits to be set on the same matrix element, and the same two-dimensional parameter space: the DM mass vs cutoff scale Λ.

Although EFTs were commonplace across many DM experiments, it was soon realized that they were being widely used outside their regime of validity [74–78]. In particular, at Large Hadron Collider (LHC) searches, the momentum transfer is of the TeV scale, while for many WIMP type theories, the mediator mass is not sufficiently larger than a TeV. Furthermore, as will be discussed in Chapters 2 and 3, many of the EFTs considered also do not respect the electroweak gauge symmetries of the SM, and were invalid even before the cutoff, at the electroweak scale.

These issues motivated the consideration of a less minimal framework. EFTs were gradually replaced by "Simplified Models", where one dark mediator is explicitly included, and limits are set on the mediator couplings, mass, and width, as well as the DM mass. This allows for richer phenomenology, as searches for mediators themselves are also possible. In 2015, a group of DM theorists and experimentalists agreed on "benchmark simplified models" in which to interpret experimental results (focusing on the LHC) [79], which are an s-channel spin-1 mediator, s-channel spin-0, and t-channnel colored scalar, as shown in Fig. 1.11. By their simplified nature, simplified models are not intrinsically capable of capturing full phenomenology of UV complete theories. For example, full theories may have several dark sector fields, but simplified models are designed to be used in limiting cases, such that for example these fields are sufficiently heavy they are unobservable. Unfortunately, simplified models are also plagued by some of

[5] A standard set of operators have been listed in Refs.[71, 72] (see also [73])

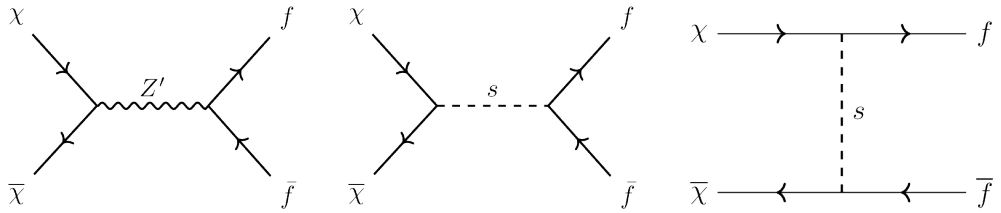

FIGURE 1.11: Benchmark simplified models for DM searches: s-channel spin-1 mediator, s-channel spin-0, and t-channnel colored scalar (left to right).

the issues of EFTs — a spin-1 mediator with axial-couplings violates unitarity at high energies, and requires a scalar to cancel the bad high energy behaviour [80]. The s-channel spin-0 model is not SM gauge invariant, as the SM fermions are charged under $SU(2)_L$, but the scalar mediator is not. Importantly, once gauge invariance is enforced, new important phenomenology can appear at experiments, which is completely missed in the simplified model framework. Such issues will be discussed in more detail in this thesis. As we will show, issues with gauge invariance have motivated next generation, "less simplified models", where benchmarks are not considered in isolation, and minimal ingredients of complete theories are included in the theoretical framework. We now discuss the DM searches themselves.

1.4.2 Collider Searches

Colliders are an excellent tool for precision measurements of new physics, as they are controlled detection environments with well-studied systematic uncertainty. Collider experiments accelerate two particle beams to high kinematic energies, and upon beam impact allow for studies of both the substructure of the beam (if any), and the production of any additional particles. Experimental collaborations feature hundreds or thousands of physicists working on specialised searches around the world. There are many types of collider experiments, past and present, which are used to test the SM as well as new physics. These include the Large Electron-Positron collider, LEP, which while no longer running, still provides the most stringent measurements of particular interaction types, due to the relatively clean electron beam source. In particular, it provides the best measure of EW precision parameters [81].

The highest powered proton-proton collider, the Large Hadron Collider (LHC), can provide a centre of mass energy up to 14 TeV (only some fraction of this is delivered to each parton, as determined by their parton distribution functions (PDFs)). This beam source produces complicated hadronic showers, requiring sometimes significant distanglement of potential signals from background. While its proton-antiproton predecessor, the Tevatron, found a 2.9 sigma hint of the Higgs boson after conclusion of operation [82], it was the LHC which finally confirmed the existence of the Higgs boson [83, 84].

At all collider experiments, DM is too weakly interacting to be recorded directly by any detector; it passes through detectors. Instead, conservation of momentum is used to determine if any momentum is unaccounted for in a collision. However, the initial state parton momentum in an individual event is not well known due to the probabilistic nature of PDFs, and so it is difficult to accurately reconstruct missing momentum in the beamline direction. Therefore, missing *transverse* momentum, MET, or $\not{E}_T$, is the key experimental parameter used to hunt for dark matter (this is also often refered to as missing transverse energy). Importantly,

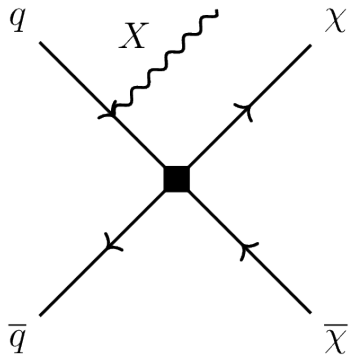

FIGURE 1.12: Common class of DM searches at the LHC, "mono-X" searches, where X is some SM particle.

dark matter $\not{E}_T$ searches are possible if some SM particles are produced in the final state alongside the DM. In particular, the most popular DM LHC searches are refered to as "mono-X" searches; they consist of a SM particle recoiling against the missing transverse momentum attributed to the non-interacting DM, as shown in Fig. 1.12. The leading experimental collaborations at the LHC searching for these signals are ATLAS and CMS [72, 85–113]. To date, there has been no DM signal at the LHC, and instead increasingly strong constraints can be set on the DM parameter space. In particular, di-jet searches can wipe out most of the parameter space which provides a thermal relic, for a standard WIMP. Summary of the current limits from ATLAS for spin-1 simplified models in shown in Fig. 1.13.

Original work on collider searches for DM will feature in Part II of this thesis.

1.4.3 Direct Detection Searches

Direct detection experiments are nestled deep in the Earth, shielded from cosmic-rays and most of other backgrounds. They wait, burrowed deep underground, with hopes of DM bouncing off the target nuclei, such that the recoil energy of SM particles can be measured, indicating some particular DM-SM scattering cross section σ_A. Quantitatively, the DM-nucleus recoil rate for DM scattering with a target nucleus with mass m_A is

$$\frac{dR}{dE} = \frac{\sigma_A}{2m_\chi \mu_A^2} \rho_\chi \eta(E,t) \tag{1.31}$$

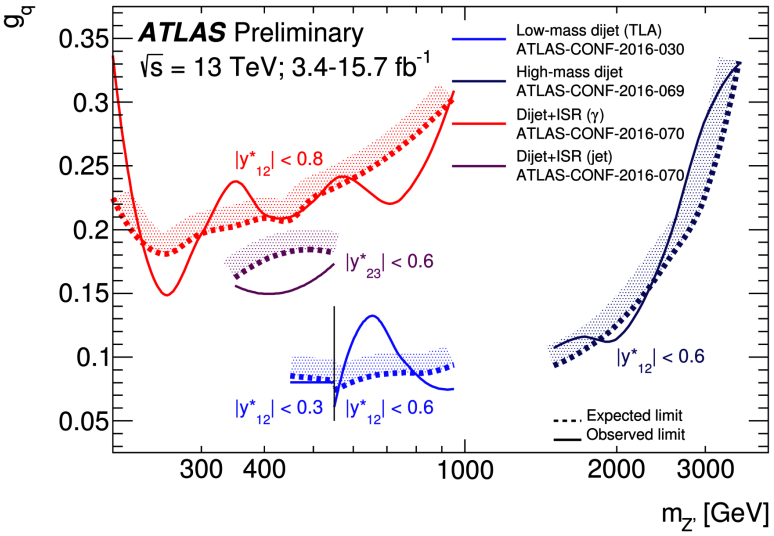

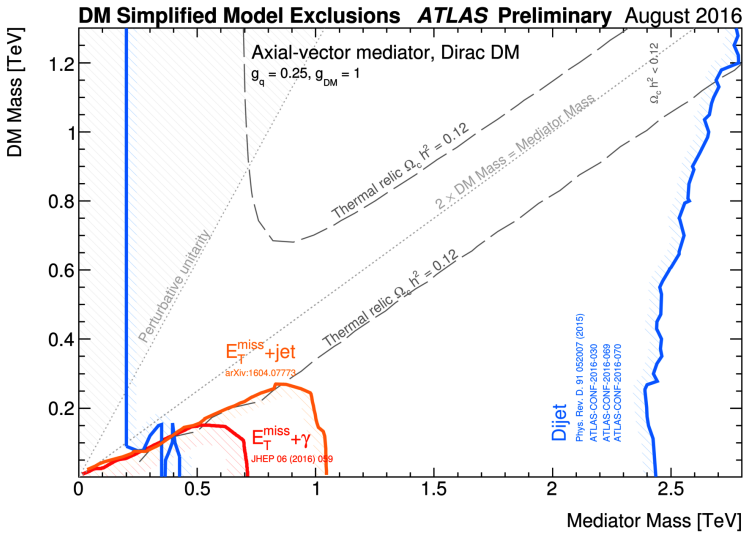

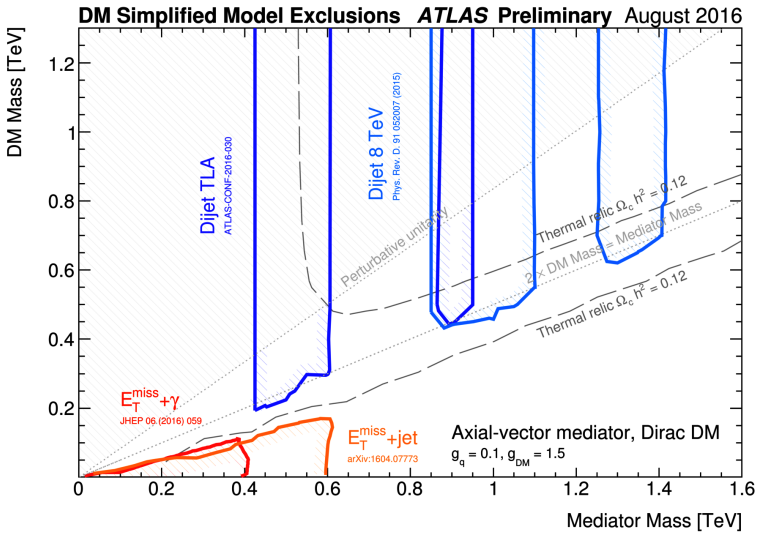

FIGURE 1.13: Current limits from ATLAS analyses for DM and a Z' mediator. Top: Limits on leptophobic Z' model described in Ref. [79]. Middle and bottom: Dirac DM with axial-vector Z' limits, with couplings as labelled [114].

where ρ_χ is the local DM density, μ_A is reduced mass of the nucleus-DM system,

$$\mu_A = \frac{m_\chi m_A}{m_\chi + m_A}, \tag{1.32}$$

and $\eta(E,t)$ is the DM velocity integral,

$$\eta(E,t) = \int_{|v|>\sqrt{m_A E/2\mu_A^2}}^{\infty} \frac{f(v,t)}{|v|} d^3v, \tag{1.33}$$

with $f(v,t)$ the DM velocity distribution in the detector frame. Importantly, astrophysical uncertainties in local DM distribution and velocities can affect reported expected direct detection rates and limits, and so there are significant efforts to present results independent of astrophysical halo models [115, 116].

The largest DM scattering rate can be obtained at experiments which are sensitive to the spin-independent scattering cross section. This is because spin-independent scattering involes a coherent sum across all target nuclei. Assuming a point like nucleus, the contribution to the spin-independent cross section is [117]

$$\frac{d\sigma_A^{SI}}{dE} = \frac{4\mu_A^2}{\pi}\left(Z f_p + (A-Z) f_n\right)^2, \tag{1.34}$$

where $A = Z + N$ is the mass number of the target (total number of protons Z and neutrons N), f_p and f_n are the effective couplings of DM to protons and neutrons respectively. If DM couples comparably to both protons and neutrons in the target, the scattering rate is enhanced by A^2, motivating targets with large masses for spin-independent searches.

Spin-dependent experiments only study independent recoils from either protons or neutrons, within the nuclei. The spin-dependent scattering cross section is linked to the spin J of the target, as

$$\frac{d\sigma_A^{SD}}{dE} = \frac{32\mu_A^2 G_F^2}{\pi}\frac{J+1}{J}\left(a_p\langle S_p\rangle + a_n\langle S_n\rangle\right)^2, \tag{1.35}$$

where G_F is Fermi's constant, a_p and a_n are effective couplings of DM to protons and neutrons respectively, and $\langle S_{p,n}\rangle = \langle N|S_{p,n}|N\rangle$ are the expectation values of the proton and neutron spin operators (in the zero momentum transfer limit). The best spin-independent limits are currently set by LUX [118, 119] and PandaX-II [120]. The most stringent spin-dependent limits are currently set by LUX [121] and PandaX-II [122] for neutron scattering, and PICO-2L [123, 124] and PICO-60 [125] for proton scattering.

As models with unsuppressed spin-independent scattering interactions must satisfy severe bounds on the properties of DM from direct detection experiments, model properties are often chosen such that the spin-independent contribution is either absent or suppressed, to avoid wiping out most of the parameter space. We will show in Chapter 8 that in such a scenario, strong complementary limits

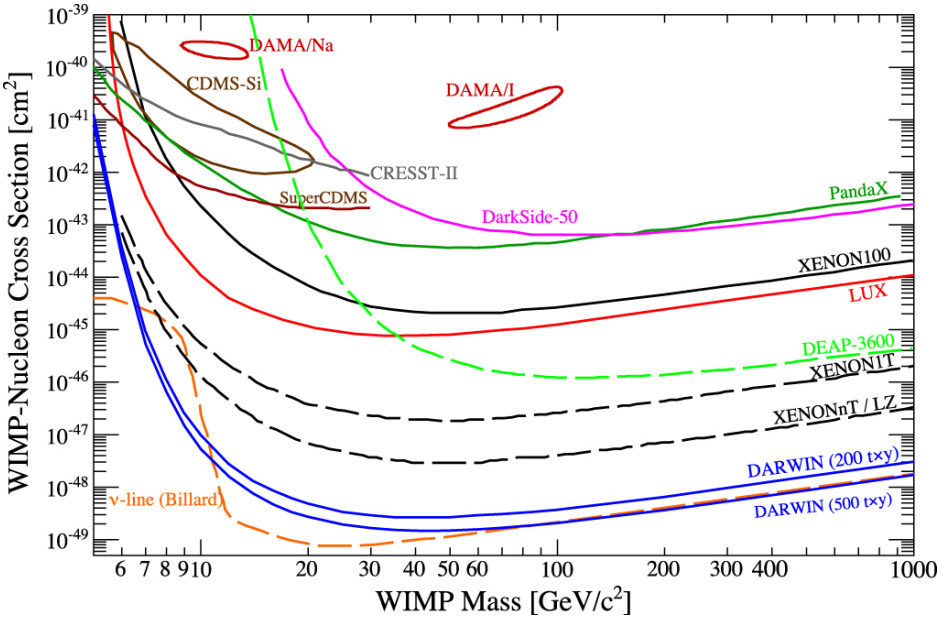

FIGURE 1.14: Summary of limits and sensitivity to DM-nucleon spin-independent scattering cross section at current and upcoming direct detection experiments [126, 127]. Note the PandaX limit has since increased at PandaX-II, to be comparable with the LUX limit shown [120].

on the DM SD-scattering cross section can still arise from gamma-ray or neutrino telescopes, if the DM exists in a dark sector with a long-lived mediator which annihilates in the Sun.

1.4.4 Indirect Detection Searches

Astrophysical searches for DM and new particles are particularly interesting, as there already exists a playground of celestial bodies which can be used to observe many types of new interactions. Indirect detection searches for DM study the sky for any unexplained excesses, which may be explained as DM annihilation products[6].

Gamma-ray Signals

Gamma rays are excellent messengers of DM annihilation, as they are not easily perturbed, and can provide significant detail of the location and nature of DM. The gamma ray flux Φ from photons with energy E_γ resulting from dark matter annihilation into a fermion species f is

$$\frac{d^2\Phi}{d\Omega dE_\gamma} = \frac{\langle\sigma v\rangle}{8\pi m_\chi^2}\left(\sum_f \frac{dN}{dE_\gamma} Br_f\right) J(\phi,\gamma), \tag{1.36}$$

[6]Depending on the astrophysical source under examination, understanding signals be inherently difficult, owing not only to large systematic uncertainties often associated with astrophysical measurements, but also due to the amount of model dependent assumptions required in order to interpret the data at all.

where Br_f is the branching fraction to the particular fermion species. The J factor is the integral over the line of sight of the DM density $\rho(r)$ squared, at a distance r from the center of the galaxy [128],

$$J(\phi, \gamma) = \int \rho^2(r) dl, \tag{1.37}$$

where ρ is the galactic DM density profile. The thermally averaged cross section, $\langle \sigma v \rangle$, is usually expressed in terms of partial waves,

$$\langle \sigma v \rangle = a + b\langle v^2 \rangle + d\langle v^4 \rangle \ldots \tag{1.38}$$

where a is the leading s-wave contribution to the cross section, b contains the leading p-wave and d contains the leading d-wave contribution. Depending on the particular DM model, the leading annihilation term may or may not have velocity dependence. The significance is that the DM velocity in the universe today is very low, $v \sim 10^{-3}$. So if the leading annihilation contribution proceeds in the p-wave, it is suppressed by a factor of $v^2 \sim 10^{-6}$, rendering indirect detection very unlikely. If the largest contribution to the cross section has no velocity suppression (is s-wave) it typically will dominate the DM signal.

Key features of the spectral shape of the gamma-ray flux can be used to identify DM, as shown in Fig. 1.15. DM annihilation directly to γX where $X = \gamma, Z, H$ creates a monochromatic line with energy $E_\gamma = m_\chi(1 - m_X^2/4m_\chi^2)$, which could appear prominently over astrophysical backgrounds, allowing the DM mass to directly be measured. Bremsstrahlung decays of DM also can feature prominently over backgrounds: Virtual Internal Bremsstrahlung as well as Final or Initial State Radiation [129–131]. Other striking spectral features are boxes [132], triangles [133] or higher-order polynomial shapes [134].

There have been many tentative identifications of gamma-ray signals of DM from the sky, but many can be described by other astrophysical phenomena. Some astrophysical regions with potential gamma-ray signals, such as the galactic centre, are DM dense and so have been a popular location to search for DM. Unfortunately, it is also a high density region for *everything else*. These means that potential signals can often be dismissed as *another cosmic prank* by pulsars. Fortunately, there do exist other DM dense regions without significant backgrounds. Dwarf spheroidal galaxies (dSphs) are extremely matter dense but hardly luminous, owing to the high DM density and low baryonic density. These currently provide the best gamma-ray limits on the DM annihilation rate, probing below the thermal relic scale for a standard, minimal WIMP, as shown in Fig. 1.16.

Other than Fermi-LAT [135, 136] other gamma-ray telescopes searching for DM include H.E.S.S. [137, 138], DAMPE [139], MAGIC [140], VERITAS [141], and HAWC [142].

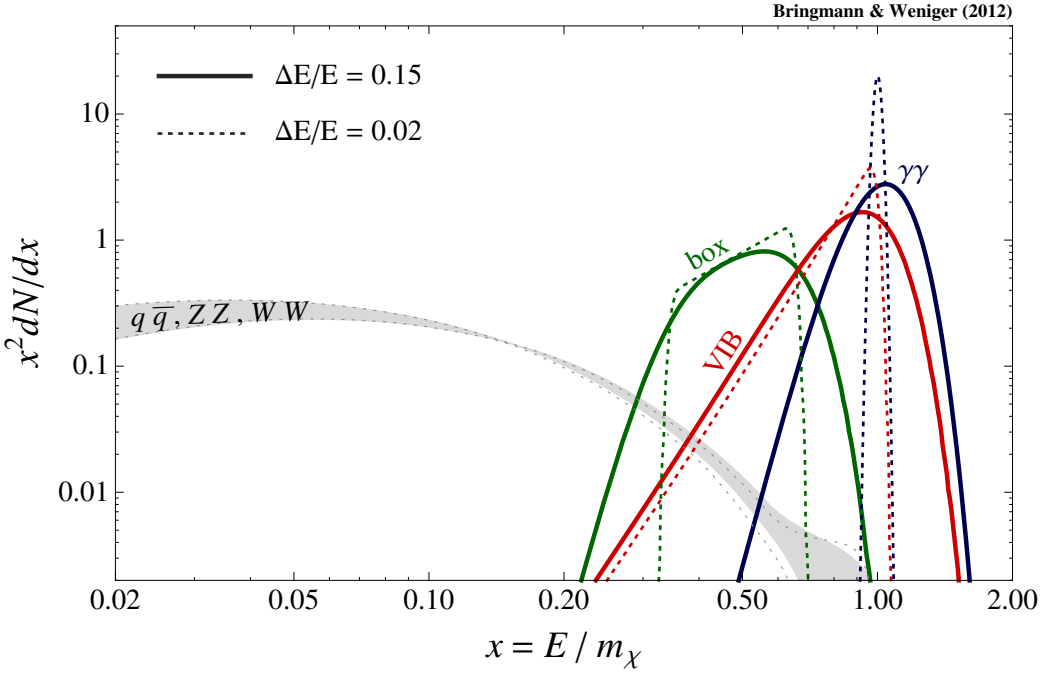

FIGURE 1.15: Gamma-ray spectral shapes for various DM annihilation processes, normalised to $N(x > 0.1) = 1$, with experimental energy resolutions $\Delta E/E$ as shown. [143].

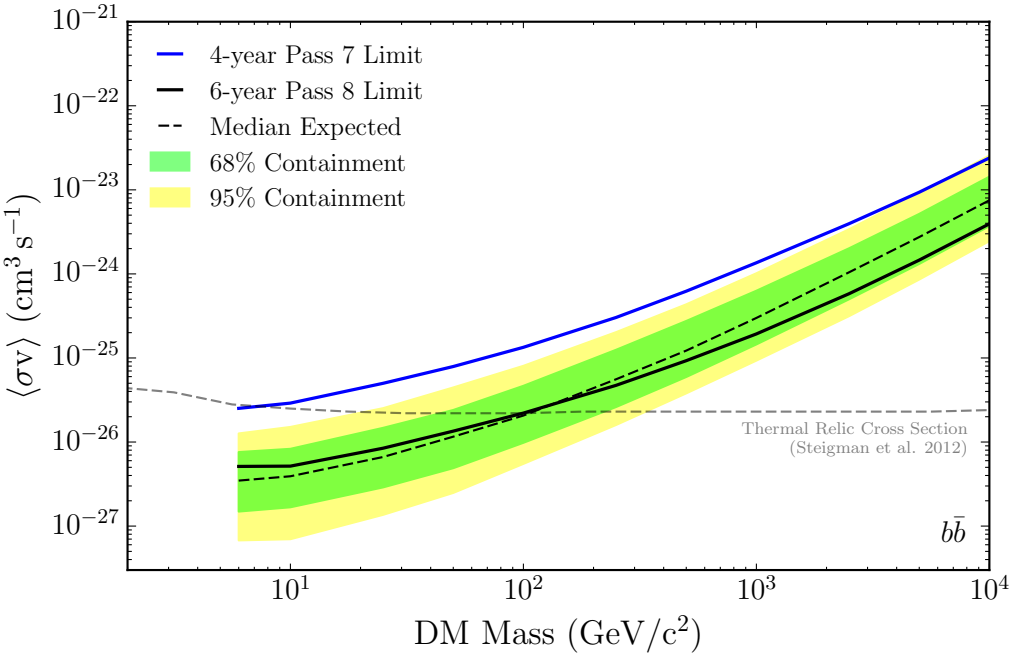

FIGURE 1.16: DM annihilation limit to $b\bar{b}$ from Fermi-LAT Pass 8 data on dwarf spheroidal galaxies. 100 percent branching fraction is assumed [135].

Positron and Neutrino Signals

Alternatively, excesses in anti-particles can be seen as a smoking gun signal for DM, as anti-particles are not generally observed in the universe except for small quantities, for example from cosmic-ray interactions or from supernovae. A potential excess in the positron fraction of cosmic rays was seen by experiments AMS-02 [144], Fermi [145], and PAMELA [146], but it is now generally accepted to be explained by pulsars. The AMS-02 data has recently been extended, as shown in Fig. 1.17, and is consistent with 1 TeV dark matter [147].

Lastly, searches for astrophysical neutrinos can reveal properties of DM, as neutrinos are very weakly interacting, allowing interactions deep inside astrophysical structures to be probed which would otherwise be lost with other final states. Searches for high-energy neutrinos in the Sun from DM annihilation are particularly promising, and currently provide some of the strongest limits on the spin-dependent DM scattering cross section. These are searched for at neutrino telescopes IceCube [148, 149], Super-K [150], Antares [151]. The upcoming gigaton neutrino detector KM3Net [152] will have similar sensitivity to IceCube. Current limits from IceCube and Super-K are shown in Fig. 1.18.

Original work on astrophysical searches for DM will feature in Part III of this thesis.

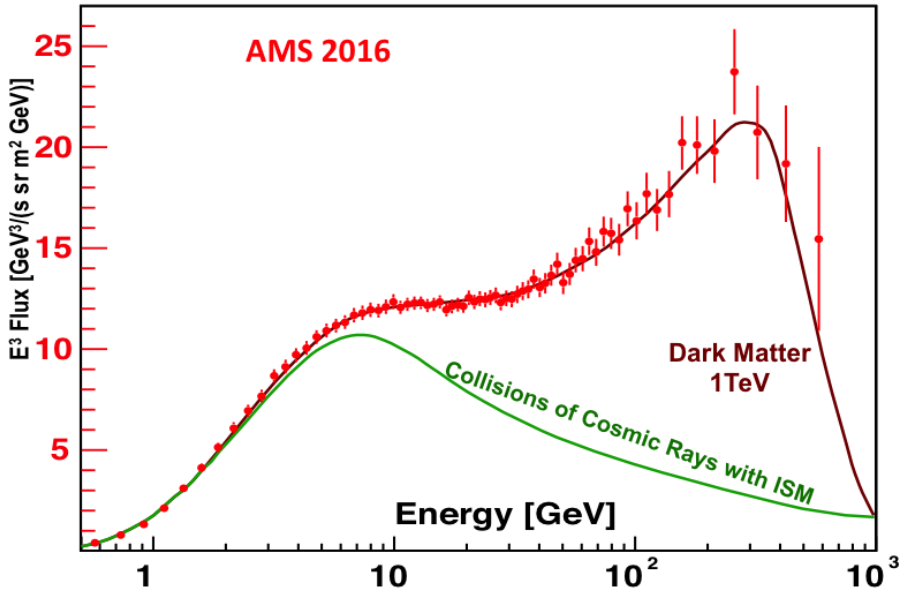

FIGURE 1.17: Positron excess flux reported by AMS-02 consistent with 1 TeV DM [147].

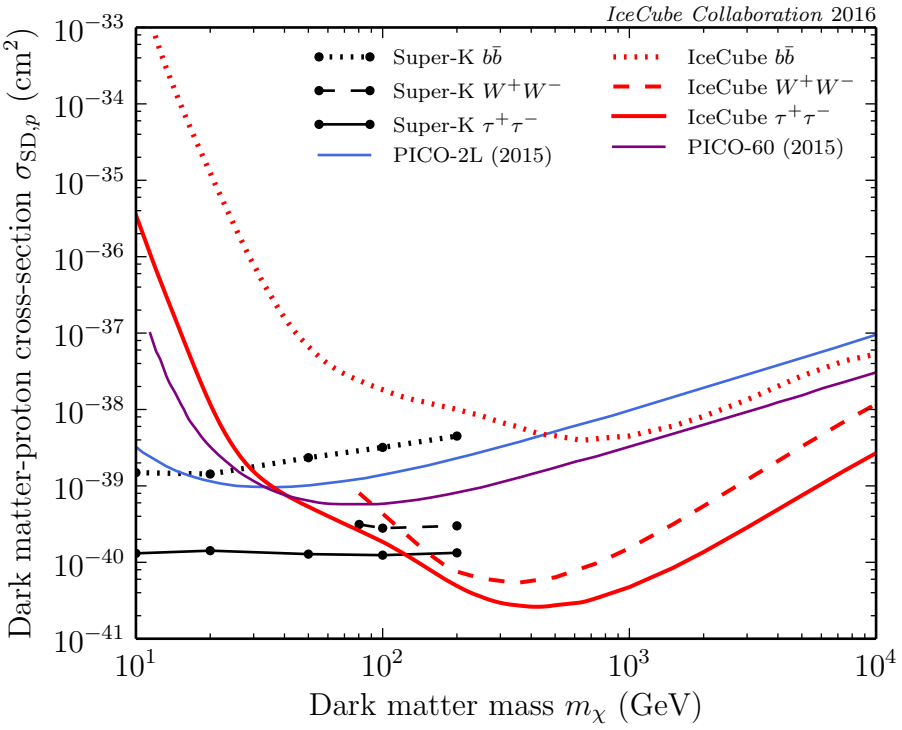

FIGURE 1.18: Limits on the DM-proton spin-dependent scattering cross section from direct detection experiments PICO-2L and PICO-60, and neutrino telescopes IceCube [148] and Super-K [150], for final states as labelled. [148].

Part II

Dark Matter at the Large Hadron Collider

In Part II of this thesis, we explore signals for dark matter at the Large Hadron Collider (LHC). This will include studies of the validity of effective field theories and gauge invariance at the LHC, in the context of the popular mono-X searches (in particular, the mono-W signal). We will also study a scenario where mono-X signatures are not possible, due to the absence of direct couplings of the dark sector to hadrons, in a setup called leptophilic dark matter, providing alternate collider signatures.

Chapter 2

Effective Field Theories and Gauge Invariance

Effective field theory (EFT) formulations of dark matter interactions are a convenient and popular way to quantify LHC bounds on dark matter. However, some EFT operators considered do not respect the weak gauge symmetries of the Standard Model. These operators break down at the electroweak scale, rather than the energy scale of new physics, and are invalid at LHC energies. We carefully discuss the circumstances in which such operators can arise, and use the mono-W process to illustrate potential issues in their interpretation and application. We also discuss a simple UV complete model that avoids such difficulties.

This chapter is based on the publication: *N. F. Bell, Y. Cai, J. B. Dent, R. K. Leane and T. J. Weiler, "Dark matter at the LHC: Effective field theories and gauge invariance", Phys. Rev. D92, no. 5 053008 (2015) [arXiv:1503.07874 [hep-ph]].* [153]

2.1 Introduction

While the EFT description is very useful at low energies, such as those relevant for direct detection, it now well appreciated that the EFT approach may be unsuitable at LHC energies. Specifically, if the momentum transfer in a process is comparable to or larger than the mass of the mediator, the EFT will not provide an accurate description of the underlying physics. Many recent papers have attempted to quantify the point at which an EFT description is no longer valid [74–78] or have proposed the use of simplified models as an alternative framework for undertaking DM searches at colliders [78, 154–159].

In this chapter we make a more subtle point: if an EFT operator does not respect the weak gauge symmetries of the SM, it may be invalid at energies comparable to the electroweak scale, $v_{\rm EW} \approx 246$ GeV, rather than the energy scale of new physics, Λ. For example, if we attempt to use electroweak gauge symmetry violating operators at LHC energies, serious difficulties can be encountered soon above the EW scale, such as the bad high energy behaviour of cross sections. An example is

the well-known unitary violation rising as $s/(4\,m_W^2)$ in $W_L W_L$ scattering, due to the longitudinal modes induced by the symmetry breaking of $SU(2)_L$ invariance. In the SM, the violations are removed by an internal Higgs particle, but in the EFT formalism internal fields are "integrated out". Thus, the limit of validity for the operator is the weak scale if any internal W, Z or Higgs particle, or a Higgs vev insertion, is present in the interaction. More generally, sacred symmetries like the electroweak Ward identity can be violated, which implies a weak-scale cutoff, as we explain later in this chapter.

2.2 EFT operators and gauge invariance

The standard list of DM-SM effective operators [72] contains several operators which violate the SM weak gauge symmetries. We argue that if an EFT operator does not respect the weak gauge symmetries of the SM, it necessarily carries a pre-factor of the Higgs vev to some power, a remnant of the $SU(2)_L$ scalar doublet

$$\Phi \equiv \begin{pmatrix} \phi^+ \\ \phi^0 = \frac{1}{\sqrt{2}}(H + v_{\rm EW} + i\Im\phi^0) \end{pmatrix}. \tag{2.1}$$

Acting as an $SU(2)_L$ doublet, enough powers of Φ are required to form an $SU(2)_L$ invariant operator. The fields $\phi^\pm$ and $\Im\phi$ are gauged away to become, in unitary gauge, the longitudinal modes of the $W^\pm$ and Z. So, in fact, it is the real, neutral field $\frac{1}{\sqrt{2}}(H + v_{\rm EW})$ whose n^{th} power appears in the operator. Commonly, the H part of the expression is omitted, leaving just an implicit $v_{\rm EW}^n$ in the coefficient. Of course, the $v_{\rm EW}^n$ must come with a Λ^{-n}. Omission of the H part in the operator may ignore some interesting phenomenology. In this chapter, we will also ignore the H contributions to operators, and focus on the operators proportional to $(v_{\rm EW}/\Lambda)^n$. Such terms in the coefficients of $SU(2)$-violating operators clearly satisfy the criterion that as $SU(2)$ symmetry is restored, $v_{\rm EW} \to 0$, the operator's coefficient vanishes, and the operator decouples. [1]

2.2.1 Scalar operator

Consider the scalar (or pseudo scalar) operators

$$\frac{m_q}{\Lambda^3}\,(\overline{\chi}\chi)\,(\overline{q}q) = \frac{m_q}{\Lambda^3}\,(\overline{\chi}\chi)\left(\overline{q}_L q_R + h.c.\right). \tag{2.2}$$

This operator is clearly not $SU(2)_L$ invariant, as χ and q_R are $SU(2)_L$ singlets, while q_L is a component (either u_L or d_L) of the usual left-handed SM doublet,

[1] In what follows, we will assume that there is but a single vev, $v_{\rm EW}$. If there were further vevs, the good relation $m_W = \cos\theta_W\, m_Z$ requires the additional vevs to come from additional doublet fields, or to be be small if coming from non-doublet fields. The vevs then add in quadrature to give $(2\,m_W/g_2)^2$. Thus, any individual vev will offer an energy-scale below the SM vev. In the sense that we will argue against larger energy-scales for effective operators, our assumption of a single EW vev is conservative.

Q_L. A coupling to the Higgs boson has been anticipated by the factor of m_q in the coefficient. Most authors invoke minimal flavor violation to motivate this choice of normalization. Although this $SU(2)_L$ violating effective operator can be a good low energy description of new physics, notice that its coefficient cannot be arbitrarily large as it is controlled by the Higgs vev. Although formally a dimension 6 operator, it is competitive only with dimension 7 operators, given its $1/\Lambda^3$ normalization.

2.2.2 Vector operator:

Now consider vector (or axial vector) operators of the form

$$\frac{1}{\Lambda^2}\left(\overline{\chi}\gamma^\mu\chi\right)\left(\overline{q}\gamma_\mu q\right) = \frac{1}{\Lambda^2}\left(\overline{\chi}\gamma^\mu\chi\right)\left(\overline{q}_L\gamma_\mu q_L + \overline{q}_R\gamma_\mu q_R\right) . \tag{2.3}$$

These operators respect $SU(2)_L$ provided that the coefficients of the u_L and d_L operators are equal[2]. Any $(\overline{u}_L\gamma_\mu u_L)$ operator that does not have a matching d_L term should be suppressed by two powers of $v_{\rm EW}/\Lambda$ (one for each unmatched u_L):

$$\frac{v_{\rm EW}^2}{\Lambda^4}(\overline{\chi}\gamma^\mu\chi)(\overline{u_L}\gamma_\mu u_L). \tag{2.4}$$

Including the suppressed coefficient, this SU(2)-violating operator competes with dimension 8 operators, i.e., while the $SU(2)$ conserving (axial)vector operators are dimension 6, $SU(2)$ violating (axial)vector operators compete with subdominant, higher-order, dimension 8 operators.

2.3 Mono-W and $SU(2)_L$ invariance

Issues arise if one tries to use gauge symmetry violating operators at LHC energies. For particular processes, the lack of gauge invariance can manifest as a violation of unitarity in high energy scattering. As an example of a problem encountered with an $SU(2)_L$ violating EFT, consider the following operator:

$$\frac{1}{\Lambda^2}\left(\overline{\chi}\gamma^\mu\chi\right)\left(\overline{u}\gamma_\mu u + \xi\overline{d}\gamma_\mu d\right). \tag{2.5}$$

This Lagrangian violates $SU(2)_L$, unless $\xi = 1$. The case of unequal u and d couplings was considered in Ref. [162], where a very strong constructive(destructive) "interference effect" was found for $\xi = -1(+1)$, the degree of which depends on the energy scale. The analysis of Ref. [162] was subsequently repeated by the LHC experimental collaborations ATLAS [163, 164] and CMS [165, 166]. We shall demonstrate that the large cross section enhancement for $\xi \neq +1$ is in fact

[2]Isospin violating operators, such as those invoked in [160, 161], can obviously be crafted from the right handed quark fields.

due the production of longitudinally polarized W's as a result of breaking gauge invariance.

At parton level, the mono-W process is $u(p_1)\overline{d}(p_2) \to \chi(k_1)\overline{\chi}(k_2)W^+(q)$. The relevant diagrams are given in Fig.2.1, and the corresponding contributions to the amplitude $\mathcal{M} \equiv \mathcal{M}^\alpha \epsilon^\lambda_\alpha(q) \equiv (\mathcal{M}^\alpha_1 + \mathcal{M}^\alpha_2)\epsilon^\lambda_\alpha(q)$ are

$$\begin{aligned} \mathcal{M}^\alpha_1 &= \frac{1}{\Lambda^2}\left[\bar{v}(p_2)\gamma^\alpha \frac{-g_W}{\not{p}_2 - \not{q}}\gamma^\mu \frac{P_L}{\sqrt{2}}u(p_1)\right]\left[\bar{u}(k_1)\gamma_\mu v(k_2)\right], \\ \mathcal{M}^\alpha_2 &= \frac{\xi}{\Lambda^2}\left[\bar{v}(p_2)\gamma^\mu \frac{g_W}{\not{p}_1 - \not{q}}\gamma^\alpha \frac{P_L}{\sqrt{2}}u(p_1)\right]\left[\bar{u}(k_1)\gamma_\mu v(k_2)\right], \end{aligned} \tag{2.6}$$

where g_W is the weak coupling constant, and ϵ^λ_α is the polarization vector of the W. We note that the W longitudinal polarization vector at high energy is

$$\epsilon^L_\alpha = \frac{q_\alpha}{m_W} + O\left(\frac{m_W}{E}\right) \sim \frac{\sqrt{s}}{m_W}. \tag{2.7}$$

Thus the high energy W_L contribution to the usual polarization sum, $\sum_\lambda \epsilon^\lambda_\alpha \epsilon^{\lambda\,*}_\beta = -g_{\alpha\beta} + \frac{q_\alpha q_\beta}{m_W^2}$, is $\epsilon^L_\alpha \epsilon^{L\,*}_\beta \approx q_\alpha q_\beta / m_W^2 \sim s/m_W^2$.

We can verify that the sum of the two amplitudes of Fig.2.1 is not gauge invariant unless $\xi = 1$, by observing that the relevant Ward identity is not satisfied. At high energy, the Goldstone boson equivalence theorem requires that the amplitude for emission of a longitudinally polarized W_L is equivalent to that for the emission of the corresponding Goldstone boson. Since the Goldstone boson couples to quarks with strength proportional to their mass, these terms are close to zero. (See Ref.[167] for a similar discussion about the related process $\chi\chi \to veW$.) The Ward identity for the longitudinal W at high energy therefore takes the form

$$\mathcal{M}^\alpha \epsilon^L_\alpha \approx \frac{q_\alpha}{m_W}\mathcal{M}^\alpha(q, ...) = i\mathcal{M}(\phi^+(q)) \simeq 0. \tag{2.8}$$

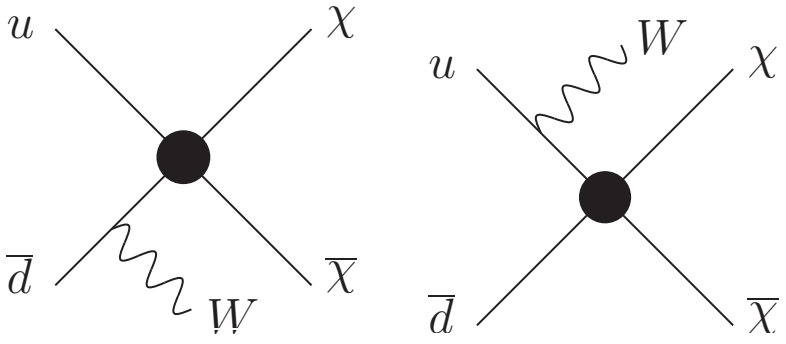

(a) $\mathcal{M}_1$ (b) $\mathcal{M}_2$

FIGURE 2.1: Contributions to the mono-W process $u(p_1)\overline{d}(p_2) \to \chi(k_1)\overline{\chi}(k_2)W^+(q)$, in the effective field theory framework.

For the sum of the mono-W amplitudes of Fig.2.1 we find

$$q_\alpha \mathcal{M}^\alpha = \frac{g_W}{\Lambda^2}\left[\bar{v}(p_2)\,(1-\xi)\,\gamma^\mu \frac{P_L}{\sqrt{2}} u(p_1)\right]\left[\bar{u}(k_1)\gamma_\mu v(k_2)\right], \tag{2.9}$$

which clearly vanishes only for $\xi = 1$.

The "interference effect" seen in the mono-W process is not truly due to constructive/destructive interference as previously claimed, but is just a manifestation of the fact that the breaking of electroweak gauge-invariance has given rise to a W_L component. The increased cross section for $\xi \neq 1$ is in fact due to unphysical terms that grow like s/m_W^2, which originate from the $+q_\alpha q_\beta/m_W^2$ term in the polarization sum. At high energy, these terms would grow large enough to violate unitarity. But even at lower energy, their presence may be problematic.

To explicitly demonstrate this behaviour, we now derive an analytic expression for the parton-level mono-W process $\bar{d}u \to \overline{\chi}\chi W^+$. We work in the center-of-mass frame, and follow the phase space parametrization described in Section V of Ref.[168]. We define θ to be the angle of the W w.r.t. the beam line and $x = 2E_W/\sqrt{s}$, where $\sqrt{s}$ is the total invariant mass. For simplicity we take $m_\chi = 0$ (the cross section will be approximately independent of m_χ for $m_\chi^2 \ll s$). We include a factor of 1/3 from averaging over initial state quark colors.

For $\xi = 1$ the differential cross section is well behaved and is given by

$$\left.\frac{d^2\sigma}{dx\,d\cos\theta}\right|_{\xi=1} = \frac{A}{3^2 2^8 \pi^3 \Lambda^4 \left(s^2x^2\sin^2\theta + 2sm_W^2\left(\cos(2\theta) - 2x + 1\right) + 4m_W^4\right)^2}, \tag{2.10}$$

where

$$\begin{aligned} A = {} & s^2 g_W^2 \sqrt{x^2 - \frac{4m_W^2}{s}}\left(1 - x + \frac{m_W^2}{s}\right)\Big[s^3x^2\sin^2\theta\left(\cos(2\theta)\,x^2 + 3x^2 - 8x + 8\right) \\ & + 2s^2m_W^2\left(\cos(4\theta)\,x^2 + 2\cos(2\theta)\left(x^3 - x^2 - 4x + 4\right) - 2x^3 + 17x^2 - 24x + 8\right) \\ & - 4sm_W^4\left(\cos(4\theta) + \cos(2\theta)\left(x^2 + 4x - 8\right) - x^2 + 20x - 17\right) + 16m_W^6\left(\cos(2\theta) + 3\right)\Big], \end{aligned}$$

If we take the limit $m_W \to 0$, remove the color factor 1/3, and replace $g_W/\sqrt{2}$ with the electron charge e, we find Eq. 2.10 reproduces the cross section for the $e^+e^- \to \overline{\chi}\chi\gamma$ monophoton process reported by Ref.[168, 169] for $m_\chi = 0$ and unpolarized e^+e^- beams. This provides a useful check for our more complicated mono-W calculation.

For $\xi \neq 1$, however, the cross section is not well behaved at high energy. The $+q_\alpha q_\beta/m_W^2$ term in the polarization sum

$$\sum_\lambda \epsilon_\alpha^\lambda \epsilon_\beta^{\lambda\,*} = -g_{\alpha\beta} + \frac{q_\alpha q_\beta}{m_W^2}, \tag{2.11}$$

contributes to the cross section a term

$$\left.\frac{d^2\sigma}{dx\,d\cos\theta}\right|_{q_\alpha q_\beta/m_W^2} = \frac{(\xi-1)^2 s^2 g_W^2\sqrt{x^2-4m_W^2/s}}{3^2 2^{13}\pi^3\Lambda^4 m_W^2} \times\left(2x^2\sin^2\theta - 16x + 16 + \frac{4m_W^2}{s}\left(\cos(2\theta)+3\right)\right), \tag{2.12}$$

which violates unitarity when $s \gg m_W^2$.

The total cross sections, for $m_\chi = 0$, are plotted in Figs. 2.2 as a function of $\sqrt{s}$. We also calculate the cross sections in MadGraph [170], and find the results agree. For brevity of notation, we have defined σ_1 and σ_2 to be the contributions to the cross section from the $-g_{\alpha\beta}$ and $+q_\alpha q_\beta/m_W^2$ terms in the polarization sum, respectively. The $\xi = 0, -1$ cross sections grow faster with $\sqrt{s}$ than for $\xi = 1$. At LHC energies the cross sections are already dominated by the unphysical terms arising from the longitudinal polarization, unless $\xi \simeq 1$.

2.4 Renormalizable models and EFTs

We now consider a renormalizable, gauge invariant, model of DM interactions, and examine the way in which unequal couplings to u and d quarks can be obtained. Consider the case where $\overline{q}q \to \overline{\chi}\chi$ is mediated by the exchange of a t-channel scalar. The Lagrangian is given by

$$\begin{aligned}\mathcal{L}_{\rm int} &= f\overline{Q_L}\eta\chi_R + h.c \\ &= f_{ud}\left(\eta_u\overline{u}_L + \eta_d\overline{d}_L\right)\chi_R + h.c.,\end{aligned} \tag{2.13}$$

where $Q_L = (u_L, d_L)^T$ is the quark doublet, $\eta = (\eta_u, \eta_d)^T \sim (3, 2, 1/3)$ is a scalar field that transforms under the SM gauge group like Q_L, and f is a coupling constant. Such couplings are present in supersymmetric (SUSY) models, with χ identified as a neutralino and η a squark doublet, and have been considered as a simplified model for DM interactions in Refs. [171–174].

If we take the EFT limit, assuming the η are very heavy, the lowest order operators are of dimension 6:

$$\frac{1}{\Lambda_u^2}(\overline{u}\Gamma u)(\overline{\chi}\Gamma\chi) \quad \text{and} \quad \frac{1}{\Lambda_d^2}(\overline{d}\Gamma d)(\overline{\chi}\Gamma\chi), \tag{2.14}$$

where the suppression scales are $\Lambda_{u,d} \propto m_{\eta_{u,d}}/f$. The relevant Lorentz structure Γ is a sum of vector and axial vector terms as can be seen by Fierz transforming the t-channel matrix elements obtained from Eq.3.2 to s-channel form [175].

The strength of DM interactions with u and d quarks can differ if the masses of η_u and η_d are non-degenerate. However, given that (η_u, η_d) form an electroweak doublet, their mass splitting must be controlled by $v_{\rm EW}$. The relevant terms in the

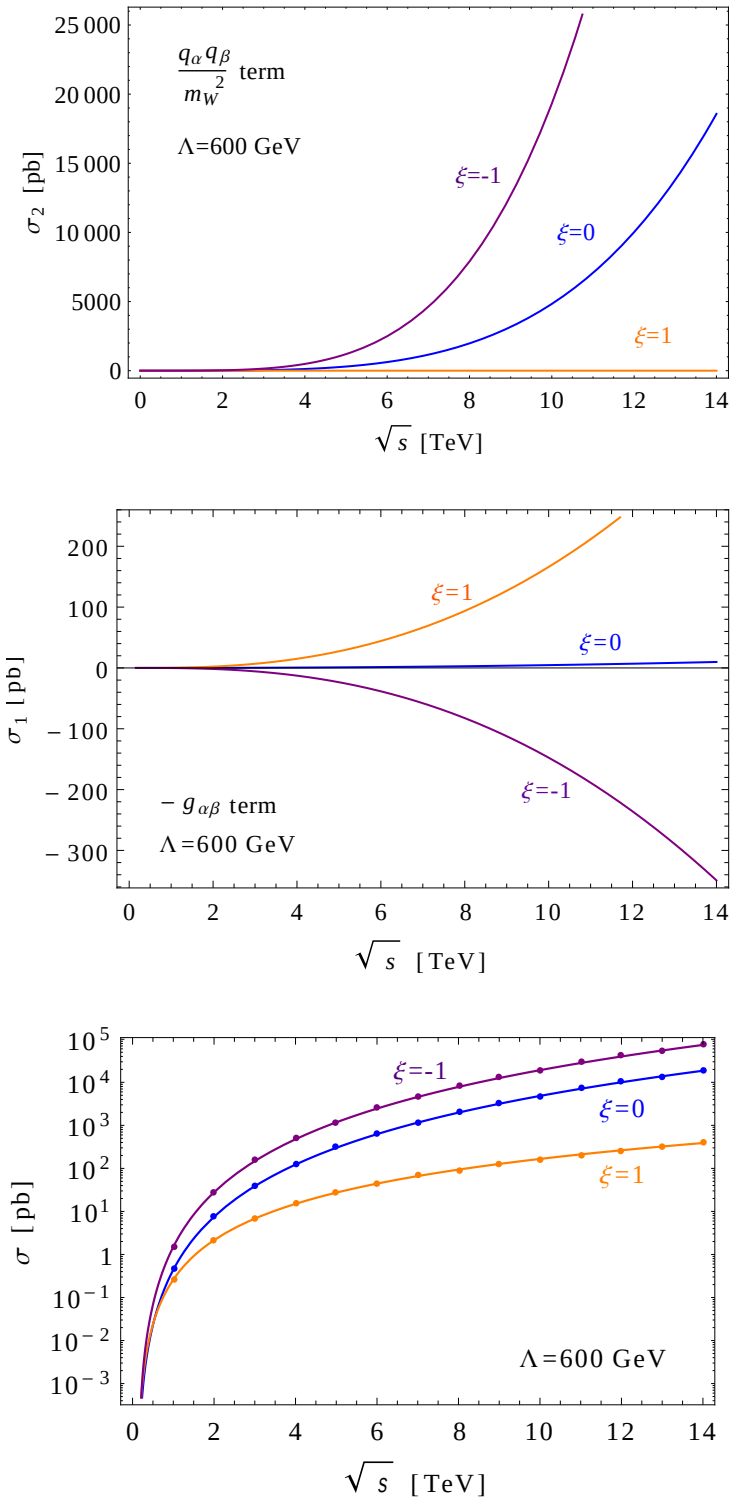

FIGURE 2.2: Total parton-level cross sections as a function of energy, for $\Lambda = 600$ GeV and particular choices of ξ. **Top:** contribution from the $+q_\alpha q_\beta / m_W^2$ term in the polarization sum. The cross section scales simply as $(1-\xi)^2$. **Middle:** contribution of the $-g_{\alpha\beta}$ term in the polarization sum. At LHC energies the $q_\alpha q_\beta$ terms dominates unless $\xi \simeq 1$. (Notice the differing vertical scales between the upper and lower panels.) **Bottom:**Total parton-level cross sections for $\Lambda = 600$ GeV, for particular choices of ξ. Solid lines are the analytic calculation and dots are the MadGraph calculation.

scalar potential are [176]

$$\begin{aligned} V &= m_1^2(\Phi^\dagger\Phi) + \frac{1}{2}\lambda_1(\Phi^\dagger\Phi)^2 + m_2^2(\eta^\dagger\eta) + \frac{1}{2}\lambda_2(\eta^\dagger\eta)^2 \\ &+ \lambda_3(\Phi^\dagger\Phi)(\eta^\dagger\eta) + \lambda_4(\Phi^\dagger\eta)(\eta^\dagger\Phi). \end{aligned} \tag{2.15}$$

If $m_1^2 < 0$ and $m_2^2 > 0$, the SM Higgs doublet obtains a non-zero vev, while the η does not. The presence of λ_4 splits the η masses as

$$m_{\eta_d}^2 = m_2^2 + \lambda_3 v_{\rm EW}^2 + \lambda_4 v_{\rm EW}^2, \tag{2.16}$$

$$m_{\eta_u}^2 = m_2^2 + \lambda_3 v_{\rm EW}^2 , \tag{2.17}$$

implying that $\delta m_\eta^2 \equiv m_{\eta_d}^2 - m_{\eta_u}^2 = \lambda_4\, v_{\rm EW}^2$. However, although we have engineered unequal scalar masses and thus unequal DM couplings to u and d quarks, the scenario of Ref. [162] can not be realised, as we shall explain below.

If we attempt to naively connect our renormalizable model with an EFT like that of Eq.3.1, we find that the parameter ξ is given by $\xi = 1/(1 + \delta m_\eta^2/\Lambda^2) = 1/(1 + \lambda_4\, v_{EW}^2/\Lambda^2)$. For $\Lambda \gtrsim 1$ TeV and a perturbative value for λ_4, ξ will not deviate far from 1. (Negative ξ can not be obtained from this renormalizable model.) Furthermore, it is clear that $SU(2)_L$ violating effects enter the EFT at order v_{EW}^2/Λ^4, i.e., the same order in Λ as a dimension 8 operator. If we consider effects of this order we must, for self consistency, consider other dimension 8 operators that arise from the model. Inclusion of these operators, with appropriate coefficients, will be essential for gauge invariance.

In the renormalizable model, the mono-W process proceeds via the gauge invariant set of diagrams in Fig.3.1 [3] [4] [101, 177, 178]. In the EFT limit, the diagrams in Fig.3.1(a) and (b) map onto those in Fig.2.1(a) and (b) respectively. The diagram in Fig.3.1(c), in which the W is radiated from the η propagator, is suppressed by an additional heavy scalar propagator and is hence subdominant to the ISR diagrams. It enters the EFT as a dimension 8 operator [179], contributes on an equal footing with the $SU(2)$ violating contributions of diagrams (a) and (b), and enforces the cancellation of unphysical W_L contributions to cross sections.

Although we have framed the discussion in terms of a particular renormalizable model, the general features will hold for all UV completions of Eq.3.1 in which $\xi \neq 1$. The violation of the Ward Identity in Eq.2.9 indicates that the two diagrams of Fig.2.1 are not a gauge invariant set, hence there must be an additional diagram. While the form of the missing diagram(s) will depend on the particular

[3] In the good EW $SU(2)$ limit, the η_u and η_d are mass degenerate, and the massless $W^\pm$ emitted in diagram (c) establishes the validity of the EW Ward identity [177, 178]. When EW $SU(2)$ is broken, the η_u and η_d masses are split, and the new massive-W longitudinal mode must restore the EW Ward identity by coupling to the η proportional to δm_η^2 [176]. This argument provides an interpretation of the result found earlier in [176] that the internal longitudinal mode couples proportional to δm_η^2. In fact, in [176] it was shown that this longitudinal W mode will dominate the W emission probability for some range of model parameters.

[4] Note that in the renormalizable theory, in the high energy limit, W_L production arises solely from the amplitude of Fig.3.1(c), and only when $\delta m_\eta^2 \neq 0$.

UV completion, their presence is dictated by gauge invariance. No matter the size of ξ, these extra diagrams prevent large unphysical W_L enhancements.

2.5 Conclusion

An important observation of Ref.[162] is that, of the mono-X processes, the mono-W is unique in its ability to probe different DM couplings to u and d quarks. This important insight is correct. However, in this chapter we have argued that the size of any $SU(2)_L$ violating difference of the u and d quark couplings must be protected by the EW scale, and therefore cannot be arbitrarily large. $SU(2)_L$ violating operators can be obtained by integrating out the SM Higgs or by including Higgs vev insertions. Therefore, they should have coefficients suppressed by powers of $(v_{\rm EW}/\Lambda)$ or $(m_{\rm fermion}/\Lambda)$ and thus are of higher order in $1/\Lambda$ than they would naively appear. To include $SU(2)$ violating effects in a way that is self consistent and properly respects the EW Ward identity, one should use a renormalizable, gauge invariant, model rather than an EFT, to avoid spurious W_L contributions. These observations will be an important guide to the LHC collaborations in the interpretation of their current [163–166] and forthcoming mono-W dark matter search results, and to theorists constructing dark matter models.

Chapter 3

Mono-W Simplified Models and Gauge Invariance

In this chapter we study mono-W signals of dark matter (DM) production at the LHC, in the context of gauge invariant renormalizable models. We analyze two simplified models, one involving an s-channel Z' mediator and the other a t-channel colored scalar mediator, and consider examples in which the DM-quark couplings are either isospin conserving or isospin violating after electroweak symmetry breaking. While previous work on mono-W signals have focused on isospin violating EFTs, obtaining very strong limits, we find that isospin violating effects are small once such physics is embedded into a gauge invariant simplified model. We thus find that the 8 TeV mono-W results are much less constraining than those arising from mono-jet searches. Considering both the leptonic (mono-lepton) and hadronic (mono fat jet) decays of the W, we determine the 14 TeV LHC reach of the mono-W searches with 3000 fb^{-1} of data. While a mono-W signal would provide an important complement to a mono-jet discovery channel, existing constraints on these models imply it will be a challenging signal to observe at the 14 TeV LHC.

This chapter is based on the publication: *N. F. Bell, Y. Cai and R. K. Leane, "Mono-W Dark Matter Signals at the LHC: Simplified Model Analysis", JCAP 01 (2016) 051 [arXiv: 1512.00476 [hep-ph]].* [102]

3.1 Introduction

In the previous chapter, we demonstrated that EFT operators which violate weak gauge symmetries can feature spurious cross section enhancements at LHC energies. This is particularly pertinent for previous mono-W searches for dark matter at the LHC [163, 164, 166], which have largely focused on $SU(2)$ violating EFTs such as [162]

$$\frac{1}{\Lambda^2}\left(\overline{\chi}\gamma^\mu\chi\right)\left(\overline{u}\gamma_\mu u + \xi\overline{d}\gamma_\mu d\right), \tag{3.1}$$

with $\xi \neq 1$. The large mono-W cross sections for such an EFT are in fact a manifestation of the violation of weak gauge invariance in the form of unphysical

longitudinal W contributions. Previous work has used these unphysical enhancements of the mono-W cross section to place very strong limits on dark matter EFTs. However, when gauge invariance is enforced we shall see that the limits arising from the mono-W process will in general be weaker than those arising from the mono-jet. Nonetheless, the mono-W process remains an important complementary channel to explore the properties of dark matter.

In this chapter we will study mono-W signals in renormalizable models in which gauge invariance is enforced from the outset. We choose two example simplified models, one involving t-channel exchange of a new colored scalar, and the other s-channel exchange of a new Z' vector boson. We outline these two models in Section 3.2. In Section 4.5 we explore the LHC phenomenology of these models, to determine the current constraints and the 14 TeV LHC reach for the mono-W signal. In Section 3.4 we explore the possibility of obtaining $SU(2)$ violating operators, like that of Eq. (3.1), from a gauge invariant model after electroweak symmetry breaking. While such operators would allow for the production of longitudinal W_L bosons, potentially enhancing mono-W cross sections, we explain why these effects are constrained to be small.

3.2 Simplified Models for the Mono-W

3.2.1 t-channel Colored Scalar Mediator

We first examine a scenario in which DM-quark interactions are mediated by the exchange of a t-channel scalar. The interaction Lagrangian is given by

$$\begin{aligned} \mathcal{L}_{\text{int}} &= f\overline{Q}_L \eta \chi_R + h.c. \\ &= f_{ud}\left(\eta_u \overline{u}_L + \eta_d \overline{d}_L\right)\chi_R + h.c., \end{aligned} \tag{3.2}$$

where $Q_L = (u_L, d_L)^T$ is the quark doublet, $\eta = (\eta_u, \eta_d)^T \sim (3, 2, 1/6)$ is a scalar field that transforms under the SM gauge group like Q_L, and f is the coupling strength of the interactions[1]. The DM, χ, transforms as a singlet under the SM gauge symmetries. An analogue of this scenario is realized in supersymmetric (SUSY) models, where we identify η with a squark doublet and χ the neutralino. Simplified models with such t-channel interactions have been examined recently in Refs. [171, 173, 174, 180–183], with the collider analyses focusing on the mono-jet process.

In this model, the mono-W process proceeds via the gauge invariant set of diagrams in Fig. (3.1) [101, 153, 177, 178]. Diagrams (3.1a) and (3.1b) dominate in the EFT limit when $\sqrt{s} \ll m_\eta$, while diagram (3.1c) becomes important for smaller

[1]One can write down a similar model involving a coupling to right handed (RH) quark fields. While most of the phenomenology would be very similar, such a model would not permit a mono-W signal. Isospin violating models with RH quark fields were considered in [160, 161].

m_η. We shall initially assume $m_{\eta_u} = m_{\eta_d} = m_\eta$. Deviation from this equality will be discussed in Section 3.4.

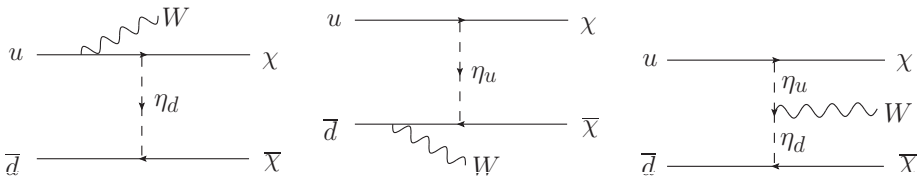

FIGURE 3.1: Contributions to the mono-W process $u(p_1)\overline{d}(p_2) \to \chi(k_1)\overline{\chi}(k_2)W^+(q)$, in a t-channel colored scalar model.

3.2.2 s-channel Z' Mediator

We also consider another generic simplified model in which the DM-quark interactions are mediated by a neutral spin-1 Z' boson. The relevant interaction terms are

$$\mathcal{L}_{\text{int}} \supset g_\chi \overline{\chi}\gamma^\mu\gamma^5\chi Z'_\mu + g_q \overline{q}\gamma^\mu\gamma^5 q Z'_\mu, \tag{3.3}$$

where g_χ is the coupling strength of the Z' to dark matter χ, and g_q is the coupling to SM quarks. Simplified models with such s-channel interactions have been examined recently in Refs. [78, 155, 184–198]. We assume the Z' has axial vector type interactions. Vector interactions would lead to large spin-independent DM-nucleon elastic scattering cross sections, and as a result are strongly constrained by DM direct detection experiments, to the extent that parameters which can correctly account for the DM relic density are significantly excluded. We therefore focus on the more phenomenologically viable axial vector interactions. We shall also assume that the Z' couples only to quarks, and not to leptons, to avoid tight constraints from di-lepton searches.

The pertinent processes for mono-W search are shown in Fig. (3.2). In contrast to the t-channel model above, no radiation from the mediator occurs. This would change in the presence of Z-Z' mixing, as will be discussed in Section 3.4.

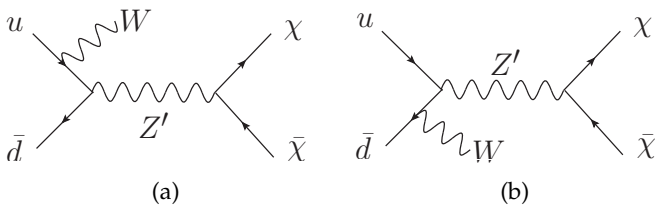

FIGURE 3.2: Contributions to the mono-W process $u(p_1)\overline{d}(p_2) \to \chi(k_1)\overline{\chi}(k_2)W^+(q)$, in an s-channel Z' model.

3.3 LHC Constraints and Reach

We now examine the LHC phenomenology of the two models described in Eqs. (3.2) and (3.3). In the following, we determine the limits and reach of the searches for DM via the mono-W process, for both the leptonic and hadronic decay channels of the W.

3.3.1 Mono lepton channel

We first consider the scenario where the W boson decays to a charged lepton and a neutrino. The neutrino contributes to the missing energy ($\not{E}_T$) along with dark matter, such that the signal is a mono-lepton. In this channel the key kinematic variable is the transverse mass of the lepton-$\not{E}_T$ system,

$$M_T = \sqrt{2p_T^\ell \not{E}_T (1 - \cos\Delta\phi_{\ell,\not{E}_T})}\,, \tag{3.4}$$

where $\Delta\phi_{\ell,\not{E}_T}$ is the azimuthal opening angle between the charged lepton's transverse momentum p_T and the direction of $\not{E}_T$.

The domininant background for the mono-lepton search is $W \to \ell\nu$, and $W \to \tau\nu_\tau \to \nu_\tau\nu_\tau\ell\nu_\ell$ where $\ell = e, \mu$. This is because the M_T distribution of these channels has a large tail in the signal region. We use the electron channel to set limits, since it is the stronger one of two lepton channels and also comparable to the combined limits of both channels. Following Ref. [166], the following selection cuts are made on all backgrounds and signal for the 8 TeV limits:

- E_T of the leading electron > 100 GeV
- E_T of the next-to-leading electron < 35 GeV
- At least one electron
- M_T for the electron, $M_T^e > 220$ GeV
- Pseudorapidity for the electron must be in the range $-2.1 < \eta(\ell_e) < 2.1$
- Jet $P_T < 45$ GeV
- The electron P_T and $\not{E}_T$ ratio must be in the range $0.4 < P_T/\not{E}_T < 1.5$
- $\Delta\phi_{e,\not{E}_T} > 2.5$.

After cuts, the events are scaled by the relevant efficiences. To investigate the phenomenology, both models are implemented in FeynRules [199]. For the mono-lepton search, events are generated in MadGraph/MadEvent [170, 200], hadronized in Pythia [201], interfaced with Fastjet [202] for jet-finding and Delphes [203] for detector effects. We then implement our cuts in Root [204], and

set the model significance σ at 95 % confidence level (C.L.), which is set by the number of signal events S and background events B as

$$\sigma = \frac{S}{\sqrt{S + B + (\delta B * B)^2}} \,, \tag{3.5}$$

where δB is the systematic uncertainty, which we take to be 5% for our analysis. To ensure a thorough sampling of events and sufficient statistics at high M_T, we generate event samples at two different regions for both signal and background, $100 < p_T^\ell < 500$ GeV, and $p_T^\ell > 500$ GeV. The samples from these two regions are then combined to produce the background and signal events. We find that we reproduce the model independent limit on the cross section for a mono-lepton signal as found in Ref. [166], at 8 TeV. We then perform the analysis at 14 TeV and 3000 fb^{-1} integrated luminosity. To produce our 95% C.L. reach, we optimize our 14 TeV selection criteria by increasing the M_T cut to $M_T^e > 1000$ GeV. In Fig. (3.3) we show the M_T distribution for the t-channel model for various choices of the DM mass. (Similar results are found for the s-channel model.) As the shape of the M_T distribution is approximately independent of the DM mass, we adopt $M_T > 1000$ GeV as an optimal selection cut across all parameter choices.

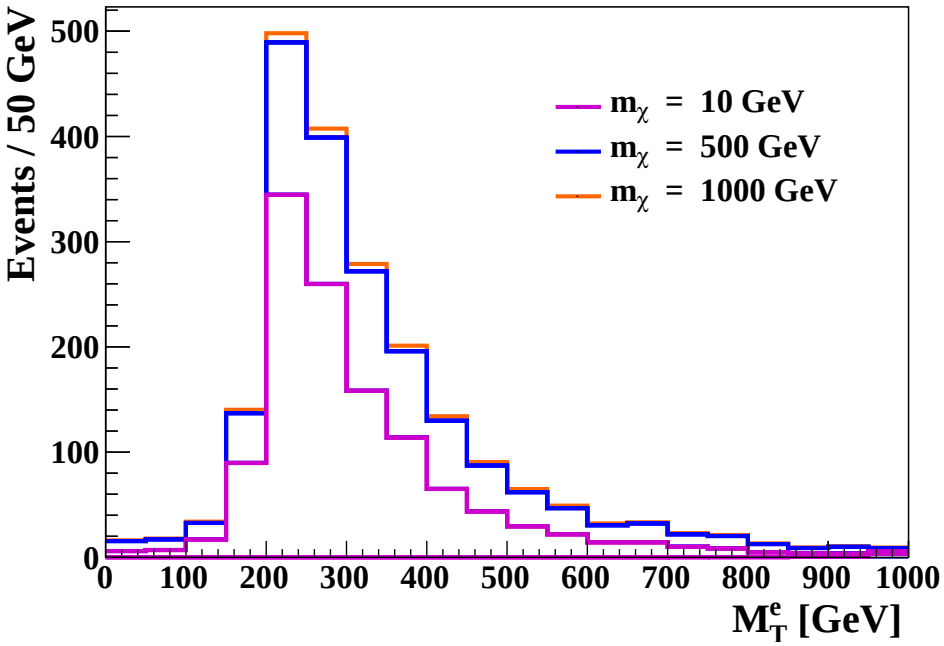

FIGURE 3.3: M_T distribution for $m_{\eta_u} = m_{\eta_d} = 200$ GeV, $g = 1$, $m_\chi = 10, 500, 1000$ GeV in the t-channel model, at 14 TeV and $\mathcal{L}_{int} = 3000$ fb^{-1}. It can be seen that the distribution is independent of DM mass.

3.3.2 Mono fat jet channel

We also consider the limits and reach from the hadronic W decays. Such decays have been searched for by ATLAS [163], where the signal is a hadronically decaying W or Z boson plus missing energy. As our simplified models allow both mono-W and mono-Z processes, both must be included in our generated signal. We refer to this channel as the "mono fat jet" channel as the hadronic decay products jj of the W/Z can be strongly boosted such that they appear together as one wide jet, making the signal this "fat jet" along with $\not{E}_T$ from DM.

The relevant backgrounds for this search are $Z \to \nu\bar{\nu}$, $W \to \ell^{\pm}\nu$, $Z \to \ell\ell$, WW WZ ZZ, $t\bar{t}$ and top production. We generate backgrounds in Herwig++ [205], where events are also hadronized. Using both our models implemented in FeynRules [199], signal events are generated in MadGraph/MadEvent [170, 200] and are hadronized in Pythia [201]. Both signal and background events are then passed to external Fastjet [202], where we implement jet finding algorithms and cuts, followed by Delphes [203] for detector effects and efficiencies. Specifically, in order to discriminate between background jets and those produced by the W/Z, a mass-drop filtering procedure is used. Here, large radius jet candidates which mostly come from the decay of the W/Z are first reconstructed via the Cambridge-Aachen algorithm [206] with a radius parameter of 1.2. Then, the internal structure of this large radius jet is examined, and the subjets, called "narrow jets", are reconstructed using the anti-kt jet clustering algorithm [207] with a radius parameter of 0.4. The mass-drop is performed on the two leading subjets, where the subjet with the largest p_T, p_{T1} differs from the momentum of the next to leading subjet p_{T2} by

$$\sqrt{y} = min(p_{T1}, p_{T2}) \frac{\Delta R}{m_{jet}}, \tag{3.6}$$

where ΔR is the separation of the two leading subjets and m_{jet} is the mass of the large radius jet. For 8 TeV, following the analysis of [163], we also require:

- $\not{E}_T > 350$ GeV
- At least one large radius jet with $P_T > 250$ GeV
- $\sqrt{y} > 0.4$
- $50 < m_{jet} < 120$ GeV
- $-1.2 < \eta < 1.2$
- No more than one narrow jet with $P_T > 40$ GeV and $-4.5 < \eta < 4.5$ which is separated from the leading large radius jet as $\Delta R > 0.9$
- $\Delta\phi(jet, \not{E}_T) < 0.4$ for narrow jets.

As the $Z \to \nu\nu$ background process in this channel has low statistics after cuts, to ensure a thorough probe of phase space we generate and average 6 sets of 50,000 events at 14 TeV for this background. For the other background processes, we generate 50,000 events per process. We set the model significance at 95 % C.L. , as per Eq. (3.5). For the 14 TeV reach, we optimize the search by adjusting three of the 8 TeV selection criteria; we now require at least one large radius jet with $P_T > 400$ GeV, require $\not{E}_T > 500$ GeV and $70 < m_{jet} < 90$ GeV.

3.3.3 Results

For the t-channel model, the current limits are compared with the 14 TeV mono-W reach in Fig. (3.4) for $f_{u,d} = 1$. We also include current constraints on the parameter space from mono-jet and multi-jet searches, which are adopted from Ref. [180]. The region labelled "stability" is forbidden as it corresponds to parameters where $m_\chi > m_\eta$ and thus the DM would be unstable to decay. For the mono-lepton search, we find that both the current 8 TeV exclusion and 14 TeV reach are not competitive with existing constraints from mono-jet searches. Owing to small signal size and large backgrounds, it is too weakly constraining to be featured on our t-channel summary plot. For the mono fat jet search, we find that the 8 TeV exclusions are also not competitive with existing constraints from mono-jet searches. We show the 14 TeV reach in the mono fat jet channel with 3000 fb^{-1} of data, which is able to probe a region of parameter space unconstrained by existing mono-jet results.

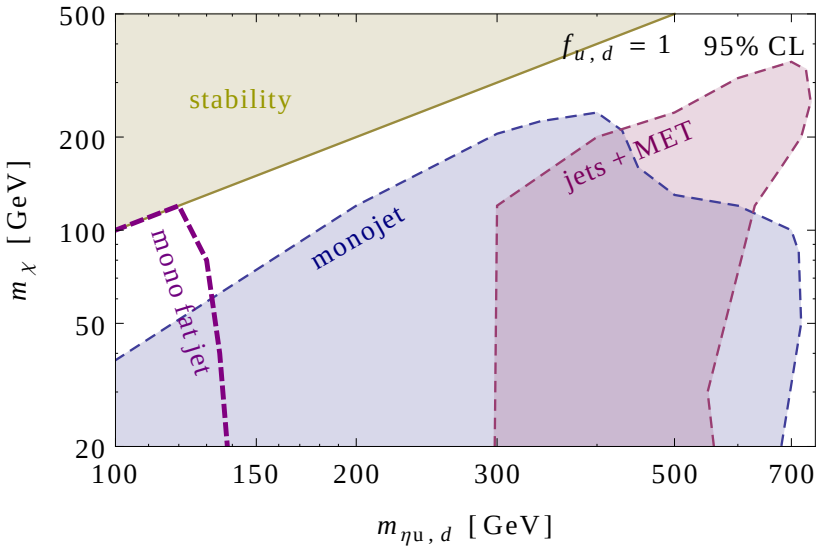

FIGURE 3.4: Parameter space for the t-channel colored scalar model, for $f_{u,d} = 1$. Exclusions are shown as shaded regions for the mono and multi jet at 8 TeV, and the reach is shown for the mono fat jet at 14 TeV 3000 fb^{-1}.

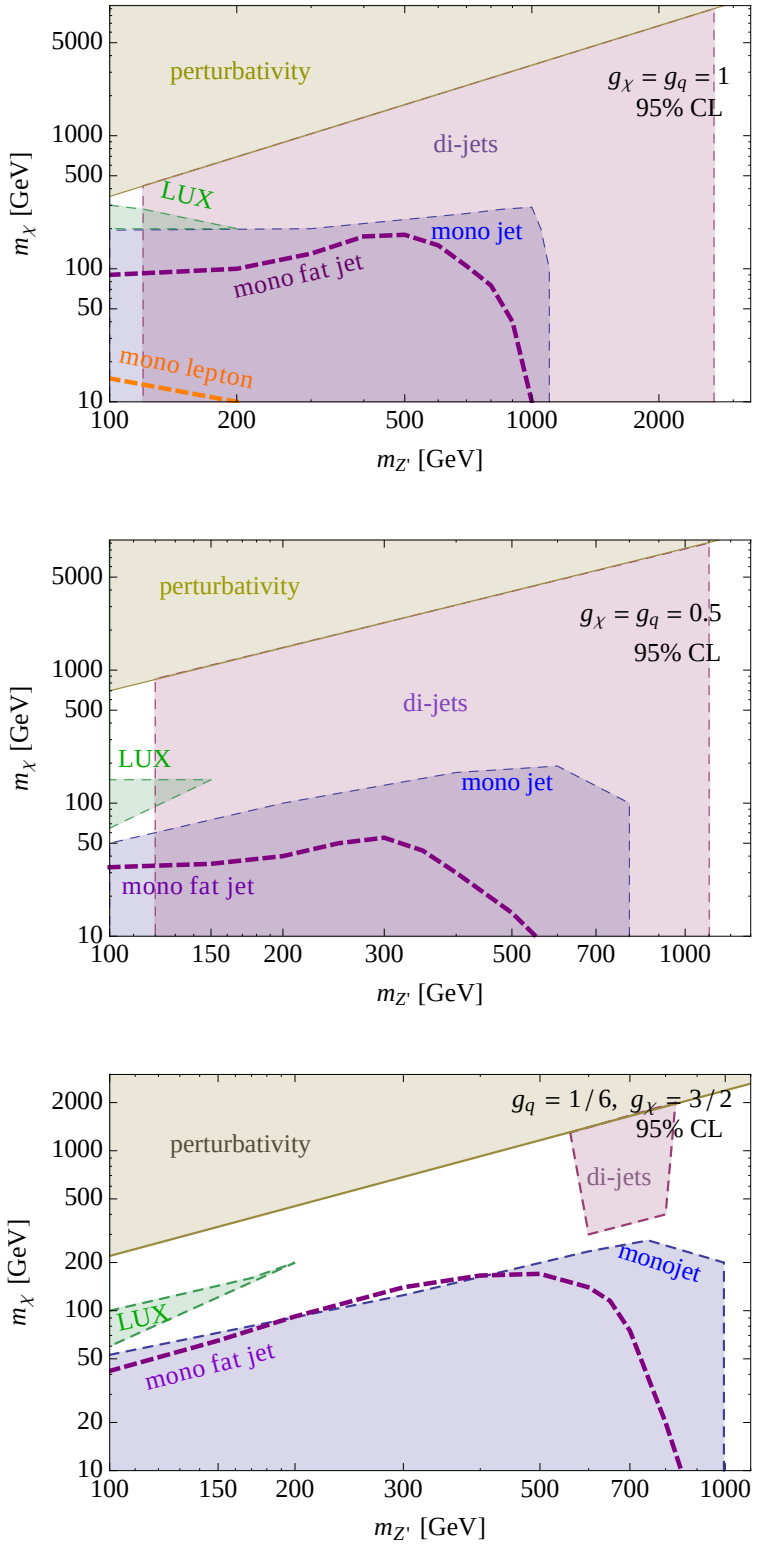

FIGURE 3.5: Parameter space for the s-channel Z' model, for choices of (a) $g_q = g_\chi = 1$ and (b) $g_q = g_\chi = 0.5$ and (c) $g_q = 1/6$ and $g_\chi = 3/2$. Exclusions are shown as shaded regions for LUX and for mono-jet and di-jets at 8 TeV, and the reaches are shown for the mono lepton ((a) only) and mono fat jet searches at 14 TeV 3000 fb^{-1}. Note differing axes.

For the s-channel model, our results are shown in Fig. (3.5) for three choices of the Z' couplings to DM and quarks, as labelled. The relevant mono-jet, di-jet and LUX [118] direct detection limits shown are adopted from Ref. [208]. Note that the LUX limit assumes the actual (sub-critical) contribution to the DM relic density implied by the model parameters, rather than assuming a full relic density. We also include perturbativity limits for the s-channel model. As has been recently shown in [80, 208], the s-channel model with axial couplings may have perturbativity and unitarity issues without the inclusion of additional new physics such a dark Higgs scalar which generates the DM and Z' mass. Perturbative unitarity implies that the Z' cannot be much lighter than the DM, and should satisfy $m_\chi \lesssim \frac{\sqrt{4\pi}}{g_\chi} m_{Z'}$. This is shown on the s-channel plots as the perturbativity region. While this is not a concrete exclusion, it is an important issue for this region of parameter space.

For the mono-lepton search, the current 8 TeV exclusion is too weak to be shown on the plots, while the 14 TeV reach is shown only for $g_q = g_\chi = 1$, as it is very weakly constraining for the other coupling choices. As with the t-channel model, the mono fat jet channel has better sensitivity than the mono-lepton channel, and the 14 TeV reach is shown for each of the coupling choices. However, even with the hadronic decay mode, the mono-W signals will be challenging to observe, with the parameter space accessible at 14 TeV already substantially probed by 8 TeV mono-jet searches.

3.4 $SU(2)$ Breaking Effects and Enhancements from W_L Production

Previous work on the mono-W signal has focused primarily on EFT operators that violate $SU(2)_L$. The strong constraints on these models were shown to arise from unphysical high-energy contributions from longitudinally polarized W bosons, a manifestation of the lack of gauge invariance [153]. The strength of the limits on these W_L dominated processes arose from two effects:

- enhancement of the cross section, due to a leading s/m_W^2 dependence for large s (arising from the W_L contribution to the polarization sum) [153] and
- a harder M_T distribution [166], which allowed better separation of signal and background.

By contrast, the gauge invariant simplified models that we considered above, which feature only transverse W_T contributions in the high energy limit, do not benefit from these effects. However $SU(2)$ violating effects, such as the unequal coupling of DM to u and d type quarks of Eq. (3.1), can be generated at higher order by electroweak symmetry breaking. This would permit some high energy W_L contributions to the mono-W process, potentially leading to stronger constraints. We analyze the size of such effects in variations of our simplified models, and show that it is always small.

3.4.1 Isospin Violation in the t-channel Model

In the t-channel model, the DM interaction with the u and d quarks can be of unequal strength if the masses of the respective mediators, η_u and η_d, are non-degenerate. Inspection of the scalar potential reveals that this situation can be realised once the SM Higgs field gains a vev. The scalar potential is [176]

$$V = m_1^2(\Phi^\dagger\Phi)+\frac{1}{2}\lambda_1(\Phi^\dagger\Phi)^2+m_2^2(\eta^\dagger\eta)+\frac{1}{2}\lambda_2(\eta^\dagger\eta)^2+\lambda_3(\Phi^\dagger\Phi)(\eta^\dagger\eta)+\lambda_4(\Phi^\dagger\eta)(\eta^\dagger\Phi), \tag{3.7}$$

where Φ is the SM Higgs and λ_n are coupling constants. In the case where $m_1^2 < 0$ and $m_2^2 > 0$, the SM Higgs doublet obtains a vev, while η does not. After electroweak symmetry breaking, a non-zero value of λ_4 would split the η masses as

$$m_{\eta_d}^2 = m_2^2 + (\lambda_3 + \lambda_4)v_{\rm EW}^2, \tag{3.8}$$

$$m_{\eta_u}^2 = m_2^2 + \lambda_3 v_{\rm EW}^2\,, \tag{3.9}$$

so that

$$\delta m_\eta^2 \equiv m_{\eta_d}^2 - m_{\eta_u}^2 = \lambda_4\, v_{\rm EW}^2. \tag{3.10}$$

So we appear to have broken the degeneracy of the DM interactions with u and d type quarks, as in the EFT of Eq. (3.1). Does this indeed allow for W_L production, and how can this be understood?

It is instructive to appeal to the Goldstone boson equivalence theorem to understand where W_L production arises. In the high energy limit, we may replace W_L with the corresponding Goldstone boson that (in unitary gauge) provides the gauge boson mass, i.e., we replace W_L^+ with ϕ^+. Now consider the 3 diagrams contributing to the mono-W process shown in Fig. (3.1). The ϕ^+ couples to the quarks with strength given by the quark Yukawa constants, which vanish in the limit that the quarks are massless. Under these conditions, there is no W_L contributions from the diagrams of Fig. (3.1a) and (3.1b).

We now turn to the diagram of Fig. (3.1c) in which the W is radiated from the η mediator. In general, this diagram will feature both W_T and W_L contributions. From inspection of the λ_4 term in Eq. (3.7), we deduce that ϕ^+ will couple to η according to [176]

$$v_{\rm EW}\lambda_4\eta_d\eta_u^*\phi^+ + h.c., \tag{3.11}$$

and thus the size of the $\eta_d\eta_u^*W_L^+$ vertex is determined by λ_4. Therefore, switching on $\lambda_4 \neq 0$ and hence $\delta m_\eta^2 \neq 0$ opens a $pp \to \chi\chi W_L$ channel that does not suffer from suppression by the quark Yukawas. (By contrast, in the example studied in Section 4.5 where where $\lambda_4 = 0$ and $\delta m_\eta^2 = 0$, we expect that the high energy regime will feature only transversely polarized W-bosons, $pp \to \chi\chi W_T$.)

Cross Section Enhancement from W_L Contribution

We have seen that the amplitude for W_L production at high energy is controlled by λ_4. However, λ_4 also increases the mass splitting, making η_d heavier than η_u. Therefore, increasing λ_4 will suppress the contribution of Fig. (3.1a) due to the heavier η_d propagator, while enhancing the contribution of Fig. (3.1c) due to W_L production. The former effect dominates for small values of λ_4, while the latter compensates or dominates if λ_4 is sufficiently large.

In Fig. (3.6) we show the ratio of the cross sections for the mono-W and mono-jet processes at hadron level at the 14 TeV LHC, as a function of λ_4. (Although we have illustrated this behavior for a particular choice of the χ and η_u masses, we obtain similar behavior for other parameter choices.) While the mono-jet cross section monotonically decreases as λ_4 is increased, caused by the heavier η_d propagator, the mono-W cross section first decreases and then increases again when radiation of W_L from the η propagator takes over. However, in order to achieve a significant enhancement of the ratio of the mono-W to mono-jet cross sections, very large values of λ_4 are required. If we restrict this parameter to perturbative values, $\lambda_4 < 4\pi$, a relative enhancement cannot be achieved.

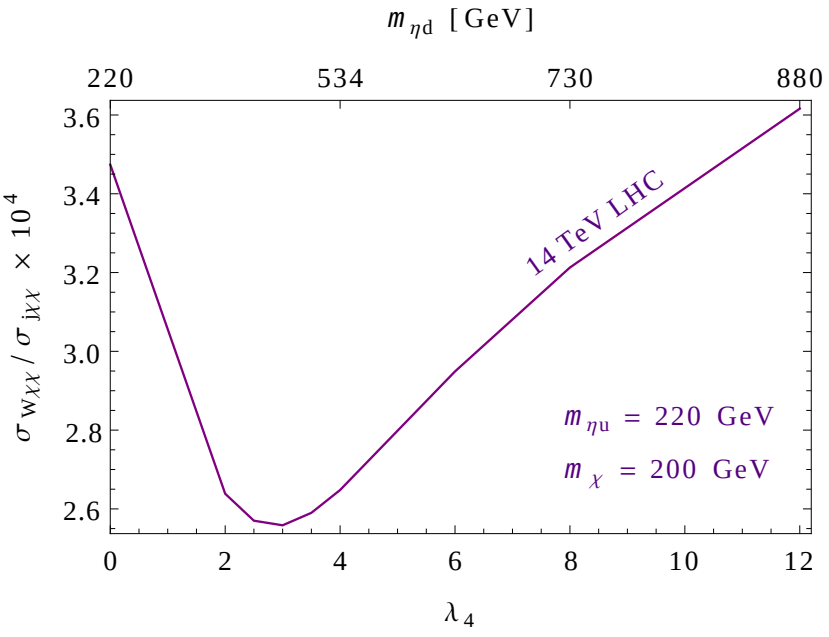

FIGURE 3.6: Ratio of the hadron level cross sections for the mono-W process $pp \to \chi\overline{\chi}W$, $\sigma_{W\chi\chi}$, to the mono-jet process $pp \to \chi\chi j$, $\sigma_{j\chi\chi}$ at 14 TeV, in a renormalizable t-channel scalar model with isospin violation. Upon increasing the mass splitting, the cross section decreases at first due to suppression from an increased propagator mass, until the longitudinal W contribution begins to dominate. The mono-jet cross section is monotonically decreasing with increase in propagator mass.

This behavior differs greatly to that seen in $SU(2)$ violating EFTs, where gauge non-invariant contributions from the analogue of Fig. (3.1 a,b) lead to large W_L

contributions. In our renormalizable model, where all 3 diagrams of Fig. (3.1 a,b,c) are properly included, the high energy behavior of the cross section is tamed.

$SU(2)$ Breaking and the M_T Spectrum

We now consider the M_T distribution of the mono-W events. For the EFT model of Eq. (3.1), the mono-W M_T distributions were found to be sensitive to the parameter ξ [166]. Compared to the $SU(2)$ conserving choice $\xi = 1$, the $SU(2)$ breaking choice of $\xi \neq 1$ resulted in a harder M_T distribution, with a higher peak and significantly more high M_T events. This was useful in differentiating the signal from background via appropriate cuts on the minimum value of M_T.

To explore this effect in our t-channel simplified model, we plot the M_T distribution for various choices of λ_4, shown in Fig. (3.7). We see that increasing the mass splitting parameter λ_4 produces no noticeable shift in the peak or shape of the M_T distribution. Therefore, the shape of the M_T distribution cannot be exploited to increase sensitivity.

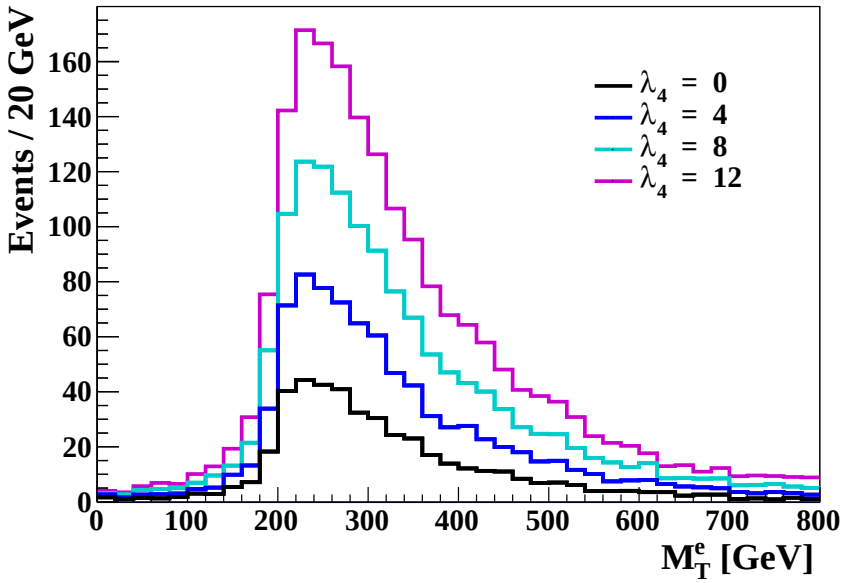

FIGURE 3.7: M_T distribution for $m_{\eta_u} = 220$ GeV, $g = 1$, $m_\chi = 200$ GeV in the t-channel model with isospin violation, at 14 TeV and $\mathcal{L}_{int} = 300\ fb^{-1}$. Despite the increase in λ_4 and therefore the mass splitting, the peak of the M_T distribution does not increase, leading to no strong advantage in the mono-lepton channel compared to other channels.

3.4.2 Isospin Violating Effects in s-channel Models

We now consider $SU(2)$ violating interactions of DM with quarks in the context of the s-channel Z' model. In the example model presented in Section 3.2, the Z' boson was taken to couple with equal strength to the u and d type quarks. This would be expected in a scenario in which the SM quarks were charged under

the new $U(1)_{Z'}$. However, if the SM quarks were not charged under $U(1)_{Z'}$, and the Z'-quark couplings were to arise only via mixing of the Z' with the SM Z, then weak isospin violating interactions would result – see section A2 of Ref. [79]. In fact, these weak isospin violating interactions would be the lowest order DM-quark interaction terms present.

In the Z-Z' mixing scenario the quark-Z' couplings are proportional to the quark-Z couplings, which are of opposite sign for u and d quarks due to their weak isospin assignments of $T_3 = \pm 1/2$. In the EFT limit, where the Z' is integrated out, this would result in the operator of Eq. (3.1) with a negative value of ξ. However, the strength of the DM-quark interactions would be suppressed by the Z-Z' mixing angle, which is of order $v_{\rm EW}^2/M_{Z'}^2$, and thus the operator arises only at order $1/\Lambda^4$. The relevant diagrams for the mono-W process are shown in Fig.(3.8). Unlike the Z' model of Section 3.2, there is now a diagram in which the W is radiated from the Z/Z' mediator. This diagram occurs at the same order in $1/\Lambda$ as the first two contributions[2]. While the third diagram will allow W_L production, the gauge invariance of the underlying theory prevents any bad high energy behavior, limiting any W_L driven cross section enhancement. Moreover, given that the Z-Z' mixing angle is constrained to be small, isospin violating effects will be difficult to observe.

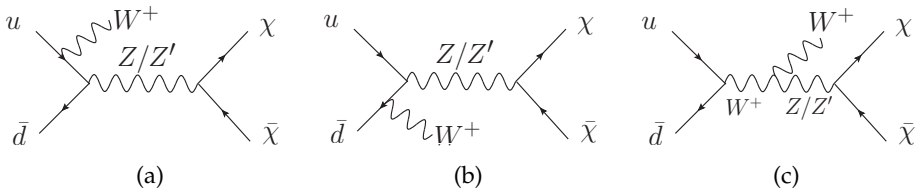

FIGURE 3.8: Contributions to the mono-W process $u(p_1)\overline{d}(p_2) \to \chi(k_1)\overline{\chi}(k_2)W^+(q)$, in the Z-Z' mixing model.

Finally, weak isopin violating effects would also occur in a model in which a new s-channel scalar mediator mixes with the SM Higgs. In this case the effects are suppressed by the small SM quark Yukawa couplings. In addition, if the DM is lighter than the Higgs, the Higgs invisible branching fraction would constrain the scalar-Higgs mixing.

3.5 Conclusion

Observation of DM production at the LHC is now one of the foremost goals of the particle physics community. To analyze the sensitivity of these searches, it is important to use a theoretically consistent framework for describing the DM interactions. The goal of this chapter was to explore mono-W signals of dark matter production, in simplified models in which invariance under the SM

[2]If we included only the first two diagrams, e.g., by assuming only the operator of Eq. (3.1), we would encounter unphysical W_L effects whose origin could be traced to the lack of gauge invariance.

weak gauge symmetries is enforced. We therefore considered popular simplified models with an s-channel Z' mediator or a t-channel colored scalar mediator, both with and without isospin violating effects arising from electroweak symmetry breaking.

We first analyzed the simplified models in which the DM-quark couplings preserve isospin. Considering both the leptonic and hadronic decay modes of the W, we found that the 8 TeV mono-W sensitivity is not competitive with the 8 TeV mono-jet results. At 14 TeV the hadronic (mono fat jet) decay channel is the most promising, although 3000 fb^{-1} of data is required to significantly probe parameter space. While we anticipate that the experimental collaborations will be able to better optimize their analyses than the estimates we present here, we expect these general conclusions to hold.

Previous mono-W analyses have focused primarily on EFT operators that violate $SU(2)_L$, obtaining limits that are competitive with, or stronger than, those arising from the mono-jet. Therefore, we explored the possibility of obtaining isospin-violating DM-quark couplings in our gauge invariant simplified models, after electroweak symmetry breaking. This can be achieved in the t-channel model through the mass splitting of the squark-like scalar $SU(2)$ doublet, or in the s-channel model via Z-Z' mixing. For the both t-channel and s-channel models we find that these isospin violating effects must be small, in contrast to the non gauge invariant EFTs scenarios considered previously in the literature. As such, isospin violating DM-quark couplings are unlikely to increase the sensitivity of mono-W searches.

If DM is detected in future LHC data, it is likely that the mono-jet process will be the discovery channel. However, observation of a mono-jet signal alone would not be sufficient to elucidate the particular DM model. Complementary information from other channels such as the mono-W would eventually play an essential role. However, it will be challenging to observe these complementary signals at the 14 TeV LHC unless the model parameters fall just beyond the 8 TeV mono-jet reach. The observation of a mono-W signal at the 14 TeV LHC would therefore point toward very specific DM models. While mono-W signals can, in principle, probe isospin violation of the DM-quark couplings, encoding important information about the specific DM model, it may take a future collider for such effects to be observed.

Chapter 4

Leptophilic Dark Matter with Z' Interactions

In this chapter, we consider a scenario where dark matter (DM) interacts exclusively with Standard Model (SM) leptons at tree level. Due to the absence of tree-level couplings to quarks, the constraints on leptophilic dark matter arising from hadron based experiments are weaker than those for a generic WIMP. We study a simple model in which interactions of DM with SM leptons are mediated by a leptophilic Z' boson, and determine constraints on this scenario arising from relic density, current LHC searches, and project the future LHC discovery reach. We show that, despite the absence of direct interactions with quarks, this scenario can be strongly constrained.

This chapter is based on the publication: *N. F. Bell, Y. Cai, R. K. Leane and A. D. Medina, "Leptophilic dark matter with Z′ interactions", Phys. Rev. D 90, no. 3, 035027 (2014) [arXiv:1407.3001 [hep-ph]].* [209]

4.1 Introduction

The non-observation of WIMPs thus far has begun to place meaningful constraints on the WIMP parameter space. Experiments at the LHC, have not identified a DM signal. Direct detection (DD) experiments, which require nucleon-DM interactions, similarly do not report a DM signal and are placing tough limits on DM-nucleon cross-sections [118, 210], approaching the neutrino floor. However, the exclusions from these experiments are based on DM-hadron interactions, perhaps hinting that either the DM does not interact in such a way, or such interactions are suppressed. To relax constraints on the DM parameter space, we shall consider an alternate framework where direct DM-hadron interactions do not occur, and instead the DM couples exclusively to SM leptons at tree level. This is referred to as leptophilic dark matter (LDM) [211–227].

A leptophilic DM model may be tested via the three usual DM searches: direct detection, indirect detection and collider searches. However, the phenomenology of leptophilic DM is quite different to that of a generic WIMP. Although leptophilic

DM does not couple to quarks at tree-level, such couplings will inevitably exist at higher order. DM detection processes involving quarks will thus still yield limits, though they will be relaxed by the presence of loop factors and/or additional coupling constants, thereby increasing the allowed parameter space. For example, there exists a loop-suppressed direct detection process shown in Fig. 4.1 [216], which can still place meaningful constraints on leptophilic dark matter [216, 228].

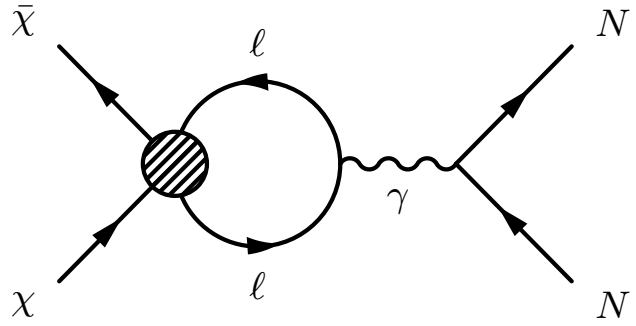

FIGURE 4.1: Loop-suppressed direct detection signal for leptophilic dark matter.

Indirect detection experiments are a scan of the astrophysical sky, searching for unexplained fluxes which may be a produced as a result of DM annihilation or decay. For low DM masses, interesting indirect detection bounds have been placed using Fermi observations of dwarf spheroidal galaxies [229]. At higher DM masses, significant interest in leptophilic DM was sparked by an excess in the cosmic ray positron fraction measured by the PAMELA [146], Fermi [145] and AMS [144] experiments. Given that no corresponding antiproton excess was seen, this suggested models in which DM annihilates, with a large cross section, to leptonic final states. However, these signals are subject to significant astrophysical uncertainties, and may in fact be produced by nearby pulsars [230, 231]. Moreover, as noted above, a model can only be "leptophilic" at lowest order with higher order process inevitably producing hadrons with non-negligible fluxes [232]. In this work, we shall not attempt to explain the positron results, but instead focus on relic density and LHC bounds on leptophilic dark matter.

Collider searches at the LHC and LEP [218, 233] have placed interesting limits on standard WIMPs. The most generic, model independent limits are those obtained from the mono-X searches [98, 101, 162, 163, 234–236] (mono-jet, mono-photon or mono-W/Z). These signals are obtained when a single SM particle recoils against missing momentum, attributed to dark matter particles which escape undetected. However, the mono-X searches at the LHC require that dark matter to couples to quarks, and are thus not applicable for a leptophilic scenario. There exist mono-photon limits from LEP [233], however these are only relevant for DM coupling to electrons (rather than muons or taus) and only extend to low DM masses. The LHC collider signals for leptophilic DM are very different from the mono-X signals, and will be the focus on this chapter.

The outline of the chapter is as follows: We introduce a simple leptophilic model in Section 5.2, consider relic density requirements in Section 4.3, and discuss other constraints in Section 8.7. We focus on the LHC collider phenomenology for leptophilic dark matter, as discussed in Section 4.5, and our main results are summarized in Fig. 4.9, 4.10 and 4.11.

4.2 Leptophilic Model

To fully investigate a LDM scenario, we shall adopt a particular simple model. We introduce a new spin-1 vector boson, Z', which mediates interactions between SM leptons and the DM. Such a setup can be described via the Lagrangian

$$\begin{aligned}\mathcal{L} &= \mathcal{L}_{SM} - \frac{1}{4}Z'_{\mu\nu}Z'^{\mu\nu} - \frac{\epsilon}{2}Z'_{\mu\nu}B^{\mu\nu} + i\bar{\chi}\gamma_\mu\partial^\mu\chi \\ &\quad + \bar{\chi}\gamma^\mu(g^V_\chi + g^A_\chi\gamma^5)\chi Z'_\mu + \bar{\ell}\gamma^\mu(g^V_\ell + g^A_\ell\gamma^5)\ell Z'_\mu \\ &\quad - m_\chi\bar{\chi}\chi + \frac{1}{2}m^2_{Z'}Z'_\mu Z'^\mu,\end{aligned} \tag{4.1}$$

where ϵ is the kinetic mixing parameter of Z' and SM hypercharge gauge boson, $\ell = e, \mu, \tau, \nu_e, \nu_\mu, \nu_\tau$ are the SM leptons, $g_\ell = g_e, g_\mu, g_\tau$ are the Z' coupling strengths to each SM lepton flavor, and g_χ is the coupling strength of the Z' to DM. We allow both vector (V) and axial-vector (A) couplings of the Z'. The parameters to investigate, therefore, are $g_\chi, g_\ell, m_{Z'}, m_\chi$, along with relevant cross sections. In this general setup, a mass generation mechanism for the Z' and DM is not specified.

At low energies, such as those relevant for direct detection, the Z' interactions can be well approximated by an effective contact operator,

$$\mathcal{L}_{eff} = \frac{1}{\Lambda^2}(\bar{\chi}\Gamma_\chi\chi)(\bar{\ell}\Gamma_\ell\ell), \tag{4.2}$$

where the effective cut-off scale is

$$\Lambda = \frac{m_{Z'}}{\sqrt{g_\chi g_\ell}}. \tag{4.3}$$

Given the form of the Z' interactions in Eq. 4.1, the possible Lorentz structures are combinations of vector (V) and axial-vector (A) bilinears: $\Gamma_\chi \otimes \Gamma_\ell = V \otimes V$, $A \otimes V$, $V \otimes A$ or $A \otimes A$. However, in order to permit SM Yukawa couplings without breaking $U(1)_L$ gauge invariance, the Z' coupling to the SM leptons must be vectorlike, thus we shall require $\Gamma_\ell = V$. We list the possible Lorentz structures in Table 4.1, and summarise their pertinent features.

There has been some previous work on vector bosons which couple only to leptons. Considering only SM fields, the symmetries $U(1)_{L_i - L_j}$ are anomaly free and can thus be gauged [237–239]; models in which DM interacts via a $L_\mu - L_\tau$ gauge boson have recently been explored in [225, 226, 240]. We take a different

TABLE 4.1: Lorentz structure of the Z' couplings. For axial vector couplings to leptons, the loop-level direct detection signal vanishes [216]. However, in order for the SM Yukawa couplings to respect $U(1)_L$ gauge invariance, the Z' couplings to leptons should be vectorlike. Also note that $\Gamma_\chi = V$ is not permitted for Majorana DM.

$\Gamma_\chi \otimes \Gamma_\ell$	$\sigma(\chi\chi \to \bar{\ell}\ell)$	$\sigma(\chi N \to \chi N)$	Gauge invariant?
$V \otimes V$	s-wave	1 (1-loop)	Yes
$A \otimes V$	p-wave	v^2 (1-loop)	Yes
$V \otimes A$	s-wave	-	No
$A \otimes A$	p-wave	-	No

approach in the present work and consider a leptophilic Z' which couples to a single lepton flavor, taking each flavour in turn. Phenomenologically, this is a natural choice because the experimental constraints depend on which lepton flavor is being considered. With this approach, new dark sector particles must be chosen with the correct quantum numbers to cancel anomalies. However, any hidden sector particles other than the DM candidate can be taken to be heavy enough to be decoupled from our Lagrangian, while light enough to still contribute to anomaly cancellation. We thus take the coupling strengths g_ℓ^V and $g_\chi^{A,V}$ as free parameters to be constrained.

4.3 Dark Matter Relic Density

In our leptophilic framework the dominant DM annihilation channels are

$$\chi\bar{\chi} \to \ell^-\ell^+, \bar{\nu}_\ell\nu_\ell, Z'Z', \tag{4.4}$$

with the corresponding Feynman diagrams shown in Fig. 4.2. To determine the parameter space allowed by relic density constraints, we implemented our model with FeynRules [241] and generated model files for MicroMEGAs [242] for the relic density calculation. We then performed a scan over $m_{Z'}, m_\chi, g_\ell, g_\chi$ to determine the parameters which yield the correct relic density, $\Omega_\chi h^2 = 0.1187 \pm 0.0017$ [243].

In Fig. 4.9 and 4.11, we plot relic density curves in the $g_\ell = g_\chi$ vs $m_{Z'}$ plane, for various choices of the DM mass, and in Fig. 4.10 for $4g_\mu = g_\chi$ and $8g_\mu = g_\chi$. Parameters must lie on these curves to produce the correct relic density. Larger values of the couplings would lead to a subdominant contribution to the relic density, while smaller couplings would overclose the universe unless additional annihilation channels were present.

The features of the relic density curves can be easily understood: The $Z'Z'$ channel is kinematically open only for $m_{Z'} < m_\chi$, while for $m_{Z'} > m_\chi$ the freeze-out is determined by annihilation to leptons. The annihilation cross section to

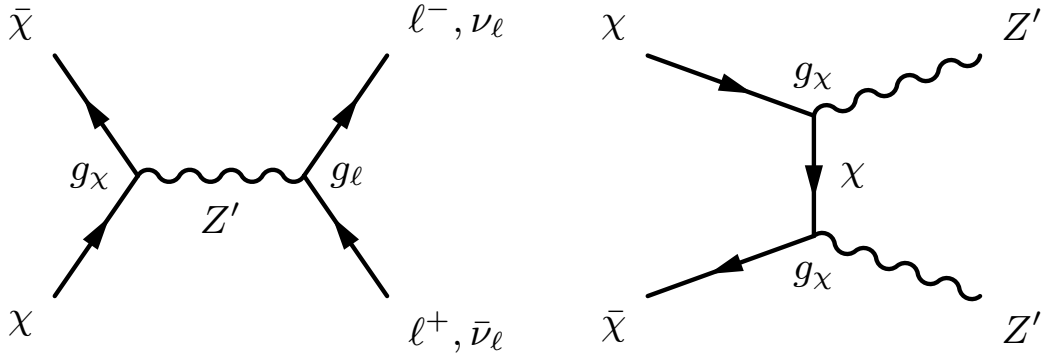

FIGURE 4.2: DM annihilation processes, which determine the relic density at freezeout.

leptons has an s-wave contribution when $\Gamma_\chi = V$, but proceeds via a velocity suppressed p-wave contribution when $\Gamma_\chi = A$. Resonant production of DM occurs when $m_{Z'} \approx 2m_\chi$, seen as strong dips in the relic density curves.

4.4 Constraints from $(g-2)_\ell$, LEP and other searches

We now outline further constraints on our scenario. These limits predominantly depend sensitively on the lepton flavour. Measurements of $(g-2)_\ell$ constrain the coupling of a Z' to each of the lepton flavours, resulting in a strong bound for the μ flavour, and weaker bounds for e and τ. Very stringent Z' bounds from LEP apply to the electron flavour alone, as do the LEP mono-photon bounds [1].

$(g-2)_\ell$: A Z' which couples to leptons will make a contribution to the lepton anomalous magnetic dipole of [244]

$$\Delta(g-2)_\ell \sim \frac{g_\ell^2}{6\pi^2}\frac{m_\ell^2}{m_{Z'}^2}. \tag{4.5}$$

Upper limits on any additional contribution to $(g-2)_\ell$ are $4\times10^{-10}, 8\times10^{-9}$ and 8×10^{-2} for the electron, muon and tau respectively [27]. This requires the Z' coupling strengths to be

$$g_e \lesssim 0.3\frac{m_{Z'}}{\text{GeV}}, \tag{4.6a}$$

$$g_\mu \lesssim 6\times10^{-3}\frac{m_{Z'}}{\text{GeV}}, \tag{4.6b}$$

$$g_\tau \lesssim \frac{m_{Z'}}{\text{GeV}}. \tag{4.6c}$$

Neutrino scattering: The Liquid Scintillator Neutrino Detector (LSND) measured the cross section for the elastic scattering process $\nu_e + e^- \to \nu_e + e^-$, placing a further

[1] Note that, as recently pointed out in Ref. [228], running of the couplings can induce LEP limits from other lepton flavours. However, this can require some fine-tuning.

constraint on the Z' coupling strength to electrons [245],

$$g_e \lesssim 3 \times 10^{-3} \frac{m_{Z'}}{\text{GeV}}. \tag{4.7}$$

This constraint is weaker than LEP for electrons.

LEP-II Z′ constraints: The coupling of a Z' to electrons is constrained by results of the LEP-II experiments. For Z' masses greater than 209 GeV, the largest center-of-mass energy at which LEP operated, the constraints are expressed in terms of four-fermion contact operators, known as the compositeness bounds [246]. For a vector coupling to electrons this bound can be expressed as [246, 247]

$$g_e \lesssim 0.044 \times m_{Z'}/(200\ \text{GeV}). \tag{4.8}$$

For Z' masses below about 200 GeV, the four-fermion description is not valid, as the Z' mass is not large compared to the LEP beam energy, and resonant production is possible. A conservative limit can be taken as $g0.04$ for $m_{Z'} \lesssim 200$ GeV. Much stronger limits should hold for a Z' mass close to one of the centre of mass energies at which LEP ran, however no detailed analysis exists.

LEP-II mono-photon constraints: Monophoton searches at LEP-II place bounds on the couplings [233], which again are relevant only when the Z' couples to electrons. These constraints depend sensitively on the Z' decay width and thus on the ratio g_e/g_χ. If we assume $g_e \simeq g_\chi$, then for $m_\chi \lesssim m_{Z'}/2$ and $m_{Z'} \gtrsim 30$ GeV these constraints are stronger than those expected from direct detection [228], but are comparable to the LEP Z' bounds. For masses outside of this range, direct detection can be more constraining [228].

Electroweak Precision Measurements: In addition to the limits on kinetic mixing as discussed in section II, there are constraints on the ratio of the decay width of a Z' which couples to electrons and $m_{Z'}$ from precision measurements of the line shape of the Z^0 [248, 249]. However they do not constrain the $g_e - m_{Z'}$ parameter space any further than the limits listed above.

4.5 LHC Phenomenology

We now consider the LHC phenomenology for a leptophilic Z'. Because the Z' does not couple directly to quarks, the lowest order Z' production process is $pp \to \ell^+\ell^- Z'$, in which a Z' is radiated from a lepton in a Drell-Yan process, as shown Fig. 4.3. The Z' production cross section is shown in Fig. 4.4. The cross section is large when $m_{Z'} < m_Z$, because the process in Fig. 4.3 can proceed via an on-shell Z. For $m_{Z'} > m_Z$, however, the cross section falls rapidly with increasing Z' mass, such that detecting a Z' with mass beyond about 500 GeV would be challenging.

The Z' decays either to DM (or neutrinos) or to charged leptons, resulting in a pair of opposite sign di-leptons plus missing E_T, or two pairs of opposite sign di-leptons, respectively. The 2-lepton plus missing E_T signal competes with substantial SM backgrounds, in particular from the process Z+jets, such that detection prospects are poor. However, the 4-lepton signal is very distinctive and is examined in detail below.

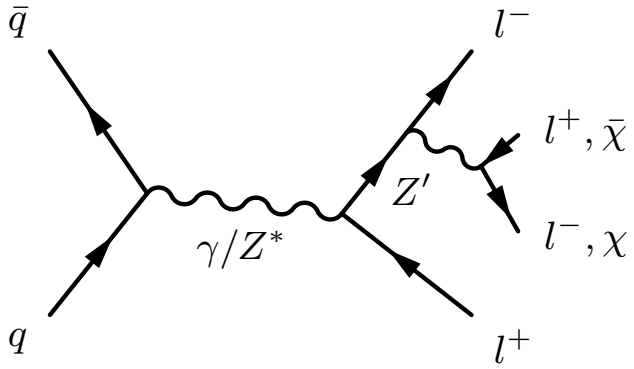

FIGURE 4.3: Production of the Z' at a hadron collider. The Z' is radiated from a lepton in the Drell Yan process, and subsequently decays to either leptons or DM.

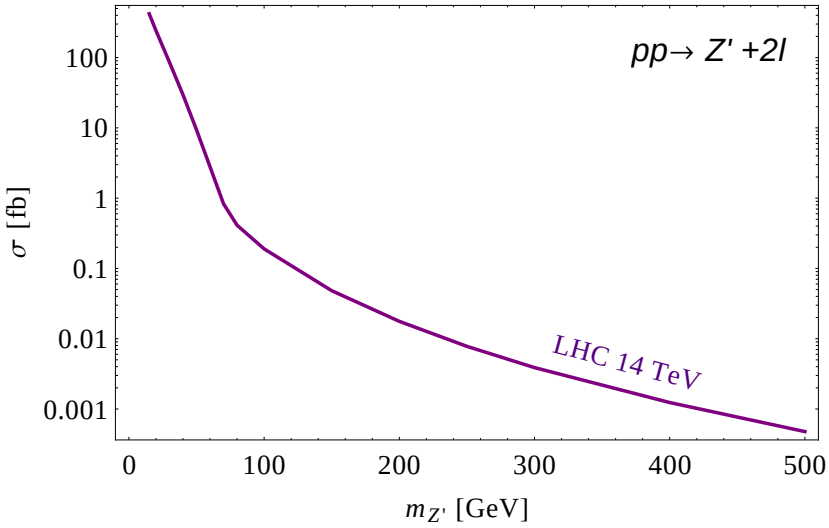

FIGURE 4.4: Z' production cross section at the 14 TeV LHC, via the process $pp \to \ell^+\ell^- Z'$. We have set $g_\ell = 0.1$.

The signal rates depend on the branching fraction of the Z' to charged leptons or DM, which depend on the mass and coupling strength of the Z'. For $g_\chi = g_\ell$, and in the limit $m_{Z'} \gg m_\chi$, we have

$$Br(Z' \to \ell\ell) = Br(Z' \to \chi\chi) = 2Br(Z' \to \nu_\ell \nu_\ell). \tag{4.9}$$

For other parameters, the branching ratios are evaluated numerically in our analysis.

4.5.1 Z' Decay to Leptons

We now consider the 4 lepton process, $pp \to \ell^+\ell^- Z' \to \ell^+\ell^-\ell^+\ell^-$, in detail. The main SM backgrounds for this process are

$$pp \to \ell^+\ell^- Z \to \ell^+\ell^-\ell^+\ell^-, \tag{4.10a}$$

$$pp \to ZZ \to \ell^+\ell^-\ell^+\ell^-, \tag{4.10b}$$

with Eq. 4.10a making the dominant contribution. The $pp \to 4\ell$ cross section has been measured at the Z resonance by the LHC experiments, ATLAS and CMS. The most constraining limits arise from the ATLAS analysis, which used an $\sqrt{s} = 8$ TeV dataset at an integrated luminosity of 20.7 fb^{-1}, and measured the number of events to be consistent with the SM expectation. A similar analysis performed by CMS used only the $\sqrt{s} = 7$ TeV data [250] and is less constraining. We reproduce the ATLAS analysis to find the current exclusion limits for our Z' model using the $Z \to 4l$ search [251].[2] We also simulate events at $\sqrt{s} = 14$ and higher luminosities, to project the future reach of the LHC.

To simulate our Z' signal and the relevant SM background, we implement our model with FeynRules [241], generate parton level events in MadGraph [170] and then interface with Pythia [254] to produce hadronic level events. For processes involving electrons, we also interface the Pythia output with the PGS detector simulation. Finally, we use MadAnalysis [255] to analyse the events. We determine the significance according to

$$\sigma = N_{Z'}/\sqrt{N_{Z'} + N_{SM}}, \tag{4.11}$$

where $N_{Z'}$ is the number of simulated events for the Z' model, and N_{SM} is the number of ATLAS events observed, which is consistent with the predicted number of SM events. Excluded parameters are those which have a deviation from the SM of $\sigma \gtrsim 3.0$. We neglect systematic uncertainties, as they are very low for our purely leptonic final states [251]. Given that the number of signal and background events are comparable, a small systematic uncertainty will not have a significant effect on the results.

We consider only the $Z \to 4\mu$ and $Z \to 4e$ part of the ATLAS analysis. Mixed flavour final states are not possible, because we assume the Z' couples to a single lepton flavour. For the case of the 4μ signal, we perform different analyses for low mass ($m_{Z'} < m_Z$) and high mass ($m_{Z'} > m_Z$) Z' bosons. For the $4e$ signal, however, we perform only the low mass analysis, as the LEP Z' searches already eliminate the high mass parameter space that could be probed at the LHC.

There is no available analysis for a four tau final state, as tau reconstruction is significantly more difficult and suffers a much lower efficiency than detecting μ

[2] A similar analysis has been performed recently for the 4 muon final state in Refs. [252, 253].

or e. Therefore, there are no current collider constraints which can be placed on a scenario in which the Z' couples only to the tau flavour.

Four Electron Final State: $m_{Z'} < m_Z$

We replicate the ATLAS $pp \to 4e$ analysis at the Z resonance, for which the candidate events have two pairs of opposite sign electrons. The following selection cuts are made:

- $p_{T,e} > 7$ GeV and $|\eta| < 2.47$ for individual electrons
- Candidate separation of $\Delta R_{ee} > 0.1$
- $M_{e^-,e^+} > 20, 5$ GeV for the leading pair and next to leading pair in momentum
- $p_{T,e} > 20, 15, 10$ GeV for the leading three electrons
- Invariant mass of electron quadruplet is restricted to events near the Z resonance: $80 < M_{4e} < 100$ GeV

For the four electron case, the hadronic level events generated by Pythia [201] are interfaced with the PGS detector simulator before being interfaced to MadAnalysis at reconstruction level [255]. This is necessary for electrons, as they are reconstructed from energy clusters in an electromagnetic calorimeter, which are matched to reconstructed electron tracks in the inner detector [256], for which detector effects and efficiencies are not negligible. With this procedure, our simulated number of SM events was consistent with that measured by ATLAS.

The current ATLAS exclusion based on the $4e$ process at 20.7 fb^{-1} is shown in Fig. 4.11, assuming $g_\ell = g_\chi$. We also show future discovery curves at the higher luminosities of 300 and 3000 fb^{-1}.

Four Muon Final State: $m_{Z'} < m_Z$

We replicate the ATLAS $pp \to 4\mu$ analysis at the Z resonance, for which the candidate events have two pairs of opposite sign muons. The following selection cuts are made:

- $p_{T,\mu} > 4$ GeV and $|\eta| < 2.7$ for individual muons
- Candidate separation of $\Delta R_{\mu\mu} > 0.1$
- $M_{\mu^-,\mu^+} > 20, 5$ GeV for the leading pair and next to leading pair in momentum
- $p_{T,\mu} > 20, 15, 8$ GeV for the leading three muons
- Invariant mass of muon quadruplet is restricted to events near the Z resonance: $80 < M_{4\mu} < 100$ GeV

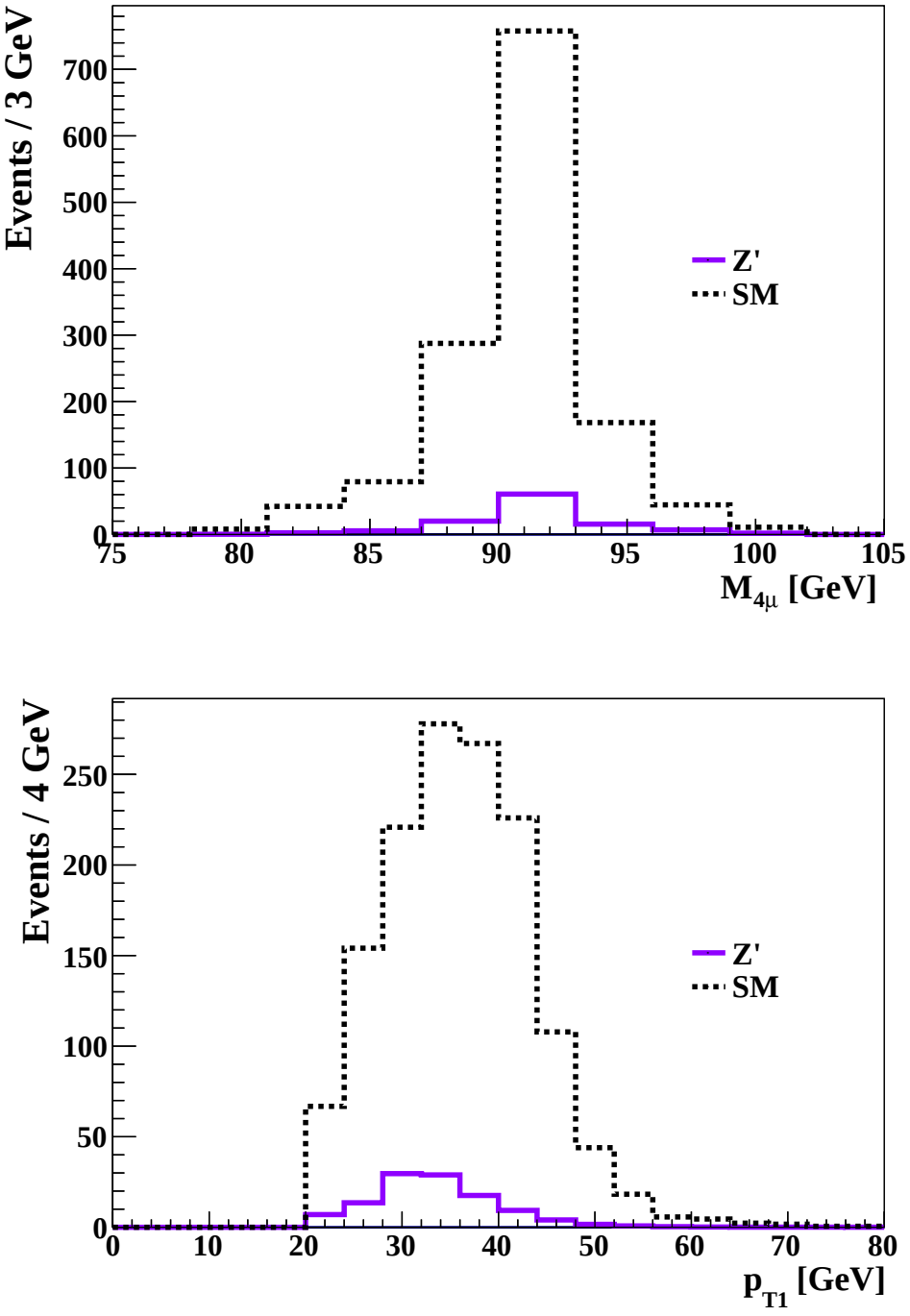

FIGURE 4.5: Invariant mass for four muons (left) and transverse momentum p_T for leading in p_T muon (right) for $pp \to 4\mu$ in the SM and Z' model (with $m_{Z'} = 60\,\text{GeV}$, $m_\chi = 10\,\text{GeV}$, $g_\mu = g_\chi = 0.1$), at $\sqrt{s} = 14$ TeV and $\mathcal{L} = 300\ fb^{-1}$. The peak in the four muon invariant mass spectrum is a reconstruction of the Z mass.

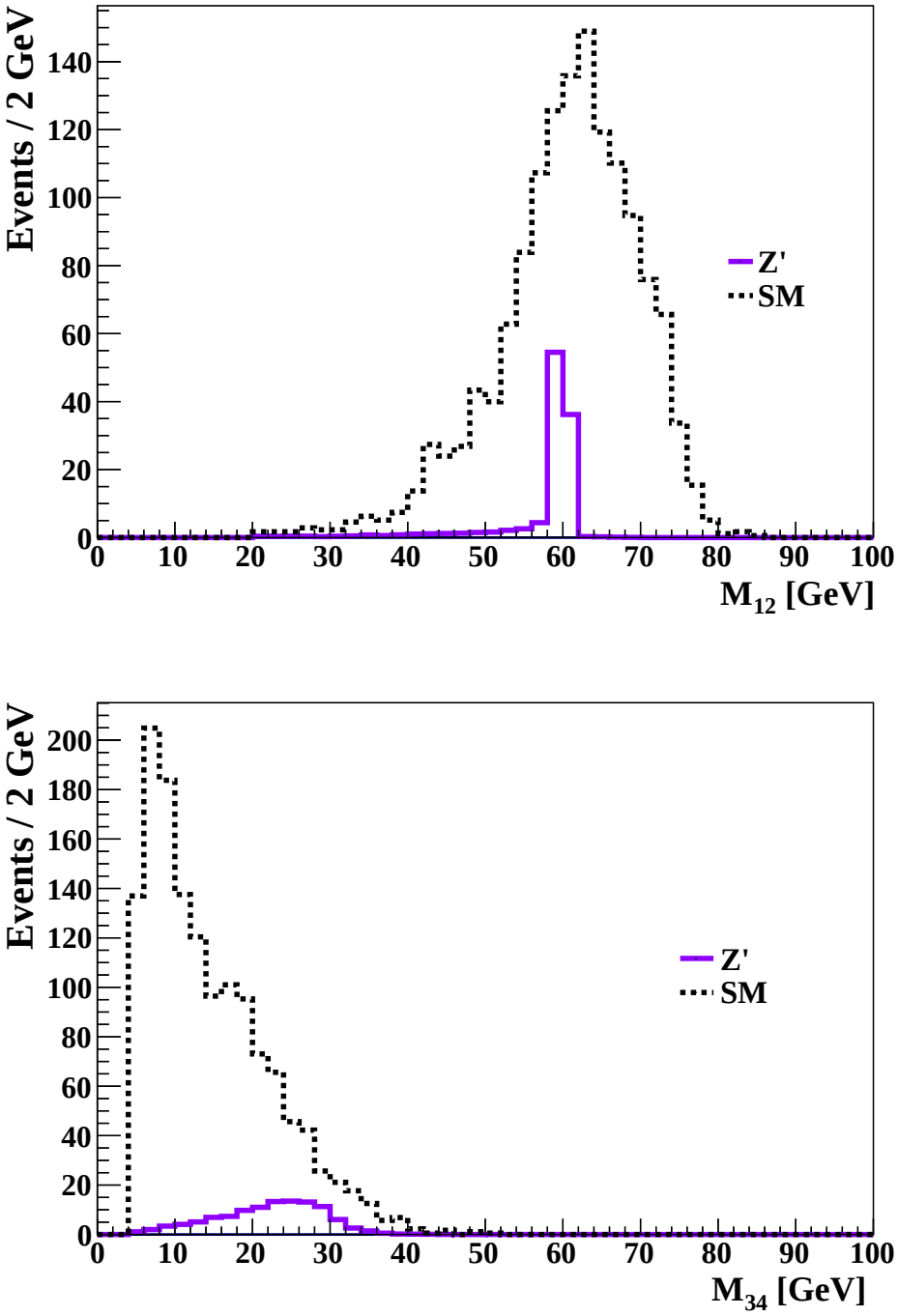

FIGURE 4.6: Invariant mass for first and second leading muons in p_T (left) and third and fourth leading muons in p_T (right) for $pp \to 4\mu$ in the SM and Z' model (with $m_{Z'} = 60$ GeV, $m_\chi = 10$ GeV, $g_\mu = g_\chi = 0.1$), at $\sqrt{s} = 14$ TeV and $\mathcal{L} = 300\ fb^{-1}$. The mass of the Z' can be seen clearly as the resonance at $m_{Z'} = 60$ GeV in the invariant mass spectrum M_{12}.

We do not perform a detector simulation for the $pp \to 4\mu$ analysis, as detection efficiencies are very high and the small smearing of data due to detector effects has a negligible effect on our results.

The current ATLAS exclusion based on the 4μ process at 20.7 fb^{-1} is shown in Fig. 4.11, assuming $g_\ell = g_\chi$. We also show future discovery curves at the higher luminosities of 300 and 3000 fb^{-1}. We show a selection of kinematic plots in Fig. 4.5, 4.6 for an example choice of parameters: $m_{Z'} = 60$ GeV, $m_\chi = 10$ GeV, $g_\mu = g_\chi = 0.1$. (The relevant Z' branching fractions are $Br(\mu^+\mu^-) = 0.428$, $Br(\bar{\nu}_\mu \nu_\mu) = 0.214$ and $Br(\bar{\chi}\chi) = 0.358$.) These parameters are allowed by the $\sqrt{s} = 8$ TeV ATLAS results, but sit on the 3σ curve corresponding to $\mathcal{L} = 300\ fb^{-1}$ at $\sqrt{s} = 14$ TeV, and thus can be discovered or ruled out with future LHC data.

Note that the choice of g_χ affects the cross section by controlling the relative sizes of the Z' branching ratios to lepton or dark matter final states. We can weaken constraints from the four muon search by increasing the Z' coupling strength to dark matter, with results for $4g_\mu = g_\chi$ and $8g_\mu = g_\chi$ shown in Fig. 4.10.

Four Muon Final State: $m_{Z'} > m_Z$

We now consider higher Z' masses than those probed by the 4 lepton search at the Z resonance, i.e., $m_{Z'} > m_Z$. The Z' production via the diagram in Fig. 4.3 now proceeds via an off-shell Z^*, with a much lower cross section as seen in Fig. 4.4. We perform a similar analysis to that described in the previous section, with appropriate changes tailored to this higher mass case. Specifically, we remove the cut on the 4 muon invariant mass, so that we are no longer restricted to events near the Z-resonance, and place cuts on the di-muon invariant masses to remove the Z-peak (arising from processes in which the Z' in Fig. 4.3 is replaced by a SM Z.)

We implement the following selection cuts:

- $p_{T,\mu} > 4$ GeV and $|\eta| < 2.7$ for individual muons
- Candidate separation of $\Delta R_{\mu\mu} > 0.1$
- $M_{\mu^-,\mu^+} > 100$ GeV for both the leading pair and next to leading pair in momentum
- $p_{T,\mu} > 120, 100, 8$ GeV for the leading three muons

Due to the low cross sections, large luminosities are required to constrain the high Z' masses. In Fig. 4.9 we show the projected 3σ exclusion curve at 3000 fb^{-1}. Notice that in the high $m_{Z'}$ searches at high luminosities one is able to probe Z'-masses up to $m_{Z'} \sim 500$ GeV. We show a selection of kinematic plots in Fig. 4.7, 4.8 for an example choice of parameters ($m_{Z'} = 150$ GeV, $m_\chi = 10$ GeV, $g_\mu = g_\chi = 0.28$) which fall on this curve. The effectiveness of the kinematic cuts can be seen by comparing the LH and RH panels of Fig. 4.8, which display the M_{34} distributions before and after cuts, respectively.

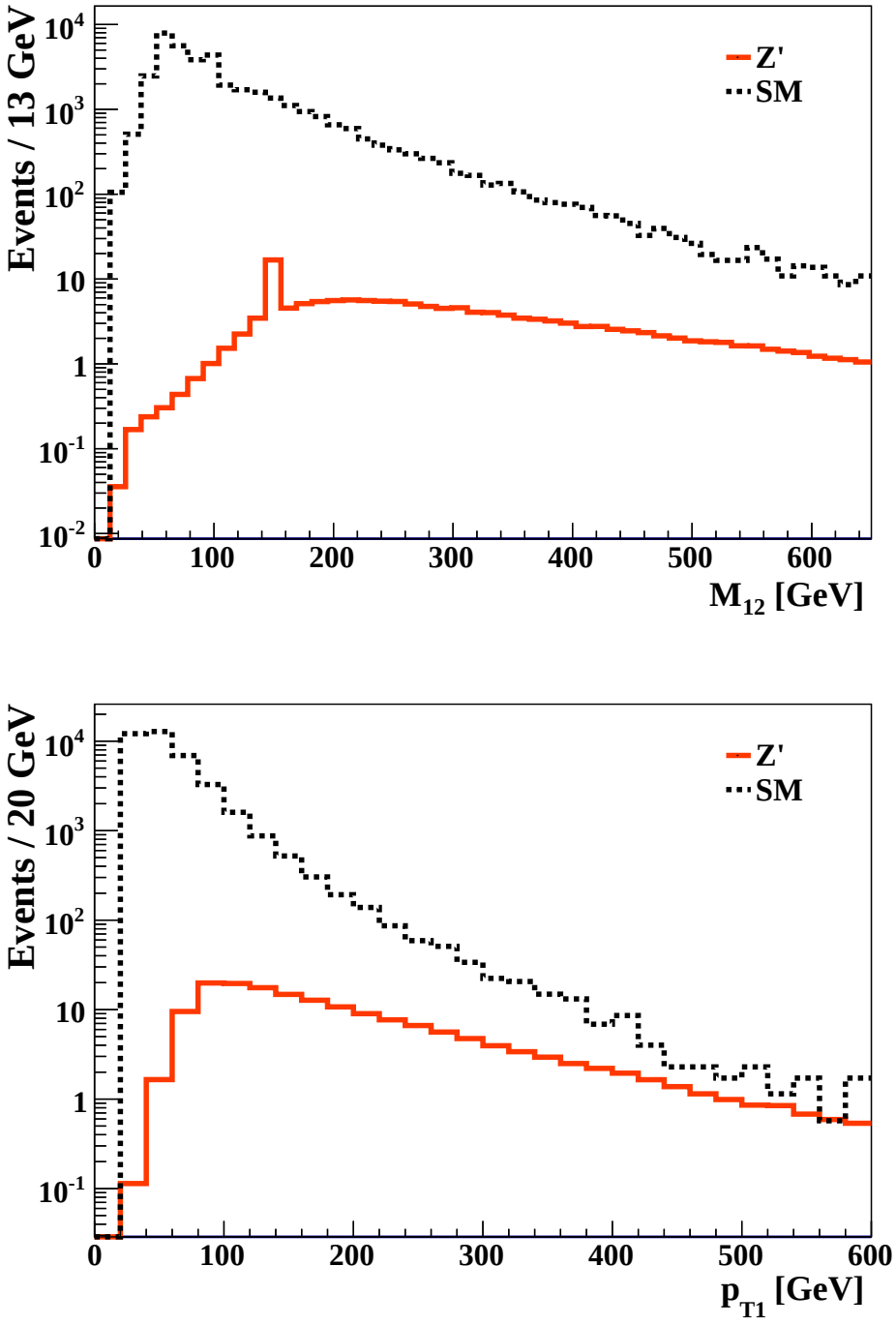

FIGURE 4.7: Invariant mass for first and second leading muons in p_T (left) and transverse momentum p_T for p_T leading muon (right) both before cuts, for $pp \to 4\mu$ in the SM and Z' model (with $m_{Z'} = 150$ GeV, $m_\chi = 10$ GeV, $g_\mu = g_\chi = 0.19$), at $\sqrt{s} = 14$ TeV and $\mathcal{L} = 3000\ fb^{-1}$.

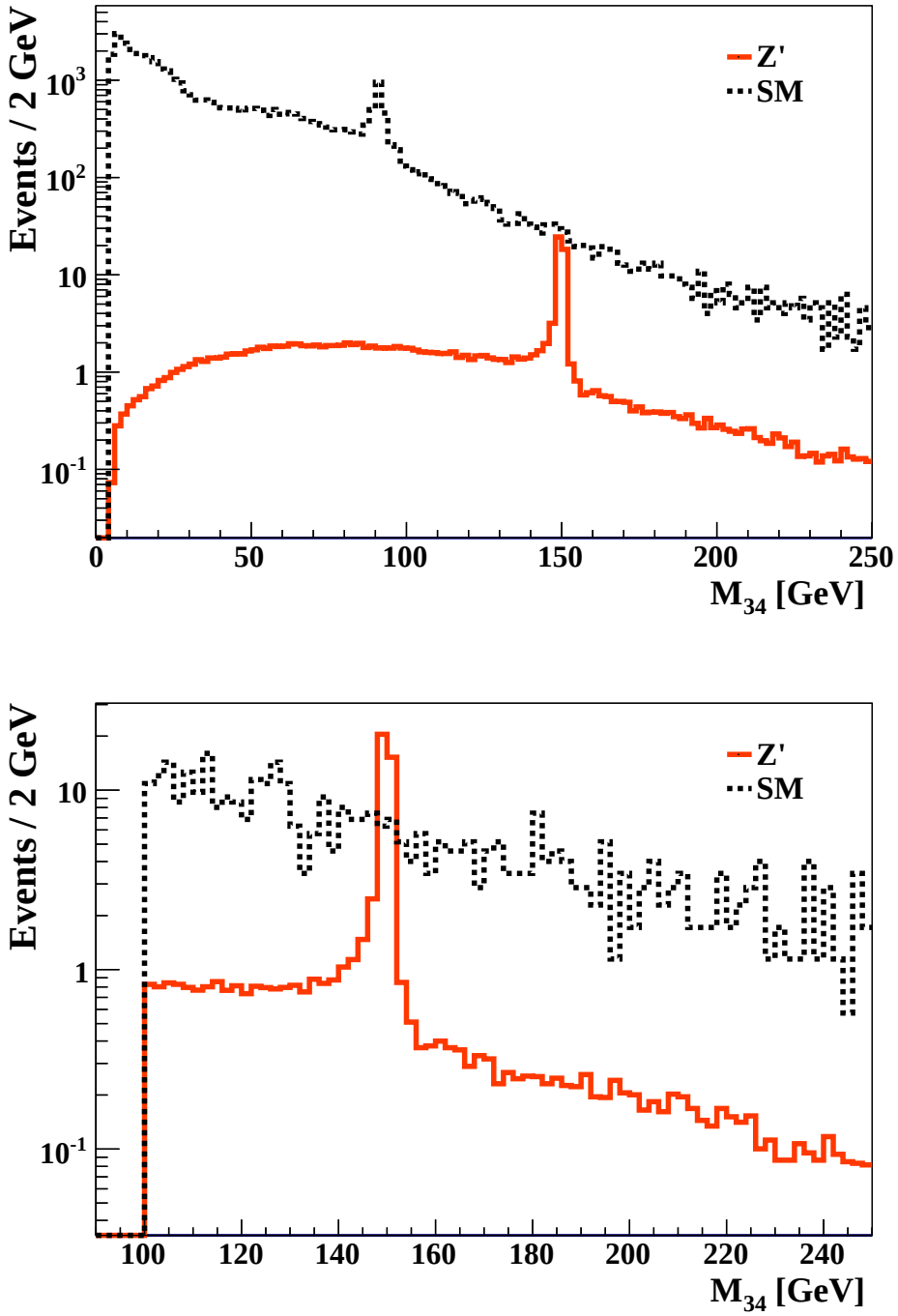

FIGURE 4.8: Invariant mass of third and fourth leading in p_T muons before cuts (left) and after cuts (right), for $pp \to 4\mu$ in the SM and Z' model (with $m_{Z'} = 150$ GeV, $m_\chi = 10$ GeV, $g_\mu = g_\chi = 0.19$), at $\sqrt{s} = 14$ TeV and $\mathcal{L} = 3000\ fb^{-1}$.

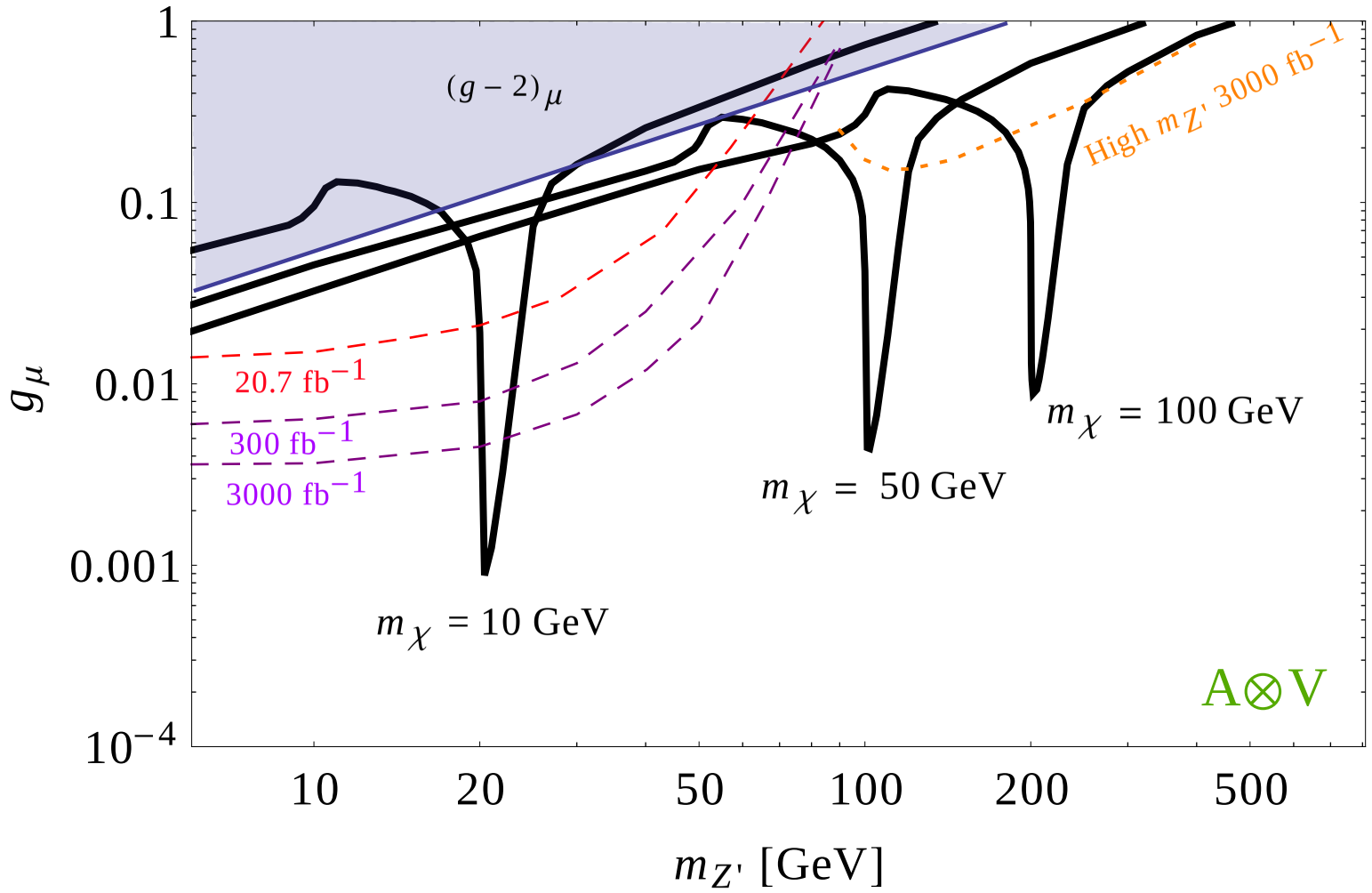

FIGURE 4.9: Parameter space for g_μ vs. $m_{Z'}$ with $g_\chi = g_\mu$. Shown are excluded regions from $(g-2)_\mu$, and relic density curves are shown in black for $m_\chi = 10, 50, 100$ GeV. Dashed lines are ATLAS exclusions and reaches: top dashed curve is ruled out by ATLAS data at $\sqrt{s} = 8$ TeV and $\mathcal{L} = 20.7 fb^{-1}$, middle is the ATLAS discovery reach at $\sqrt{s} = 14$ TeV and $\mathcal{L} = 300 fb^{-1}$, and the bottom dashed curve is the ATLAS discovery reach at $\sqrt{s} = 14$ TeV and $\mathcal{L} = 3000 fb^{-1}$. The dotted line shows the ATLAS reach at $3000 fb^{-1}$ for a high mass Z'. The LHC limits all assume $m_\chi = 10$ GeV.

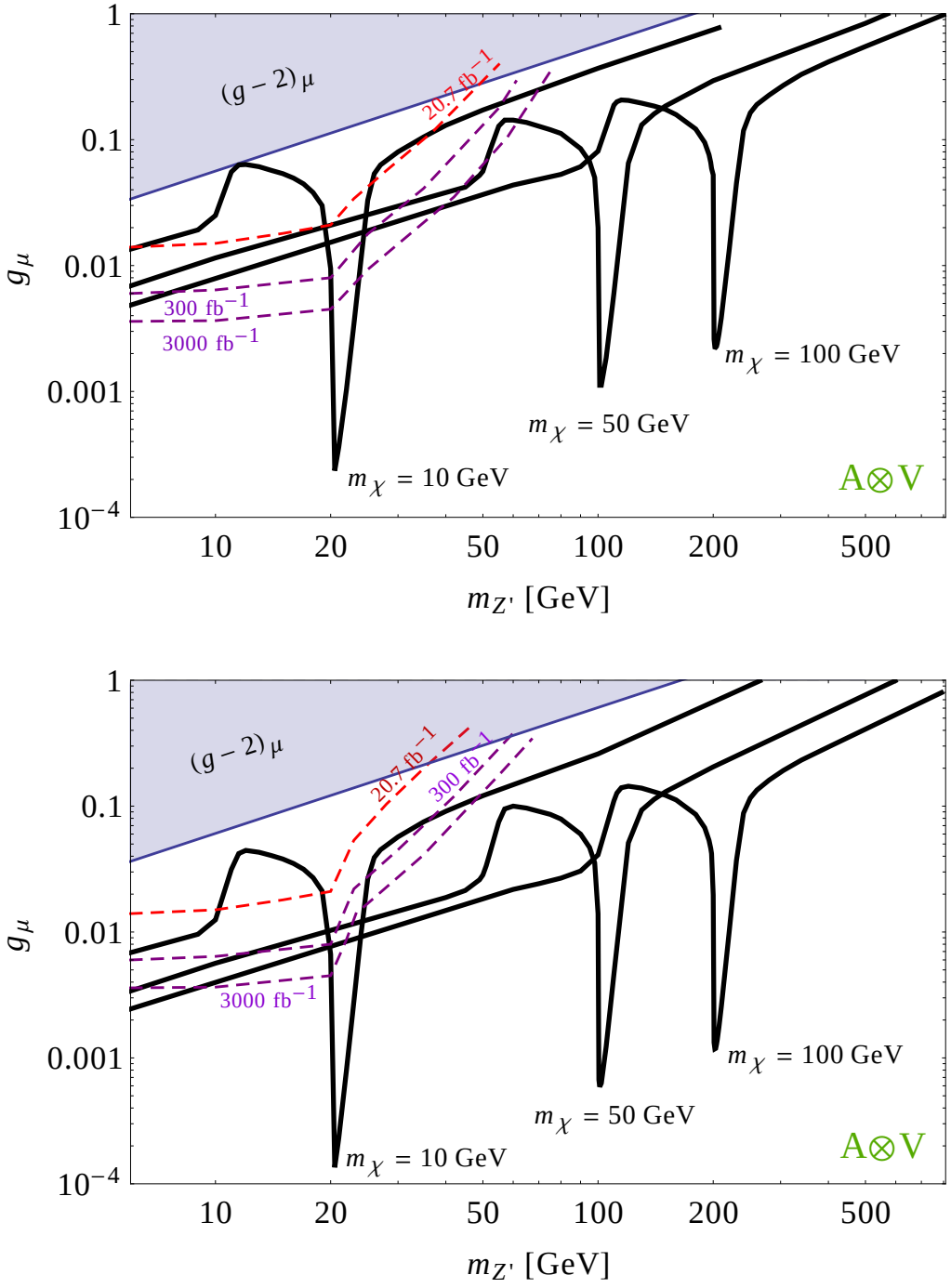

FIGURE 4.10: Parameter space for g_μ vs. $m_{Z'}$, where $g_\chi = 4g_\mu$ (left) and $g_\chi = 8g_\mu$ (right). Shown are excluded regions from $(g-2)_\mu$, and relic density curves are shown in black for $m_\chi = 10, 50, 100$ GeV. Dashed lines are ATLAS exclusions and reaches: top is ruled out by ATLAS data at $\sqrt{s} = 8$ TeV and $\mathcal{L} = 20.7 fb^{-1}$, middle is the ATLAS discovery reach at $\sqrt{s} = 14$ TeV and $\mathcal{L} = 300 fb^{-1}$, and bottom is the ATLAS discovery reach at $\sqrt{s} = 14$ TeV and $\mathcal{L} = 3000 fb^{-1}$. These exclusion/discovery curves are the same as for the $g_\mu = g_\chi$ case when $m_{Z'} < 2m_\chi$. The LHC limits all assume $m_\chi = 10$ GeV.

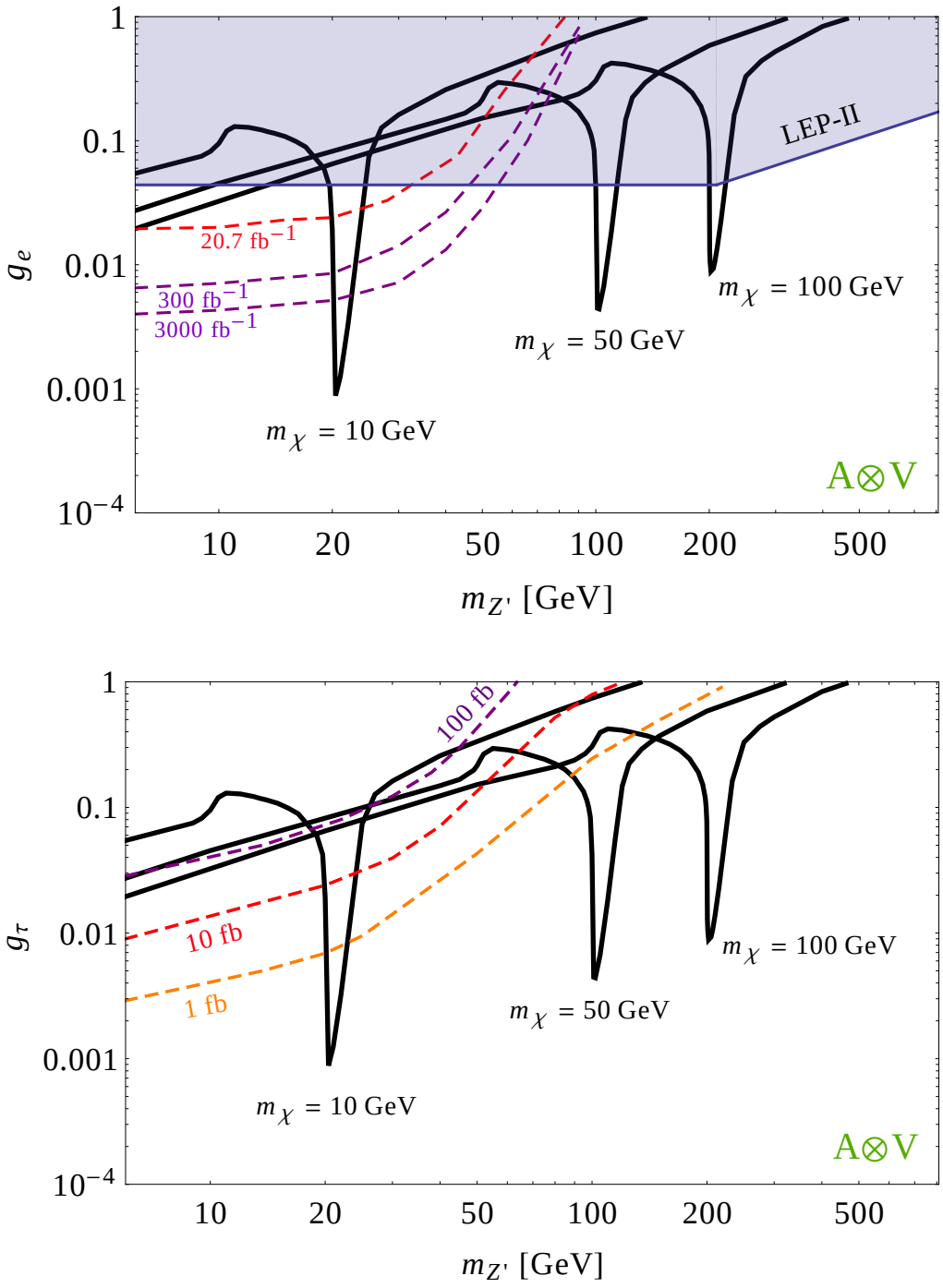

FIGURE 4.11: Parameter space for g_e vs. $m_{Z'}$ with $g_\chi = g_e$ (left) and g_τ vs. $m_{Z'}$, with $g_\chi = g_\tau$ (right). Relic density curves are shown in black for $m_\chi = 10, 50, 100$ GeV. Exclusions from LEP-II (electrons only) shown on the top. Dashed lines on the electron plot (left) are ATLAS exclusions and reaches: top is ruled out by ATLAS data at $\sqrt{s} = 8$ TeV and $\mathcal{L} = 20.7 fb^{-1}$, middle is the ATLAS discovery reach at $\sqrt{s} = 14$ TeV and $\mathcal{L} = 300 fb^{-1}$, and bottom is the ATLAS discovery reach at $\sqrt{s} = 14$ TeV and $\mathcal{L} = 3000\ fb^{-1}$. The LHC limits all assume $m_\chi = 10$ GeV. For the tau plot (bottom), there are no collider limits due to low efficiencies for reconstructing a four tau final state. Instead, dashed lines show contours of Z' production cross sections of 1, 10 and 100 fb.

4.5.2 Z' Decay to Dark Matter

We now consider the process $pp \to \ell\ell\chi\chi$ (see Fig. 4.3) for which the signal is a pair of opposite sign leptons plus missing E_T. Unlike the 4 lepton signal, the 2 lepton + missing E_T signal is subject to significant backgrounds, which render the detection prospects very poor. The dominant SM backgrounds arise from

$$pp \to Z + \text{jets} \to \ell^+\ell^- + \text{jets}, \tag{4.12a}$$

$$t\bar{t} \to b\bar{b}WW \to b\bar{b}\ell^+\ell^-\nu_\ell\bar{\nu}_\ell. \tag{4.12b}$$

The Z + jets background, with soft jets from the underlying QCD process, produces an enormous number of dileptons plus missing E_T events, where the missing energy arises from jet misidentification or energy mismeasurement. To overcome this background we would need to select events with $E_T \gtrsim 200$ GeV. However, a signal in this range would require a Z' greater than 200 GeV, for which the production cross section is extremely small. Nonetheless, despite being unable to detect the DM production process, the presence of the Z' coupling to DM still affects the collider phenomenology through the Z' width and branching fractions, as can be seen by comparing Fig. 4.9 and 4.10. Finally, we note that this dilepton plus missing E_T signal could be a relevant discovery channel in a future lepton collider such as the ILC, where the Z+jets background is not present.

4.6 Discussion

Our main results are summarized in Fig. 4.9, 4.10, 4.11 for $\Gamma_\chi \otimes \Gamma_\ell = A \otimes V$. Note that because $V \otimes V$ is highly constrained by direct detection [228], we have explored the $A \otimes V$ case in much greater detail.

In Fig. 4.9, we summarise the results for a Z' that couples to the muon flavour. We see that $(g-2)_\mu$ can place non-trivial constraints on low mass DM. In particular, for values of $m_\chi \lesssim 30$ GeV, it rules out those parameters for which the relic density can be explained, unless the masses fall in the vicinity of a resonance at $m_{Z'} \sim 2m_\chi$. The LHC results place complementary constraints. For a low mass Z' (those with $m_{Z'} < m_Z$), the collider limits rule out smaller values of the coupling g_ℓ than can be probed by $(g-2)$. The projected limits (or discovery sensitivity) for the 14 TeV LHC at 3000 fb^{-1} significantly covers the low $m_{Z'}$ parameter space, even for parameters for which the DM relic density is controlled by resonant annihilation. For a higher mass Z' ($m_{Z'} > m_Z$) the production cross section at the LHC is suppressed, and hence only the 3000 fb^{-1} results are shown in the figure. It is clear that, for sufficiently large m_χ or $m_{Z'}$, it will be possible to find parameters which satisfy the relic density requirement and escape all constraints.

The constraints on a Z' which couples to the e flavour are shown in top panel of Fig. 4.11. For electrons, the $(g-2)$ constraint is much weaker than for muons.

However, the e-flavour is subject to LEP-II Z' constraints, which are very strong and eliminate much parameter space that is open for the μ-flavour. As a result, the relic density constraints cannot be met unless one lives very close to a resonance.

Finally, we consider the τ flavour in the RH panel of Fig. 4.11. Here the $(g-2)$ constraints are too weak to be shown on the plot. As we mentioned above, there were no current collider analyses for this case, due to the difficulties associated with tau reconstruction. Instead, we indicate in Fig. 4.11 the Z' production cross section, as a crude indication of the sensitivity that could be obtained were a dedicated analysis for the 4-τ final state to be performed.

In Fig. 4.9 and 4.11, we assumed the Z' couples with equal strength to the DM and leptons, i.e. $g_\chi = g_\ell$. If instead we take $g_\chi > g_\ell$, the constraints are relaxed and thus the allowed region of parameter space enlarged. This is illustrated in Fig. 4.10, in which we take $g_\chi = 4g_\mu$ (left panel) and $g_\chi = 8g_\mu$ (right panel). We see that increased g_χ lowers the relic density curves. The LHC curves are independent of the choice of g_χ when $m_{Z'} < 2m_\chi$; for $m_{Z'} > 2m_\chi$ the constraints on g_ℓ become weaker as we enlarge g_χ, due to the increased branching ratio of the Z' to invisible final states. In Figs. 4.9 and 4.10, this occurs for $m_{z'} > 20$ GeV, and we note an upturn in the LHC curves at that point.

The LHC curves shown in Fig. 4.9, 4.10 and 4.11 assume $m_\chi = 10$ GeV. For other DM masses, the exclusion curves are approximately the same, except for a change to the point where $m_{Z'} = 2m_\chi$, beyond which the Z' is heavy enough for the dark branching ratio to be non-zero.[3]

4.7 Conclusions

We have considered a leptophilic WIMP scenario in which DM does not couple to SM quarks at tree-level, and instead couples only to SM leptons. In this scenario, the DM has WIMP-scale interaction with leptons, accounting for the relic density, but suppressed signals in direct detection experiments and hadron colliders, consistent with the null results from these searches to date.

We explored such a leptophilic DM in the context of a simple Z' model, in which DM-lepton interactions are mediated by the exchange of a new vector boson which couples to one of the SM leptons flavours, $\ell = e$, μ, or τ, with Lorentz structure $A \otimes V$.

Production of leptophilic Z' at the LHC occurs via the radiation of a Z' from Drell-Yan leptons. We determined exclusion limits for the Z' mass and coupling strength, using results from an ATLAS analysis of $pp \to Z \to 4e$ or 4μ, at $\sqrt{s} = 8$ TeV and $\mathcal{L} = 20.7\ fb^{-1}$. We also projected the future exclusion/discovery reach for $\sqrt{s} = 14$ TeV and higher luminosities, for both low and high mass Z' bosons.

[3]Even when $Br(\text{DM})$ is non-zero, if $g_\chi \sim g_\ell$ the cross section and thus the exclusion curves change only by a modest factor.

For $\ell = e$, the combination of the LHC, and relic density and LEP constraints excludes most parameter space, except that for which the DM annihilation at freezeout is resonantly enhanced. For $\ell = \mu$, some non-resonant parameter space remains open for $m_\chi \lesssim 50\,\text{GeV}$, while for $\ell = e$ this is eliminated by LEP-II bounds. For $\ell = \tau$, however, no LHC bounds exist, and much more parameter space is open.

In conclusion, despite the absence of tree-level interactions with quarks, this leptophilic dark matter model can be strongly probed at hadron collider experiments—most significantly at low DM and mediator masses.

Part III

Dark Matter in the Sky

In Part III of this thesis, we examine signatures for dark matter in the sky. This will include the use of simplified models in indirect detection searches, searches for hidden sector mediators in galaxies, using dark bremsstrahlung to boost the dark matter annihilation rate, and searches for dark matter via long-lived mediators in the Sun.

Chapter 5

Dark Forces in the Sky: Signals from Z' and the Dark Higgs

In this chapter, we consider the indirect detection signals for a self-consistent hidden $U(1)$ model containing a Majorana dark matter candidate, χ, a dark gauge boson, Z', and a dark Higgs, s. Compared with a model containing only a dark matter candidate and Z' mediator, the addition of the scalar provides a mass generation mechanism for the dark sector particles and is required in order to avoid unitarity violation at high energies. We find that the inclusion of the two mediators opens up a new two-body s-wave annihilation channel, $\chi\chi \to sZ'$. This new process, which is missed in the usual single-mediator simplified model approach, can be the dominant annihilation channel. This provides rich phenomenology for indirect detection searches, allows indirect searches to explore regions of parameter space not accessible with other commonly considered s-wave annihilation processes, and enables both the Z' and scalar couplings to be probed. We examine the phenomenology of the sector with a focus on this new process, and determine the limits on the model parameter space from Fermi data on dwarf spheriodal galaxies and other relevant experiments.

This chapter is based on the publication: *N. F. Bell, Y. Cai and R. K. Leane, "Dark Forces in the Sky: Signals from Z' and the Dark Higgs", JCAP 08 (2016) 001 [arXiv:1605.09382 [hep-ph]].* [257]

5.1 Introduction

Simplified models remain a popular interpretation of experimental data. However, due to their simplified nature and reduced number of parameters, the benchmark simplified models are not intrinsically capable of capturing the full phenomenology of many realistic UV complete theories. Furthermore, separate consideration of these benchmarks can lead to physical problems and inconsistencies, such as breaking gauge invariance and unitarity violation at high energies [74–78, 80, 102, 153, 258–264].

These issues motivate a scenario in which the vector and the scalar mediators appear together within the same theory[1]. Specifically, a simplified model with a spin-1 mediator and axial-vector couplings to fermions will lead to unitarity violation at high energies unless some additional new physics, such a scalar degree of freedom, is introduced to the simplified model setup [80]. This scalar is exceedingly well motivated if it is also taken to provide a mass generation mechanism for the dark sector, as the "dark Higgs". The purpose of this chapter is to explore the indirect detection signals for a gauge invariant model where the dark sector consists of a fermionic DM candidate, a spin-1 mediator, and a dark Higgs field. In doing so, we shall encounter important phenomenology that cannot be captured by a single-mediator model.

In the indirect detection context, simplified models have commonly been used to investigate annihilation processes and place limits on the dark matter parameter space. Only annihilations which proceed via an s-wave process contribute substantially to DM signals in the universe today, as p-wave contributions are highly suppressed by a velocity squared factor, $v_\chi^2 \approx 10^{-6}$. Within the simplified model framework, spin-1 mediators provide two possible two-body s-wave annihilation processes for fermionic dark matter, as shown in Fig. (5.1). (i) $\chi\chi \to f f$ has an s-wave component provided the mediator has axial-vector couplings to SM fermions, f while (ii) $\chi\chi \to Z'Z'$ has an s-wave component for any (vector or axial-vector) coupling of the Z' to χ. The latter process, with the Z' pair produced on-shell, is commonly studied in the indirect detection context; it is capable of producing large annihilation signals while avoiding strong constraints imposed by collider and direct detection searches [269–273].

For spin-0 mediators, $\chi\chi \to f f$ is s-wave if the mediator is a pseudoscalar, but the couplings to SM fermions are strongly constrained, such that a thermal relic cross section is not easily obtained, nor a large indirect detection signal. The remaining 2-body annihilation processes for spin-0 mediators are all p-wave, meaning that to obtain a non-negligble indirect detection signal with non-excluded parameters, one needs to resort to the case where three spin-1 fields, s, are produced[2] as $\chi\chi \to sss$. While this is an s-wave process provided that the mediator is a pseudoscalar, it suffers from three-body phase space suppression [270]. These processes are shown in Fig. (5.2).

[1] Some recent work on multi-mediator models can be found in Refs. [265–268].

[2] A two-body s-wave process is possible for combinations of multiple distinct scalars [270, 271, 274], but this extends beyond the simplified model framework and requires more detailed model building.

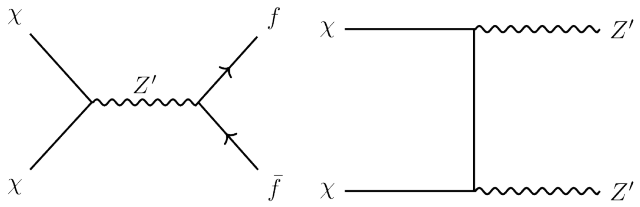

FIGURE 5.1: Spin-1 simplified model annihilation processes. Left: This process has an s-wave component only if the mediator has axial-vector couplings to SM fermions, f. However, the non-observation of a direct detection or LHC signal makes it difficult to obtain a thermal relic scale cross section from this diagram. Right: This process is s-wave for all field or coupling types and, as it can avoid LHC and direct detection bounds in the hidden on-shell mediator scenario, is often considered in the indirect detection context.

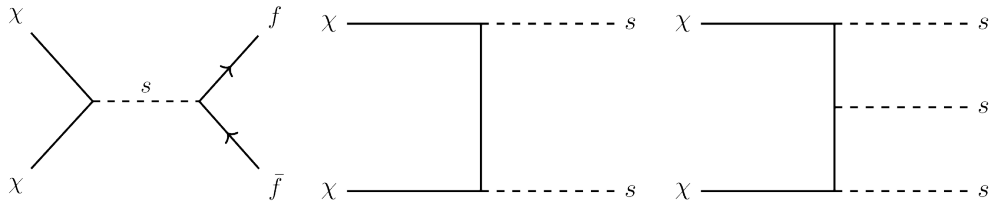

FIGURE 5.2: Spin-0 simplified model annihilation processes. Left: This process has an s-wave component if the spin-0 field is a pseudoscalar. However, the non-observation of a direct detection or LHC signal makes it difficult to achieve a thermal relic density with this process. Middle: This process is p-wave for all field or coupling types. Right: This process has an s-wave contribution if the spin-0 field is a pseudoscalar, but it is three-body phase space suppressed. There is no s-wave process for fermionic DM annihilation to a spin-0 field with scalar couplings.

In this chapter, we will show that once the dark Higgs is added to the dark sector, the indirect detection phenomenology considered previously was incomplete. Of particular interest will be the new s-wave annihilation process,

$$\chi\chi \to sZ'. \tag{5.1}$$

This is always an s-wave process, irrespective of whether the DM-Z' coupling is vector or axial-vector, and irrespective of whether s is a scalar or pseudoscalar. This process allows for new, rich phenomenology. It allows the spin-0 particle to play an important role in indirect detection, which is not possible in models with only a spin-0 mediator due to the velocity or phase space suppressions of the annihilation diagrams in the pseudoscalar mediator case, and the complete absence of any s-wave annihilation processes in the scalar mediator case. Importantly, although both the $\chi\chi \to sZ'$ and $\chi\chi \to Z'Z'$ annihilation channels have an s-wave

component, the sZ' channel tends to dominate when it is kinematically accessible. Neglecting this important annihilation process would lead to dramatically different results.

Hidden sector models [269–273, 275–297] are a specific realization of simplified models, commonly adopted in the indirect detection scenario because their small direct couplings to the SM ameliorate the tension between strong constraints from collider and direct detection experiments, and the goal of a sizeable indirect detection signal. If the DM annihilates to on-shell mediators (rather than directly to SM particles via off-shell mediators) the smallness of the dark-SM couplings are irrelevant for indirect detection, provided of course that the dark-sector mediators eventually decay to visible sector particles with lifetime shorter than the age of the galaxy. The signal size for indirect detection is instead set by the size of the dark sector couplings, which can often be taken to be quite large.

In this chapter, we will investigate the phenomenology of these indirect detection signals for a self-consistent hidden $U(1)$ sector, with a focus on the impact of this new $\chi\chi \to sZ'$ annihilation channel. In Section 5.2, we will describe the model in detail. We will then list all the annihilation processes of interest in this model, along with the relevant cross sections and decay widths, in Section 5.3. In Section 8.3.4, we will simulate the consequent γ-ray spectra, which we will use in Section 5.5 to calculate the limits on the cross section and parameter space from Fermi-LAT data on dwarf spheriodal galaxies, the most dark matter dense objects in our sky, as well as AMS-02. Finally we will consider relevant limits from unitarity and other experiments in Section 5.6, and summarize in Section 6.8.

5.2 Model Setup

The gauge symmetry group for our model is $SU(3)_c \otimes SU(2)_W \otimes U(1)_Y \otimes U(1)_\chi$, such that the covariant derivative is $D_\mu = D_\mu^{SM} + iQ' g_\chi Z'_\mu$ with Q' being the dark $U(1)_\chi$ charge of the relevant fields. We introduce new fields: a Majorana fermion DM candidate χ, a spin-1 dark gauge boson Z', and the dark Higgs field S. We have chosen χ to be Majorana, as a well-motivated example that must involve axial-vector couplings to the Z', given that vector couplings of Majorana particles vanish. The significance of axial-vector couplings is that perturbative unitarity would be violated at high energy in the absence of S [80]. The dark Higgs is mandatory in this set-up.

The vacuum expectation value (vev) of the dark Higgs field provides a mass generation mechanism for the dark sector fields Z' and χ. For the χ-S Yukawa terms to respect the $U(1)_\chi$ gauge symmetry, the charge assignments[3] can be chosen, without loss of generality, to be $Q'(S) = 1$ and $Q'(\chi) = -\frac{1}{2}$. The dark Higgs

[3]In order to cancel anomalies, additional fermions with $U(1)_\chi$ charge will be required. However, these states can be made sufficiently heavy that they do not affect by the dark sector phenonenology discussed here. For example, anomaly cancellation can be achieved by introducing an additional Majorana fermion, with $U(1)_\chi$ charge equal in magnitude but of opposite sign to that of χ. It is

can mix with the SM Higgs H through mass mixing, with strength parameterized by λ_{hs}, while the $U(1)_\chi$ field strength tensor $Z'_{\mu\nu}$ kinetically mixes with the SM hypercharge field strength $B_{\mu\nu}$ controlled by the kinematic mixing parameter ϵ. Explicitly, before electroweak and dark symmetry breaking, the Lagrangian is written as

$$\begin{aligned}\mathcal{L} = \quad & \mathcal{L}_{SM} + \frac{i}{2}\overline{\chi}\not{\partial}\chi - \frac{1}{4}g_\chi Z'^\mu \overline{\chi}\gamma_5\gamma_\mu\chi - \frac{1}{2}y_\chi\overline{\chi}\left(P_L S + P_R S^*\right)\chi \; - \frac{\sin\epsilon}{2}Z'^{\mu\nu}B_{\mu\nu} \\ + \quad & \left[(\partial^\mu + ig_\chi Z'^\mu)S\right]^\dagger\left[(\partial_\mu + ig_\chi Z'_\mu)S\right] - \mu_s^2 S^\dagger S - \lambda_s(S^\dagger S)^2 - \lambda_{hs}(S^\dagger S)(H^\dagger H).\end{aligned} \tag{5.2}$$

After symmetry breaking and mixing the terms of interest are

$$\begin{aligned}\mathcal{L} \quad \supset \quad & \frac{1}{2}m_{Z'}^2 Z'^\mu Z'_\mu - \frac{1}{2}m_s^2 s^2 - \frac{1}{2}m_\chi\overline{\chi}\chi - \frac{1}{4}g_\chi Z'^\mu\overline{\chi}\gamma_5\gamma_\mu\chi - \frac{y_\chi}{2\sqrt{2}}s\overline{\chi}\chi \\ + \quad & g_\chi^2 w Z'^\mu Z'_\mu s - \lambda_s w s^3 - 2\lambda_{hs}(hvs^2 + swh^2) + g_f\sum_f Z'^\mu\overline{f}\Gamma_\mu f,\end{aligned} \tag{5.3}$$

where the component fields of S and H are defined in the broken phase as $S \equiv \frac{1}{\sqrt{2}}(w + s + ia)$ and $H = \left\{G^+, \frac{1}{\sqrt{2}}(v + h + iG^0)\right\}$ with G^+, G^0 and a being the Goldstone bosons of W, Z and Z' respectively, while s and h are real scalars. In the limit that the mixing parameter λ_{hs} is small, the vev of the dark Higgs satisfies $w^2 = -\mu_s^2/\lambda_s$. After symmetry breaking, the masses are

$$m_{Z'} = g_\chi w, \tag{5.4a}$$

$$m_\chi = \frac{1}{\sqrt{2}}y_\chi w, \tag{5.4b}$$

$$m_s^2 \simeq -\mu_s^2, \tag{5.4c}$$

$$m_h \simeq -\mu_h^2. \tag{5.4d}$$

For all couplings to remain perturbative, only certain combinations of the dark gauge coupling and dark sector masses are allowed. From the above equations, the relation between the dark yukawa coupling y_χ and the $U(1)_\chi$ gauge coupling g_χ is

$$\frac{y_\chi}{g_\chi} = \frac{\sqrt{2}\,m_\chi}{m_{Z'}}. \tag{5.5}$$

The final term of Eq. (6.9a) describes the coupling of Z' to the SM fermions; its structure is dictated by the kinetic mixing, and the explicit form can be found, for example, in Ref. [27]. As Z' decays to the SM through the hypercharge portal, the Z' couples to the same SM fields as the SM Z, and no flavor specific tuning is permitted. This enforces strong di-lepton resonance bounds and EWPT limits on

sufficient to consider only the lighter of the two fermions as the DM candidate, with the heavier making a subdominant contribution to the relic density [296].

Z-Z' mixing. Regardless, the small values of ϵ we consider allow these bounds to be easily satisfied.

Within this model, there are two possible routes for dark sector interactions with the visible sector: the Higgs portal controlled by parameter λ_{hs}, or the hypercharge portal controlled by parameter ϵ. To demonstrate the new phenomenology of the combination of both the Z' and dark Higgs in this model, we will take small values of these parameters consistent with the hidden model setup, and assume both s and Z' decay on-shell to SM fermions. As the Higgs couples to fields proportional to their masses, the dark Higgs decays predominantly to b-quarks in the mass range we consider, although we will fully simulate all final states. The dark Higgs may also decay into two Z' which then may decay into SM fermions, however for simplicity when setting limits we will focus on the region of parameter space where this is not kinematically allowed.

We emphasize that this is the most general scenario involving the interaction of a Majorana fermion with a Z' gauge boson. Given that vector currents vanish for Majorana fermions, leaving only axial-vector interactions, the inclusion of the dark Higgs is unavoidable in order to provide a mass for the Z' within a gauge invariant model that respects perturbative unitarity. Furthermore, it is not possible to include a Majorana mass term for the χ without breaking the $U(1)_\chi$ symmetry. The case of Dirac dark matter with vector couplings to a Z' would be very different. In that case, the Z' may obtain mass via the Stueckelberg mechanism, and a bare mass term for χ is possible, leaving no need for a dark Higgs.

5.3 Dark Matter Annihilation Processes for Indirect Detection

In this section we will calculate the annihilation cross sections and branching fractions relevant for indirect detection.

5.3.1 Annihilation Cross Sections

The novel process for DM annihilation in the universe today is $\chi\chi \to sZ'$, which is shown in Fig. (5.3). This process has not been considered in previous work, despite being a consequence of a self-consistent Z' model with axial-vector couplings. The cross section for $\chi\chi \to sZ'$ is s-wave for both scalar and pseudoscalar interactions, and vector or axial-vector Z'-DM couplings. For Majorana DM and a real scalar the annihilation cross section is given by

$$\langle \sigma v \rangle_{\chi\chi \to sZ'} = \frac{g_\chi^4 \left(m_s^4 - 2m_s^2 \left(m_{Z'}^2 + 4m_\chi^2 \right) + \left(m_{Z'}^2 - 4m_\chi^2 \right)^2 \right)^{3/2}}{1024\pi m_\chi^4 m_{Z'}^4}, \tag{5.6}$$

where Eq. (5.5) has been used to replace y_χ. Here, only the s-channel diagram of Fig. (5.3) contributes an s-wave component.

The other dominant s-wave process in this model is $\chi\chi \to Z'Z'$, which is shown in Fig. (5.4). For Majorana DM, the s-wave contribution to its cross section is given by[4]

$$\langle \sigma v \rangle_{\chi\chi \to Z'Z'} = \frac{g_\chi^4 \left(1 - \frac{m_{Z'}^2}{m_\chi^2}\right)^{3/2}}{256\pi m_\chi^2 \left(1 - \frac{m_{Z'}^2}{2m_\chi^2}\right)^2}\,, \tag{5.7}$$

where the s-wave contributions only come from the t and u channel diagrams, making the indirect signal for the $Z'Z'$ process the same as that found in the spin-1 simplified model benchmark.

Previously, annihilation of fermionic dark matter to spin-0 mediators featured an s-wave component only for the three-body phase-space suppressed process in Fig. (5.2), and only for pseudoscalars. For a simplified model with a scalar mediator, there is no s-wave annihilation process at all. We make the important observation that annihilation of fermionic dark matter to a spin-0 plus spin-1 final state will always be s-wave, for both scalars and pseudoscalars. This allows indirect detection to have comparable sensitivity for spin-0 and spin-1 mediators, in models where the two mediators are both present. This is realized naturally in the very simple gauge invariant model we have presented in this chapter.

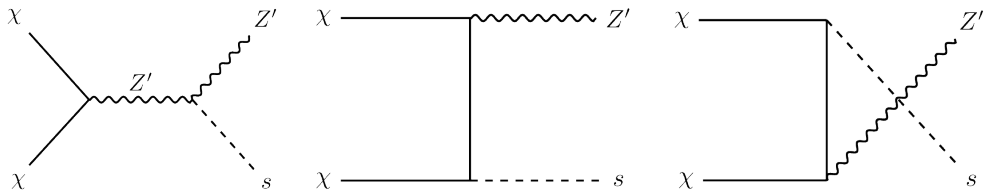

FIGURE 5.3: Annihilation diagrams for the s-wave processes $\chi\chi \to sZ'$. The scalar and the Z' then can decay to SM fermion final states. For some regions of parameter space this is the only kinematically allowed process, while in others it can have a cross section larger than the process in Fig. (5.4). This process can be achieved by considering the simplified model benchmarks together.

As this new s-wave annihilation process is a consequence of enforcing perturbative unitarity at high energies, its presence is inevitable for axial-vector Z'-DM couplings. This means that the limits on indirect detection signals using the $Z'Z'$ process alone will lead to inaccurate conclusions. This can be seen in Fig. (5.5), where we plot the annihilation cross sections to both the $Z'Z'$ and sZ' final states. If the s is lighter than the Z', there are values of DM mass $m_s + m_{Z'} < 2m_\chi < 2m_{Z'}$ where sZ' is the only kinematically accessible final state. If we were to only consider the $Z'Z'$ process, it would not be possible to produce a limit for these low DM

[4]The factor of 16 difference between our cross section and that given in other papers is due to the $(Q'_\chi)^4 = (1/2)^4$ charge contribution to the coefficient.

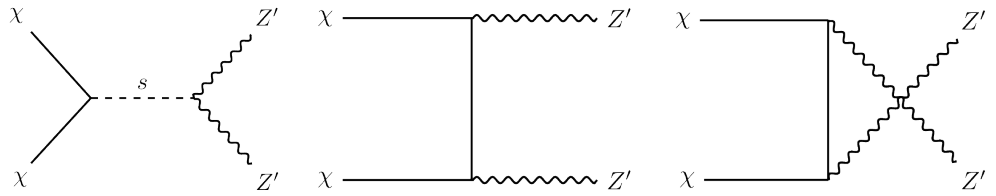

FIGURE 5.4: Annihilation diagrams for the s-wave processes $\chi\chi \to Z'Z'$. The Z' then can decay into SM fermion final states. In the spin-1 mediator simplified model benchmark, only the t-channel and u-channel diagrams appear, leading to unitarity issues at high energies for axial couplings. In our gauge invariant model, the s-channel diagram restores perturbative unitarity. Consideration of only $\chi\chi \to Z'Z'$, without the accompanying $\chi\chi \to sZ'$ process of Fig. (5.3) will lead to inaccurate conclusions.

masses (where, in fact, the indirect detection limits are the strongest). When both sZ' and $Z'Z'$ are kinematically accessible, sZ' becomes the dominant process. In the limit $m_\chi^2 \gg m_{Z'}^2, m_s^2$, the cross section to sZ' is enhanced relative to that for $Z'Z'$ by a factor of $(m_\chi/m_{Z'})^4$, arising due to the longitudinal Z' polarization. It is important to note, however, that the DM mass and Z' mass are related via the dark Higgs vev, and thus satisfy Eq. (5.5). As a result, it is not possible to make the DM mass arbitrarily large while retaining a perturbative value for the Yukawa coupling y_χ. For the mass ranges plotted in Fig. (5.5), we have ensured that all parameters take reasonable values.

The s-wave annihilations to sZ' and $Z'Z'$ are by far the dominant processes for indirect detection, for which the total annihilation cross section is obtained by summing the contributions from these channels. In setting indirect detection limits, the energy spectra should be computed by properly combining the spectra arising from the sZ' and $Z'Z'$ final states. These s-wave processes will also be the most important for the determination of relic density at freezeout. However, p-wave processes will also play a role at freezeout, where the DM relative velocity is much larger than in the universe today. Note that as the cross sections in Fig. (5.5) each scale as g_χ^4, the correct thermal relic density can easily be obtained simply by adjusting the value of the dark gauge coupling.

5.3.2 Decay Widths of the Dark Higgs and Z'

To compare our annihilation processes to indirect detection signals, it is necessary to first multiply the thermal averaged cross sections for our on-shell processes by relevant branching fractions. The Z' decays to SM states via the hypercharge portal, and so couplings to all fermion flavors must be considered. The partial decay width of the Z' into SM fermions is given by

$$\Gamma(Z' \to f\bar{f}) = \frac{m_{Z'} N_c}{12\pi} \sqrt{1 - \frac{4m_f^2}{m_{Z'}^2}} \left[g_{f,V}^2 \left(1 + \frac{2m_f^2}{m_{Z'}^2}\right) + g_{f,A}^2 \left(1 - \frac{4m_f^2}{m_{Z'}^2}\right) \right], \qquad (5.8)$$

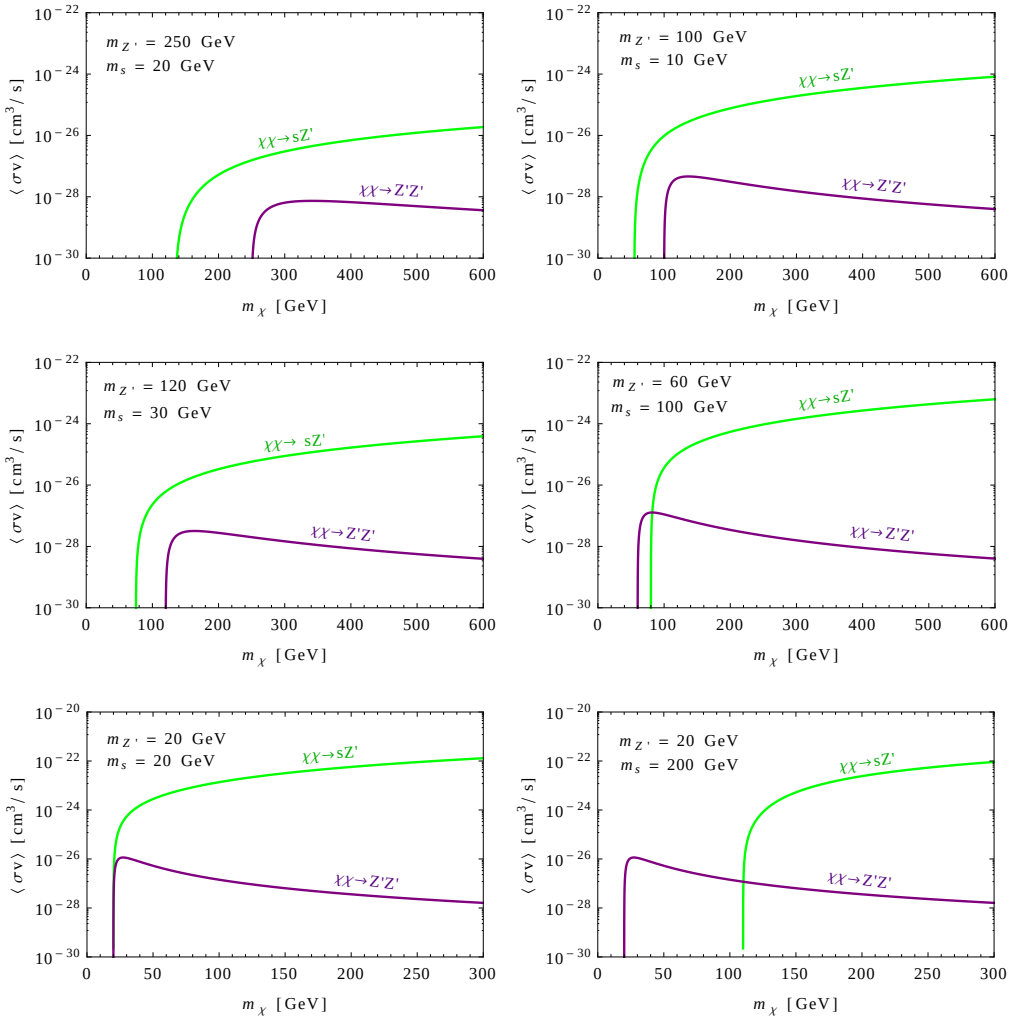

FIGURE 5.5: Relative cross section sizes for the two dominant s-wave diagrams, $\chi\chi \to sZ'$ (green) and $\chi\chi \to Z'Z'$ (purple), for some example parameter choices for the dark Higgs mass m_s and the Z' mass $m_{Z'}$, as labelled on each plot. For all plots the gauge coupling is set to $g_\chi = 0.1$, but as all cross sections are directly proportional to g_χ^4 they can easily be scaled by adjusting this parameter. Note the lower two plots have a different m_χ range to the upper plots, so that the y_χ coupling is restricted to $O(1)$ values.

where N_c is a color factor, relevant for hadronic decays. The $g_{f,V}$ (vector) and $g_{f,A}$ (axial-vector) coupling structures of the Z' to the SM are inherited from the kinetic mixing with the SM. The total decay width for the Z' is simply the sum of all the fermionic decays,

$$\Gamma'_Z = \sum_f \Gamma(Z' \to f\bar{f}). \tag{5.9}$$

The dark Higgs decays to the SM due to mass mixing with the SM Higgs. As it couples to fermions through their mass, the decay will be predominantly to b quarks in the mass ranges we are considering, however we include all SM final states for accuracy. The dark Higgs is also permitted to decay to pairs of Z', although for simplicity we will choose parameters where this decay is not kinematically permitted. As loop decays and higher order corrections can be relevant for the dark Higgs decays, to ensure an accurate calculation of the branching fractions, we use the Fortran package HDecay [298], which takes these effects into account.

5.4 γ-ray Energy Spectra

The gamma ray flux Φ from photons with energy E_γ resulting from dark matter annihilation into a fermion species f is

$$\frac{d^2\Phi}{d\Omega dE_\gamma} = \frac{\langle\sigma v\rangle}{8\pi m_\chi^2}\left(\sum_f \frac{dN}{dE_\gamma} Br_f\right) J(\phi,\gamma), \tag{5.10}$$

where Br_f is the branching fraction to the particular fermion species. For the Z' we take this as the ratio of Eq. (6.17) and Eq. (5.9). For the dark Higgs, we generate values using HDecay [298]. The J factor is the integral over the line of sight of the DM density $\rho(r)$ squared, at a distance r from the center of the galaxy [128],

$$J(\phi,\gamma) = \int \rho^2(r) dl, \tag{5.11}$$

where the DM density is taken to be modelled by the Navarro-Frenk-White (NFW) profile. The numerical values of the J-factors and their uncertainties together with other properties of the dSphs are listed in Tab. I of Ref. [135].

To obtain our γ-ray spectra, we simulate the annihilation cascade for a given DM mass with an effective resonance in Pythia [299]. In our setup, it is possible to have two different on-shell states which decay to SM fermions: the Z' and the dark Higgs. To model for our different states, we produce one diagram with two Z' and one with two dark Higgs, both with effective resonances in their center of mass frames. We then average these to produce the effective spectra for a given DM mass. Specifically, the effective resonances for different Z' and dark Higgs s

masses are respectively given by [27]

$$E^{Z'}_{CoM} = \frac{s + m^2_{Z'} - m^2_s}{2\sqrt{s}}, \quad E^{s}_{CoM} = \frac{s + m^2_s - m^2_{Z'}}{2\sqrt{s}}. \tag{5.12}$$

Example gamma ray spectra including all possible fermionic SM final states are shown in Fig. (5.6), as well as a comparison of the sZ' and $Z'Z'$ spectra for example parameters.

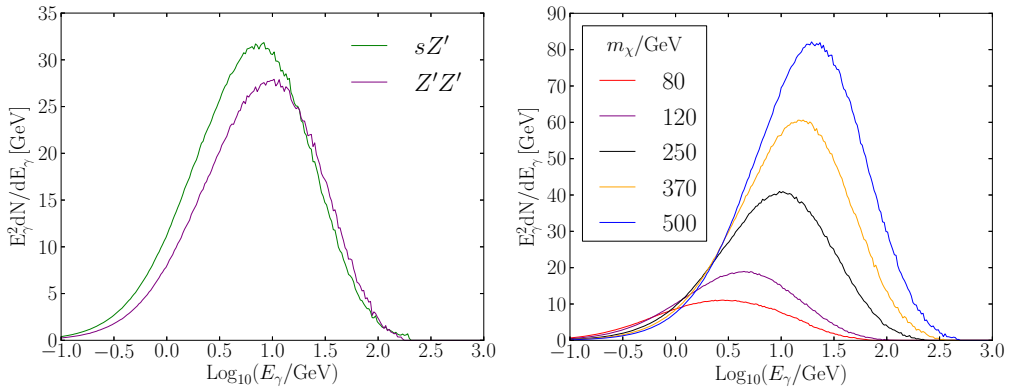

FIGURE 5.6: Left: Comparison of gamma ray spectra for DM annihilation into sZ' vs. $Z'Z'$ for example parameters m_s = 100 GeV, $m_{Z'}$ = 60 GeV and m_χ = 200 GeV. Right: Gamma ray spectra for DM annihilation to sZ' with m_s = 30 GeV and $m_{Z'}$ = 120 GeV, for various DM masses. These plots include decays to all SM final states.

5.5 Annihilation Limits from Dwarf Spheriodal Galaxies and AMS-02

Currently, two of the strongest constraints on dark matter annihilation processes come from AMS-02, for low DM masses and electron-positron final states, and from Fermi-LAT limits placed on signals from dwarf spheriodal satellite galaxies of the Milky Way [135]. Dwarf spheriodal galaxies (dSphs) are particularly useful in constraining dark matter models, as according to kinematic data they are one of the most dark matter dense objects in the sky, and have relatively low backgrounds. However, the limits published by Fermi-LAT assume a 100% branching fraction to a particular SM final state, and within our kinetically mixed Z' model this will not be true due to the flavor universal nature of the mixing. It is also not trivial to simply scale the dSphs limits with our branching fractions, as not only are the kinematics are different, but as there can be cross-polution of photon contributions from different final states. Furthermore, our new process $\chi\chi \to sZ'$ has two different final state particles with different masses, and the resulting spectra will depend on the specific masses of these particles. Therefore it is necessary to recast

the limits for this specific setup, comparing to the dSphs likelihood functions released by Fermi-LAT.

To find the limit on the cross section from dSphs, we use our spectra generated with Pythia [299], as described in the previous section. We then use the maximal likelihood method to compare our spectra against those for the dSphs publically provided by Fermi-LAT in the Pass 8 data, with the J factor taken to be a nuisance parameter as per Ref. [135]. The Pass 8 data is six years of LAT data taken from 2008-08-04 to 2014-08-05 and further selected with Pass 8 SOURCE-class in the energy range between 500 MeV and 500 GeV. We take spectra from 15 dSphs: Bootes I, Canes Venatici II, Carina, Coma Berenices, Draco, Fornax, Hercules, Leo II, Leo IV, Sculptor, Segue 1, Sextans, Ursa Major II, Ursa Minor, and Willman 1. The 95% C.L. limits on the annihilation cross section from dSphs for both $Z'Z'$ and sZ' spectra are shown for some example parameters in Fig. (6.9).

In Fig. (6.9), limits are set on the individual sZ' and $Z'Z'$ cross sections, where the benchmark parameters demonstrate the variation between expected results for different masses; we show examples where $m_s = m_{Z'}$, $m_s > m_{Z'}$ and $m_s < m_{Z'}$. In general, the limits arising from the spectral shape of the DM annihilation to sZ' is slightly more constraining than that from $Z'Z'$. This is likely due to the peak of the gamma ray spectra produced by the scalar being higher than that produced by the Z'. Which limit is relevant depends on which of the final states is kinematically accessible. When sZ' is accessible it greatly dominates, and hence the cross section limit is given by the solid green sZ' line. If $Z'Z'$ but not sZ' is accessible then the solid purple $Z'Z'$ line shows the relevant limit, which is shown for the lower mass region in the benchmark for $m_s > m_{Z'}$: $m_s = 100$ GeV and $m_{Z'} = 60$ GeV. All other mass choices will resemble these examples, depending on the hierarchy of the masses of the Z' and the dark Higgs. The heavier (lighter) the masses are, the weaker (stronger) the cross section limit will be. However, it is clear when comparing the cases of $m_{Z'} = 20$ GeV and 250 GeV (Fig. (6.9) top left and bottom right), the difference in the limit is minimal, apart from the fact that the limit will begin at higher DM masses for the processes to be kinematically accessible. The purple dotted line corresponds to the limit on annihilation to $Z'Z'$ alone, as would occur in a simplified model with only a Z' mediator and no dark Higgs. This allows for a comparision of the simplified model with our scenario.

To find the limit from AMS-02, it is sufficient to only consider electron-positron final states, as these provide the strongest limits. As the dark Higgs couples to particles through their mass, there will be negligible production of electron final states via decay of the s. This means that the Z' decays will provide effectively all the electron-positron signal. In the low DM mass range, where AMS-02 is most constraining, the limit on the cross section is approximately flat for cascade decays to two identical final state particles [273]. Therefore, we scale the cross section limit on electron final states by the branching fraction of Z' to electron-positron pairs. This is stronger than the dSphs limit only for low DM masses (and hence

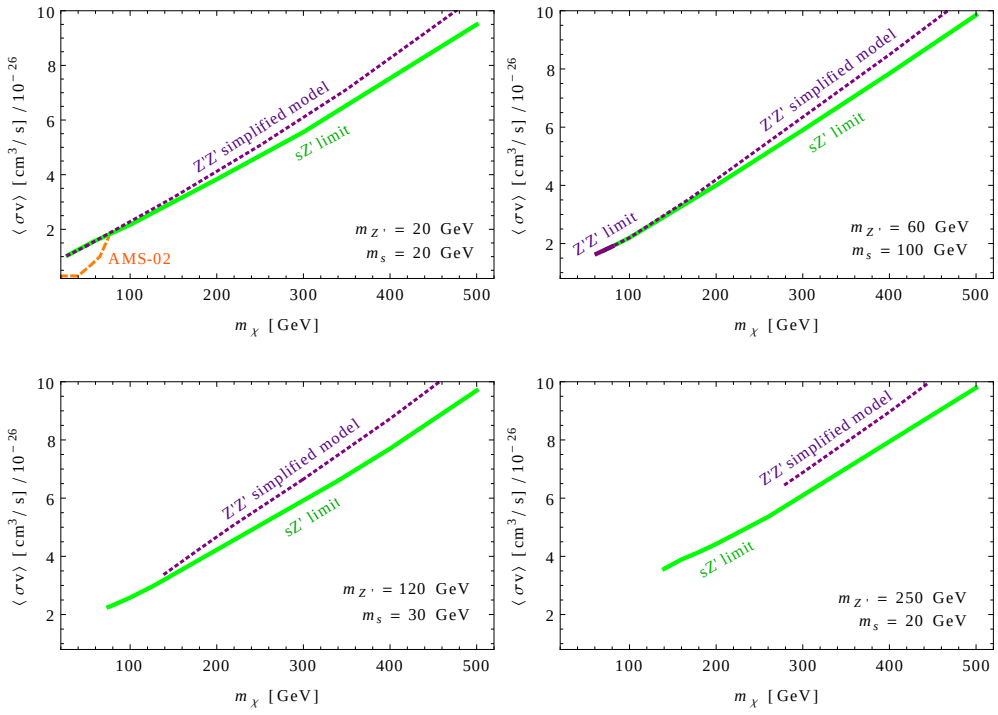

FIGURE 5.7: 95% confidence limits (C.L.) on the annihilation cross section from Fermi data on 15 dwarf spheroidal galaxies. All solid lines are limits on our model: the purple line is the cross section limit arising from the $Z'Z'$ process is alone; the green line is the cross section limit for the sZ' process alone. The purple dotted line is the $Z'Z'$ limit alone as per the simplified model with no dark Higgs. The approximate limit from AMS-02 is shown in orange. Masses are as labelled in each plot.

low s and Z' masses). As a result, AMS-02 limits are relevant only for low mass parameters, and shown on only one of the plots of Fig. (6.9) for which the Z' and s masses are both small.

5.6 Other Model Constraints

The indirect detection constraints are determined purely by the couplings of the mediators to DM, controlled by g_χ, and the mass parameters m_χ, $m_{Z'}$ and m_s. The exact size of the small couplings of the mediators to SM fermions, controlled by the mixing parameters ϵ and λ_{hs}, does not affect the indirect detection signals, as the mediators have long astrophysical time scales over which to eventually decay. However, other experimental probes, such as direct detection and collider experiments, are directly sensitive to the size of the small dark-SM couplings.

5.6.1 Collider and Direct Detection Constraints

As the couplings between the dark and visible sectors are taken to be very small, it is possible to completely escape the strong WIMP DM constraints from the LHC and direct detection. This provides a compelling scenario which is consistent with the null results of these experiements to date, while still allowing a large indirect detecion signal.

5.6.2 BBN and CMB Constraints

A lower limit on the size of the couplings between the sectors comes from Big Bang Nucleosynthesis (BBN), which requires that the mediators have a lifetime of $\tau < 1$s [300]. This leaves a large range of values (several orders of magnitude) for the kinematic mixing parameter ϵ and Higgs portal parameter λ_{hs}. In addition, CMB measurements can also provide constraints on the annihilation cross sections, however they are weaker than those arising from AMS-02 and dSphs [273].

5.6.3 Unitarity

As discussed above, the dark Higgs is included not only to provide a mass generation mechanism for the dark sector, but to ensure perturbative unitarity is not violated at high energies. In the absence of the scalar, unitarity violation would arise at high energy due to the longitudinal mode of the Z' gauge boson in processes such as $\chi\chi \to Z'Z'$.

In the indirect detection context, where it is appropriate to take the zero velocity limit, it turns out that the cross section for $\chi\chi \to Z'Z'$ receives no contribution from the scalar exchange diagram of Fig. (5.4). However, at high energies where the $v = 0$ threshold approximation is no longer valid (including at freezeout) the scalar diagram cannot be neglected [296]. Regardless, the scalar is mandatory

in any model in which the Z' has axial-vector couplings to fermions, in order to properly respect gauge invariance and perturbative unitarity [80].

5.7 Summary

We have considered a self-consistent dark sector containing a Majorana fermion DM candidate, χ, a dark gauge boson, Z', and a dark Higgs, s, which transform under a dark $U(1)_\chi$ gauge symmetry. This is the minimal consistent model in which a Majorana DM candidate couples to a spin-1 mediator. In this scenario, the coupling of the DM to the Z' must be of axial-vector form, as vector couplings of Majorana fermions vanish. The dark Higgs field provides a mass generation mechanism for both the Z' gauge boson and the DM χ, and is required in order for the model to properly respect gauge invariance and perturbative unitarity.

We have investigated the indirect detection phenomenology of this model, focusing on the processes where the DM annihilates to on-shell dark sector mediators. We found that the presence of a spin-0 and spin-1 mediator in the same model opens up an important new s-wave annihilation channel, $\chi\chi \to sZ'$, which can dominate over the well-studied process $\chi\chi \to Z'Z'$. This is to be contrasted to the situtation in simplified models that contain a single mediator: there is no s-wave annihilation process to scalar mediators; s-wave annihilation to pseudoscalar mediators is suppressed by 3-body phase space; the process $\chi\chi \to Z'Z'$ is the only s-wave annihilation to vector or axial-vector mediators (which, in the case of an axial mediator, violates unitarity at high energy). The inclusion of the scalar and vector mediator in the same model allows sizable production of the scalar mediator via s-wave annihilation, which was previously not thought possible, and provides a very plausible way to discover the dark Higgs. This important phenomenology is missed in the single-mediator simplified model approach.

We have calculated indirect detection limits on the sZ' and $Z'Z'$ annihilation processes, using Fermi-LAT gamma ray data for dwarf spheriodal galaxies. The gamma ray energy spectra resulting from the two annihilation modes are similar. Depending on the masses of the dark sector particles, there are regions of parameter space where only one of the sZ' and $Z'Z'$ final states are kinematically accessible. As such, the new process allows a broader range of DM masses to be probed via indirect detection. In the limit that $m_\chi^2 \gg m_{Z'}^2, m_s^2$, where both processes are kinematically allowed, the cross sections to sZ' is much greater than that to $Z'Z'$. Neglecting the sZ' process, as done in the simplified model setup, would lead to highly inaccurate constraints on the model parameters.

An important observation is that the mass and coupling parameters in the dark sector may be intrinsically related to each other. In our case, the various parameters are related via the gauge coupling constant and the dark Higgs vev, such that we do not have the freedom to vary all parameters independently. The absence of this feature is one of the shortcomings of the (albeit very useful)

simplified model approach. In general, renormalizable models in which gauge invariance is enforced will be a superior approach. Not only are unitarity problems avoided, but the phenomenology is potentially richer.

Chapter 6

Impact of Mass Generation for Simplified Dark Matter Models

In the simplified dark matter models commonly studied, the mass generation mechanism for the dark fields is not typically specified. In this chapter, we demonstrate that the dark matter interaction types, and hence the annihilation processes relevant for relic density and indirect detection, are strongly dictated by the mass generation mechanism chosen for the dark sector particles, and the requirement of gauge invariance. We focus on the class of models in which fermionic dark matter couples to a spin-1 vector or axial-vector mediator. However, in order to generate dark sector mass terms, it is necessary in most cases to introduce a dark Higgs field and thus a spin-0 scalar mediator will also be present. In the case that all the dark sector fields gain masses via coupling to a single dark sector Higgs field, it is mandatory that the axial-vector coupling of the spin-1 mediator to the dark matter is non-zero; the vector coupling may also be present depending on the charge assignments. For all other mass generation options, only pure vector couplings between the spin-1 mediator and the dark matter are allowed. If these coupling restrictions are not obeyed, unphysical results may be obtained such as a violation of unitarity at high energies. These two-mediator scenarios lead to important phenomenology that does not arise in single mediator models. We survey two-mediator dark matter models which contain both vector and scalar mediators, and explore their relic density and indirect detection phenomenology.

This chapter is based on the publication: *N. F. Bell, Y. Cai and R. K. Leane, "Impact of Mass Generation for Simplified Dark Matter Models", JCAP 01 (2017) 039 [arXiv:1610.03063 [hep-ph]].* [301]

6.1 Introduction

Simplified models for DM are an improvement over the effective field theory approach [71–73] which was used for many recent collider and non-collider WIMP

searches, yet suffers from unitarity issues when used outside the region of validity [74–78, 153, 258–261, 264]. However, the simplified models are still far from ideal. Indeed, by their simplified nature, they are are not intrinsically capable of capturing the realistic phenomenology of many UV complete theories, which may have multiple dark-sector field content. More critically, separate consideration of the benchmark simplified models can lead to scenarios that are not physically viable. Indeed, the simplified models suffer some of the same issues that plague the effective field theory approach, such as violations of perturbative unitarity that arise because gauge invariance is not respected [74–78, 80, 102, 153, 258–264].

As an example of such an issue, simplified models in which the DM has a non-zero axial-vector coupling to a spin-1 mediator will violate perturbative unitarity at high energies [80, 296]. This can be remedied by introducing a dark Higgs field to unitarize the longitudinal component of the Z' [80, 257, 268, 296]. The dark Higgs may also provide mass to the DM itself. The minimal self-consistent approach is then a multi-mediator model, featuring both spin-1 and spin-0 mediators[1]. This of course can alter the phenomenology, even at low energies. In the previous chapter, we considered indirect detection signals in a scenario with a Majorana DM candidate χ, in which the couplings of a Z' and scalar, s, are related by gauge invariance. In this scenario, the presence of both the s and Z' mediators opens a dominant s-wave annihilation channel, $\chi\chi \to sZ'$, that does not arise when a single-mediator is considered in isolation [257]. This has a dramatic impact on the indirect detection phenomenology.

An important consideration for DM models is the mass generation mechanism for the dark sector fields. Although commonly left unspecified in the simplified model approach, with mass terms simply added by hand, we shall argue that the mechanism of mass generation has significant consequences that cannot be ignored. For a spin-1 mediator with only vector couplings, a standard procedure is to appeal to the Stueckelberg mechanism to introduce a mass for the vector boson. However, this is valid only for a pure vector, with vanishing axial-vector couplings to fermions. This is a very specific scenario, and there is no reason to assume it is correct. In fact, the Higgs mechanism is the only mass generation mechanism for fundamental particles we know is realized by nature[2], as confirmed by the recent experimental discovery of the SM Higgs boson. As such, it is well motivated to consider a variety of scenarios where different dark sector fields acquire their mass by various methods: the Stueckelberg mechanism, a dark Higgs mechanism, or in cases where it is allowed, simply with a bare mass term.

We will show that the annihilation processes, and hence both the relic density and indirect detection constraints, are strongly dictated by the mass generation mechanisms. Interestingly, we will also show that depending on the choice of

[1]Multi-mediator models have also been considered recently in Refs. [257, 265–268].

[2]Other non-fundamental mass generation mechanisms are realized in strongly coupled regimes. The parallel for the dark sector would be some bound dark state, which we do not consider in this work.

mass generation mechanism, only particular interactions types are allowed, as dictated by dark gauge invariance. In most cases, only pure vector couplings of the spin-1 mediator to fermionic DM are allowed. Conversely, if a single dark Higgs mechanism gives mass to all the dark sector fields, the axial-vector coupling of the spin-1 mediator to the DM is required to be non-zero. Such restrictions do not map to the single-mediator simplified models, despite being a compelling possibility (or in some cases, a requirement). Again, this phenomenology is not accurately captured by the single mediator simplified model framework.

The purpose of this chapter is to undertake a more complete study of simplified models that contain both a scalar and vector mediator. In all cases, we will be sure to enforce gauge invariance with respect to the dark $U(1)_\chi$ interaction (dark gauge invariance), which is important to ensure physically well behaved cross sections. We will consider Dirac DM, which allows for a wider combination of coupling types, each with their own distinct phenomenology. Results for Majorana DM can be obtained in the limit of one of the scenarios we investigate in this chapter. We focus, in particular, on hidden-sector type models [269–273, 275–295], where the DM annihilates directly to the mediators, which then decay to SM particles via small couplings between the dark and visible sectors. In section 8.6 we outline mass generation for spin-1 simplified models, and in section 6.3 we briefly discuss the standard assumption for mass generation in spin-1 models, before investigating three other compelling mass generation scenarios in sections 6.4, 6.5 and 6.6, detailing models, annihilation processes and relic density constraints. We present indirect detection constraints in section 6.7 and summarize our findings in section 6.8.

6.2 Mass Generation for Spin-1 Simplified Models

The mass generation mechanism for fermionic DM in spin-1 simplified models is tightly correlated with the DM interaction type. In the case that DM is Majorana, the Z' can have only axial-vector couplings to the DM, as vector couplings of Majorana particles vanish. In the case where DM is Dirac, both vector and axial-vector couplings to the Z' can simultaneously be present. For both DM types, the presence of an axial-vector coupling is significant, as it implies that

1. The DM mass must arise after symmetry breaking, as the $U(1)_\chi$ gauge symmetry prevents a bare mass term for χ, and

2. A $U(1)_\chi$ symmetry breaking mechanism is required to give the Z' mass, in order to unitarize the longitudinal component of the Z'.

A single dark Higgs field is an economical solution to these issues. In the following sections, we will show that the only scenario in which an axial-vector coupling is possible in a spin-1 mediator model is if there is a dark Higgs which interacts with both the DM and the dark gauge boson. Moreover, the axial coupling is not merely

possible in this case, but in fact required to be non-zero by gauge invariance. We take the DM to be Dirac, as this permits the broadest range of possible coupling types. A related model involving Majorana fermions can be found in Ref. [257] and is closely related to a specific realization of scenario II presented below.

For Dirac DM, it is possible to have pure vectorlike couplings to the Z' and so it is possible to include a bare mass term for DM, and use the Stueckelberg mechanism[3] to provide a mass for the Z', such that no dark Higgs is needed. Nonetheless, even in the case of pure vector couplings, a dark Higgs may still provide mass for one or both of the Z' and DM. Furthermore, when the Z' and DM masses arise from different mechanisms, the coupling of the DM to the scalar and vector mediators are no longer related to each other, and hence the phenomenology is less constrained. We are thus led to a spectrum of models in which both scalar and vector mediators would be present. We outline the phenomenologically distinct scenarios in Tab. 6.1.

6.3 Scenario I: Bare DM Mass and Z' Mass from Stueckelberg Mechanism

Interaction type required: Pure Vector

This is the most minimal gauge-invariant scenario, and is permitted only if there are pure vectors couplings between the DM and the Z'. Unlike the axial-vector scenario, a dark Higgs is not mandatory in the pure vector case because

1. The Z' gauge boson can acquire a mass via the Stueckelberg mechanism.
2. As χ is vectorlike with respect to the $U(1)_\chi$, i.e. $Q_{\chi_R} = Q_{\chi_L}$, a bare χ mass term is permitted.

6.3.1 Model

The Lagrangian for this case is simply

$$\mathcal{L} = \mathcal{L}_{SM} + i\,\overline{\chi}(\partial_\mu + i g_\chi Q_V Z'_\mu)\gamma^\mu \chi - \frac{\sin\epsilon}{2} Z'^{\mu\nu} B_{\mu\nu} - m_\chi \overline{\chi}\chi + \frac{1}{2} m^2_{Z'} Z'^\mu Z'_\mu, \quad (6.1)$$

where Q_V is the vectorlike $U(1)_\chi$ charge of the DM, which can be chosen freely, and the ϵ term describes kinetic mixing of the $U(1)_\chi$ gauge boson with the SM hypercharge gauge boson. This is the only spin-1 mediator scenario where it is possible to avoid the inclusion of a dark Higgs.

[3] In Abelian gauge theories, the Stueckelberg mechanism can be taken as the limit of the Higgs mechanism where the mass of the real scalar is sent to infinity and only the pseudoscalar is present; however it is not always easily realized in more complicated scenarios. In particular, unitarity is already violated at tree-level in a non-Abelian theory with a Stueckelberg Lagrangian and thus the theory is not renormalizable [302–310]. In general the Stueckelberg mechanism should be treated as an alternative to the Higgs mechanism for mass generation.

Scenario	χ **mass**	Z' **mass**	**Required** $\chi - Z'$ **coupling type**	**Annihilation processes**	Z' **pol**
I	Bare mass term	Stueckelberg mechanism	Vector	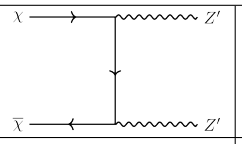	Z'_T
II	Yukawa coupling to Dark Higgs	Dark Higgs mechanism	Vector & axial-vector or pure axial-vector. The $U(1)$ charge assignments of χ_L and χ_R determine the relative size of the V and A couplings. **The axial-vector coupling must be non-zero**.	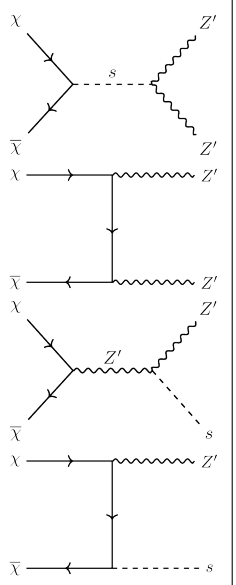	Z'_T & Z'_L
III	Yukawa coupling to Dark Higgs	Stueckelberg mechanism	Vector	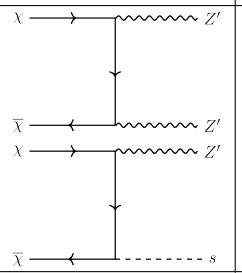	Z'_T
IV	Bare mass term	Dark Higgs mechanism	Vector	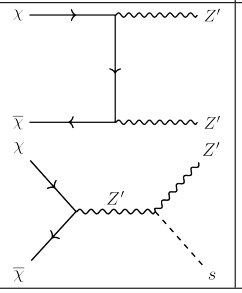	Z'_T

TABLE 6.1: The spectrum of scenarios with distinct phenomenology once mass generation is specified. All t-channel annihilation processes have an accompanying u-channel process which is not shown. All processes shown are s-wave, except for $\chi\overline{\chi} \to s \to Z'Z'$ diagram in scenario II, which while p-wave when considered alone, is part of the process $\chi\overline{\chi} \to Z'Z'$. For scenario III, as the dark Yukawa and gauge coupling are not correlated, the p-wave annihilation to two dark Higgs, $\chi\overline{\chi} \to ss$, can have an impact on the relic density if the gauge coupling is sufficiently small to suppress the s-wave processes. Otherwise, the s-wave processes shown dominate, even at freeze-out. The final column displays the polarization of the Z' bosons produced by these annihilation processes (in the $E^2_{Z'} \gg m^2_{Z'}$ limit) .

6.3.2 Cross Sections

In this scenario there is only one annihilation process, $\chi\overline{\chi} \to Z'Z'$ (in the limit $\epsilon \to 0$). The s-wave contribution to the cross section is given by

$$\langle \sigma v \rangle_{\chi\overline{\chi}\to Z'Z'} = \frac{g_\chi^4 Q_V^4 \left(1-\eta_{Z'}\right)^{3/2}}{4\pi m_\chi^2 \left(\eta_{Z'}-2\right)^2}, \tag{6.2}$$

where $\eta_{Z'} = m_{Z'}^2/m_\chi^2$. The $Z'Z'$ annihilation process in this case is identical to that for Scenarios III and IV. In these cases, there only exist transverse polarizations of the Z'. Obviously, there is no sZ' annihilation process present, and so the phenomenology is quite minimal. This case has been thoroughly covered in the literature (for a review see, e.g., [311]), however it is important to note that axial-vector couplings are sometimes incorrectly included.

6.3.3 Relic Density

An important requirement for a DM model is to produce the correct relic density. Note, however, that a full DM model may have more dark sector fields than the simplified models considered here, which may impact the relic density determination. Nonetheless, we shall determine the relic density constraints for our simplified models, to serve as a guide to the viable regions of parameter space.

We use micrOMEGAs 3 [242] to calculate the DM relic density, and compare with the recent determination by the Planck collaboration [243],

$$\Omega_\chi h^2 = 0.1196 \pm 0.0031. \tag{6.3}$$

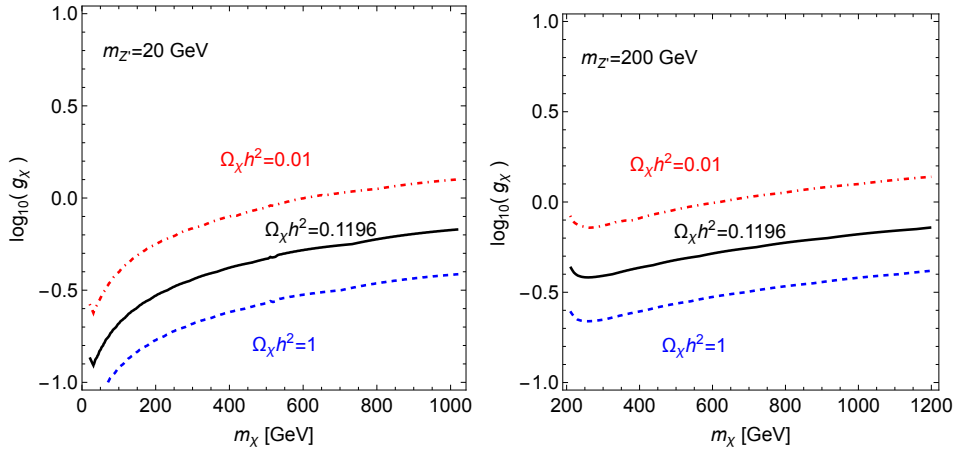

FIGURE 6.1: DM relic density contours as a function of DM mass and dark gauge coupling in scenario I, for $\Omega_\chi h^2 = 0.01$, 0.1196, and 1 in red dot-dashed, black solid and blue dashed lines. We have taken $Q_V = 1$, and set the dark Z' mass to $m_{Z'} = 20$ GeV and 200 GeV in the left and right panels respectively.

In Fig. 6.1, we show the relic density contours as a function of DM mass m_χ and dark gauge coupling g_χ for fixed dark Z' mass $m_{Z'}$ = 20 GeV and 200 GeV in the left and right pannels respectively. The contours for $\Omega_\chi h^2 = 0.01, 0.1196$ and 1 are plotted in red dot-dashed, black solid and blue dashed lines. Obviously for reasonably perturbative dark gauge coupling g_χ and DM mass, we can always obtain the observed relic density, as shown with the black line in Fig. 6.1.

6.4 Scenario II: DM Mass and Z' Mass both from Dark Higgs Mechanism

Interaction type required: Non-Zero Axial-Vector

We now consider the case where both the DM and the dark gauge boson acquire mass from a single dark Higgs. We will show that this requires the axial-vector DM-Z' interaction to be non-zero. The reason is simple: the dark Higgs field, S, must clearly carry $U(1)_\chi$ charge if its vacuum expectation value (vev) is to break that symmetry. A Yukawa coupling of the dark Higgs to the DM of the form $y_\chi \chi_R \chi_L S$ is then possible only if the DM is chiral, i.e. χ_L and χ_R carry different $U(1)_\chi$ charges. This guarantees that the axial couping is non-zero (while the vector couplings may be either zero or non-zero depending on the $U(1)_\chi$ charge assignments).

6.4.1 Model

We investigate the phenomenology of the most minimal model containing a dark gauge boson and a dark Higgs field, by simply extending the Standard Model by an extra $U(1)$. The gauge group is thus: $SU(3)_c \otimes SU(2)_W \otimes U(1)_Y \otimes U(1)_\chi$. Here the covariant derivative is $D_\mu = D_\mu^{SM} + iQg_\chi Z'_\mu$, where Q denotes the $U(1)_\chi$ charge. The SM field content is augmented by a Dirac fermion DM candidate, χ, a spin-1 dark gauge boson, Z', and a dark Higgs field S. The vev of the dark Higgs field provides a mass generation mechanism for the dark sector fields Z' and χ. Before electroweak and $U(1)_\chi$ symmetry breaking, the most general Lagrangian is

$$\begin{aligned}\mathcal{L} = \mathcal{L}_{\rm SM} + i\overline{\chi}_L \not{D} \chi_L + i\overline{\chi}_R \not{D} \chi_R - (y_\chi \overline{\chi}_R \chi_L S + h.c.) \\ + (D^\mu S)^\dagger (D_\mu S) - \mu_s^2 S^\dagger S - \lambda_s (S^\dagger S)^2 - \lambda_{hs} (S^\dagger S)(H^\dagger H) - \frac{\sin\epsilon}{2} Z'^{\mu\nu} B_{\mu\nu}.\end{aligned} \tag{6.4}$$

We assume that the SM fields are not charged under $U(1)_\chi$. There are thus only two possible terms that couple SM and dark-sector fields: the kinetic mixing of the $U(1)$ gauge boson with the hypercharge gauge boson, controlled by the kinetic mixing parameter ϵ, and mixing of the dark Higgs, S, with the SM Higgs, H, controlled by the Higgs mixing parameter λ_{hs}.

In order for the χ-S Yukawa term to be gauge invariant, the charges of the dark sector field must be chosen to satisfy[4]

$$Q_{\chi_R} - Q_{\chi_L} = Q_S \ . \tag{6.5}$$

We can set the dark Higgs charge to be $Q_S = 1$, without loss of generality, as any other choice can be absorbed into a rescaling of the dark gauge coupling. The χ charges therefore satisfy

$$Q_A \equiv \frac{1}{2}(Q_{\chi_R} - Q_{\chi_L}) = \frac{1}{2}, \tag{6.6}$$

$$Q_V \equiv \frac{1}{2}(Q_{\chi_R} + Q_{\chi_L}) = \frac{1}{2} + Q_{\chi_L}. \tag{6.7}$$

These charges determine the vector and axial-vector couplings of the Z' to the χ. We see that the axial-vector coupling is completely determined, while there is freedom to adjust the vector coupling by choosing $Q_{\chi_{L,R}}$ appropriately. For instance, $Q_{\chi_L} = 0$ would lead to equal vector and axial-vector couplings, while $Q_{\chi_L} \gg 1$ would lead to a vector coupling much larger than the axial-vector. Pure axial-vector is obtained with $Q_{\chi_L} = -1/2$; this produces phenomenology similar to the Majorana model studied in [257]. Pure vector, on the other hand, can only be approximately reached in the limit $Q_V \gg 1$, but never fully realized[5], as dark gauge invariance prevents the axial-vector from being exactly zero.

Both S and H obtain vevs, breaking $SU(3)_c \otimes SU(2)_L \otimes U(1)_Y \otimes U(1)_\chi$ down to $SU(3)_c \otimes U(1)_{em}$. In the broken phase, the terms of interest are

$$\begin{aligned}\mathcal{L} \supset & -\frac{1}{2}m_s^2 s^2 + \frac{1}{2}m_{Z'}^2 Z'^\mu Z'_\mu - m_\chi \overline{\chi}\chi \\ & + g_\chi^2 w Z'^\mu Z'_\mu s - \lambda_s w s^3 - 2\lambda_{hs} h\, s(v\, s + w\, h) + g_f \sum_f Z'_\mu \overline{f}\Gamma_f^\mu f \\ & - g_\chi Q_V Z'_\mu \overline{\chi}\gamma^\mu \chi - g_\chi Q_A Z'_\mu \overline{\chi}\gamma^\mu\gamma_5\chi - \frac{y_\chi}{\sqrt{2}} s\overline{\chi}\chi \ ,\end{aligned} \tag{6.8}$$

where the component fields of S and H are defined in the broken phase as $S \equiv \frac{1}{\sqrt{2}}(w + s + ia)$ and $H = \left\{G^+, \frac{1}{\sqrt{2}}(v + h + iG^0)\right\}$ with G^+, G^0 and a being the Goldstone bosons of W, Z and Z' respectively, while s and h are real scalars. The coupling g_f, which controls the interactions of the Z' with SM fermions, is dictated by the kinetic mixing; the explicit form can be found, e.g., in Ref. [27].

[4]For anomaly cancellation there must be additional fields charged under the dark $U(1)$. However, we include only the lightest of such fields as the DM candidate, as the others can be made heavier such that the phenomenology is not affected, as they make a subdominant contribution to the relic density, as can be seen from section 6.4.3. Details of anomaly cancellation for new axial-vector bosons were also discussed in Ref. [312].

[5]It is also important to note that there exist relations between the axial-vector coupling size and the masses of the dark sector fields [80]. Therefore, for almost all mass choices of the dark sector fields, it is not possible to make the axial-vector coupling vanishingly small relative to the vector coupling without the vector coupling becoming non-perturbative. Thus, the axial-vector coupling is effectively never negligible and cannot be neglected even in limiting cases.

We assume that the scalar mixing parameter λ_{hs} is small, which implies that the the SM Higgs is not significantly perturbed by the new physics. In this limit, the dark Higgs vev satisfies $w^2 = -\mu_s^2/\lambda_s$ and the various masses are:

$$m_{Z'} = g_\chi w, \tag{6.9a}$$

$$m_\chi = \frac{1}{\sqrt{2}} y_\chi w, \tag{6.9b}$$

$$m_s^2 \simeq -2\mu_s^2, \tag{6.9c}$$

$$m_h^2 \simeq -2\mu_h^2 \,. \tag{6.9d}$$

Importantly, because both the DM and Z' masses are both proportional the to vev of the dark Higgs, their masses and couplings are not all independent parameters but instead are related as

$$y_\chi / g_\chi = \sqrt{2} m_\chi / m_{Z'}. \tag{6.10}$$

6.4.2 Cross Sections

The relevant annihilation process for this scenario are shown in Tab. 6.1. The $\chi\overline{\chi} \to sZ'$ annihilation receives contributions from both s and t/u channel processes, while s-wave contributions to the $\chi\overline{\chi} \to Z'Z'$ process arise only from the t/u channel diagrams. (Note, however, that the contribution of the s-channel scalar exchange diagram to the annihilation to $Z'Z'$ is necessary to unitarize the cross section at high energy. Without this contribution, longitudinal Z'_L contributions would lead to unphysical high energy behavior of the p-wave term.) The s-wave contributions to the annihilation cross sections are given by

$$\langle \sigma v \rangle_{\chi\overline{\chi}\to Z'Z'} = \frac{g_\chi^4 \left(1-\eta_{Z'}\right)^{3/2} \left(16 Q_V^4 \eta_{Z'} + 8 Q_V^2 \left(4 - 3\eta_{Z'}\right) + \eta_{Z'}\right)}{64\pi m_\chi^2 \left(\eta_{Z'} - 2\right)^2 \eta_{Z'}}, \tag{6.11}$$

and

$$\begin{aligned} \langle \sigma v \rangle_{\chi\overline{\chi}\to sZ'} = {} & \frac{g_\chi^4 \sqrt{\left(\eta_s - \eta_{Z'} - 4\right)^2 - 16\eta_{Z'}}}{1024\pi m_\chi^2 \left(\eta_{Z'} - 4\right)^2 \eta_{Z'}^2 \left(\eta_s + \eta_{Z'} - 4\right)^2} \times \\ & \Big\{ \left(\eta_{Z'} - 4\right)^2 \left(\eta_s + \eta_{Z'} - 4\right)^2 \left(\left(\eta_s - \eta_{Z'} - 4\right)^2 - 16\eta_{Z'}\right) \\ & + 4 Q_V^2 \eta_{Z'} \Big[\eta_s^4 \eta_{Z'} - 16\eta_s^3 \eta_{Z'} - 2\eta_s^2 \left(\eta_{Z'}^3, - 44\eta_{Z'}^2, + 80\eta_{Z'} - 64\right) \\ & + 64\eta_s \left(\eta_{Z'} - 4\right)^2 \left(\eta_{Z'} - 1\right) + \left(\eta_{Z'} - 4\right)^4 \left(\eta_{Z'} + 8\right) \Big] \Big\}, \end{aligned} \tag{6.12}$$

where $\eta_{s,Z'} = m_{s,Z'}^2 / m_\chi^2$. As explained above, we have set $Q_S = 1 = 2Q_A$ without loss of generality, while Q_V is left as a free parameter. Also note that we have used Eq. (6.10) to replace the Yukawa coupling y_χ with the gauge coupling g_χ.

These annihilation cross sections are plotted in Fig. 6.2. Comparing the first

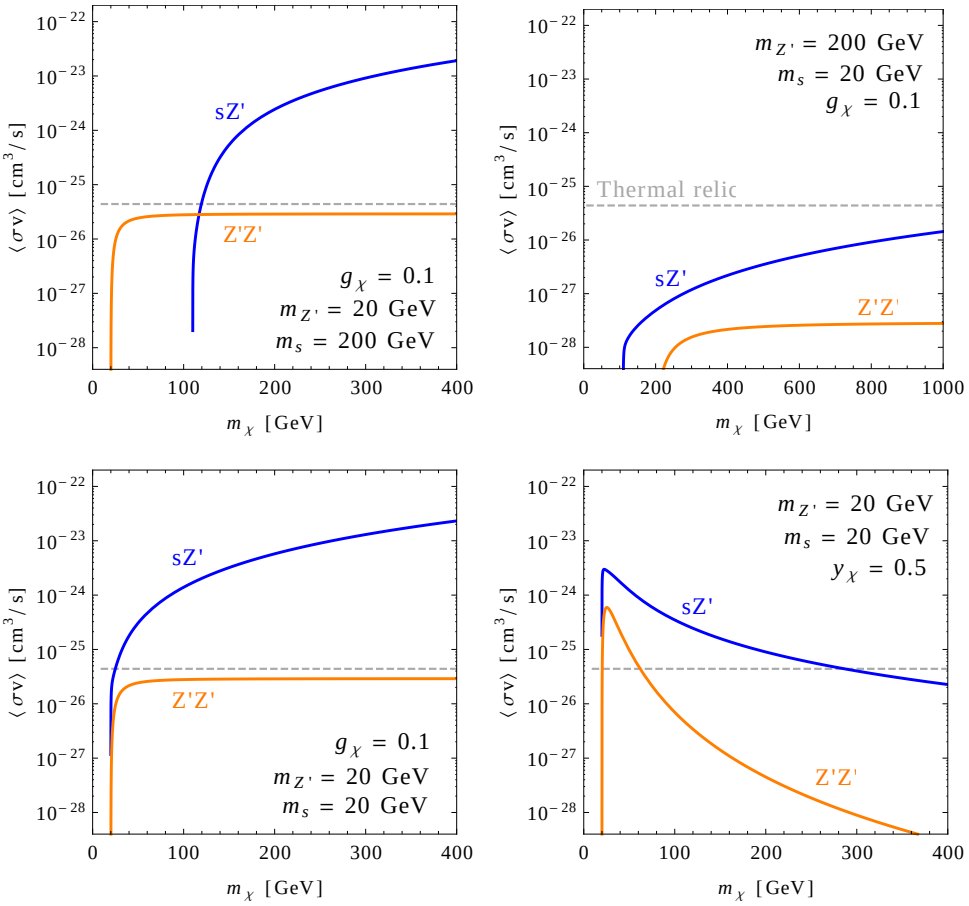

FIGURE 6.2: Relative cross sections for the two dominant s-wave annihilation processes in scenario II, $\chi\overline{\chi} \to sZ'$ (blue) and $\chi\overline{\chi} \to Z'Z'$ (orange), for example choices of the dark Higgs mass and the Z' mass, as labeled. This scenario requires $2Q_A = Q_S = 1$, and we have chosen $Q_V = 1/2$. The gauge coupling has been set to $g_\chi = 0.1$ in the first three panels, and for comparison in the last panel, the yukawa coupling is instead fixed and is set to $y_\chi = 0.5$. Note differing axes. For reference, the approximate thermal relic cross section is shown as the gray dashed line.

three panels, we see that the $Z'Z'$ cross section becomes approximately independent of the DM mass when $m_\chi \gg m_{Z'}$, while the sZ' cross section rises[6] with m_χ. (This is to be contrasted with the behavior in cases III and IV, where all cross sections decline as m_χ is increased.) This is an interesting consequence of having both vector and axial-vector interactions present: For the $Z'Z'$ process, there is a $V-A$ interference which gives rise to longitudinal Z' domination in the $m_\chi \gg m_{Z'}$ limit[7]. The sZ' process is also dominated by Z'_L contributions in this limit. This can be understood by appealing to the Goldstone boson equivalence theorem which, in the high energy limit, relates the amplitude for emission of a longitudinally polarized gauge boson (Z'_L) with that for the emission of the corresponding Goldstone boson (the pseudoscalar a). For the $\chi\overline{\chi} \to sZ'$ process, in addition to the transverse contributions we have $\chi\overline{\chi} \to sZ'_L$, which in the high energy limit is equivalent to $\chi\overline{\chi} \to sa$. As this scalar plus pseudoscalar final state is odd under parity, this is an s-wave process. For the $\chi\overline{\chi} \to Z'Z'$ process, if both Z'_L are replaced by their Goldstones we would have $\chi\overline{\chi} \to aa$, which is even under parity and thus p-wave. However, a combination of longitudinal and transverse modes are possible, $\chi\overline{\chi} \to Z'_L Z'_T$, which is equivalent to the s-wave process $\chi\overline{\chi} \to aZ'_T$ and thus dominates at high energy. Notice that the sZ' process, in addition to external Z'_L contributions, also receives contributions from the longitudinal Z' mode in the s-channel Z' propagator. This contribution leads to four powers of $m_{Z'}$ in the denominator of the sZ' cross section. In contrast, the $Z'Z'$ cross section receives Z'_L contributions only from a single final state Z', and so has only two powers of $m_{Z'}$ in the denominator. The $Z'Z'$ process is thus is sub-dominant to the sZ' process when both are kinematically allowed[8].

6.4.3 Relic Density

As in the previous section, we use micrOMEGAs 3 to calculate the DM relic density. For different Z' and dark Higgs mass, we scan the parameter space and find that the DM relic density can be saturated fairly easily. We show the relic contours in Fig. 6.3 as a function of m_χ and g_χ for fixed $m_{Z'}$ and m_s, and $Q_V = 1/2$. In each panel, the observed relic density, $\Omega_\chi h^2 = 0.1196$, is depicted by a black solid line, while red dot-dashed and blue dotted lines show contours for $\Omega_\chi h^2 = 0.01$ and 1.0 respectively. The central panel clearly shows the resonant enhancement of the annihilation to $Z'Z'$ through the s-channel scalar exchange, as a spike near $m_\chi \sim 100$ GeV, while the dip at $m_\chi \sim 110$ GeV in the right panel is

[6] In the first three panels of Fig. 6.2, the Yukawa coupling y_χ increases as the DM mass increases. In the last (lower right) panel we instead fix the Yukawa (which implies that as we increase m_χ, the vev increases and thus g_χ decreases). The decrease of the cross section with m_χ in this panel is thus due to this decrease in g_χ.

[7] If Q_V were chosen to be zero, such that the Z' coupling were pure axial, there would be no $V-A$ interference and the s-wave part of the $Z'Z'$ cross section would *not* be enhanced by longitudinal Z' modes. This situation maps onto the Majorana DM case studied in Ref. [257].

[8] Note that because the Yukawa and gauge coupling constants are related via Eq. (6.10), it is not possible to change the relative size of the annihilation to $Z'Z'$ and sZ' by adjusting these parameters.

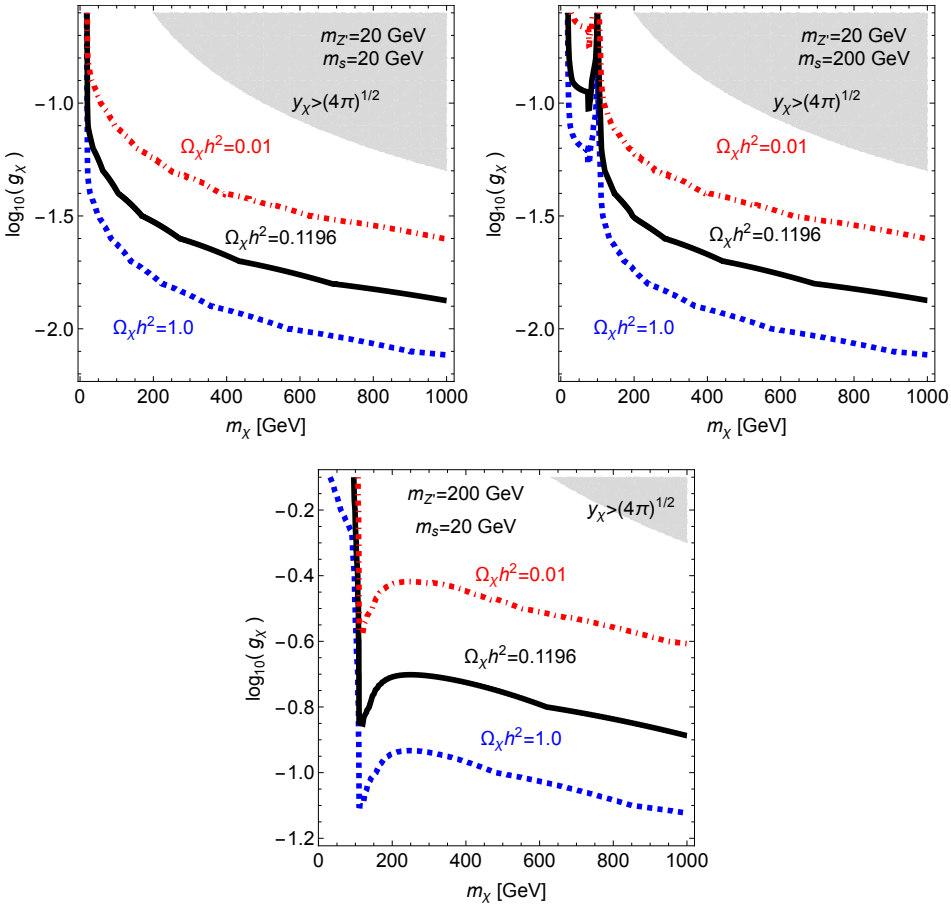

FIGURE 6.3: DM relic density contours in scenario II, as a function of m_χ and g_χ, for various choices of the dark Higgs and Z' mass, as labeled. This scenario requires $2Q_A = Q_S = 1$, and we have chosen $Q_V = 1/2$. The red dot-dashed, the black solid and the blue dotted lines denote the contours for $\Omega_\chi h^2 = 0.01,\ 0.1196$ and 1.0 respectively. In the shaded region the Yukawa coupling y_χ is larger than $\sqrt{4\pi}$.

due to the opening of the of the sZ' final state. As the annihilation cross sections are dominated by the longitudinal Z' modes (in the $m_\chi \gg m_{Z'}$ limit), the relic density is sensitive to the Z' mass. By comparision, in scenarios I, III and IV, where the only transverse Z' modes are produced, the the cross sections and thus the relic density are insensitive to the Z' mass in the $m_\chi \gg m_{Z'}$ limit. (Note that the parameter regions shown in Fig. 6.3 all satisfy $\lambda_s < \sqrt{4\pi}$.)

6.5 Scenario III: DM Mass from Dark Higgs Mechanism, Z' Mass from Stueckelberg Mechanism

Interaction type required: Pure Vector

We now consider a scenario where the mass of the χ and Z' arise from different mechanisms. Specifically, we assume the χ mass is due to a Higgs mechanism, while the Z' mass arises from the Stueckelberg mechanism. As a result only pure vector interactions of the χ and Z' are permitted. Here the dark $U(1)_\chi$ remains unbroken, and instead the dark Higgs must break some other symmetry under which the DM is charged. This scenario divorces the Z' physics from the dark Higgs physics[9].

6.5.1 Model

The most minimal Lagrangian for this setup is

$$\begin{aligned}\mathcal{L} = \mathcal{L}_{SM} \quad &+ \quad i\,\overline{\chi}\left(\partial\!\!\!/ + i g_\chi Q_V Z\!\!\!/'\right)\chi - \frac{y_\chi}{\sqrt{2}}\overline{\chi}\chi\phi \\ &+ \quad \frac{1}{2}\partial_\mu\phi\partial^\mu\phi - \frac{1}{2}\mu_s^2\phi^2 - \frac{1}{4}\lambda_s\phi^4 - \frac{1}{2}\lambda_{hs}\phi^2(H^\dagger H) - \frac{\sin\epsilon}{2}Z'^{\mu\nu}B_{\mu\nu},\end{aligned} \tag{6.13}$$

with the real scalar $\phi = w + s$, where w is the vev of ϕ and s is the dark Higgs. The vectorlike charge Q_V can be chosen freely. Again, the dark sector interacts with the visible sector in two ways: via kinetic mixing or Higgs mass mixing.

As the dark Higgs is responsible only for generating fermion masses, a real scalar is sufficient to accomplish this task. (The dark Higgs must break the $U(1)_\chi$ in all other scenarios we consider, which requires a complex scalar.) If we introduce a complex scalar instead, the extra degree of freedom will be a massless Goldstone boson and will contribute to the radiation energy density of the universe. If the Goldstones had the same temperature as the SM neutrinos, they would make a contribution equivalent to $N_{\text{eff}}^\nu = 4/7$, in marginal agreement with current experimental observations. However, their contribution to N_{eff}^ν would be

[9]This situation has a SM analogue where χ is replaced by the electron and Z' is replaced by the photon: the electrons have vector couplings to the photon of an unbroken $U(1)_{\text{QED}}$; the electron mass comes from breaking the electroweak symmetry with the SM Higgs; the SM Higgs does not couple to the photon or contribute to the photon mass. The annihilation $\chi\overline{\chi} \to sZ'$ is then the analogue of $e^+e^- \to h\gamma$.

suppressed if they decoupled early enough to not be heated by the annihilations of some SM species [313].

6.5.2 Cross Sections

As shown in Tab. 6.1, both the $Z'Z'$ and sZ' processes receive contributions only from the t/u channel diagrams, as the absence of a Z'–s interaction eliminates the s-channel diagrams of scenario II. The $Z'Z'$ cross section is therefore identical to that of Scenario I, given by Eq. (6.2), while the s-wave contribution to the sZ' cross section is

$$\langle \sigma v \rangle_{\chi\overline{\chi}\to sZ'} = \frac{g_\chi^2 Q_V^2 y_\chi^2 \sqrt{(\eta_s - \eta_{Z'} - 4)^2 - 16\eta_{Z'}}\left((\eta_s - \eta_{Z'} - 4)^2 + 8\eta_{Z'}\right)}{64\pi m_\chi^2 \left(\eta_s + \eta_{Z'} - 4\right)^2}, \quad (6.14)$$

where $\eta_{s,Z'} = m_{s,Z'}^2/m_\chi^2$.

The relative size and behavior of these cross sections can be seen in Fig. 6.4. Given that the Z' obtains mass from the Stueckelberg mechanism, there are no contributions to the cross sections from longitudinal Z' modes. Therefore, all cross sections decrease with increasing DM mass. It is possible to dial the strength of one annihilation process relative to the other by adjusting the dark Yukawa coupling y_χ and the dark gauge coupling g_χ, which are independent parameters. (This freedom was not available in scenario II, where the couplings were related.) This is shown in the top two panels of Fig. 6.4. This also means that if $g_\chi \ll y_\chi$ then p-wave processes such as $\chi\overline{\chi} \to ss$ (which scale as y_χ^4) may have an important effect on the relic density, as the otherwise dominant $Z'Z'$ and sZ' processes (which scale as g_χ^4 and $g_\chi^2 y_\chi^2$ respectively) would be suppressed by the small gauge coupling. However, it is difficult to make the annihilation to ss dominate in the universe today, where the p-wave modes are suppressed by $v_\chi^2 \approx 10^{-6}$. To do so would require $g_\chi^2 \sim 10^{-6} y_\chi^2$ which, while possible, is a very tuned scenario that we shall not consider. The relevant diagrams for annihilation to ss are shown in Fig. 6.6.

6.5.3 Relic Density

In Fig. 6.5, we show the relic density contours as a function of DM mass m_χ and the dark gauge coupling g_χ for various values of the Z' mass, dark Higgs mass, $Q_V = 1$ and fixed ratios of y_χ/g_χ. The color codes for the contours are the same as in the previous scenario. The different choices of y_χ/g_χ are embodied in the thickness of the lines: thinner for $y_\chi/g_\chi = 1$ and thicker for $y_\chi/g_\chi = 5$. Obviously for the same g_χ, a larger y_χ/g_χ ratio results in a larger cross section for $\chi\overline{\chi} \to sZ'$ and thus a smaller relic density; a smaller g_χ is thus needed to obtain the same relic density, resulting in an overall downward shift of the contours. In this scenario, the quartic coupling λ_s can be expressed as $\lambda_s \simeq y_\chi^2 m_s^2/(4m_\chi^2)$. The perturbativity

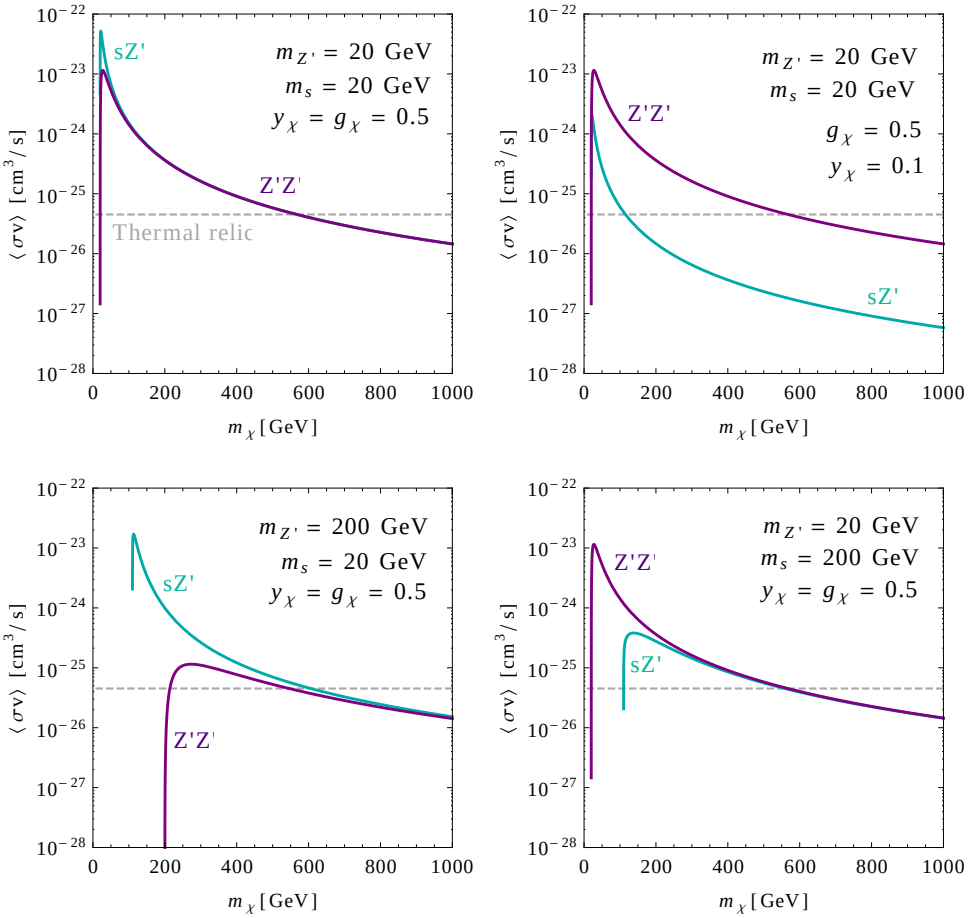

FIGURE 6.4: Cross section for the two dominant s-wave annihilation processes of scenario III, $\chi\overline{\chi} \to sZ'$ (blue) and $\chi\overline{\chi} \to Z'Z'$ (purple), for some example choices of the dark Higgs mass, the Z' mass, and the dark gauge and Yukawa couplings, as labeled. Here $Q_V = 1$. Notice, by comparing the top two panels, that either process can be chosen to dominate by varying the dark gauge coupling and the dark Yukawa coupling. The approximate thermal relic cross section is shown as the gray dashed line.

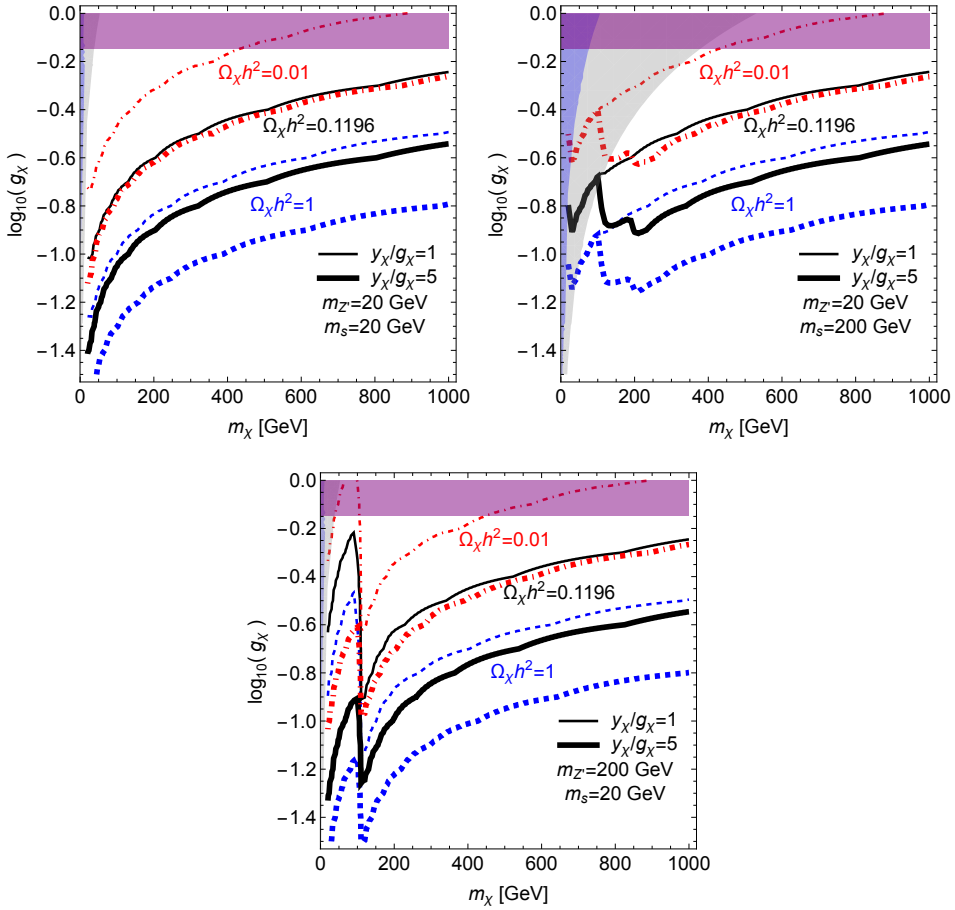

FIGURE 6.5: Relic density contours for scenario III, as a function of m_χ and g_χ, for various choices of the dark Higgs and Z' mass and ratio of couplings constants, as labeled. The thin (thick) red dot-dashed, solid black and dotted blue lines denote $\Omega h^2 = 0.01, 0.1196$ and 1, respectively, for $y_\chi/g_\chi = 1$ (5). In the light purple shaded regions, the Yukawa coupling y_χ is larger than $\sqrt{4\pi}$ for $y_\chi/g_\chi = 5$; it is always perturbative in the parameter space shown when $y_\chi/g_\chi = 1$. The region shaded blue (gray) on the left side of each panel shows the perturbativity bound for λ_s with $y_\chi/g_\chi = 1$ (5) .

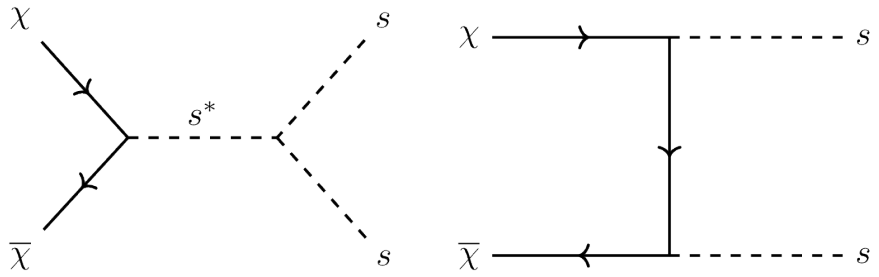

FIGURE 6.6: DM annihilation to two dark Higgs bosons, $\chi\overline{\chi} \to ss$. Despite being p-wave suppressed, these processes can make a non-negligible impact on the relic density at freeze-out, particularly if the gauge coupling is sufficiently small to suppress the s-wave processes.

bounds for λ_s are shown by the shaded gray regions, while the parameter space where $y_\chi > \sqrt{4\pi}$ ($y_\chi/g_\chi = 5$ only) is shown as the light purple region.

Comparing three panels of Fig. 6.5, we see that dark matter relic density is saturated with the same set of parameter values if DM is much heavier than the dark Higgs and dark Z'. In the heavy DM limit, the dark Higgs and dark Z' can be treated as massless particles and only dimensionless couplings affect the DM annihilation cross section. (This is not true in scenario II, where longitudinal Z' contributions introduce a $1/m_Z^{\prime 2}$ dependence to the cross section.) Thus to reproduce the right relic density, the same set of couplings have to be chosen. When DM has comparable mass as dark Higgs and dark Z', the mass generation mechanism plays a major role in determing the shape of the relic density contours. First of all, there are dips near the kinematic threshold of each annihilation channel. In the left panel, where $m_{Z'} = m_s = 20\,\text{GeV}$, all three channels, sZ', $Z'Z'$ and ss, are open at the same time and no dips occur beyond this mass. For the middle and right panels of Fig. 6.5, there is a dip at $m_\chi \simeq 110\,\text{GeV}$ corresponding to the sZ' channel. In the middle panel, the ss channel begins to contribute around $m_\chi \simeq 200\,\text{GeV}$; the effect is more pronounced for larger y_χ, leading to a prominent dip for $y_\chi/g_\chi = 5$ but not for $y_\chi/g_\chi = 1$. In the right panel, however, there is no dip around 200 GeV for the $Z'Z'$ channel, since the $Z'Z'$ cross section is always subdominant to the sZ' cross section for the couplings chosen.

6.6 Scenario IV: Bare DM Mass, Z' Mass from Dark Higgs Mechanism

Interaction type required: Pure Vector

An alternative scenario in which the mass of the DM and Z' arise from different mechanisms, is to have a bare mass for the χ and use a dark Higgs mechanism to

provide mass for the Z'. In this scenario, again, only pure vector interactions of the χ and Z' are permitted.

6.6.1 Model

In this scenario, the most minimal gauge invariant Lagrangian is

$$\begin{aligned}\mathcal{L} &= \mathcal{L}_{SM} + i\overline{\chi}\left(\not{\partial} + ig_\chi Q_V \not{Z}'\right)\chi - \frac{\sin\epsilon}{2}Z'^{\mu\nu}B_{\mu\nu} - m_\chi\overline{\chi}\chi - \lambda_{hs}(S^\dagger S)(H^\dagger H) \\ &+ \left[(\partial^\mu + ig_\chi Q_S Z'^\mu)S\right]^\dagger\left[(\partial_\mu + ig_\chi Q_S Z'_\mu)S\right] - \mu_s^2 S^\dagger S - \lambda_s(S^\dagger S)^2. \qquad (6.15)\end{aligned}$$

The vectorlike charge Q_V and dark Higgs charge Q_S under the dark $U(1)_\chi$ can be chosen freely. Again the dark sector interacts with the visible sector in two ways: via kinetic mixing or Higgs mass mixing.

6.6.2 Cross Sections

As shown in Tab. 6.1, the annihilation to $Z'Z'$ proceeds via the t/u and channel diagrams, as in scenarios I and III, with the s-wave contribution given by Eq. (6.2). The annihilation to sZ' proceeds only via the s-channel diagram, as the DM does not interact directly with the dark Higgs. The s-wave contribution is given by

$$\langle\sigma v\rangle_{\chi\overline{\chi}\to sZ'} = \frac{g_\chi^4 Q_V^2 Q_S^2\sqrt{(\eta_s - \eta_{Z'} - 4)^2 - 16\eta_{Z'}}\left((\eta_s - \eta_{Z'} - 4)^2 + 32\eta_{Z'}\right)}{256\pi m_\chi^2\,(\eta_{Z'} - 4)^2}, \qquad (6.16)$$

where $\eta_{s,Z'} = m_{s,Z'}^2/m_\chi^2$. The behavior of these cross sections is depicted in Fig. 6.7. We see that the shapes of the sZ' and $Z'Z'$ cross sections are similar, as both fall off with DM mass as $1/m_\chi^2$. There is no production of longitudinal Z'_L modes in the high energy limit, which is consistent with the fact that the DM does not interact with Goldstone modes, given the absence of a DM-Higgs coupling. Because Q_V and Q_S are independent, the relative size of the $Z'Z'$ and sZ' processes can again be scaled relative to each other by appropriate choices of these charges.

6.6.3 Relic Density

We plot the relic density contours for this scenario in Fig. 6.8. As the dark Higgs is responsible for the Z' mass, the quartic coupling may be expressed as $\lambda_s \simeq g_\chi^2 m_s^2/(2m_{Z'}^2)$. Parameters excluded by the perturbativity bound on λ_s are shaded gray; this bound is relevant only for the middle panel of Fig. 6.8, where the ratio of $m_s/m_{Z'}$ is larger. Because there is no direct coupling of the scalar to the DM, there is no annihilation to ss. As a result, the features of the relic density contours are generally simpler than in the previous scenario. For the chosen values of $Q_{V,S}$, the annihilation to sZ' is subdominant to the $Z'Z'$ process when both are kinematically allowed. This leads to a dip in the contours of the

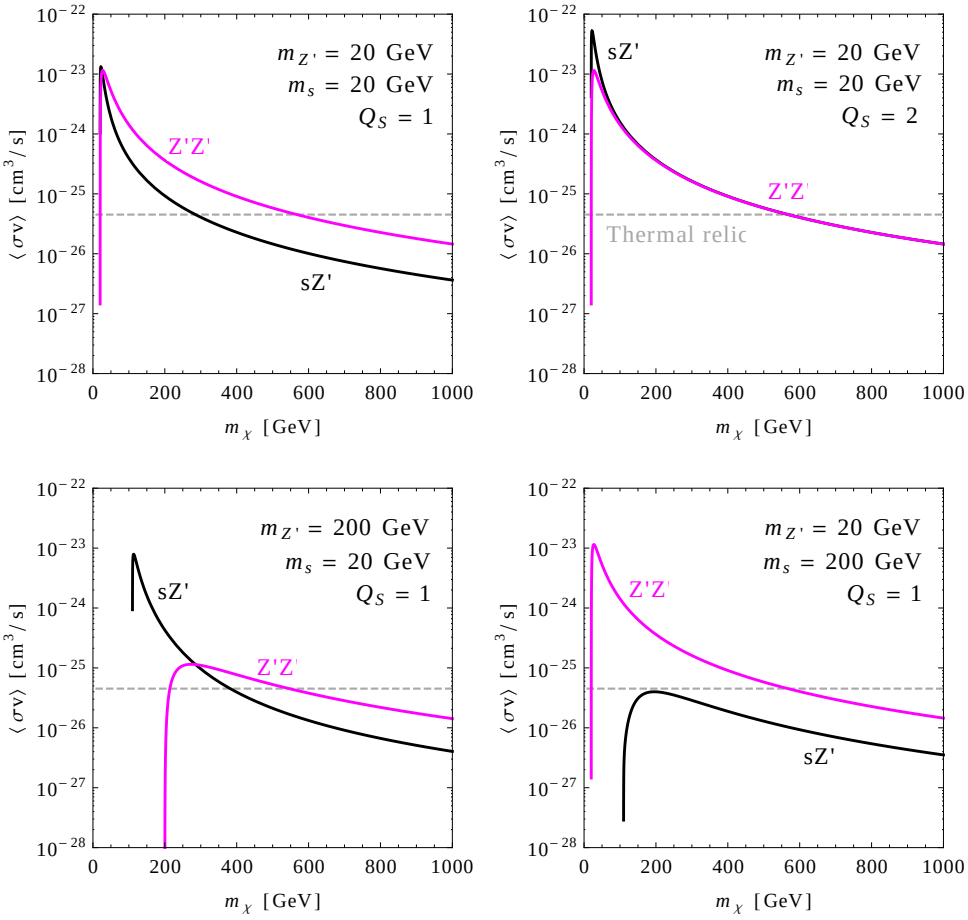

FIGURE 6.7: Relative cross section for the two dominant s-wave annihilation processes in scenario IV, $\chi\overline{\chi} \to sZ'$ (black) and $\chi\overline{\chi} \to Z'Z'$ (magenta), for some example parameter choices for the dark Higgs mass and Z' mass, as labeled. Here $Q_V = 1$. Example dark charges Q_S =1,2 are shown, which demonstrate how either process can be made to dominate, or both can be made comparable, if kinematically allowed. For all plots the gauge coupling is set to $g_\chi = 0.5$. As all cross sections are directly proportional to g_χ^4 they can easily be scaled by adjusting this parameter. The approximate thermal relic cross section is shown as the gray dashed line.

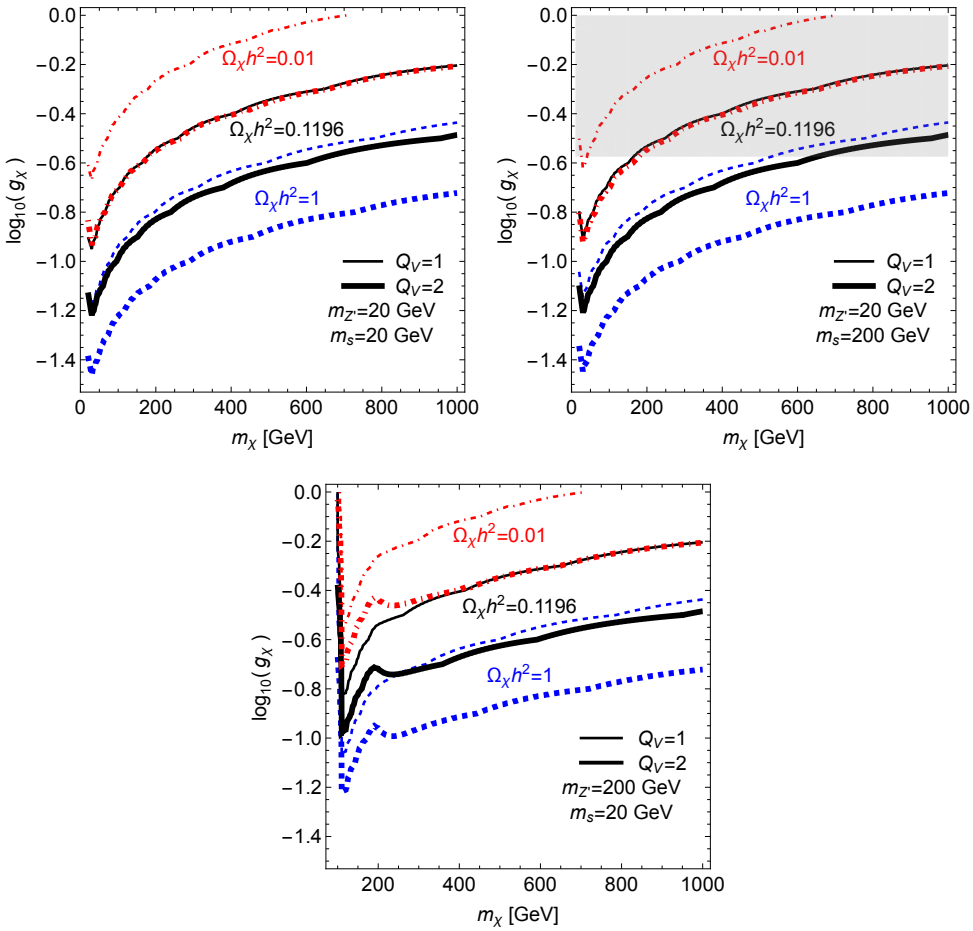

FIGURE 6.8: DM relic density contours for scenario IV as a function of m_χ and g_χ, for various choices of m_s, $m_{Z'}$ and Q_V, as labeled. The thin (thick) red dot-dashed, solid black and dotted blue lines denote $\Omega h^2 = 0.01, 0.1196$ and 1, respectively, for $Q_V = 1$ (2). We have taken $Q_S = 1$. For the chosen values of $Q_{V,S}$, the sZ' contribution is subdominant to that from $Z'Z'$ when both are kinematically allowed, which accounts for the features of the curves. The light gray shaded region at the top of the middle panel shows the parameter space excluded by perturbativity bound for λ_s.

right panel at $m_\chi \simeq m_{Z'}$, where the $Z'Z'$ modes becomes allowed, but not in the left and center panels where the $Z'Z'$ mode always plays the dominant role.

6.7 Indirect Detection Phenomenology

We now determine indirect detection constraints on the dominant annihilation modes for the scenarios discussed, $\chi\overline{\chi} \to Z'Z'$ and $\chi\overline{\chi} \to sZ'$. The Z' and s produced in these annihilations decay to SM particles, and subsequent hadronization/decay of these SM states leads to gamma-ray and other fluxes that we may compare with observational limits.

We generate our gamma-ray spectra as per the method outlined in Ref. [257], where a more detailed description can be found. The kinetic mixing of the Z' with the SM hypercharge boson permits the decay $Z' \to f\overline{f}$, with a partial width given by

$$\Gamma(Z' \to f\bar{f}) = \frac{m_{Z'}N_c}{12\pi}\sqrt{1-\frac{4m_f^2}{m_{Z'}^2}}\left[g_{f,V}^2\left(1+\frac{2m_f^2}{m_{Z'}^2}\right)+g_{f,A}^2\left(1-\frac{4m_f^2}{m_{Z'}^2}\right)\right], \quad (6.17)$$

where N_c is a color factor, relevant for hadronic decays. The $g_{f,V}$ (vector) and $g_{f,A}$ (axial-vector) structure of the Z'–f couplings are inherited from the kinetic mixing [27]. The total decay width for the Z' is then approximately given by the sum over all the final state fermions[10], $\Gamma_{Z'} \simeq \sum_f \Gamma(Z' \to f\bar{f})$. The dark Higgs decays to the SM due to mass mixing with the SM Higgs, and so it decays preferentially to heavier particles. The dark Higgs is also permitted to decay to pairs of Z'. In order to take into account loop decays and higher order corrections, we calculate the dark Higgs decay widths numerically with the Fortran package HDecay [298].[11]

The spectra generated are then compared to the strongest indirect detection limits available for our processes[12]: the Fermi-LAT Pass 8 data on dwarf spheroidal galaxies (dSphs) of the Milky Way [135]. To find the limit on the cross section from dSphs, we use the maximal likelihood method to compare our spectra against those for the dSphs publicly provided by Fermi-LAT in the Pass 8 data, with the J factor taken to be a nuisance parameter as per Ref. [135]. We take spectra from 15 dSphs: Bootes I, Canes Venatici II, Carina, Coma Berenices, Draco, Fornax,

[10] If kinematically allowed, Z' can also decay to W^+W^-, Zs or Zh. Their decay branching fraction will be of similar size as any of the lepton channels if Z' is sufficient heavy. Even so, these three channel are still negligible compared with the fermion channels combined due to the large multiplicity from both flavor and color factors.

[11] Generally s can decay to $Z'Z'$ or $Z'Z'^*$ if kinematically allowed, which is not suppressed by the small Higgs portal coupling. In the benchmarks we considered in this work, however, $Z'Z'$ is kinematically forbidden and $Z'Z'^*$ is deeply suppressed by the small kinetic mixing parameter, which makes HDecay an ideal tool to calculate the branching ratios.

[12] We also include the approximate limit from AMS-02 at low DM masses, adapted from [273]. This approximate limit is only applicable if the sum of the final state mediators is less than about 70 GeV.

Hercules, Leo II, Leo IV, Sculptor, Segue 1, Sextans, Ursa Major II, Ursa Minor, and Willman 1. The 95% C.L. limits on the annihilation cross section are shown Fig. 6.9, for various dark Higgs and Z' masses, for both sZ' and $Z'Z'$ processes.

The limits we show are independently set on either the $\chi\overline{\chi} \to sZ'$ process or the $\chi\overline{\chi} \to Z'Z'$ process. They can then be applied to any of the scenarios we study in this chapter, assuming that one of the modes dominates. Indeed, they can also be applied to any model that features annihilations to a sZ' or $Z'Z'$ final state, provided the Z' and s communicate with the SM via kinetic or Higgs mass mixing respectively, as the cross section limits depend only on the gamma-ray spectral shape that characterizes a given annihilation mode. From Fig. 6.9 it is clear that the limit on the cross section does not vary greatly with the mediator mass provided it is kinematically allowed; it is instead the DM mass with which the energy of final state photons and thus cross section limits is tightly correlated.

The thermal relic cross section required to reproduce the correct relic density for non-self conjugate DM is approximately $\langle\sigma v\rangle \approx 4.4\times10^{-26}$ cm^3/s [314], which excludes the low DM mass region where the Fermi limits surpass this sensitivity. However, this statement assumes that the s-wave contributions to the annihilation cross section dominate both at freeze-out and in the universe today. In fact in some cases, such as scenario III, the p-wave processes can make a non-negligible contribution at freeze-out. This means that the relic density constraint could be satisfied, yet the cross section in the universe today suppressed, escaping indirect detection bounds even for low DM mass.

6.8 Discussion and Summary

We have surveyed a spectrum of phenomenologically distinct two-mediator DM models, containing both a dark vector and dark scalar, where gauge invariance is respected and the mass terms for the dark sector fields are introduced in a self-consistent way. These two-mediator DM models correctly capture important phenomenology which is missing in the single mediator approach. Specifically, we modified the usual simplified model setup to incorporate mass generation for the DM candidate and vector mediator, by using combinations of bare mass terms, Higgs mechanisms and Stueckelberg mechansims. We found that the DM interaction types and annihilation processes, and hence both the relic density and indirect detection constraints, are strongly dictated by the mass generation mechanism we choose for the dark sector particles:

- Unless the DM and Z' masses both receive contributions from the vev of the same dark Higgs field, pure vector couplings of the spin-1 mediator and DM are required, as discussed in scenarios III and IV. In these scenarios DM annihilates to both sZ' and $Z'Z'$, with the relative rates to these final states controlled by independent coupling constants. Moreover, in the high energy limit, only the Z'_T polarization is produced by these annihilations.

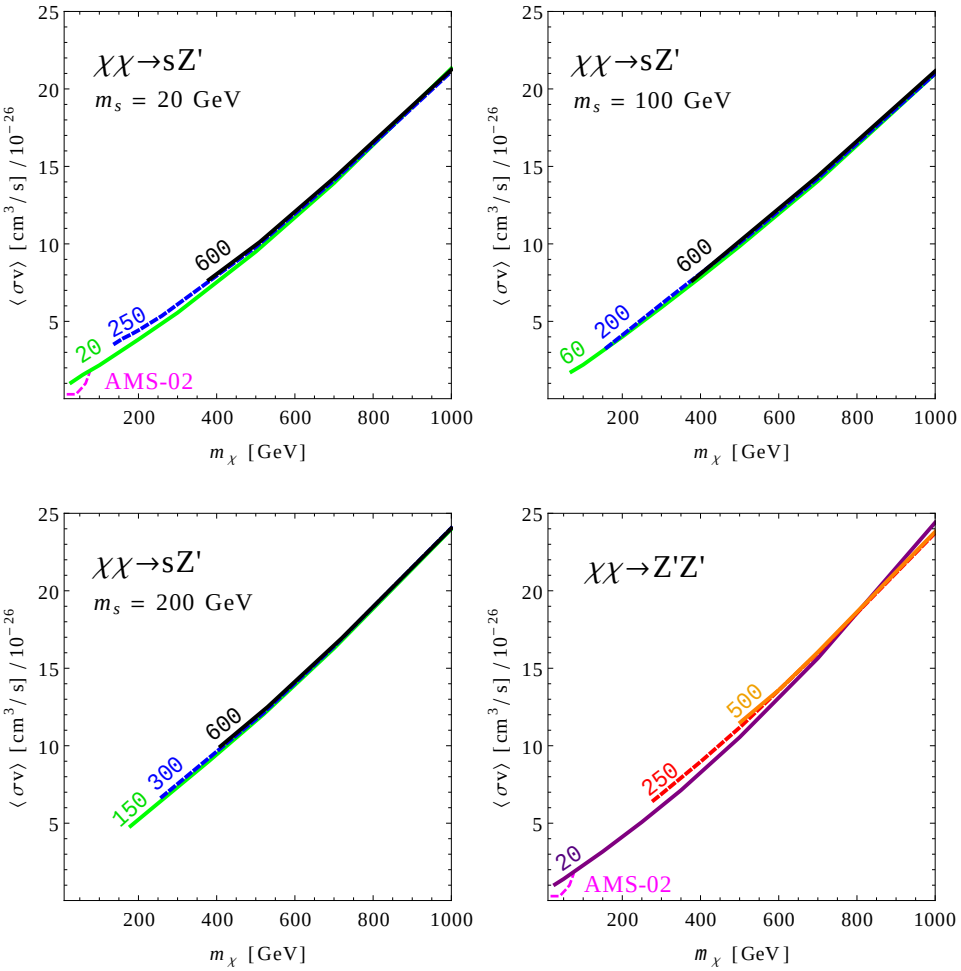

FIGURE 6.9: 95% confidence limits (C.L.) on the annihilation cross section from Fermi Pass 8 data on 15 dwarf spheroidal galaxies. Limits on the sZ' process are shown for dark Higgs masses of 20, 100 and 200 GeV, for various Z' masses as labeled in the plots. Z' masses stated are in GeV. Limits on the $Z'Z'$ process are shown for Z' masses of 20, 250 and 500 GeV. The approximate limit from AMS-02 is shown as a dashed magenta line, and is only applicable if the sum of the final state mediators is less than about 70 GeV. Intermediate mediator mass limits can be simply obtained from interpolation of these plots. All these plots can be applicable to any of the scenarios outlined in this chapter: the appropriate limit of sZ' or $Z'Z'$ will depend on the specific choices of the couplings, masses and for which process is kinematically allowed.

- However, if a dark Higgs mechanism gives mass to all the dark sector fields, as per scenario II, the axial-vector coupling between the spin-1 mediator and DM must be non-zero. In this scenario, the sZ' and $Z'Z'$ DM annihilation channels are intrinsically linked. Furthermore, production of the Z'_L polarization enhances the annihilation to sZ'. If both the vector and axial-vector couplings are non-zero, the annihilation to $Z'Z'$ is also enhanced by Z'_L (via the $V - A$ interference) though it remains subdominant to the sZ' mode when both are kinematically allowed.

One may imagine generalizations of scenarios III and IV in which the Z' and χ masses arise from *two different* Higgs mechanisms. Indeed, we would recover scenario III (Stueckelberg Z' mass) in the limit that the Higgs responsible for the Z' mass is taken to infinity. Likewise, we would recover scenario IV (bare χ mass) in the limit that the Higgs responsible for the χ mass is taken very large. In these generalizations, the χ-Z' coupling remains of pure vector form. Axial couplings always imply that a Higgs which Yukawa couples to the χ must carry $U(1)_\chi$ charge, and hence its vev also contributes to the Z' mass, as in scenario II. Such two-scalar models would lead to additional complexity via mixing in the scalar sector, but would not introduce any qualitatively new Z' physics.

Our results are not captured by the single mediator approach, where the mass generation mechanism is left unspecified and constraints on the coupling types are not usually applied. This means that by continuing to use simplified models with a single spin-1 mediator, (i) we are at best only testing a very specific subset of the possibilities: Dirac DM with a bare mass and pure vector couplings to a Z' with a Stueckelberg derived mass (i.e. scenario I) or (ii) at worst, experimental constraints may not be meaningful because the models have been oversimplified. Option (i) is not particularly appealing in that it does not cover well motivated possibilities such as Higgs mass generation (which, after all, is a mechanism we know is realized by nature) or Majorana DM. The remaining option, (ii), is far from desirable.

Chapter 7

Enhancing Dark Matter Annihilation Rates with Dark Bremsstrahlung

MANY dark matter interaction types lead to annihilation processes which suffer from p-wave suppression or helicity suppression, rendering them sub-dominant to unsuppressed s-wave processes. We show that the natural inclusion of initial state dark radiation of a dark scalar or dark vector from fermionic dark matter can open an unsuppressed s-wave annihilation channel and thus provide the dominant dark matter annihilation process for particular interaction types.

This chapter is based on the publication: *N. F. Bell, Y. Cai, J. Dent, R. K. Leane, and T. Weiler, "Enhancing Dark Matter Annihilation Rates with Dark Bremsstrahlung" [arXiv:1705.01105 [hep-ph]] [315].*

7.1 Introduction

The particle nature of dark matter (DM) remains unknown. In order to significantly probe its properties in indirect detection experiments, large or unsuppressed annihilation rates are desirable. The DM annihilation rate will generally be largest if it proceeds via an unsuppressed s-wave process. Unfortunately, there are a number of well motivated DM models in which the s-wave annihilation to Standard Model (SM) products, $f\overline{f}$, is absent or helicity suppressed. This renders indirect detection very unlikely, as the p-wave term is suppressed by a factor of the DM velocity squared (with $v^2 \sim 10^{-6}$ in the present universe) while a helicity suppression factor of $(m_f/m_\chi)^2$ can be significant for annihilation to light fermions. These suppressions are well-known features of neutralino annihilation in SUSY, but in fact are more general.

It is well known that such suppressions can be lifted via the bremsstrahlung of a SM particle. For example, an unsuppressed s-wave can be opened via the radiation of a photon [129, 131, 220, 316–318] or electroweak gauge boson [175–179,

319–321] during the DM annihilation processes. This has led to much recent work on the importance of SM radiative corrections in dark matter annihilation [129, 131, 167, 175–179, 220, 232, 316–337]. Despite the bremsstrahlung annihilation process having a 3-body final state, it can be the dominant annihilation channel in the universe today (if not at freeze out) because the suppression from additional coupling and phase space factors is small compared to the $v \sim 10^{-6}$ suppression of the p-wave contributions. Past work has primarily used final state radiation (FSR) or virtual internal bremsstrahlung (VIB) to lift the suppression. If the DM is a SM gauge singlet, initial state radiation (ISR) of a SM particle is obviously not possible, however ISR of a W or Z boson from $SU(2)$ charged DM is possible, and has been considered in [338–340].

An interesting possibility is that helicity or p-wave suppressions can instead be lifted by the ISR of a *dark sector* field. In this scenario, an initial state dark bremsstrahlung process can dominate over other suppressed channels. This will require that the dark sector contains more particles than just the DM candidate itself which, in fact, is very well motivated: it is what is observed in the visible sector, and multiple dark sector fields are a common feature of many self-consistent, gauge-invariant, and renormalizable models. For example, mass generation in the dark sector can require the introduction of new fields, such as a dark Higgs, while DM stability may arise from a charge under a new dark sector gauge group, requiring the introduction of dark photons. More generally, models in which DM interactions are mediated by the exchange of only an axial-vector mediator are not gauge invariant. They require the addition of a dark Higgs to unitarize the longitudinal component of the gauge boson, and to give mass to both the gauge boson and DM [80, 257, 268, 296, 301, 341]. Indeed, the simultaneous presence of both spin-1 and spin-0 mediators lead to new indirect detection phenomenology that does not arise in single mediator models [257, 268, 301].

In this chapter, for the first time, we explore the possibility that helicity or p-wave suppressions of the DM annihilation process are lifted by dark bremsstrahlung from the initial state. We investigate the case where fermionic DM, χ, radiates either a dark spin-1 field, Z', or spin-0 field, ϕ, to give the ISR processes $\chi\chi \to f\overline{f}Z'$ or $\chi\chi \to f\overline{f}\phi$, respectively.

Bremsstrahlung annihilation processes are very closely related to the mono-X processes utilized in collider DM searches [71, 72, 98–103, 107–109, 153], as they are controlled by the same matrix element. For example, the radiation of photons from fermions in the FSR annihilation process $\overline{\chi}\chi \to \overline{f}f\gamma$ is the analogue of the collider ISR mono-photon process $\overline{f}f \to \overline{\chi}\chi\gamma$. Likewise, the ISR radiation of a dark spin-0 or spin-1 field from the initial state χ in the $\overline{\chi}\chi \to \overline{f}f\phi$ or $\overline{\chi}\chi \to \overline{f}fZ'$ annihilation processes are then the analogue of the FSR mono-Z' [110–112, 342] or mono-dark Higgs [341] collider processes, respectively.

For the purpose of illustration, we shall assume the $\chi\chi \to f\overline{f}$ process is adequately described by an effective field theory (EFT operator) of the form

$(1/\Lambda^2)(\overline{\chi}\Gamma\chi)(\overline{f}\Gamma f)$. We will see that the s-wave contribution to the ISR process scales as $\langle\sigma v\rangle_{\rm ISR} \propto O(1/\Lambda^4)$, i.e., the same order in Λ as the 2-body annihilation $\chi\chi \to f\overline{f}$. In comparison, the well-studied lifting of helicity suppressions via FSR or VIB radiation can occur only at higher order in $1/\Lambda$, with cross sections scaling as $\langle\sigma v\rangle_{\rm FSR,\,ISR} \propto O(1/\Lambda^8)$ [1].

In Section 7.2 we provide an overview of suppressions to the annihilation cross section of fermionic DM, and discuss annihilation both directly to SM particles, and to dark mediators. In Section 7.3 we outline possible dark ISR annihilation processes, and investigate two interesting cases in more detail in Sections 7.4 and 7.5. We present our conclusions in Section 7.6.

7.2 Overview of Fermionic Dark Matter Annhilation

7.2.1 Direct annihilation to SM particles

If DM is a Majorana fermion, the possible interactions which can mediate a $\chi\chi \to f\overline{f}$ annihilation process are:

- s-channel exchange of an axial vector: helicity suppressed s-wave,
- s-channel exchange of a scalar: no s-wave,
- s-channel exchange of a pseudo-scalar: unsuppressed s-wave, or
- t-channel exchange of a sfermion-like scalar: helicity suppressed s-wave.

In the t-channel case, Fierz rearrangement to s-channel form gives $A \otimes A$ and $A \otimes V$ structures. The $A \otimes A$ has a helicity suppressed s-wave, while the $A \otimes V$ has no s-wave. For Majorana DM, we thus see that the s-channel exchange of a pseudo-scalar is the only case of an unsuppressed s-wave. All other possibilities feature either helicity or v^2 suppressions.

For Dirac DM, there are additional possibilities because vector couplings (forbidden for Majorana particles) are also allowed. Note, however, that while the exchange of a vector results in an unsuppressed s-wave annihilation cross section, these models are also well constrained because they lead to unsuppressed SI scattering in direct detection experiments.

A summary of the cross section suppression factors, for both annihilation and scattering, for all possible Lorentz structures for $\chi\chi \to \overline{f}f$, is given in Ref. [343].

7.2.2 Direct annihilation to dark mediators

Table 7.1 details whether DM annihilation to two different mediators ($\chi\chi \to M_1M_2$) is s- or p-wave, depending on the Lorentz structures of the DM-mediator interactions. For annihilation to any two spin-1 mediators, the rate is s-wave.

[1] This observation was also made in the case of ISR of a W/Z boson from $SU(2)$ doublet DM [338–340].

$\Gamma_{M_1} \otimes \Gamma_{M_2}$	$S \otimes S$	$S \otimes P$	$P \otimes P$	$V \otimes V$	$V \otimes A$	$A \otimes A$	$S \otimes V$	$S \otimes A$	$P \otimes V$	$P \otimes A$
$\chi\chi \to M_1 M_2$	v^2	1	v^2	1	1	1	1	v^2	1	v^2

TABLE 7.1: Suppression factors for DM annihilation to two different mediators M_1 and M_2, which have varying Lorentz structures. The combination of mediators can be two spin-0 final states, two spin-1 final states, or a mixed spin-0 plus spin-1 final state. Note for Majorana DM, the V cases do not exist.

For any two spin-0 mediators, the rate is p-wave unless one scalar and one pseudoscalar are both present. For a mixed spin-0 and spin-1 final state, if the spin-1 is a vector, the processes are s-wave, while if the spin-1 is an axial-vector, the processes will be p-wave[2].

If one of these mediators is off-shell while the other is on-shell, it is equivalent to the dark ISR process discussed in the following section — where the on-shell mediator corresponds to the dark ISR radiation, and the off-shell mediator has been integrated out to give the EFT vertex. As such, the annihilation type for dark ISR is related to the underlying Lorentz structures of the mediators. We now discuss the dark ISR processes in detail.

7.3 Dark Initial State Radiation

In this section, we consider the scenario where initial state radiation of a dark sector particle lifts helicity or p-wave suppression in DM annihilation processes.

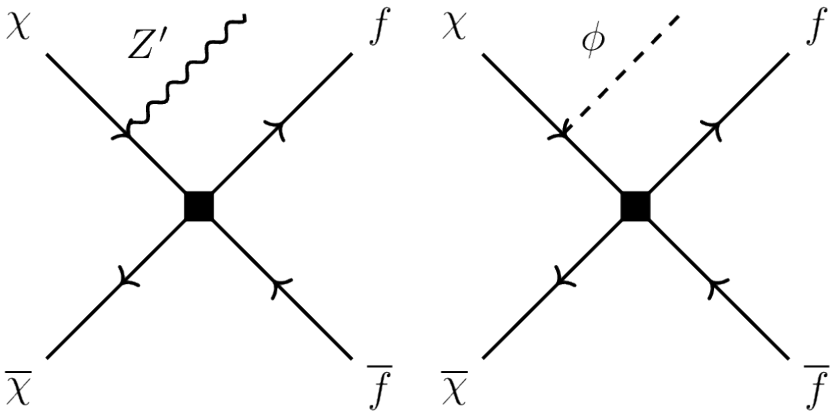

FIGURE 7.1: Dark vector (left) and dark scalar (right) ISR. Note in both cases that there is also an additional diagram from emission from the anti-DM particle.

Figure 7.1 demonstrates the dark sector ISR in DM annihilation. For the sake of illustration, we use an effective field theory (EFT). The qualitative effects we

[2]If there exist direct couplings between the dark mediators themselves, it is possible to have an s-wave process with a spin-0 plus spin-1 final state where the spin-1 is an axial-vector [257, 301]. Details of such couplings are model dependent, and we do not consider such processes in this work.

$\Gamma_\chi \otimes \Gamma_f$	$\chi\overline{\chi} \to f f$	$\chi\overline{\chi} \to f f Z'$		$\chi\overline{\chi} \to f f \phi$	
		$\Gamma_{Z'} = V$	$\Gamma_{Z'} = A$	$\Gamma_\phi = S$	$\Gamma_\phi = P$
$V \otimes V$	1	1	1	1	1
$A \otimes V$	v^2	1	1	v^2	v^2
$V \otimes A$	1	1	1	1	1
$A \otimes A$	$(m_f/m_\chi)^2$	1	1	v^2	v^2
$S \otimes S$	v^2	1	v^2	v^2	1
$P \otimes S$	1	1	v^2	1^*	v^2
$S \otimes P$	v^2	1	v^2	v^2	1^*
$P \otimes P$	1	1	v^2	1	v^2

TABLE 7.2: Suppression factors for DM annihilation with varying Lorentz structures: vector (V), axial-vector (A), scalar (S) or pseudoscalar (P). In some cases, helicity suppression ($\propto (m_f/m_\chi)^2$) or p-wave suppression ($\propto v^2$) can be lifted to s-wave ($\propto 1$) by including dark bremsstrahlung, to produce a new s-wave process with no relative suppression factors. Note that for any vector or axial-vector ISR, the s-wave process $\chi\chi \to Z'Z'$ will also be induced. An asterisk indicates that the s-wave process $\chi\chi \to \phi_1\phi_2$ will be induced via scalar(ϕ_1)-pseudoscalar(ϕ_2) mixing in a CP violating scenario. Note for Majorana DM, the V cases do not exist.

discuss are relevant for UV completions which map to the relevant cases. We assume one mediator is sufficiently heavy, such that the EFT description can safely be used without unitarity issues.

Table 7.2 details the annihilation type and relative suppression of all processes (whether they are s-wave, p-wave, or helicity suppressed). This reveals which Lorentz structures for particular ISR will lift suppression in DM annihilation.

We see that the most promising dark ISR scenario is with a dark vector: radiating a vector lifts the suppression in DM annihilation for several Lorentz structures: $S \otimes S$, $A \otimes A$, and $A \otimes V$. Radiating an axial vector lifts suppression in $A \otimes A$ and $A \otimes V$ annihilation processes. Radiating a scalar fails to lift any suppression of the annihilation cross section. Radiating a pseudo-scalar, however, can make a process with a $S \otimes S$ structure s-wave. In the case of $S \otimes P$ or $P \otimes S$, any scalar with such a structure will not have well-defined CP properties. Thus the mixing between the heavy scalar and the pseudo-scalar is inevitable, and a $2 \to 2$ s-wave contribution will be induced.

It is also important to note that once an additional dark sector field is included as dark ISR, there can also be s-wave annihilations of DM into the dark radiation. For spin-1 ISR, the direct annihilation to mediators $\chi\chi \to Z'Z'$ is s-wave (as shown in Fig. 7.3) for both vector and axial-vector couplings, and can dominate the total DM annihilation rate for some choices of the coupling strength or masses. In the case that the dark radiation is a spin-1 field, the $\chi\chi \to \phi\phi$ process is p-wave suppressed for both scalar and pseudoscalar couplings, and so can very naturally be sub-dominant to the suppression-lifting ISR process.

Note that to avoid the "dark radiation" contributing to the relic density, it must eventually decay to SM states. This can easily be arranged without introducing other consequences, e.g., via a gauge or Higgs portal to the SM, which can naturally appear for inclusion of a gauge boson or scalar, respectively.

We now study in detail two particular cases of the lifting helicity or p-wave suppression: $A \otimes A$ with vector ISR and $S \otimes S$ with pseudo-scalar ISR. We choose the former as an example of lifting helicity suppression. We choose the latter as it is the only scenario where introducing dark ISR to lift a p-wave cross section does not induce an additional competing $2 \to 2$ s-wave process. Other scenarios and Lorentz structures can dominate in particular regions of parameter space. Note also that in all the scenarios discussed, UV completions with the same Lorentz structures would map to the same results we present. Our results are not specific to EFTs, rather than to the underlying Lorentz structures.

7.4 Lifting Helicity Suppression in $A \otimes A$ Interactions

In this section, we demonstrate how helicity suppression can be lifted through dark vector ISR, in the case of Lorentz structures $\Gamma_\chi \otimes \Gamma_f = A \otimes A$. Such a structure

is very natural for Majorana DM, but is also possible with Dirac DM. We will also discuss any new competing annihilation processes.

7.4.1 Helicity suppressed $\overline{\chi}\chi \to \overline{f}f$

For Lorentz structures $\Gamma_\chi \otimes \Gamma_f = A \otimes A$, the lowest order four-fermi operator, without any higher order corrections, is

$$\mathcal{L}_{\text{int}} \supset \frac{1}{\Lambda^2}(\overline{\chi}\gamma^\mu\gamma^5\chi)(\overline{f}\gamma^\mu\gamma^5 f), \tag{7.1}$$

where χ is a fermionic DM candidate (we take to be Majorana for the calculation), f are SM fermions and Λ is the cutoff scale for new physics, representing a heavy field which has been integrated out.

The operator in Eq. (7.1) yields a helicity suppressed DM annihilation cross section for $\overline{\chi}\chi \to \overline{f}f$,

$$\langle\sigma v\rangle_{\overline{\chi}\chi\to\overline{f}f} = \frac{m_f^2\sqrt{1-m_f^2/m_\chi^2}}{2\pi\Lambda^4}, \tag{7.2}$$

where m_f is the mass of the SM fermion and m_χ is the DM mass. In the limit that $m_f \to 0$, this process is vanishing. We now explicitly show that for such an operator, including dark vector radiation of a Z' lifts this suppression, and the dominant s-wave process can be $\overline{\chi}\chi \to f\overline{f}Z'$.

7.4.2 Dark vector ISR, $\overline{\chi}\chi \to \overline{f}fZ'$

To consider a minimal scenario, in addition to the EFT interaction in Eq. (7.1), we incorporate a coupling $g_{Z'}$ of DM to a new vector Z', such that the Lagrangian is

$$\mathcal{L}_{\text{int}} \supset \frac{1}{\Lambda^2}\left(\bar{\chi}\gamma_\mu\gamma_5\chi\right)\left(\overline{f}\gamma^\mu\gamma_5 f\right) + g_{Z'}\overline{\chi}\gamma^\mu\chi Z'_\mu. \tag{7.3}$$

While some complete model may have relations between the couplings and masses of the dark sector particles, for the sake of illustration, in this case we take all masses and couplings to be independent parameters. For dark ISR through the process $\overline{\chi}\chi \to \overline{f}fZ'$, Eq. (7.3) yields an annihilation cross section of

$$\begin{aligned}\langle\sigma v\rangle_{\overline{\chi}\chi\to\overline{f}fZ'} &= \frac{g_{Z'}^2 m_\chi^2}{36\pi^3\Lambda^4}\times \\ &\Big\{4 + 24\rho^3(1+5\rho^2)\sqrt{1-\rho^2}\tan^{-1}\frac{\sqrt{1-\rho^2}}{\rho} \\ &- 27\rho^2 - 60\rho^4 + 83\rho^6 + 12\rho^4(10\rho^2-3)\ln\rho\Big\},\end{aligned} \tag{7.4}$$

where $\rho = m_{Z'}/2m_\chi$. We see that this process no longer has the helicity suppressed (m_f^2/m_χ^2) dependence. It also has no velocity suppression, and so is

s-wave. Furthermore, it scales $\propto O(1/\Lambda^4)$, i.e., the same order in Λ as the ff annihilation which scales as $\propto O(m_f^2/\Lambda^4)$. Lifting of helicity suppression via FSR or VIB radiation only occurs at higher order in $1/\Lambda$, with cross section scaling $\propto O(1/\Lambda^8)$.

7.4.3 Competition with $\chi\chi \to Z'Z'$

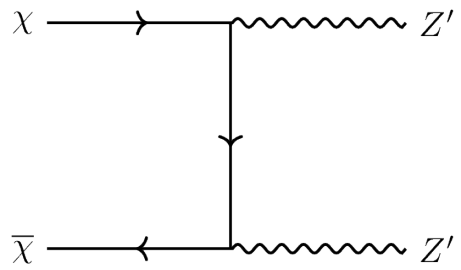

FIGURE 7.3: s-wave process for DM annihilation to dark vectors. Note there is also a contribution from the u-channel diagram.

The inclusion of an additional vector induces an additional two-body annihilation process, $\bar{\chi}\chi \to Z'Z'$. For any couplings of Z', this process is also s-wave, and so the dominant annihilation channel will be a competition between $\bar{\chi}\chi \to Z'Z'$ and $\bar{\chi}\chi \to \overline{f}fZ'$, and depending on the region of parameter space, either of these processes may dominate. The annihilation cross section for $\bar{\chi}\chi \to Z'Z'$ is given by

$$\langle \sigma v \rangle_{\overline{\chi}\chi \to Z'Z'} = \frac{g_{Z'}^4 \left(1 - 4\rho^2\right)^{\frac{3}{2}}}{16\pi m_\chi^2 (1 - 2\rho^2)^2}, \tag{7.5}$$

where again $\rho = m_{Z'}/2m_\chi$.

Figure 7.2 displays the annihilation cross sections for both processes, demonstrating the region of parameter space where either process may be the dominant annihilation channel. We show both processes for varying $g_{Z'}$ coupling. In the case that the $g_{Z'}$ coupling is smaller, the two powers of the DM coupling in the $Z'ff$ cross section can more easily dominate over the four powers in $Z'Z'$. As the coupling becomes larger, $Z'Z'$ dominates for more of parameter space. If the Z' is particularly heavy, the dark ISR process can also dominate over $Z'Z'$ due to kinematic constraints.

7.5 Lifting p-wave suppression in $S \otimes S$ interactions

In this section, we demonstrate how p-wave suppression can be lifted through dark pseudoscalar ISR, in the case of Lorentz structures $\Gamma_\chi \otimes \Gamma_f = S \otimes S$. Such a structure is possible for both Majorana and Dirac DM. We will also discuss any new competing annihilation processes.

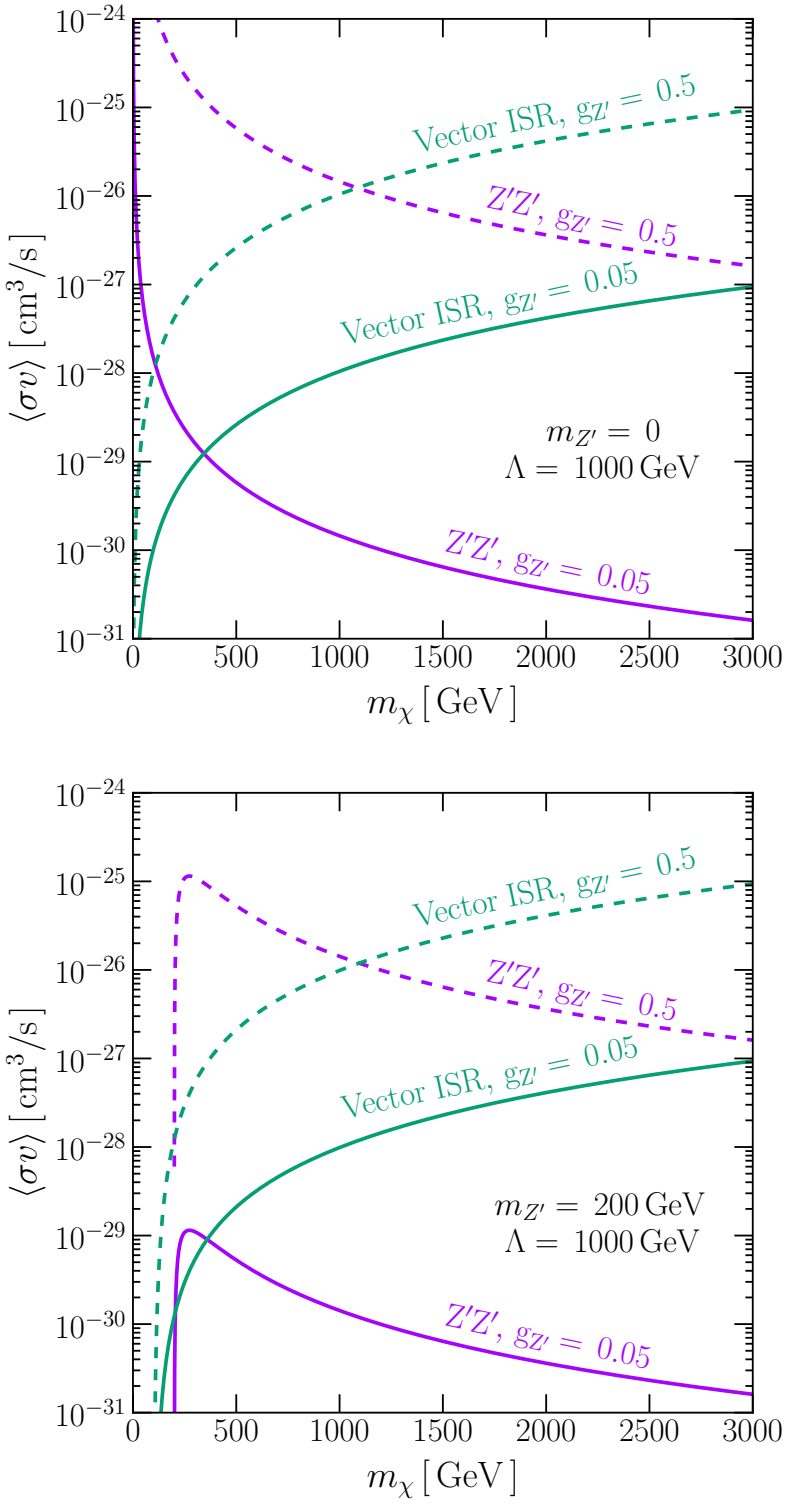

FIGURE 7.2: Comparison of s-wave cross sections for dark vector ISR process (green) and 2-body $Z'Z'$ (purple), for $m_{Z'}$ and Λ as labeled and couplings as stated. Note differing axes, with largest value of m_χ corresponding to maximum perturbative value of $\sqrt{g_\chi g_f} \sim \sqrt{4\pi}$ for EFT mediator.

7.5.1 p-wave suppressed $\chi\chi \to \overline{f}f$

For Lorentz structures $\Gamma_\chi \otimes \Gamma_f = S \otimes S$, the lowest order four-fermi operator, without any higher order corrections, is

$$\mathcal{L}_{\text{int}} \supset \frac{1}{\Lambda^2}(\overline{\chi}\chi)(\overline{f}f), \tag{7.6}$$

where χ is a fermionic DM candidate, f are SM fermions and Λ is the cutoff scale for new physics, representing a heavy field which has been integrated out.

The operator in Eq. (7.6) yields a p-wave suppressed DM annihilation cross section for $\overline{\chi}\chi \to \overline{f}f$,

$$\sigma v = \frac{v^2 m_\chi^2 \left(1 - m_f^2/m_\chi^2\right)^{3/2}}{8\pi\Lambda^4}, \tag{7.7}$$

which in the limit $m_f \to 0$ is

$$\sigma v = \frac{v^2 m_\chi^2}{8\pi\Lambda^4}. \tag{7.8}$$

The v^2 prefactor shows us that this is clearly a p-wave suppressed process. We now explicitly show that for such an operator, including dark pseudoscalar radiation lifts this suppression, and the dominant s-wave process can be $\overline{\chi}\chi \to f\overline{f}\phi$.

7.5.2 Dark pseudoscalar ISR, $\chi\chi \to ff\phi$

We consider a minimal setup with the EFT operator and a coupling g_ϕ of DM to a new real scalar ϕ, as:

$$\mathcal{L}_{\text{int}} \supset \frac{1}{\Lambda^2}(\overline{\chi}\chi)(\overline{f}f) + i\, g_\phi \phi \overline{\chi}\gamma_5\chi \tag{7.9}$$

where Λ is the new physics scale. While some complete model may have relations between the couplings and masses of the dark sector particles, for the sake of illustration, in this case we take all masses and couplings to be independent parameters. For dark ISR through the process $\overline{\chi}\chi \to \overline{f}f\phi$, Eq. (7.9) yields an annihilation cross section of

$$\begin{aligned}\langle\sigma v\rangle_{\overline{\chi}\chi\to\overline{f}f\phi} = {} & \frac{g_\phi^2 m_\chi^2}{48\pi^3\Lambda^4}\times \\ & \Big\{1 + 24\rho^3\sqrt{1-\rho^2}(5\rho^2-2)\tan^{-1}\frac{\sqrt{1-\rho^2}}{\rho} \\ & + 21\rho^2 - 105\rho^4 + 83\rho^6 + 12\rho^2(1 - 9\rho^2 + 10\rho^4)\ln\rho\Big\},\end{aligned} \tag{7.10}$$

where $\rho = m_\phi/2m_\chi$. We see that this process no longer has the velocity suppression term, and so is s-wave.

7.5.3 Competition with $\chi\chi \to \phi\phi\phi$

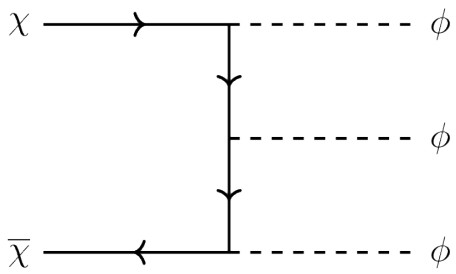

FIGURE 7.4: s-wave process for DM annihilation to pseudoscalars.

Unlike the vector radiation case, there is no additional s-wave $2 \to 2$ process induced for spin-0 fields. The $\phi\phi$ pseudoscalar final state is p-wave suppressed. In the limit $m_\phi \ll m_\chi$, the p-wave suppressed cross section for $\chi\chi \to \phi\phi$ is

$$\sigma v_{\chi\chi\to\phi\phi} \simeq \frac{g_\phi^4 v^2}{384\pi m_\chi^2}, \tag{7.11}$$

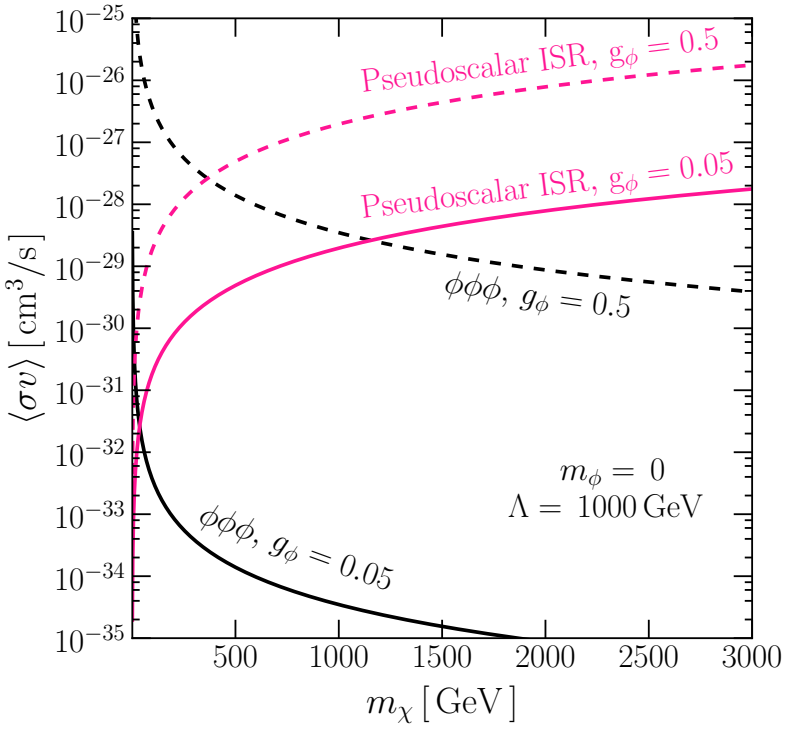

FIGURE 7.5: Comparison of s-wave cross sections for pseudoscalar ISR process (pink) and 3-body $\phi\phi\phi$ process (black) for $m_\phi = 0$ and $\Lambda = 1000$ GeV.

Instead, there can be competition from a $\phi\phi\phi$ final state, where an s-wave process is induced for pseudoscalar radiation [270], as shown in Fig. 7.4. We find

that the cross section for $\bar{\chi}\chi \to \phi\phi\phi$ is

$$\langle \sigma v \rangle_{\chi\chi\to\phi\phi\phi} = \int dx_2 \int dx_1 \frac{g_\phi^6}{2^5 3! \pi^3} \times \frac{\left(1 + 4x_1^2 - 4x_1(1-x_2) - 4x_2 + 4x_2^2 + 2\rho^2 - 3\rho^4\right)^2}{8m_\chi^2 \, (x_1 - \rho^2)^2 (x_2 - \rho^2)^2 (1 - x_1 - x_2 - \rho^2)^2}. \tag{7.12}$$

The cross section can be expressed in a compact form when ϕ is massless,

$$\langle \sigma v \rangle_{\chi\chi\to\phi\phi\phi} = \frac{g_\phi^6 (7\pi^2 - 60)}{1536\pi^3 m_\chi^2} \, . \tag{7.13}$$

Figure 7.5 displays the annihilation cross sections for the pseudoscalar ISR and three-body pseudoscalar process, demonstrating potential regions of parameter space where particular process may be the dominant annihilation channel. The pseudoscalar ISR process is particularly promising, with a larger rate than the three-body pseudoscalar process for much of the parameter space.

7.6 Conclusion

An observation of an unexplained excess flux of SM particles in the astrophysical sky can be interpreted as a DM signal. To probe the potential nature of DM, it is important to know such processes may dominate, providing the largest contribution to any potential signal, or providing the strongest constraint on DM. In this chapter, for the first time, we have explored the possibility of lifting helicity or p-wave suppression in DM annihilation processes with dark ISR, which can lead to a dominant DM signal.

We found that dark ISR can lift suppression for several different radiation types, and interaction types of the DM and mediator. For fermionic DM, the most possibilities for dominant dark ISR are provided by a dark vector: radiating a vector lifts the suppression in DM annihilation for several Lorentz structures — $S \otimes S$, $A \otimes A$, and $A \otimes V$. Radiating an axial vector lifts suppression in $A \otimes A$ and $A \otimes V$ annihilation processes. Radiating a scalar fails to lift any suppression of the annihilation cross section. Radiating a pseudo-scalar, however, can make a process with a $S \otimes S$ structure s-wave.

A nice feature of dark ISR over SM VIB or FSR, is that when s-wave, the annihilation rate proceeds scales as $\langle \sigma v \rangle_{\rm ISR} \propto O(1/\Lambda^4)$, i.e., the same order in Λ as the 2-body annihilation $\chi\chi \to f\bar{f}$ which scales as $\langle \sigma v \rangle \propto O(m_f^2/\Lambda^4)$. In comparison, the lifting of helicity suppressions via FSR or VIB radiation only occurs at higher order in $1/\Lambda$, with cross section scaling as $\langle \sigma v \rangle_{\rm FSR,\,ISR} \propto O(1/\Lambda^8)$.

When introducing new fields for dark ISR, we also found that additional processes can be induced with the new fields, which may compete with the dark ISR processes. In particular, in the case of dark vector or axial-vector ISR,

the additional process $\chi\chi \to Z'Z'$ is s-wave. For scalar of pseudoscalar ISR, there is no equivalent s-wave process, but for pseudoscalar ISR, the three body $\chi\chi \to \phi\phi\phi$ annihilation process is s-wave and can be competitive in some regions of parameter space. As such, the interplay of several process should be considered.

Similar to the visible sector, the DM may very well have multiple field content, with more than one dark-visible sector mediator. In such a scenario, it is important not to neglect the contributions to DM annihilation from dark radiative corrections, as they can be the dominant process, as we have shown in this work. Such observations will be important for setting exclusion limits and determining discovery potential on the nature of DM in the future.

Chapter 8

Powerful Solar Signatures of Long-Lived Dark Mediators

Dark matter capture and annihilation in the Sun can produce detectable high-energy neutrinos, providing a probe of the dark matter-proton scattering cross section. We consider the case when annihilation proceeds via long-lived dark mediators, which allows gamma rays to escape the Sun and reduces the attenuation of neutrinos. For gamma rays, there are exciting new opportunities, due to detailed measurements GeV solar gamma rays with Fermi, and unprecedented sensitivities in the TeV range with HAWC and LHAASO. For neutrinos, the enhanced flux, particularly at higher energies (~TeV), allows a more sensitive dark matter search with IceCube. We show that these search channels can be extremely powerful, potentially improving sensitivity to the dark matter spin-dependent scattering cross section by several orders of magnitude relative to present searches for high-energy solar neutrinos, as well as direct detection experiments.

This chapter is based on the publication: *R. K. Leane, K. C.Y. Ng, J.F. Beacom, "Powerful Solar Signatures of Long-Lived Dark Mediators", [arXiv:1703.04629 [astro-ph.HE]].* [344]

8.1 Introduction

There is overwhelming evidence that dark matter (DM) is the dominant form of matter in the universe [21]. However, across experimental tests of its annihilation, scattering, and production processes, no details of its fundamental nature have yet been revealed. For models with unsuppressed spin-independent scattering interactions, there are severe bounds on the properties of DM from direct detection experiments, such as LUX [118, 119] and PandaX-II [120]. If instead there are only spin-dependent interactions, a much larger part of the parameter space remains uninvestigated, with best limits currently set by LUX [121] and PandaX-II [122] for neutron scattering, and PICO-60 C_3F_8 [345] for proton scattering.

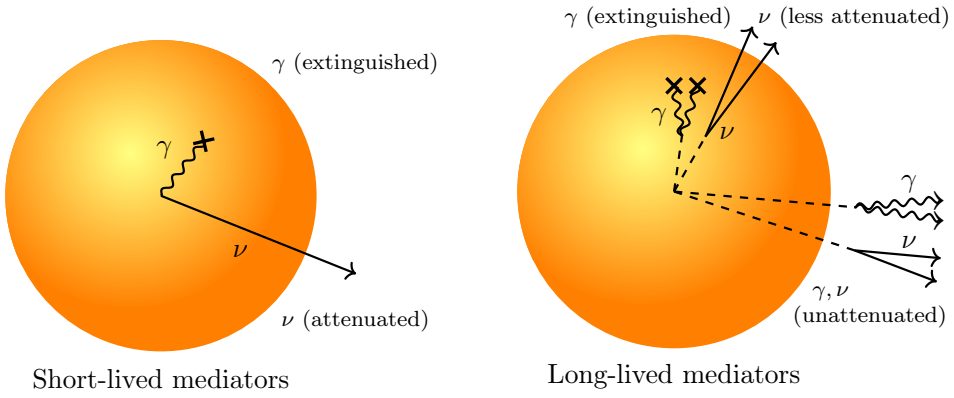

FIGURE 8.1: **Left:** Short-lived mediator scenario (usual case). Only neutrinos can escape the Sun and they are attenuated. **Right:** Long-lived dark mediator scenario. Gamma rays can escape, and neutrinos are less attenuated.

The Sun is an alternate probe, as it can gravitationally capture DM [346–349], after DM loses energy through scattering with solar nucleons. If DM is captured, it must have scattering interactions that force further energy loss and accumulation in the solar core, leading to annihilation to Standard Model (SM) particles. Measurement of these SM particles provides insight to the nature of DM. However, in order to escape the Sun for detection, the particles need to be very weakly interacting. Amongst the potential SM particles produced in the solar core, only neutrinos can escape. Even then, there is significant attenuation for neutrinos above about 100 GeV.

As DM has not yet been found, more general theoretical scenarios should be considered. A fairly minimal scenario consists of a DM candidate, along with a new particle to mediate interactions between the dark and visible sectors. An interesting possibility is that, as a consequence of particular model properties, the mediator may have a long decay lifetime. These 'long-lived dark mediators' are well motivated, and include examples such as the dark photon [350–353], dark Higgs [354], and many supersymmetric particles [355]. There is also wide interest in searches at current [297, 356–359] and future colliders [360].

Figure 8.1 illustrates how the long-lived mediator setup can strongly affect solar DM detection: the mediator can decay outside of the solar core, producing otherwise attenuated or lost solar DM signals [275, 276, 280, 300, 354, 361–370]. While it is known that prospects are improved in this scenario, investigations to date are not complete on considering the full range of data and models.

In this chapter, we examine the prospects for new gamma-ray and neutrino experiments in a model-independent framework. For gamma rays, this is particularly pertinent with new detailed measurements of the Sun in the GeV range with

the Fermi Large Area Telescope (Fermi-LAT) [371, 372], as well as unprecedented sensitivity to TeV gamma rays with upcoming analyses from the High Altitude Water Cherenkov (HAWC) Observatory [142], which began operating in 2015, and the Large High Altitude Air Shower Observatory (LHAASO) [373], which is under construction and expected to begin operating in 2020. For neutrinos, this is particularly pertinent for the multi-TeV window at IceCube [148], and future neutrino telescopes such as KM3NeT [152]. We demonstrate these telescopes and observatories can provide DM probes orders of magnitude stronger than both current searches for high-energy solar neutrinos, and direct detection experiments.

We define the sensitivity to such scenarios in the following ways: On the theory side, we consider optimal cases, for example where the mediators decay just outside the Sun. On the experimental side, we are more conservative, requiring that the new signals be as large as measurements, not just their uncertainties. Accordingly, we aim for a precision of a factor of a few, neglecting some smaller effects. This optimal scenario will demonstrate the full power of long-lived mediators for solar DM searches. Our sensitivity can be mapped to the parameter spaces of any particular model realizations, together with any other constraints, which will be a subset of the space considered. Therefore, we focus on the new signatures and the experimental sensitivity.

In Sec. 8.2, we review the processes for DM capture and annihilation in the Sun. In Sec. 8.3, we discuss the modifications for the long-lived mediator scenario. We then demonstrate the power of gamma-ray signals with Fermi-LAT, HAWC, and LHAASO in Sec. 8.4, and for neutrinos with IceCube and KM3NeT in Sec. 8.5. In Sec. 8.6, we discuss interpretations of our results in the context of popular models. Finally, other constraints are discussed in Sec. 8.7 before concluding in Sec. 8.8.

8.2 Dark Matter Solar Capture and Annihilation

The usual scenario for DM capture and annihilation in the Sun has been well studied [346–349, 354, 367, 374–379]. DM is gravitationally captured by the Sun if it loses sufficient energy after scattering with solar nuclei. As the captured DM accumulates in the Sun's core, there are more DM particles available to power DM annihilation. However, annihilation depletes the DM supplied by capture. Therefore, the total number of DM particles in the solar core is determined by an interplay of the capture rate $\Gamma_{\rm cap}$ and annihilation rate $\Gamma_{\rm ann}$. Equilibrium is reached if the equilibrium timescale is less than the age of the Sun.

In the regime that DM self-interactions [380] are not relevant, the relation of these processes and the number of DM particles N_χ in the Sun at time t is given by

$$\frac{d}{dt}N_\chi = \Gamma_{\rm cap} - C_{\rm ann}N_\chi^2\,, \tag{8.1}$$

where $\Gamma_{\rm cap}$ is the DM capture rate and $C_{\rm ann}$ is a coefficient that describes the annihilation processes. The number of DM particles in the Sun rapidly approaches equilibrium when $t > t_{\rm equil} = 1/\sqrt{\Gamma_{\rm cap} C_{\rm ann}}$. We focus on DM masses above 4 GeV, where evaporation is irrelevant [381, 382]. Equilibrium thus depends on sufficiently large scattering and annihilation cross sections. For the scenarios considered here, both conditions can be met [383]. Therefore, a simple relation between annihilation rate and capture rate is obtained,

$$\Gamma_{\rm ann} = \frac{1}{2} C_{\rm ann} N_\chi^2 = \frac{1}{2} \Gamma_{\rm cap}, \tag{8.2}$$

independent of the DM annihilation cross section.

8.3 Long-Lived Dark Mediator Scenario

8.3.1 Opportunities and Framework

The energy flux of DM annihilation products in the Sun is enormous. For example, in the case that 100 GeV or 1 TeV DM with spin-dependent scattering cross sections of $\sim 10^{-40}\,{\rm cm}^2$ (capture rates of $10^{22}\,{\rm s}^{-1}$ and $10^{20}\,{\rm s}^{-1}$, respectively) annihilates directly to gamma rays, the energy fluxes are

$$E_\gamma^2 \frac{d\Phi_\gamma}{dE_\gamma} \sim 10^{-4}\,{\rm GeV\,cm^{-2}\,s^{-1}} \quad m_\chi = 100\,{\rm GeV}, \tag{8.3a}$$

$$E_\gamma^2 \frac{d\Phi_\gamma}{dE_\gamma} \sim 10^{-5}\,{\rm GeV\,cm^{-2}\,s^{-1}} \qquad m_\chi = 1\,{\rm TeV}, \tag{8.3b}$$

where we have assumed that the gamma-ray spectrum is measured in bins one decade wide (this is ∼10 times too conservative for Fermi, but appropriate for HAWC). The best experimental sensitivity to 100 GeV solar gamma rays comes from Fermi-LAT, with sensitivity

$$E_\gamma^2 \frac{d\Phi_\gamma}{dE_\gamma} \sim 10^{-8}\,{\rm GeV\,cm^{-2}\,s^{-1}}, \tag{8.4}$$

while the best sensitivity to 1 TeV gamma rays is from HAWC,

$$E_\gamma^2 \frac{d\Phi_\gamma}{dE_\gamma} \sim 10^{-9}\,{\rm GeV\,cm^{-2}\,s^{-1}}. \tag{8.5}$$

In each case, the annihilation flux is in excess of sensitivity by a factor of 10^4. Of course, in the usual scenario, the difficulty is that it is not possible to observe these promptly extinguished gamma rays. This is why the long-lived dark mediator scenario is so compelling — gamma rays can escape the solar core, providing a probe of the immense annihilation flux.

For solar gamma rays [384], the sensitivity to long-lived mediators from these experiments has not yet been fully explored. For solar neutrinos, limits exist for short-lived mediators [148], but the improvements from long-lived mediators through less absorption of neutrinos [364] have also not been fully quantified.

The energy flux from DM annihilation in the Sun is

$$E^2\frac{d\Phi}{dE} = \frac{\Gamma_{\rm ann}}{4\pi D_\oplus^2} \times E^2\frac{dN}{dE} \times {\rm Br}({\rm Y} \to {\rm SM}) \times P_{\rm surv}, \tag{8.6}$$

where $D_\oplus = 1$ A.U. is the average distance between the Sun and the Earth, E^2dN/dE is the spectrum per DM annihilation, Br(Y $\to$ SM) is the branching fraction of the mediator Y to SM particles, and $P_{\rm surv}$ is the probability of the signal surviving to reach the detector, which includes factors such as attenuation and mediator decay length. While this factor diminishes the flux, the cost to the total flux pales in comparison to the net gain in exploiting the large annihilation flux in the Sun. In the standard scenario, $P_{\rm surv} = 0$ for gamma rays, and is exponentially suppressed for neutrinos with energies above about 100 GeV.

In the following subsections, assumptions and properties of long-lived mediators relevant to each of the terms in Eq. (8.6) are described.

8.3.2 Annihilation Rate

After equilibrium is reached, the annihilation rate of DM in the Sun, $\Gamma_{\rm ann}$, is related to the capture rate as per Eq. (8.2). We use DarkSUSY [385] to compute the annihilation rate $\Gamma_{\rm ann}$ for a given DM scattering cross section and mass. The capture rate scales $\propto m_\chi^{-1}$ up to a few 10 GeV, which follows the local DM number density. Above a few 100 GeV, it scales $\propto m_\chi^{-2}$, due to kinematic suppression of the energy loss [117, 386, 387].

8.3.3 Branching Fractions

We assume a 100% branching fraction of the mediator to each final state in turn, which is the optimal case. If only one final state produces observable signals, it is straightforward to scale our result with the branching fraction. The effects of considering multiple final states in the context of specific models are discussed in Sec. 8.6.

8.3.4 Energy Spectra

DM annihilates to long-lived mediators as

$$\chi\chi \to YY \to 2\,(\,{\rm SM} + \overline{\rm SM}\,) \to ...\gamma, \nu... \tag{8.7}$$

where the mediator Y decays to two SM particles, which consequently can decay into or radiate gamma rays or neutrinos.

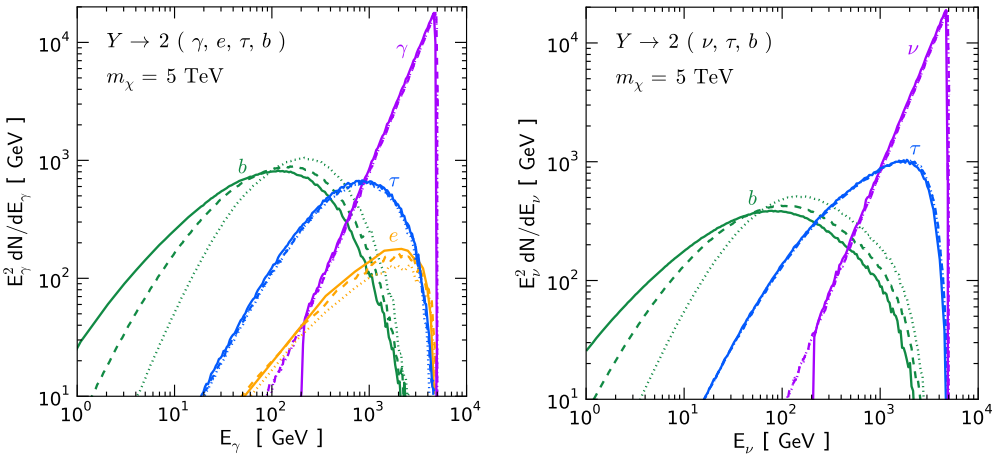

FIGURE 8.2: **Left:** Gamma-ray spectra $E_\gamma^2 dN/dE_\gamma$ for various final states, per DM annihilation, with mediator masses $m_Y = 2$ TeV (solid), $m_Y = 200$ GeV (dashed), and $m_Y = 20$ GeV (dotted). **Right:** Neutrino spectra.

We use PYTHIA [299] to generate the neutrino and gamma-ray energy spectra, where an effective resonance with energy $2m_\chi$ decays to two mediators. Depending on the final state particles, gamma rays or neutrinos can arise from direct decay to 4γ or 4ν, electroweak bremsstrahlung, or consequent particle decays. Our simulations take into account all these possibilities where relevant, and are the fully decayed spectra in vacuum.

Figure 8.2 shows that the energy spectra from DM annihilation are approximately the same for processes that are topologically identical. That is, for a given DM mass to a given n-body final state, approximately the same energy spectra is obtained regardless of the fundamental properties of the mediator, such as its mass (provided it is kinematically allowed) and spin (provided it is allowed by spin-statistics). This is because the daughters inherit the boost of the mediator. The mediator boost is m_χ/m_Y, and daughter particles have energies that are fixed fractions of m_Y, so m_Y cancels. However, this can vary for gamma rays and neutrinos made through pions. In the latter case, there are variable numbers of pions, with different fractions of energy going to gamma rays, etc., so there can be some variance. This is observed in particular for the different mediator mass and the $4b$ final state, owing to more hadronic cascade decays being available with higher mediator mass and consequently softening the spectra (this behavior for gamma-ray spectra is consistent with Ref. [272]). For direct decays to gamma rays and neutrinos, the low-energy bound of the box spectra depends on the mediator mass [132], but this is only significant if the mediator is not sufficiently boosted. Also note that for mediator decay to gamma rays, some lower energy gamma rays can be produced from radiated electrons. However, these small differences do not provide any appreciable differences to our results, which predominantly arise

from the high energy part of the spectrum.

8.3.5 Optimal Signal Conditions

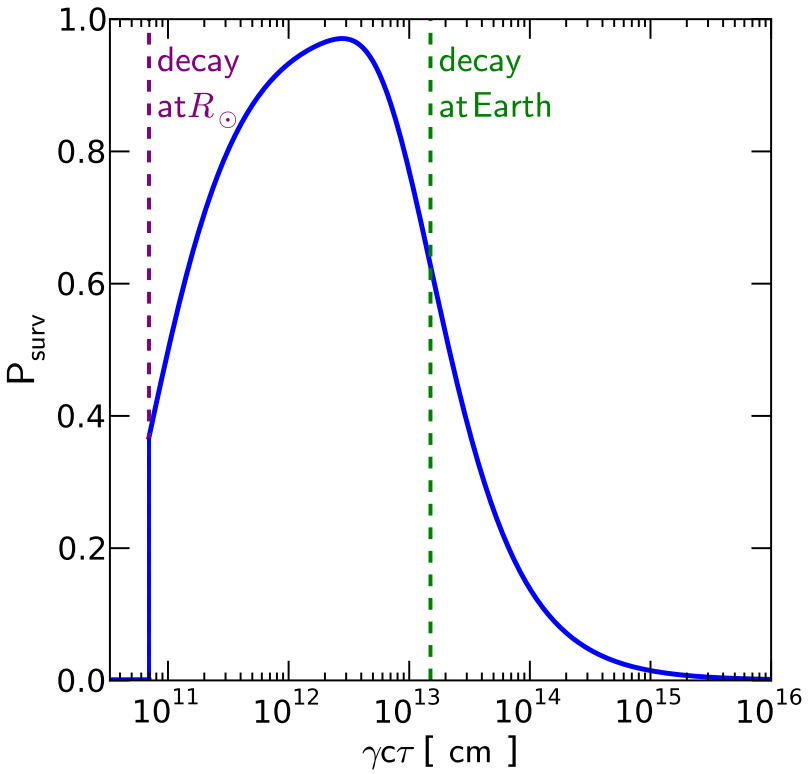

FIGURE 8.3: Probability of gamma rays from the mediator surviving and reaching a detector at Earth, for varying mediator properties. This only takes into account decay exponentials, and assumes zero signal if $\gamma c\tau < R_\odot$. In the standard scenario, $\gamma c\tau \sim 0$, and the probability is exponentially suppressed for neutrinos due to parent-particle and neutrino absorption in the solar medium.

For decay products such as gamma rays to escape the Sun, it is required that the mediator Y has a sufficiently long lifetime τ or sufficently large boost factor $\gamma = m_\chi/m_Y$, leading to a decay length L that exceeds the radius of the Sun, $R_\odot$, as

$$L = \gamma\beta\tau \simeq \gamma c\tau > R_\odot, \tag{8.8}$$

where β is the speed of the mediator and c is the speed of light. While the lifetime τ is related to the mediator mass m_Y, we just ensure combinations of the parameters are allowed by current constraints.

The probability of the signal surviving to reach the detector, P_{surv}, provided the decay products escape the Sun, is

$$P_{\text{surv}} = e^{-R_\odot/\gamma c\tau} - e^{-D_\oplus/\gamma c\tau}. \tag{8.9}$$

Figure 8.3 illustrates the survival probability for varying $\gamma c\tau$. In this work, we take $\gamma c\tau = R_\odot$. The probability is relatively insensitive to $\gamma c\tau$, as survival probability is changing only by a factor ~ 2. For gamma rays, signal production is only possible if the mediator decays outside the Sun. For neutrinos, however, mediator decay inside the Sun provides a non-zero flux, but the signal is attenuated due to parent-particle and neutrino absorption. We assume mediators pass through Sun without attenuation, though such a feature is model-dependent.

We assume the signal strength only depends on $\gamma c\tau$. However, special scenarios can arise in some limiting cases. When $\gamma \gg 1$, the decay products are boosted and maintain a small opening angle. We focus on this case, where the Sun will appear to be a point source. When $\gamma c\tau \simeq R_\odot$ and $\gamma \sim 1$, mediators decay just outside the Sun and the Sun remains effectively a point source. However, when $R_\odot \ll \gamma c\tau < D_\oplus$ and $\gamma \sim 1$, the decay products would appear to be a halo around the Sun. Typically diffuse-emission sensitivity is worse than that of point sources, and the analysis is more involved [371, 372, 388]. Thus we do not consider this case. Lastly, the Sun can absorb some of the gamma rays produced by the mediators. This only occurs when the decay length is small and the mediators have a boost component away from the observer. For typical mediator masses and boost factors, only the low-energy part of the spectrum is affected; hence our results are not affected.

Therefore, our premise assumes a high mediator boost that requires the mediator to be sufficiently lighter than the DM mass. This is easily obtained across a range of DM masses for direct decays to gamma rays, neutrinos and electrons. For heavier final states such as taus and b-quarks, larger DM masses would be required to produce a highly boosted mediator that could kinematically produce such final states. As there is not a hard cutoff for such criteria, we show sensitivity of gamma rays and neutrinos for all DM masses that could produce such final states, even if the mediator would not be highly boosted, but potential weakening of sensitivity due to such directional loss in such regions should be kept in mind.

Lastly, we neglect the extra gamma-ray component from secondary electrons inverse-Compton scattering with the ambient photons [389, 390]. This component is heavily suppressed due to the anisotropic solar photon distribution [391, 392]. We also note that the gamma-ray contribution from DM annihilation in the solar WIMP halo outside the Sun is negligible [393].

8.4 High-Energy Solar Gamma Rays

In this section we discuss our procedure and results for long-lived dark mediators using solar gamma rays with Fermi-LAT, HAWC, and LHAASO.

8.4.1 Procedure

Fermi-LAT analyses provide the best measurements of solar gamma rays. In 2011, Fermi detected 0.1–10 GeV solar gamma rays, measuring an energy flux $\sim 10^{-8}$ GeV cm^{-2} s^{-1} [371]. Since then, Fermi has collected more data and improved the data quality. This updated Fermi data are analyzed in Ref. [372], where the results are extended to 100 GeV solar gamma rays, measuring energy fluxes of $\sim 10^{-8}$ GeV cm^{-2} s^{-1}. Together, these analyses provide much improved observational studies of solar gamma rays, which have not been fully explored in the context of long-lived mediators. For higher energy gamma rays ($\sim 10^2 - 10^5$ GeV), HAWC and LHAASO could be used to observe the Sun [372, 388], but this has not yet been exploited.

In this work we demonstrate that current Fermi-LAT analyses can be used to set strong limits through solar gamma rays from long-lived mediators. We also demonstrate that upcoming analyses from HAWC [142] and LHAASO [373] are extremely sensitive to solar gamma rays from long-lived mediators.

Figure 8.4 illustrates how our new limits are obtained from existing Fermi-LAT data. For a fixed branching fraction and $P_{\rm surv}$, the spectra $E_\gamma^2 dN/dE_\gamma$ generated are scaled with arbitrary increasing annihilation rate $\Gamma_{\rm ann}$. Once the energy flux exceeds the sensitivity of Fermi-LAT in any energy bin, an upper limit on the value of $\Gamma_{\rm ann}$ from Fermi-LAT is obtained. Future HAWC and LHAASO analyses will also have strong sensitivity to this scenario, as we are the first to show.

Figure 8.5 illustrates our new limits (for Fermi-LAT) and our calculated sensitivities (for HAWC and LHAASO) to the DM scattering cross section using solar gamma rays, for mediator decay just outside the Sun ($L = \gamma c\tau = R_\odot$, implying $P_{\rm surv} \approx 0.4$). An upper limit on the annihilation rate implies an upper limit on the scattering cross section, which we obtain using DarkSUSY [385] as described in the previous section.

8.4.2 Discussion of Results

At high mass, the Fermi sensitivity weakens due to the scaling of the capture rate ($\propto m_\chi^{-2}$) and due to the peak of the spectrum moving out of its energy range. This is why the sensitivity limits for final states with harder spectra, such as direct decay to gamma rays, weaken faster than softer spectra, such as those from b-quarks. For the softer spectra, this also leads to Fermi being more sensitive than HAWC and LHAASO for some higher DM masses, even in the 1–10 TeV DM mass range. With HAWC and LHAASO, there is good sensitivity at high DM mass due to the increased energy range and flux sensitivity relative to Fermi.

The optimal long-lived mediator sensitivities with gamma rays shown in Fig. 8.5 are extremely powerful, outperforming the best spin-dependent direct detection limits from PICO by several orders of magnitude. Low DM masses are particularly promising with Fermi — in the optimal scenario the sensitivity in the

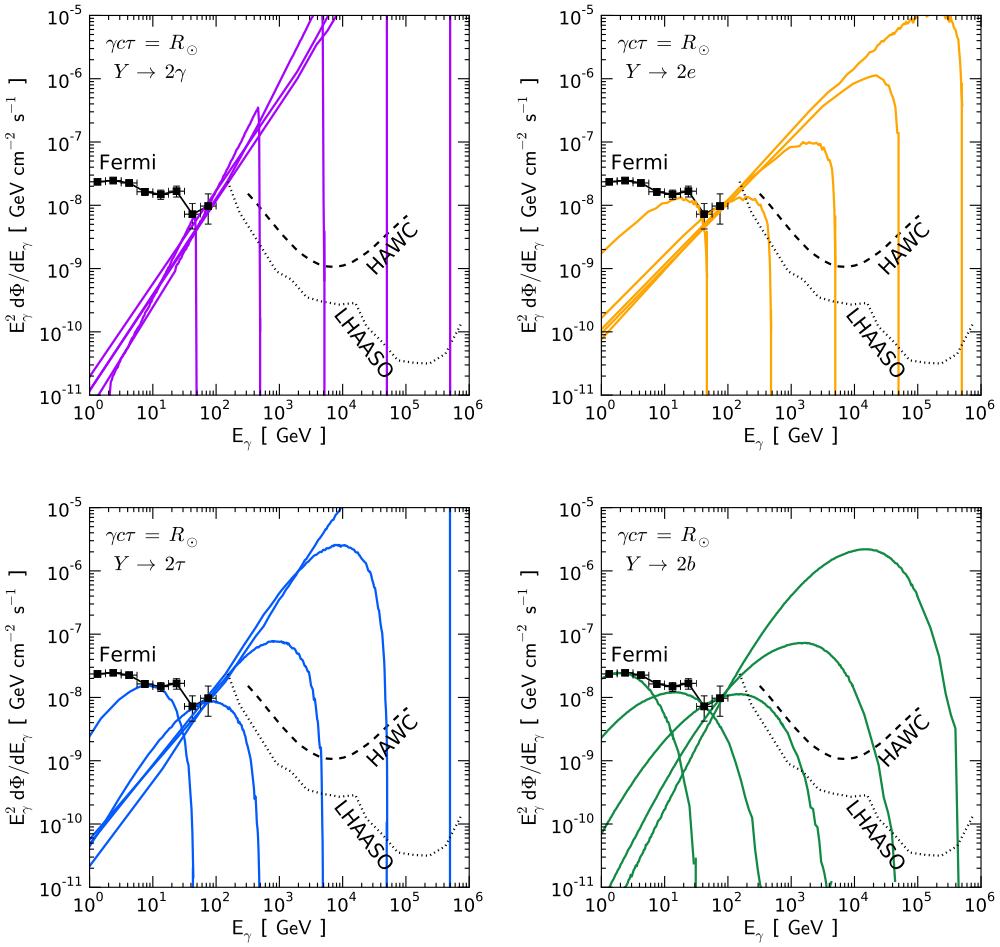

FIGURE 8.4: Estimates of presently allowed gamma-ray spectra from solar observations by Fermi-LAT, for final states as labeled and for DM masses of m_χ = 50, 500, 5000, 50000, 500000 GeV (left to right), with $\gamma c\tau = R_\odot$. The fluxes shown have been scaled by different annihilation rates for each mass and final state, such that they reach the sensitivity limit. HAWC and LHAASO do not yet provide constraints, but can do so soon.

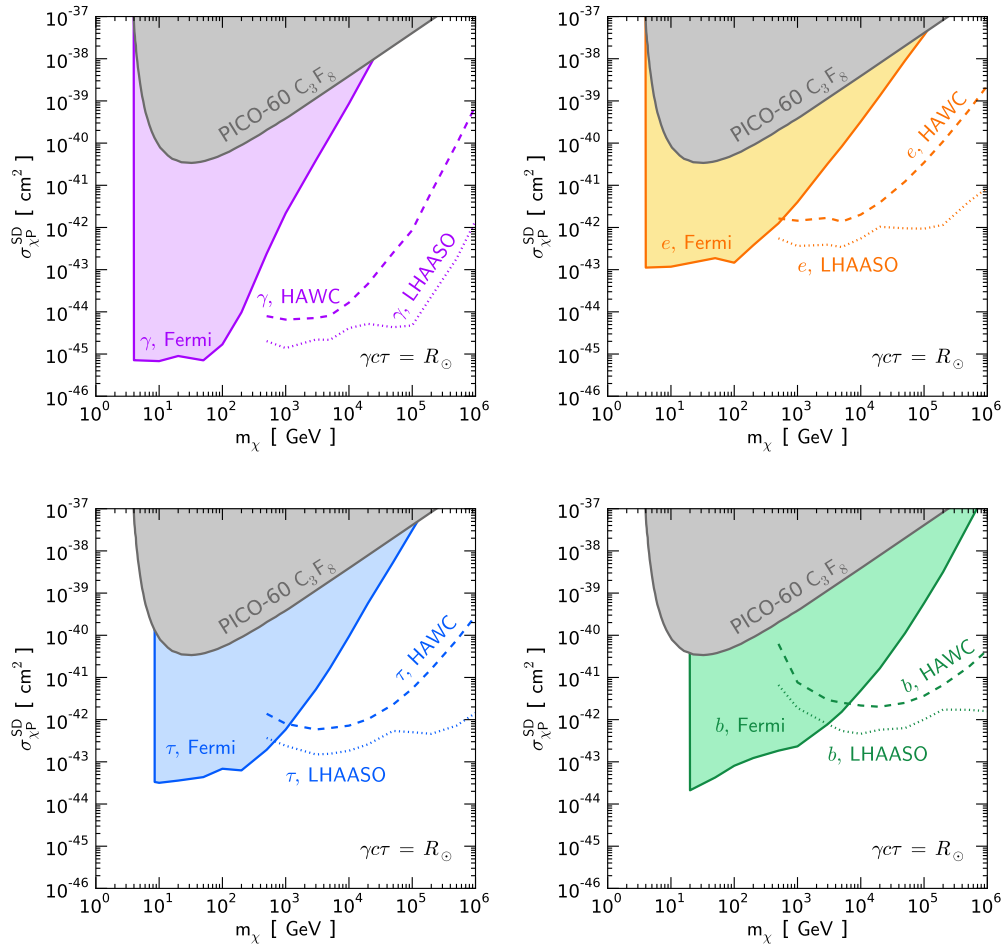

FIGURE 8.5: Optimal sensitivity for DM scattering cross sections from current and future solar gamma-ray observations, for DM in the Sun annihilating to pairs of long-lived mediators decaying to the particles labeled. Here the mediator decays just outside the Sun ($\gamma c\tau = R_\odot$). Our new limits from Fermi-LAT solar gamma-ray data are shown (shaded, solid), while our calculations of the estimated 1-year sensitivity from HAWC (dashed) and LHAASO (dotted) can be tested in future analyses. PICO-60 C_3F_8 [345] 90% C.L. limits are shown in gray.

$m_\chi \approx 20 - 100$ GeV region outperforms the best spin-dependent direct detection experiments by about six orders of magnitude. HAWC and LHAASO are similarly powerful at high DM masses.

Furthermore, for some final states the optimal sensitivity with solar gamma rays even outperforms the projected sensitivity of upcoming direct detection experiment DARWIN, which is predicted to be sensitive down to spin-dependent scattering cross sections of $\sigma_{\chi P}^{SD} \approx 10^{-43}$ cm^{-2} [394]. This means that the best probe of the DM spin-dependent scattering cross section in the near future may be from solar gamma rays, if the dark sector contains a long-lived dark mediator.

Again, it is important to note that these are the optimal sensitivities: we have assumed decay immediately outside the Sun and a 100% branching fraction to the particles detailed in the plots, and kept to an accuracy of a factor of a few. However, while there will certainly be factors that degrade the sensitivity, but they will certainly be less than the gain from allowing mediators to escape the Sun, which for gamma rays allows a non-zero flux, and for neutrinos lifts the exponential suppression of the flux due to attenuation in the Sun. Discussion of interpretation of these results in the context of some models is in Sec 8.6.

8.5 High-Energy Solar Neutrinos

In this section we discuss our method and results for long-lived dark mediators using high-energy neutrino observations with neutrino telescopes.

DM annihilations in the Sun produce neutrinos that could be detectable. In this case, muon neutrinos are the most relevant, as the final state muons retain much of the directionality, which is essential for suppressing the atmospheric neutrino background. Searches for high-energy neutrinos from the Sun with neutrino telescopes provide the strongest limits on the DM-proton spin-dependent scattering cross section [148, 150, 395]. A search has also been conducted by Antares for some specific long-lived mediator channels [151].

In models with long-lived mediators, the sensitivity is enhanced [364] compared to the case where neutrinos are promptly produced at the core of the Sun. These enhancements can be understood by two considerations:

(1) Less cooling of the secondaries. For dark matter annihilation in the Sun with short-lived mediators, high-energy neutrinos are produced inefficiently, as they come only from the rare particles, such as gauge bosons or heavy mesons, that decay before losing energy. (The more common particles, for example pions and kaons, lose energy and decay at rest, producing only low-energy neutrinos [386, 396].) However, if the mediators escape the Sun, the neutrinos from pions and kaons will be emitted at high energy, substantially increasing the flux.

(2) Less neutrino absorption from the solar matter. High-energy neutrinos (> 100 GeV) produced at the core of the Sun are exponentially suppressed due to absorption from the solar matter. If the mediators decay outside the core, beyond which the density falls exponentially, this suppression is lifted and the high-energy neutrino flux is greatly enhanced. This is especially important as neutrinos with higher energies are more detectable, due to increased cross section and decreased backgrounds.

These enhancements are especially significant for high-mass DM, where the secondary multiplicity is large and neutrino absorption is important. Therefore, we focus our discussion on large neutrino telescopes such as IceCube and KM3NeT. In any case, except for pure neutrino final states, the sensitivity to gamma rays (Sec. 8.4) is much stronger than that for neutrino detectors such as Super-K.

8.5.1 Procedure

We first consider the neutrino flux from DM annihilations through long-lived mediators. The muon neutrino flux at Earth is obtained from $(\nu_e, \nu_\mu, \nu_\tau)$ at production (8.3.4) multiplied with the weighting (0.27, 0.35, 0.38) due to mixing. For pure neutrino channel, we assume equal flavor ratio at production. The weighting assumes the neutrinos arrive as an incoherent mixture of mass eigenstates (mixing angles are obtained from Ref. [397]) due to vacuum mixing. We ignore the matter effect as we focus on mediators that decay outside the Sun. We also note that the oscillation length can approach 1 AU at ~ 10 TeV and ~ 1 PeV, which we ignore as we will integrate the spectrum over large energy bins. These are good approximations for most of the energy range that we consider, especially given that we aim for an accuracy of a factor of a few.

Figure 8.6 shows the muon neutrino fluxes where DM annihilates through long-lived mediators, $Y \to 2\tau$, with $P_{\rm surv} = 1$ (only in this figure) for easy comparison. We compare them to the muon neutrino flux from WimpSim [398], for $\chi\chi \to \tau\bar{\tau}$ at the center of the Sun (noted as the "short-lived" case).

With long-lived instead of short-lived mediators, the neutrino fluxes are larger due to less energy loss of neutrino-producing secondaries and less attenuation of the neutrinos. The spectra are also slightly softer, due to decaying into 4 final states instead of 2. While the short-lived cases are all exponentially attenuated above about 100 GeV, the long-lived cases have significantly higher flux at higher energies, which improves the sensitivity.

For comparison, in Fig. 8.6, we also show the atmospheric neutrino flux, which is the dominant background for solar DM searches. We use the all-sky averaged intensity from Ref. [399] from the South Pole, and use the parametric form in Ref. [400] to extrapolate to high energies, after matching the normalization. The

background flux is estimated by considering neutrinos within the $\nu - \mu$ opening angle, $\theta_{\nu\mu} \simeq 1^\circ \sqrt{E_\nu / 1\,\text{TeV}}$.

To estimate the sensitivity, we compute the muon spectrum from neutrino charge-current interactions using the described neutrino fluxes. The average muon energy, $\langle E_\mu \rangle$, is related the neutrino energy, E_ν, by $\langle E_\mu \rangle = E_\nu(1-y)$, where y is the average inelastic parameter [401, 402]. For simplicity, we assume $y = 0.4$ throughout our energy range of interest, and ignore the distribution of the final state muons and take $E_\mu = \langle E_\mu \rangle$.

The muons can be detected as entering muons, when the interactions occur outside the detector volume. Taking into account the energy loss and the simplified assumption above, the differential rate is [403, 404]

$$\frac{dN}{dE_\mu} \simeq \frac{N_A \rho A^\mu_{\text{eff}} T}{\rho\left(\alpha + \beta E_\mu\right)} \int_{\frac{E_\mu}{1-y}}^{\infty} dE_\nu \frac{d\Phi}{dE_\nu}(E_\nu)\sigma(E_\nu)\,, \tag{8.10}$$

where $d\Phi/dE_\nu$ is the neutrino flux, σ is the interaction cross section [401, 402], $N_A = 6.02 \times 10^{23}$ is the Avogadro number, $\rho \simeq 1\,\text{g}\,\text{cm}^{-3}$ is the density, A^μ_{eff} is the effective detecting area of muons, T is the exposure time of the detector, $\alpha = 2.0 \times 10^{-6}\,\text{TeV}\,\text{cm}^2\,\text{g}^{-1}$, and $\beta = 4.2 \times 10^{-6}\,\text{cm}^2\,\text{g}^{-1}$.

The muons can also be detected as starting muons, when the interactions occur inside the detector volume. The differential rate is

$$\frac{dN}{dE_\mu} \simeq N_A \rho V T \frac{1}{1-y}\left[\frac{d\Phi}{dE_\nu}(E_\nu)\sigma(E_\nu)\right]_{E_\nu = \frac{E_\mu}{(1-y)}}\,, \tag{8.11}$$

where V is the fiducial volume of the detector.

We consider an idealized gigaton scale detector, such as IceCube or KM3NeT, where $A^\mu_{\text{eff}} = 1\,\text{km}^2$, $V = 1\,\text{km}^3$. We take the exposure to be 0.5×317 days, matching Refs. [148, 395]. The factor of 0.5 comes from the fact that we only consider up-going muons, where the atmospheric muon background is greatly reduced. For upgoing events, neutrinos may be absorbed when they propagate through the Earth. At the South Pole, the optical depth barely reaches unity when the Sun is at the lowest point below the horizon (about 23°) for 1 PeV neutrinos [402]. For our purpose and the mass range we consider, we can therefore safely ignore Earth absorption. For a lower latitude detector, such as KM3NeT, this effect will be more important.

Figure 8.7 shows the muon spectra that can be detected, using the neutrino fluxes from Fig. 8.6. We note that the muon spectra for the short-lived cases start to be suppressed above about 100 GeV. This is important as neutrino telescopes typically do not have good muon energy resolutions below a TeV. The muon spectra are broader than the neutrino spectra because of the importance of entering muons, which lose energy outside the detector.

Finally, to estimate the sensitivity, we compute the number of signal and

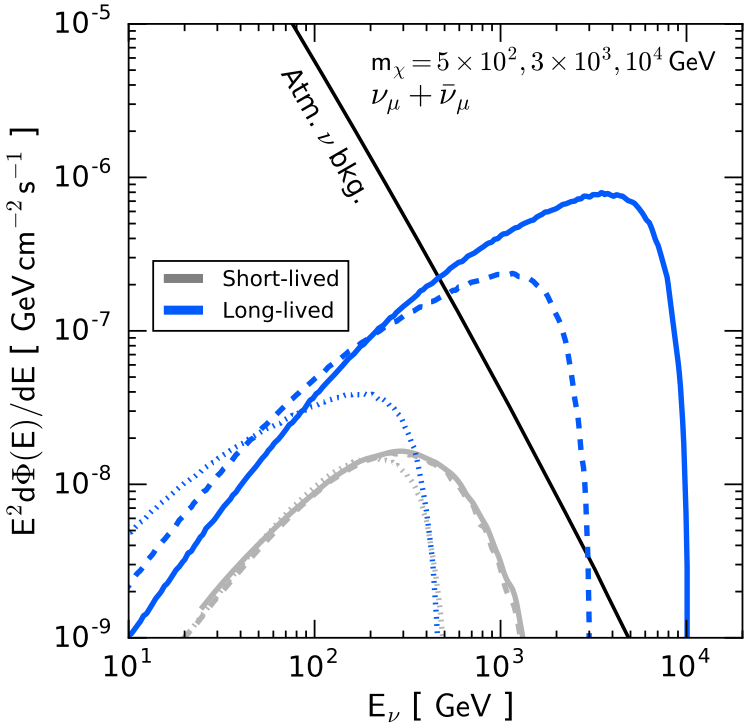

FIGURE 8.6: Neutrino flux from DM annihilating in the Sun to long-lived mediators with $Y \to 2\tau$ and $P_{\rm surv}$ is set to 1 for easy comparison (only in this figure). Also shown are the cases for short-lived mediators in the center of the Sun with $\chi\chi \to \tau\bar{\tau}$ and the atmospheric background within the neutrino–muon opening angle. The dotted, dashed, and solid lines correspond to DM masses $5\times10^2, 3\times10^3$, and 10^4 GeV, respectively. The annihilation rate is 10^{18} s^{-1} for all DM masses. The neutrino flux for long-lived cases is enhanced, especially for large m_χ.

background events in two energy bins. This is motivated by the realization that neutrino telescopes can estimate the muon energy above ~ 1 TeV, when the muon energy loss becomes radiative [405]. The sensitivity is determined when the signal counts reach the background counts in either energy bin, similar to our gamma-ray analysis. Here we also take $P_{\rm surv}$ to be ~ 0.4 ($\gamma c\tau = R_\odot$). There is some freedom in choosing the precise values for the energy bins. We find that the choice of $[10^{1.8}, 10^3]$ GeV and $[10^3, 10^6]$ GeV allows us to reproduce the IceCube limit [148] up to factors of a few for the short-lived cases. Our approach is simplifying: it is conservative to require the signal to be as high as the background; but this is compensated by the fact that we ignore the backgrounds from atmospheric muons, various detector effects, and reduction of signal efficiency from various data reductions [406]. However, for our purpose of the estimating the improved sensitivity from long-lived mediators relative to the "short-lived" case, this is sufficient.

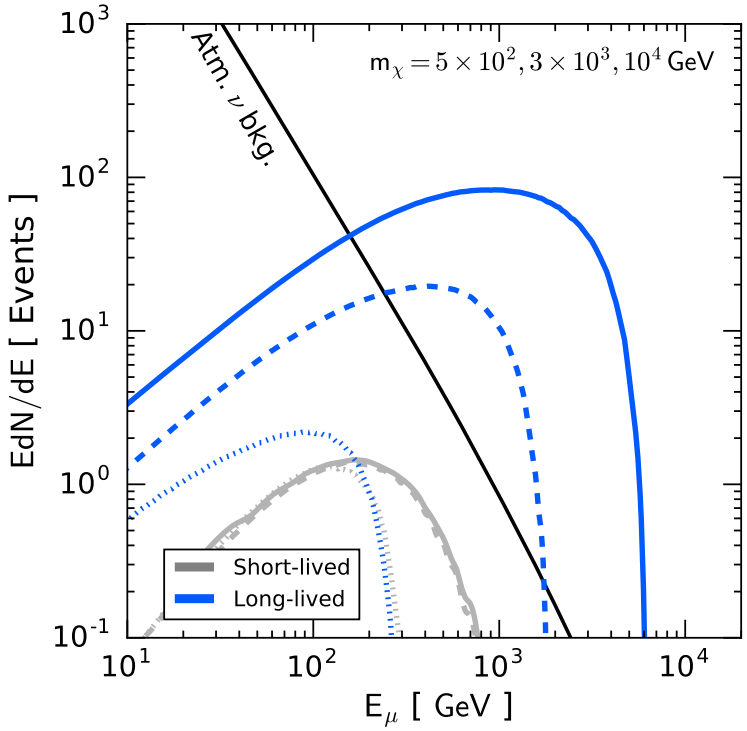

FIGURE 8.7: The muon spectrum (entering + starting) for a gigaton neutrino detector with 317 days of exposure, obtained with the neutrinos fluxes from Fig. 8.6. E_μ is defined as the energy of the muon when it first appears at the detector.

8.5.2 Discussion of Results

Figure 8.8 shows our estimated sensitivity compared with current constraints for standard WIMPs (short-lived case) from Super-K [150] and IceCube [148, 395]. We also show the result obtained by Antares [151], which searched for secluded DM via the process $\chi\chi \to YY \to \nu\bar{\nu}\nu\bar{\nu}$. We find that IceCube and KM3NeT can offer a significant improvement in sensitivity for the case of long-lived mediators, especially for high DM masses. For the τ final state, at lower masses, the long-lived mediator sensitivity is comparable to and even slightly weaker than the current limit. This is expected from softer spectra and the $P_{\rm surv}$ factor. Much of the improved sensitivity comes the high-energy bin > 1 TeV, which causes the kink near 1 TeV. Nominal WIMPs are not expected to produce such high-energy signals due to severe neutrino absorption in the Sun. Hence, a detection of a high-energy muon from the Sun could signal the existence of long-lived mediators in the dark sector.

It is interesting to note that the neutrino sensitivity at ~ 10 TeV is close to that of HAWC and LHAASO. Thus, in the case of a tentative detection by ground based gamma-ray telescopes, neutrino telescopes can be used to verify the result, and vice versa.

As mentioned above, for low mass DM (< 100 GeV), long-lived mediators do

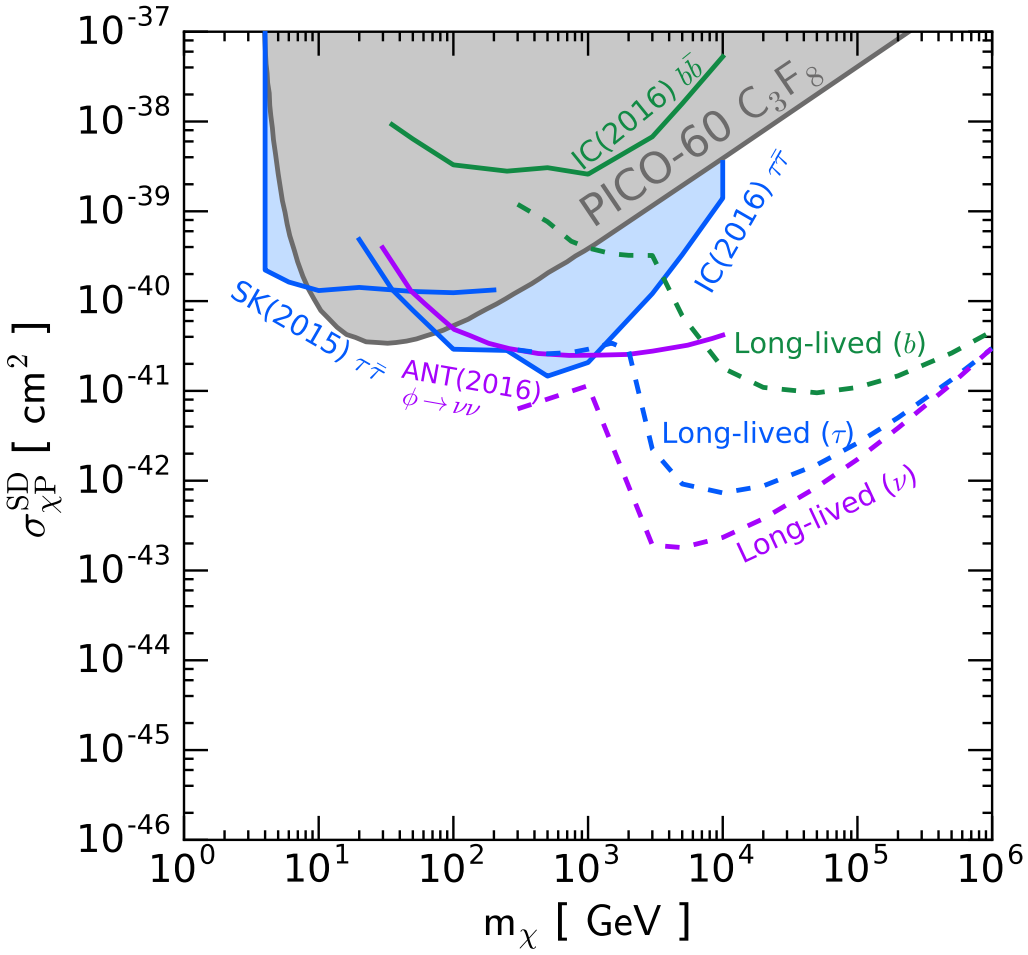

FIGURE 8.8: Constraints and sensitivities for the spin-dependent DM scattering cross section. The dashed lines are the sensitivities for DM in the Sun annihilating to pairs of long-lived mediators that decay to the particles labeled ($\gamma c\tau = R_\odot$). We also show current limits on short-lived mediators (solid lines with shaded region) from Super-K (SK), IceCube (IC), PICO-60 C_3F_8, as well as the limit from the search for secluded DM by Antares (ANT). This highlights the significantly improved sensitivity that could be achieved by long-lived mediators.

not offer much improvement to the sensitivity. In this case, gamma-ray observations by Fermi offer significantly larger potential discovery space.

8.6 Model Interpretation of Results

While the purpose of this chapter is to highlight the power of solar gamma rays and neutrinos to probe the DM parameter space in a pure phenomenological sense, rather than to be a complete study of DM models, in this section we briefly discuss potential interpretations of these results in the context of popular models.

8.6.1 Dark Vector or Axial-Vector

Spin-1 mediators cannot decay directly to two photons, by spin-statistics. Instead, final state photons may be obtained in other ways, such as electroweak bremsstrahlung, or hadronic decays. Resulting gamma ray spectra are softer than direct decays, and so the sensitivity to gamma rays in such a scenario would be closer to the b or τ channels. Of course, this is not a feature for the direct decay of a spin-1 mediator to neutrinos.

The dark photon, a gauge boson of a new $U(1)$ which kinematically mixes with SM hypercharge, is a popular spin-1 mediator. The dark photon can induce a large spin-independent scattering cross section, as the dark photon inherits Lorentz structures from kinetic mixing with the SM hypercharge, and it is difficult to remove the spin-independent contribution without fine-tuning cancellation by some other contribution. Therefore, competition with direct detection is a particularly important consideration in this scenario. Regardless, long-lived dark photon searches can still be more powerful than direct detection experiments [370].

Furthermore, there are other promising spin-1 mediator scenarios which do not have significant spin-independent scattering signals. For example, the spin-independent scattering rate can be suppressed if the scattering is predominantly inelastic, with a small mass splitting in DM states [354, 407]. Alternatively, direct detection limits can be suppressed in an axial-vector mediator scenario, or in an (almost) hidden sector setup with larger DM couplings and smaller SM couplings.

8.6.2 Fundamental Dark Scalar or Pseudoscalar

In some models, particular decay channels dominate due to properties of the mediator. For example, a dark Higgs which couples to the SM Higgs via a Higgs portal term will predominantly decay to the heaviest decay product that is kinematically available. This can motivate a choice of a near 100% branching fraction. In order to be sufficiently long-lived to escape the Sun, typically it is required that the mediator has very small couplings to its decay products, or alternatively there need to be a few orders of magnitude difference between the masses of the DM and the mediator. For a Higgs portal model, these requirements

are easily met with a light mediator which consequently can only decay into light final states such as electrons. Alternatively, in a two Higgs-doublet Higgs portal model, the dark Higgs couplings may be uncorrelated with SM Higgs couplings, for example when one of the doublets is leptophilic.

Another promising scenario is DM annihilating to axions, or any light pseudoscalar. For the axion to be both sufficiently long-lived to escape the Sun and to produce a sizable gamma-ray flux, light decay products such as gamma rays or electrons could be directly produced. For the combination of parameters where the gamma-ray flux dominates, a sharp spectral feature would be observed. Full details of such a model are comprehensively discussed in Ref. [354]. Also note that for pseudoscalar mediators, DM annihilation to a three-body pseudoscalar final state may be the dominant s-wave process, providing a different spectral shape [270, 408].

8.6.3 Multi-Mediator Scenarios

In this chapter, we consider the case that the dark sector contains a DM candidate and one dark long-lived mediator. Of course, the dark sector could be complex, with combinations of weak and strong dynamics, or several dark sector particles could be involved in the decay. If there exists a cascade of dark sector decays, the overall spectral shape will be softened. However, if there are only a few decays, this softening will not greatly affect the results [273]. This also means that the dark sector particles involved in the decay can have shorter lifetimes than required to escape the Sun, and it is only required that the sum of the lifetimes are sufficiently long to escape the Sun.

Furthermore, more than one mediator present in a model is well motivated in some scenarios. For example, in the case there is a dark spin-1 boson with axial couplings, unitarity is violated at high energies unless a scalar is also included in the setup [80, 296]. When both a vector and scalar are present, the DM annihilation and indirect detection signals can be different, with DM annihilating into a vector plus scalar final state potentially dominating when kinematically allowed [257, 268, 301]. If the masses of both mediators are of the same scale, the sensitivity limits are not drastically different and depending on final states could approximately map to our results of DM annihilation to only one type of mediator [257, 301]. Such a scenario also produces a compelling way to produce a large gamma-ray flux while evading other constraints; only one of the mediators need to satisfy conditions to escape the Sun to provide some non-zero DM flux. In fact, a particularly promising scenario arises when the scalar is long-lived and escapes the Sun, and the vector does not [354].

Generally, more than one mediator present can lead to destructive interference in direct detection signals, and consequently a blind spot in the direct detection limit. Interestingly, this may be covered by the solar spin-dependent limit we present on the scattering cross section instead.

DM may also exist in bound states, such as WIMPonium [409–417], or a dark pion, which can produce a large gamma-ray flux [418]. In such a case self-interactions of the DM would be relevant [380], leading to a potentially varied relation between scattering, annihilation, and self-interaction rates, with equilibrium reached at a different time.

8.6.4 General Considerations

The results we present are the most optimal case. Indeed, in many models, these sensitivity limits will be different. For example, there may be several decay modes of the dark mediator, reducing the branching fraction. In general, the sensitivity should be scaled accordingly. However, for a model with non-negligible direct gamma-ray decays, the gamma-ray spectra can be so sharp that it is what sets the limit across most of the parameter space (e.g., true for monochromatic gamma-ray lines, and for 4γ box spectra [132, 143]), and so a non-zero branching fraction to mixed final states may not affect the sensitivity within our accuracy of factor of a few.

When applying results to specific models, relations between parameters such as decay width, lifetime, masses and decay length will vary, and will need to satisfy the conditions in Sec. 8.3.5. In general, it is easier to fulfill requirements on parameter combinations for neutrinos. As neutrinos can propagate from inside the Sun [348, 374–379], shorter decay lifetimes are allowed for neutrino detection, leading to less stringent constraints on relationships between mediator properties. In the case where the scenario is sub-optimal, the sensitivity needs to be scaled (e.g., when $P_{\rm surv} \ll 1$ in the highly boosted case) or dedicated data analyses are required (e.g., when the Sun is no longer a point source).

Lastly, to escape increasingly strong spin-independent direct detection limits, model building efforts are often constructed such that the spin-independent DM direct detection signal is either suppressed or non-existent, and only the weaker spin-dependent direct detection constraint is relevant. In this chapter we have made the important observation that, even in such a case, very strong limits may arise on the spin-dependent scattering cross section by utilizing solar gamma rays or neutrinos, in the scenario that the dark mediator is long-lived.

8.7 Other constraints

There exist other constraints relevant for a long-lived mediator setup, but they are mostly highly model dependent. In this section, for completeness we outline other relevant constraints, which would need to be considered in a complete analysis. These are:

- **BBN:** The observed relic abundance of SM particles by Big Bang Nucleosynthesis implies any new mediator must have a lifetime $\tau < 1$s [300].

- **CMB:** DM annihilation to SM products in the early universe is constrained by the Cosmic Microwave Background [419–422].
- **Supernovae:** Relevant constraints may be obtained for mediators lighter than a GeV, from mediator decay and supernova cooling [423–427].
- **Colliders:** If the dark sector is secluded, limits from colliders may be negligible. Otherwise, limits may be set by LHC experiments Belle [428] for a dark Higgs and dark photon, BaBar [429], ATLAS [430, 431] and CMS [432].
- **Beam Dump/Fixed Target experiments:** Beam dump and fixed target experiments are most relevant when the mediator has mass lighter than a GeV. Limits on mediator properties can be set from E137 [433, 434], LSND [435–437] and CHARM [438, 439].
- **Other indirect detection signals:** Fermi-LAT and DES measurements of dwarf spheroidal galaxies can be relevant particularly at low DM mass [135, 440], and large positron signals [441] can be constrained by AMS-02 [442]. Also note that Fermi-LAT observed the Sun, searching for long-lived mediators directly decaying to electrons in the DM mass range 70–2000 GeV, which are stronger than the gamma-ray limits [443]. In such cases, helio- and geo-magnetic field effects must be taken into account, especially at lower DM masses.
- **Thermalization and Unitarity:** Thermalization can be important for > 10 TeV DM, and unitarity issues exist for DM mass $O(100)$ TeV [260, 444] for a standard WIMP, which is reached at the edge of the DM mass range we consider. Furthermore bound state effects can be relevant if DM mass becomes too large [416].

8.8 Conclusions

It has long been known that high-energy neutrinos can be used to probe DM scattering and annihilation in the Sun. If annihilation proceeds via long-lived dark mediators, gamma rays can escape the Sun, and neutrinos will be less attenuated. In this work, we have demonstrated gamma-ray and neutrino telescopes are extremely sensitive to such scenarios. Specifically, in this chapter we have:

- defined a general framework for DM annihilation to long-lived mediators in the Sun,
- calculated new solar gamma-ray limits on DM annihilation to long-lived mediators with the Fermi Gamma-ray Space Telescope,
- calculated the first solar gamma-ray projections of DM annihilation to long-lived mediators with ground-based water Cherenkov telescopes HAWC and LHAASO, and

- calculated new neutrino projections on DM annihilation to long-lived mediators in the Sun with neutrino telescopes such as IceCube and KM3NeT.

Experimentally, our results are especially pertinent due to new and upcoming opportunities in the gamma-ray and neutrino channels. For gamma rays, new detailed measurements of the Sun have been made in the GeV range with Fermi, and great increases in sensitivity in the TeV range will be available with HAWC and LHAASO. For neutrinos, the long-lived mediator scenario opens the previously inaccessible multi-TeV window, with gigaton neutrino telescopes such as IceCube and KM3NeT. If the dark sector contains a DM candidate along with a sufficiently long-lived mediator, these telescopes can improve sensitivity to the DM spin-dependent scattering cross section by several orders of magnitude, relative to present searches for high-energy neutrinos from the Sun, as well as direct detection experiments.

Models which have non-suppressed spin-independent scattering cross sections must satisfy strong constraints from direct detection experiments. For models where the spin-dependent cross section is dominant, direct detection limits are significantly weaker. However, if the model contains a long-lived mediator, a substantial part of the spin-dependent scattering cross section can instead be covered via solar gamma rays or neutrinos. Depending on model details, these searches can provide a probe of the spin-dependent DM scattering cross section stronger than the predicted sensitivity for all upcoming direct detection experiments, including DARWIN. This means that observations of solar gamma rays and neutrinos are a promising complementary avenue for the discovery of DM.

Our results define model-independent spaces, from which model-dependent results can be extracted. Demonstrating the optimal model-independent case, as we have in this chapter, highlights the maximal power of solar gamma-ray and neutrino signatures. Indeed, further theoretical work is needed to fully explore this parameter space, to interpret it in the context of particular models, and to constrain it with other considerations. Until then, the most important thing for progress is new experimental analyses, especially taking advantage of the huge increase in sensitivity possible with present HAWC and LHAASO TeV gamma-ray data, and IceCube neutrino data. Future analyses and accompanying theoretical investigations for long-lived mediators in the Sun have substantial potential to provide crucial insight to the nature of DM.

Chapter 9

Conclusion

The discovery of dark matter remains one of the foremost goals of the physics community. As shown in Part I, despite evidence for DM being clearly established, no substantial evidence of its fundamental particle nature has yet been found. In this thesis, we have explored new ways to probe properties of particle dark matter across different phenomenological settings, demonstrating the importance of theoretically consistent models, as well as novel signatures for discovery.

In Part II of this thesis, we investigated model building and signals for dark matter searches at the Large Hadron Collider (LHC). In Chapter 2, we showed that the use of effective field theories for dark matter at the LHC can lead to bad high-energy behaviour and unphysical signals. In particular, many widely used EFTs are not gauge invariant, and if such operators do not respect the electroweak gauge symmetries of the SM, vev insertions are required to restore gauge invariance. Such operators appear at higher dimension compared to gauge invariant EFTs, and as such their effects should be subdominant. In the context of the mono-W signal, we showed the "interference effect" that was searched for by ATLAS and CMS was a consequence of breaking gauge invariance, with untamed unphysical contributions from the longitudinal W modes. To avoid such issues, in Chapter 3, we employed the next iteration of a minimal DM framework, simplified models, in the context of mono-W searches. We considered renormalizable gauge-invariant models, in cases where couplings were either weak isospin conserving or violating after electroweak symmetry breaking. We found that isospin violating effects are small, and unobservable at the LHC in the context of two simple models. Lastly, for isopin conserving simplified models, we found that the mono-W signal plays a sub-dominant role to other searches at the LHC, such as mono-jet or di-jet searches, which instead are more likely to be a discovery channel. In Chapter 4, we discussed an alternative search strategy to mono-X searches at the LHC — in the case that DM does not couple directly to hadrons, the mono-X signature does not exist, and instead a leptophilic DM signature can be found at the LHC. We found that despite having a suppressed LHC signal, leptophilic DM with a spin-1 mediator can still be significantly probed, particularly at low DM and mediator masses.

In Part III of this thesis, we turned to astrophysical signals of DM. In Chapter 5,

we demonstrated that a consequence of enforcing gauge invariance in simplified DM models provides a new dominant s-wave DM annihilation process for indirect detection searches. We set limits on the annihilation cross section from Pass 8 observations of gamma rays from dwarf spheroidal galaxies by the Fermi Gamma-ray Space Telescope, finding this new process has a spectral shape which gives rise to slightly more stringent bounds. In Chapter 6, we demonstrated the impact of mass generation for simplified models, finding that the relic density and indirect detection constraints, along with the DM interaction types, are strongly dictated by the mass generation mechanism chosen. The emphasis of Chapters 5 and 6 is that traditional simplified model searches miss important phenomenology which would exist in a full UV model, implying that these models are "over-simplified". In Chapter 7, we showed that the multi-mediator approach advocated in the previous two chapters can also lead to a new dominant signal, in the form of dark initial state radiation. Finally in Chapter 8, we studied DM signals in the Sun, finding that if DM annihilates to long-lived mediators, the gamma rays produced can be strongly probed by the Fermi Gamma-ray Space Telescope, ground-based water Cherenkov telescopes HAWC and LHAASO, and similarly the neutrinos produced can be probed by neutrino telescopes IceCube and KM3Net. Interestingly, these telescopes can provide the strongest probe of the DM spin dependent scattering cross section, outperforming standard searches for high-energy solar neutrinos and direct detection experiments by several orders of magnitude.

Across this thesis, we have shown that theoretically consistent models and new ways of searching for dark matter, exploiting the complementarity of searches, are important steps forward for its discovery.

Appendix A

Full cross sections

A.1 Cross Sections

In the scenarios discussed in Chapter 6, the charges were fixed to particular values either to satisfy gauge invariance, or to demonstrate the phenomenology. The full cross sections with explicit $Q_{A,V}$ and Q_S dependence are listed in this appendix for reference.

The full s-wave cross section for $\chi\overline{\chi} \to Z'Z'$ is

$$\langle \sigma v \rangle_{\chi\overline{\chi}\to Z'Z'} = \frac{g_\chi^4 \left(1-\eta_{Z'}\right)^{3/2} \left(2Q_A^2 Q_V^2 \left(4-3\eta_{Z'}\right) + Q_A^4 \eta_{Z'} + Q_V^4 \eta_{Z'}\right)}{4\pi m_\chi^2 \left(\eta_{Z'}-2\right)^2 \eta_{Z'}}. \tag{A.1}$$

This expression gives the s-wave contribution to the $\chi\overline{\chi} \to Z'Z'$ cross section for *all* cases, as only the t/u channel diagrams contribute. (Scalar-mediator contributions only enter at the p-wave level.) We see that if either Q_A or Q_V is zero, the cross section scales as $1/m_\chi^2$ in the limit that $\eta_{Z'} = m_{Z'}^2/m_\chi^2 \ll 1$, and is dominated by Z'_T contributions only. In the case that both Q_A and Q_V are non-zero, the cross section instead scales as $1/m_{Z'}^2$, in the $\eta_{Z'} \ll 1$ limit, which arises due to the Z'_L modes. Note however, that no violation of unitarity will occur – the Z' mass cannot be made arbitrarily large while satisfying the constraint Eq. (6.10) and restricting all couplings to perturbative values. This $Z'Z'$ cross section matches that in Refs. [188, 190].

The full s-wave cross section for $\chi\overline{\chi} \to sZ'$ is

$$\begin{aligned}\langle \sigma v \rangle_{\chi\overline{\chi}\to sZ'} = {} & \frac{g_\chi^2 \sqrt{\left(\eta_s-\eta_{Z'}-4\right)^2 - 16\eta_{Z'}}}{256\pi m_\chi^2 \left(\eta_{Z'}-4\right)^2 \eta_{Z'}^2 \left(\eta_s+\eta_{Z'}-4\right)^2} \times \\ & \Big\{ g_\chi^2 Q_S^2 \left(\eta_s+\eta_{Z'}-4\right)^2 \Big[Q_A^2 \left(\eta_{Z'}-4\right)^2 \left(\left(\eta_s-\eta_{Z'}-4\right)^2 - 16\eta_{Z'}\right) \\ & + Q_V^2 \eta_{Z'}^2 \left(\left(\eta_s-\eta_{Z'}-4\right)^2 + 32\eta_{Z'}\right) \Big] \\ & + 24\sqrt{2} g_\chi Q_S Q_V^2 y_\chi \left(\eta_{Z'}-4\right) \eta_{Z'}^{5/2} \left(\eta_s^2 - 8\eta_s - \eta_{Z'}^2 + 16\right) \\ & + 4 Q_V^2 y_\chi^2 \left(\eta_{Z'}-4\right)^2 \eta_{Z'}^2 \left(\left(\eta_s-\eta_{Z'}-4\right)^2 + 8\eta_{Z'}\right) \Big\}.\end{aligned} \tag{A.2}$$

Taking $2Q_A = Q_S = 1$ and using the relation of the Yukawa and gauge coupling in Eq. (6.10) recovers the cross sections for scenario II, $Q_A = Q_S = 0$ recovers the

cross sections for scenario III, and $Q_A, y_\chi = 0$ gives the cross sections for scenario IV.

It is still important to note however that the values for the charges cannot be chosen freely and should obey the constraints discussed in Chapter 6.

Bibliography

[1] B. Kelvin. "Baltimore lectures on molecular dynamics and the wave theory of light". In: (1904).

[2] E. Opik. In: *Bull. de la Soc. Astr. de Russie* 21 (1915), 150.

[3] J. C. Kapteyn. "First Attempt at a Theory of the Arrangement and Motion of the Sidereal System". In: *Astrophys. J.* 55 (1922), pp. 302–328. DOI: 10.1086/142670.

[4] Jeans, J. H. "The motions of stars in a Kapteyn universe". In: 82 (1922), 122–132. DOI: {10.1093/mnras/82.3.122}.

[5] Lindblad. In: *Uppsala Meddelanden 11* 30 (1926).

[6] Oort, J. H. "The force exerted by the stellar system in the direction perpendicular to the galactic plane and some related problems". In: 6 (1932), 249.

[7] Gianfranco Bertone and Dan Hooper. "A History of Dark Matter". In: *Submitted to: Rev. Mod. Phys.* (2016). arXiv: 1605.04909 [astro-ph.CO].

[8] Hubble, E. and Humason, M. L. "The Velocity-Distance Relation among Extra-Galactic Nebulae". In: 74 (1931), 43.

[9] Zwicky, F. "Die Rotverschiebung von extragalaktischen Nebeln". In: *Helvetica Physica Acta* 6 (1933), 110–127.

[10] Massimo Persic, Paolo Salucci, and Fulvio Stel. "The Universal rotation curve of spiral galaxies: 1. The Dark matter connection". In: *Mon. Not. Roy. Astron. Soc.* 281 (1996), p. 27. DOI: 10.1093/mnras/281.1.27,10.1093/mnras/278.1.27. arXiv: astro-ph/9506004 [astro-ph].

[11] Babcock, H. W. "The rotation of the Andromeda Nebula". In: *Lick Observatory Bulletin* 19 (1939), 41–51. DOI: {10.5479/ADS/bib/1939LicOB.19.41B}.

[12] Rubin, V. C. and Thonnard, N. and Ford, Jr., W. K. "Extended rotation curves of high-luminosity spiral galaxies. IV - Systematic dynamical properties, SA through SC". In: *Apjl* 225 (1978), L107–L111. DOI: {10.1086/182804}.

[13] J. Wambsganss. "Gravitational Microlensing". In: *Gravitational Lensing: Strong, Weak and Micro*. Berlin, Heidelberg: Springer Berlin Heidelberg, 2006, pp. 453–540. ISBN: 978-3-540-30310-7. DOI: 10.1007/978-3-540-30310-7_4. URL: http://dx.doi.org/10.1007/978-3-540-30310-7_4.

[14] Douglas Clowe et al. "A direct empirical proof of the existence of dark matter". In: *Astrophys. J.* 648 (2006), pp. L109–L113. DOI: 10.1086/508162. arXiv: astro-ph/0608407 [astro-ph].

[15] M. Milgrom. "A modification of the Newtonian dynamics as a possible alternative to the hidden mass hypothesis". In: 270 (July 1983), pp. 365–370. DOI: 10.1086/161130.

[16] Maxim Markevitch. "Chandra observation of the most interesting cluster in the universe". In: (2005). [ESA Spec. Publ.604,723(2006)]. arXiv: astro-ph/0511345 [astro-ph].

[17] Myungkook James Jee et al. "Discovery of a Ringlike Dark Matter Structure in the Core of the Galaxy Cluster Cl 0024+17". In: *Astrophys. J.* 661 (2007), pp. 728–749. DOI: 10.1086/517498. arXiv: 0705.2171 [astro-ph].

[18] Marusa Bradac et al. "Revealing the properties of dark matter in the merging cluster MACSJ0025.4-1222". In: *Astrophys. J.* 687 (2008), p. 959. DOI: 10.1086/591246. arXiv: 0806.2320 [astro-ph].

[19] A. Mahdavi et al. "A Dark Core in Abell 520". In: *Astrophys. J.* 668 (2007), pp. 806–814. DOI: 10.1086/521383. arXiv: 0706.3048 [astro-ph].

[20] Clowe, D. and Markevitch, M. and Bradač, M. and Gonzalez, A. H. and Chung, S. M. and Massey, R. and Zaritsky, D. "On Dark Peaks and Missing Mass: A Weak-lensing Mass Reconstruction of the Merging Cluster System A520". In: 758, 128 (2012), 128. arXiv: {1209.2143}.

[21] Gianfranco Bertone, Dan Hooper, and Joseph Silk. "Particle dark matter: Evidence, candidates and constraints". In: *Phys.Rept.* 405 (2005), pp. 279–390. DOI: 10.1016/j.physrep.2004.08.031. arXiv: hep-ph/0404175 [hep-ph].

[22] Adam G. Riess et al. "Observational evidence from supernovae for an accelerating universe and a cosmological constant". In: *Astron. J.* 116 (1998), pp. 1009–1038. DOI: 10.1086/300499. arXiv: astro-ph/9805201 [astro-ph].

[23] Daniel J. Eisenstein et al. "Detection of the baryon acoustic peak in the large-scale correlation function of SDSS luminous red galaxies". In: *Astrophys. J.* 633 (2005), pp. 560–574. DOI: 10.1086/466512. arXiv: astro-ph/0501171 [astro-ph].

[24] P. A. R. Ade et al. "Planck 2015 results. XIII. Cosmological parameters". In: *Astron. Astrophys.* 594 (2016), A13. DOI: 10.1051/0004-6361/201525830. arXiv: 1502.01589 [astro-ph.CO].

[25] Suzuki, N. et al. "The Hubble Space Telescope Cluster Supernova Survey. V. Improving the Dark-energy Constraints above z 1 and Building an Early-type-hosted Supernova Sample". In: 746, 85 (2012), 85. DOI: {10.1088/0004-637X/746/1/85}. arXiv: {1105.3470} [astro-ph.CO].

[26] Richard H. Cyburt et al. "Big Bang Nucleosynthesis: 2015". In: *Rev. Mod. Phys.* 88 (2016), p. 015004. DOI: 10.1103/RevModPhys.88.015004. arXiv: 1505.01076 [astro-ph.CO].

[27] K. A. Olive et al. "Review of Particle Physics". In: *Chin. Phys.* C38 (2014), p. 090001. DOI: 10.1088/1674-1137/38/9/090001.

[28] Keisler, R. et al. "A Measurement of the Damping Tail of the Cosmic Microwave Background Power Spectrum with the South Pole Telescope". In: 743, 28 (2011), 28. arXiv: {1105.3182}.

[29] Das, S. et al. "The Atacama Cosmology Telescope: A Measurement of the Cosmic Microwave Background Power Spectrum at 148 and 218 GHz from the 2008 Southern Survey". In: 729, 62 (2011), 62. DOI: {10.1088/0004-637X/729/1/62}. arXiv: {1009.0847}.

[30] Hinshaw, G. and Larson, D. and Komatsu, E. and Spergel, D. N. and Bennett, C. L. and Dunkley, J. and Nolta, M. R. and Halpern, M. and Hill, R. S. and Odegard, N. and Page, L. and Smith, K. M. and Weiland, J. L. and Gold, B. and Jarosik, N. and Kogut, A. and Limon, M. and Meyer, S. S. and Tucker, G. S. and Wollack, E. and Wright, E. L. "Nine-year Wilkinson Microwave Anisotropy Probe (WMAP) Observations: Cosmological Parameter Results". In: 208, 19 (2013), 19. arXiv: {1212.5226}.

[31] Volker Springel, Carlos S. Frenk, and Simon D. M. White. "The large-scale structure of the Universe". In: *Nature* 440 (2006), p. 1137. DOI: 10.1038/nature04805. arXiv: astro-ph/0604561 [astro-ph].

[32] Cervantes-Cota, J. L. and Smoot, G. "Cosmology today–A brief review". In: *American Institute of Physics Conference Series*. Vol. 1396. American Institute of Physics Conference Series. 2011, 28–52. DOI: {10.1063/1.3647524}. arXiv: {1107.1789} [astro-ph.CO].

[33] Boylan-Kolchin, M. and Springel, V. and White, S. D. M. and Jenkins, A. and Lemson, G. "Resolving cosmic structure formation with the Millennium-II Simulation". In: 398 (2009), 1150–1164. DOI: {10.1111/j.1365-2966.2009.15191.x}. arXiv: {0903.3041} [astro-ph.CO].

[34] Angulo, R. E. and Springel, V. and White, S. D. M. and Jenkins, A. and Baugh, C. M. and Frenk, C. S. "Scaling relations for galaxy clusters in the Millennium-XXL simulation". In: 426 (2012), 2046–2062. DOI: {10.1111/j.1365-2966.2012.21830.x}. arXiv: {1203.3216}.

[35] Overzier, R. and Lemson, G. and Angulo, R. E. and Bertin, E. and Blaizot, J. and Henriques, B. M. B. and Marleau, G.-D. and White, S. D. M. "The Millennium Run Observatory: first light". In: 428 (2013), 778–803. DOI: {10.1093/mnras/sts076}. arXiv: {1206.6923}.

[36] Antonino Del Popolo. "Dark matter and structure formation a review". In: *Astron. Rep.* 51 (2007), pp. 169–196. DOI: 10.1134/S1063772907030018. arXiv: 0801.1091 [astro-ph].

[37] B. Moore et al. "Dark matter substructure within galactic halos". In: *Astrophys. J.* 524 (1999), pp. L19–L22. DOI: 10.1086/312287. arXiv: astro-ph/9907411 [astro-ph].

[38] A. V. Macciò et al. "Halo Expansion in Cosmological Hydro Simulations: Toward a Baryonic Solution of the Cusp/Core Problem in Massive Spirals". In: 744, L9 (Jan. 2012), p. L9. DOI: 10.1088/2041-8205/744/1/L9. arXiv: 1111.5620.

[39] T. K. Chan et al. "The impact of baryonic physics on the structure of dark matter haloes: the view from the FIRE cosmological simulations". In: 454 (Dec. 2015), pp. 2981–3001. DOI: 10.1093/mnras/stv2165. arXiv: 1507.02282.

[40] F. Englert and R. Brout. "Broken Symmetry and the Mass of Gauge Vector Mesons". In: *Phys. Rev. Lett.* 13 (9 1964), pp. 321–323. DOI: 10.1103/PhysRevLett.13.321. URL: http://link.aps.org/doi/10.1103/PhysRevLett.13.321.

[41] Peter W. Higgs. "Broken Symmetries and the Masses of Gauge Bosons". In: *Phys. Rev. Lett.* 13 (16 1964), pp. 508–509. DOI: 10.1103/PhysRevLett.13.508. URL: http://link.aps.org/doi/10.1103/PhysRevLett.13.508.

[42] G. S. Guralnik, C. R. Hagen, and T. W. Kibble. "Global Conservation Laws and Massless Particles". In: *Physical Review Letters* 13 (Nov. 1964), pp. 585–587. DOI: 10.1103/PhysRevLett.13.585.

[43] A. S. Szalay and G. Marx. "Neutrino rest mass from cosmology". In: 49 (June 1976), pp. 437–441.

[44] R. Cowsik and J. McClelland. "An Upper Limit on the Neutrino Rest Mass". In: *Phys. Rev. Lett.* 29 (10 1972), pp. 669–670. DOI: 10.1103/PhysRevLett.29.669. URL: http://link.aps.org/doi/10.1103/PhysRevLett.29.669.

[45] J Bonn et al. "The Mainz neutrino mass experiment". In: *Nuclear Physics B-Proceedings Supplements* 91.1-3 (2001), pp. 273–279.

[46] Wayne Hu, Rennan Barkana, and Andrei Gruzinov. "Cold and fuzzy dark matter". In: *Phys. Rev. Lett.* 85 (2000), pp. 1158–1161. DOI: 10.1103/PhysRevLett.85.1158. arXiv: astro-ph/0003365 [astro-ph].

[47] Bernard J. Carr and S. W. Hawking. "Black holes in the early Universe". In: *Mon. Not. Roy. Astron. Soc.* 168 (1974), pp. 399–415.

[48] K. Griest. "Galactic microlensing as a method of detecting massive compact halo objects". In: 366 (Jan. 1991), pp. 412–421. DOI: 10.1086/169575.

[49] C. Alcock et al. "The MACHO project LMC microlensing results from the first two years and the nature of the galactic dark halo". In: *Astrophys. J.* 486 (1997), pp. 697–726. DOI: 10.1086/304535. arXiv: astro-ph/9606165 [astro-ph].

[50] Kenji Kadota, Toyokazu Sekiguchi, and Hiroyuki Tashiro. "A new constraint on millicharged dark matter from galaxy clusters". In: (2016). arXiv: 1602.04009 [astro-ph.CO].

[51] JiJi Fan et al. "Double-Disk Dark Matter". In: *Phys. Dark Univ.* 2 (2013), pp. 139–156. DOI: 10.1016/j.dark.2013.07.001. arXiv: 1303.1521 [astro-ph.CO].

[52] JiJi Fan et al. "Dark-Disk Universe". In: *Phys. Rev. Lett.* 110.21 (2013), p. 211302. DOI: 10.1103/PhysRevLett.110.211302. arXiv: 1303.3271 [hep-ph].

[53] R. Foot and R. R. Volkas. "Spheroidal galactic halos and mirror dark matter". In: *Phys. Rev.* D70 (2004), p. 123508. DOI: 10.1103/PhysRevD.70.123508. arXiv: astro-ph/0407522 [astro-ph].

[54] Scott W. Randall et al. "Constraints on the Self-Interaction Cross-Section of Dark Matter from Numerical Simulations of the Merging Galaxy Cluster 1E 0657-56". In: *Astrophys. J.* 679 (2008), pp. 1173–1180. DOI: 10.1086/587859. arXiv: 0704.0261 [astro-ph].

[55] A. H. G. Peter et al. "Cosmological simulations with self-interacting dark matter - II. Halo shapes versus observations". In: 430 (Mar. 2013), pp. 105–120. DOI: 10.1093/mnras/sts535. arXiv: 1208.3026.

[56] Francis-Yan Cyr-Racine et al. "Constraints on Large-Scale Dark Acoustic Oscillations from Cosmology". In: *Phys. Rev.* D89.6 (2014), p. 063517. DOI: 10.1103/PhysRevD.89.063517. arXiv: 1310.3278 [astro-ph.CO].

[57] Andreas Ringwald. "Exploring the Role of Axions and Other WISPs in the Dark Universe". In: *Phys. Dark Univ.* 1 (2012), pp. 116–135. DOI: 10.1016/j.dark.2012.10.008. arXiv: 1210.5081 [hep-ph].

[58] Haipeng An et al. "Direct Detection Constraints on Dark Photon Dark Matter". In: *Phys. Lett.* B747 (2015), pp. 331–338. DOI: 10.1016/j.physletb.2015.06.018. arXiv: 1412.8378 [hep-ph].

[59] R. D. Peccei. "The Strong CP problem and axions". In: *Lect. Notes Phys.* 741 (2008). [,3(2006)], pp. 3–17. DOI: 10.1007/978-3-540-73518-2_1. arXiv: hep-ph/0607268 [hep-ph].

[60] Georg G. Raffelt. "Astrophysical axion bounds". In: *Lect. Notes Phys.* 741 (2008). [,51(2006)], pp. 51–71. DOI: 10.1007/978-3-540-73518-2_3. arXiv: hep-ph/0611350 [hep-ph].

[61] Kevork Abazajian, George M. Fuller, and Mitesh Patel. "Sterile neutrino hot, warm, and cold dark matter". In: *Phys. Rev.* D64 (2001), p. 023501. DOI: 10.1103/PhysRevD.64.023501. arXiv: astro-ph/0101524 [astro-ph].

[62] Scott Dodelson and Lawrence M. Widrow. "Sterile-neutrinos as dark matter". In: *Phys. Rev. Lett.* 72 (1994), pp. 17–20. DOI: 10.1103/PhysRevLett.72.17. arXiv: hep-ph/9303287 [hep-ph].

[63] Riccardo Barbieri and A. Dolgov. "Bounds on Sterile-neutrinos from Nucleosynthesis". In: *Phys. Lett.* B237 (1990), pp. 440–445. DOI: 10.1016/0370-2693(90)91203-N.

[64] A. D. Dolgov. "Neutrinos in cosmology". In: *Phys. Rept.* 370 (2002), pp. 333–535. DOI: 10.1016/S0370-1573(02)00139-4. arXiv: hep-ph/0202122 [hep-ph].

[65] Frank Daniel Steffen. "Gravitino dark matter and cosmological constraints". In: *JCAP* 0609 (2006), p. 001. DOI: 10.1088/1475-7516/2006/09/001. arXiv: hep-ph/0605306 [hep-ph].

[66] Yonit Hochberg et al. "Mechanism for Thermal Relic Dark Matter of Strongly Interacting Massive Particles". In: *Phys. Rev. Lett.* 113 (2014), p. 171301. DOI: 10.1103/PhysRevLett.113.171301. arXiv: 1402.5143 [hep-ph].

[67] Kalliopi Petraki and Raymond R. Volkas. "Review of asymmetric dark matter". In: *Int. J. Mod. Phys.* A28 (2013), p. 1330028. DOI: 10.1142/S0217751X13300287. arXiv: 1305.4939 [hep-ph].

[68] M. B. Hindmarsh and T. W. B. Kibble. "Cosmic strings". In: *Rept. Prog. Phys.* 58 (1995), pp. 477–562. DOI: 10.1088/0034-4885/58/5/001. arXiv: hep-ph/9411342 [hep-ph].

[69] Edward W. Kolb, Daniel J. H. Chung, and Antonio Riotto. "WIMPzillas!" In: *Trends in theoretical physics II. Proceedings, 2nd La Plata Meeting, Buenos Aires, Argentina, November 29-December 4, 1998*. [,91(1998)]. 1998, pp. 91–105. arXiv: hep-ph/9810361 [hep-ph]. URL: http://lss.fnal.gov/cgi-bin/find_paper.pl?conf-98-325.

[70] E. Kolb and M. Turner. *The Early Universe*. Frontiers in physics. Avalon Publishing, 1994. ISBN: 9780813346458. URL: https://books.google.co.in/books?id=Qwijr-HsvMMC.

[71] Jessica Goodman et al. "Constraints on Light Majorana dark Matter from Colliders". In: *Phys. Lett.* B695 (2011), pp. 185–188. DOI: 10.1016/j.physletb.2010.11.009. arXiv: 1005.1286 [hep-ph].

[72] Jessica Goodman et al. "Constraints on Dark Matter from Colliders". In: *Phys. Rev.* D82 (2010), p. 116010. DOI: 10.1103/PhysRevD.82.116010. arXiv: 1008.1783 [hep-ph].

[73] Mateusz Duch, Bohdan Grzadkowski, and Jose Wudka. "Classification of effective operators for interactions between the Standard Model and dark matter". In: (2014). arXiv: 1412.0520 [hep-ph].

[74] Giorgio Busoni et al. "On the Validity of the Effective Field Theory for Dark Matter Searches at the LHC". In: *Phys. Lett.* B728 (2014), pp. 412–421. DOI: 10.1016/j.physletb.2013.11.069. arXiv: 1307.2253 [hep-ph].

[75] O. Buchmueller, Matthew J. Dolan, and Christopher McCabe. "Beyond Effective Field Theory for Dark Matter Searches at the LHC". In: *JHEP* 01 (2014), p. 025. DOI: 10.1007/JHEP01(2014)025. arXiv: 1308.6799 [hep-ph].

[76] Giorgio Busoni et al. "On the Validity of the Effective Field Theory for Dark Matter Searches at the LHC, Part II: Complete Analysis for the s-channel". In: *JCAP* 1406 (2014), p. 060. DOI: 10.1088/1475-7516/2014/06/060. arXiv: 1402.1275 [hep-ph].

[77] Giorgio Busoni et al. "On the Validity of the Effective Field Theory for Dark Matter Searches at the LHC Part III: Analysis for the t-channel". In: *JCAP* 1409 (2014), p. 022. DOI: 10.1088/1475-7516/2014/09/022. arXiv: 1405.3101 [hep-ph].

[78] Ian M. Shoemaker and Luca Vecchi. "Unitarity and Monojet Bounds on Models for DAMA, CoGeNT, and CRESST-II". In: *Phys. Rev.* D86 (2012), p. 015023. DOI: 10.1103/PhysRevD.86.015023. arXiv: 1112.5457 [hep-ph].

[79] Daniel Abercrombie et al. "Dark Matter Benchmark Models for Early LHC Run-2 Searches: Report of the ATLAS/CMS Dark Matter Forum". In: (2015). Ed. by Antonio Boveia et al. arXiv: 1507.00966 [hep-ex].

[80] Felix Kahlhoefer et al. "Implications of unitarity and gauge invariance for simplified dark matter models". In: *JHEP* 02 (2016), p. 016. DOI: 10.1007/JHEP02(2016)016. arXiv: 1510.02110 [hep-ph].

[81] S. Schael et al. "Precision electroweak measurements on the Z resonance". In: *Phys. Rept.* 427 (2006), pp. 257–454. DOI: 10.1016/j.physrep.2005.12.006. arXiv: hep-ex/0509008 [hep-ex].

[82] "Updated Combination of CDF and D0 Searches for Standard Model Higgs Boson Production with up to 10.0 fb^{-1} of Data". In: 2012. arXiv: 1207.0449 [hep-ex]. URL: http://lss.fnal.gov/cgi-bin/find_paper.pl?conf-12-318.

[83] Georges Aad et al. "Observation of a new particle in the search for the Standard Model Higgs boson with the ATLAS detector at the LHC". In: *Phys. Lett.* B716 (2012), pp. 1–29. DOI: 10.1016/j.physletb.2012.08.020. arXiv: 1207.7214 [hep-ex].

[84] Serguei Chatrchyan et al. "Observation of a new boson at a mass of 125 GeV with the CMS experiment at the LHC". In: *Phys. Lett.* B716 (2012), pp. 30–61. DOI: 10.1016/j.physletb.2012.08.021. arXiv: 1207.7235 [hep-ex].

[85] Morad Aaboud et al. "Search for new phenomena in final states with an energetic jet and large missing transverse momentum in pp collisions at $\sqrt{s}$ = 13TeV using the ATLAS detector". In: *Phys. Rev.* D94.3 (2016), p. 032005. DOI: 10.1103/PhysRevD.94.032005. arXiv: 1604.07773 [hep-ex].

[86] Morad Aaboud et al. "Search for new phenomena in events with a photon and missing transverse momentum in pp collisions at $\sqrt{s}$ = 13 TeV with the ATLAS detector". In: *JHEP* 06 (2016), p. 059. DOI: 10.1007/JHEP06(2016)059. arXiv: 1604.01306 [hep-ex].

[87] Morad Aaboud et al. "Search for dark matter produced in association with a hadronically decaying vector boson in pp collisions at $\sqrt{(s)}$=13 TeV with the ATLAS detector". In: (2016). arXiv: 1608.02372 [hep-ex].

[88] "Search for Dark Matter production associated with bottom quarks with 13.3 fb^{-1} of pp collisions at $\sqrt{(s)}$ = 13 TeV with the ATLAS detector at the LHC". In: (2016). ATLAS-CONF-2016-086.

[89] "Search for Dark Matter in association with a Higgs boson decaying to b-quarks in pp collisions at $\sqrt{s}$ = 13 TeV with the ATLAS detector". In: (2016). ATLAS-CONF-2016-019.

[90] CMS Collaboration. "Search for new physics in a boosted hadronic monotop final state using 12.9 fb^{-1} of $\sqrt{s}$ = 13 TeV data". In: (2016). CMS-PAS-EXO-16-040.

[91] CMS Collaboration. "Search for dark matter and graviton produced in association with a photon in pp collisions at sqrts = 13 TeV". In: (2016). CMS-PAS-EXO-16-039.

[92] CMS Collaboration. "Search for dark matter in Z + $E_{\mathrm{T}}^{\mathrm{miss}}$ events using 12.9 fb^{-1} of 2016 data". In: (2016). CMS-PAS-EXO-16-038.

[93] CMS Collaboration. "Search for dark matter in final states with an energetic jet, or a hadronically decaying W or Z boson using 12.9 fb^{-1} of data at $\sqrt{s}$ = 13 TeV". In: (2016). CMS-PAS-EXO-16-037.

[94] CMS Collaboration. "Search for dark matter in association with a Higgs boson decaying into a pair of bottom quarks at sqrt(s) = 13 TeV with the CMS detector". In: (2016). CMS-PAS-EXO-16-012.

[95] CMS Collaboration. "Search for Dark Matter Produced in Association with a Higgs Boson Decaying to Two Photons". In: (2016). CMS-PAS-EXO-16-011.

[96] CMS Collaboration. "Search for dark matter in association with a top quark pair at sqrt(s)=13 TeV". In: (2016). CMS-PAS-EXO-16-005.

[97] CMS Collaboration. "Search for Dark Matter produced in association with bottom quarks". In: (2016). CMS-PAS-B2G-15-007.

[98] Linda M. Carpenter et al. "Collider searches for dark matter in events with a Z boson and missing energy". In: *Phys. Rev.* D87.7 (2013), p. 074005. DOI: 10.1103/PhysRevD.87.074005. arXiv: 1212.3352 [hep-ex].

[99] Linda Carpenter et al. "Mono-Higgs-boson: A new collider probe of dark matter". In: *Phys. Rev.* D89.7 (2014), p. 075017. DOI: 10.1103/PhysRevD.89.075017. arXiv: 1312.2592 [hep-ph].

[100] Alexey A. Petrov and William Shepherd. "Searching for dark matter at LHC with Mono-Higgs production". In: *Phys. Lett.* B730 (2014), pp. 178–183. DOI: 10.1016/j.physletb.2014.01.051. arXiv: 1311.1511 [hep-ph].

[101] Nicole F. Bell et al. "Searching for Dark Matter at the LHC with a Mono-Z". In: *Phys. Rev.* D86 (2012), p. 096011. DOI: 10.1103/PhysRevD.86.096011. arXiv: 1209.0231 [hep-ph].

[102] Nicole F. Bell, Yi Cai, and Rebecca K. Leane. "Mono-W Dark Matter Signals at the LHC: Simplified Model Analysis". In: *JCAP* 1601.01 (2016), p. 051. DOI: 10.1088/1475-7516/2016/01/051. arXiv: 1512.00476 [hep-ph].

[103] Andreas Birkedal, Konstantin Matchev, and Maxim Perelstein. "Dark matter at colliders: A Model independent approach". In: *Phys. Rev.* D70 (2004), p. 077701. DOI: 10.1103/PhysRevD.70.077701. arXiv: hep-ph/0403004 [hep-ph].

[104] Yuri Gershtein et al. "Discovering hidden sectors with mono-photon Z'o searches". In: *Phys. Rev.* D78 (2008), p. 095002. DOI: 10.1103/PhysRevD.78.095002. arXiv: 0809.2849 [hep-ph].

[105] Andreas Crivellin, Ulrich Haisch, and Anthony Hibbs. "LHC constraints on gauge boson couplings to dark matter". In: *Phys. Rev.* D91 (2015), p. 074028. DOI: 10.1103/PhysRevD.91.074028. arXiv: 1501.00907 [hep-ph].

[106] Frank J. Petriello, Seth Quackenbush, and Kathryn M. Zurek. "The Invisible Z' at the CERN LHC". In: *Phys. Rev.* D77 (2008), p. 115020. DOI: 10.1103/PhysRevD.77.115020. arXiv: 0803.4005 [hep-ph].

[107] Asher Berlin, Tongyan Lin, and Lian-Tao Wang. "Mono-Higgs Detection of Dark Matter at the LHC". In: *JHEP* 06 (2014), p. 078. DOI: 10.1007/JHEP06(2014)078. arXiv: 1402.7074 [hep-ph].

[108] Tongyan Lin, Edward W. Kolb, and Lian-Tao Wang. "Probing dark matter couplings to top and bottom quarks at the LHC". In: *Phys. Rev.* D88.6 (2013), p. 063510. DOI: 10.1103/PhysRevD.88.063510. arXiv: 1303.6638 [hep-ph].

[109] Patrick J. Fox et al. "Missing Energy Signatures of Dark Matter at the LHC". In: *Phys. Rev.* D85 (2012), p. 056011. DOI: 10.1103/PhysRevD.85.056011. arXiv: 1109.4398 [hep-ph].

[110] Yang Bai, James Bourbeau, and Tongyan Lin. "Dark matter searches with a mono-Z jet". In: *JHEP* 06 (2015), p. 205. DOI: 10.1007/JHEP06(2015)205. arXiv: 1504.01395 [hep-ph].

[111] Marcelo Autran et al. "Searches for dark matter in events with a resonance and missing transverse energy". In: *Phys. Rev.* D92.3 (2015), p. 035007. DOI: 10.1103/PhysRevD.92.035007. arXiv: 1504.01386 [hep-ph].

[112] Arpit Gupta, Reinard Primulando, and Prashant Saraswat. "A New Probe of Dark Sector Dynamics at the LHC". In: *JHEP* 09 (2015), p. 079. DOI: 10.1007/JHEP09(2015)079. arXiv: 1504.01385 [hep-ph].

[113] Karim Ghorbani and Leila Khalkhali. "Mono-Higgs signature in fermionic dark matter model". In: (2016). arXiv: 1608.04559 [hep-ph].

[114] ATLAS Collaboration. *Summary plots from the ATLAS Exotic physics group*. 2016. URL: https://atlas.web.cern.ch/Atlas/GROUPS/PHYSICS/CombinedSummaryPlots/EXOTICS/index.html.

[115] Patrick J. Fox, Graham D. Kribs, and Tim M. P. Tait. "Interpreting Dark Matter Direct Detection Independently of the Local Velocity and Density Distribution". In: *Phys. Rev.* D83 (2011), p. 034007. DOI: 10.1103/PhysRevD.83.034007. arXiv: 1011.1910 [hep-ph].

[116] Paolo Gondolo and Graciela B. Gelmini. "Halo independent comparison of direct dark matter detection data". In: *JCAP* 1212 (2012), p. 015. DOI: 10.1088/1475-7516/2012/12/015. arXiv: 1202.6359 [hep-ph].

[117] Gerard Jungman, Marc Kamionkowski, and Kim Griest. "Supersymmetric dark matter". In: *Phys. Rept.* 267 (1996), pp. 195–373. DOI: 10.1016/0370-1573(95)00058-5. arXiv: hep-ph/9506380 [hep-ph].

[118] D. S. Akerib et al. "First results from the LUX dark matter experiment at the Sanford Underground Research Facility". In: *Phys. Rev. Lett.* 112 (2014), p. 091303. DOI: 10.1103/PhysRevLett.112.091303. arXiv: 1310.8214 [astro-ph.CO].

[119] D. S. Akerib et al. "Improved Limits on Scattering of Weakly Interacting Massive Particles from Reanalysis of 2013 LUX Data". In: *Phys. Rev. Lett.* 116.16 (2016), p. 161301. DOI: 10.1103/PhysRevLett.116.161301. arXiv: 1512.03506 [astro-ph.CO].

[120] Andi Tan et al. "Dark Matter Results from First 98.7-day Data of PandaX-II Experiment". In: (2016). arXiv: 1607.07400 [hep-ex].

[121] D. S. Akerib et al. "Results on the Spin-Dependent Scattering of Weakly Interacting Massive Particles on Nucleons from the Run 3 Data of the LUX Experiment". In: *Phys. Rev. Lett.* 116.16 (2016), p. 161302. DOI: 10.1103/PhysRevLett.116.161302. arXiv: 1602.03489 [hep-ex].

[122] Changbo Fu et al. "Spin-dependent WIMP-nucleon cross section limits from first data of PandaX-II experiment". In: (2016). arXiv: 1611.06553 [hep-ex].

[123] C. Amole et al. "Improved dark matter search results from PICO-2L Run 2". In: *Phys. Rev. D* 93 (6 2016), p. 061101. DOI: 10.1103/PhysRevD.93.061101. URL: http://link.aps.org/doi/10.1103/PhysRevD.93.061101.

[124] C. Amole et al. "Improved dark matter search results from PICO-2L Run 2". In: *Phys. Rev.* D93.6 (2016), p. 061101. DOI: 10.1103/PhysRevD.93.061101. arXiv: 1601.03729 [astro-ph.CO].

[125] C. Amole et al. "Dark matter search results from the PICO-60 CF_3I bubble chamber". In: *Phys. Rev. D* 93 (5 2016), p. 052014. DOI: 10.1103/PhysRevD.93.052014. URL: http://link.aps.org/doi/10.1103/PhysRevD.93.052014.

[126] Laura Baudis. "Dark matter detection". In: *Journal of Physics G: Nuclear and Particle Physics* 43.4 (2016), p. 044001. URL: http://stacks.iop.org/0954-3899/43/i=4/a=044001.

[127] Marc Schumann et al. "Dark matter sensitivity of multi-ton liquid xenon detectors". In: *JCAP* 1510.10 (2015), p. 016. DOI: 10.1088/1475-7516/2015/10/016. arXiv: 1506.08309 [physics.ins-det].

[128] Marco Cirelli et al. "PPPC 4 DM ID: A Poor Particle Physicist Cookbook for Dark Matter Indirect Detection". In: *JCAP* 1103 (2011). [Erratum: JCAP1210,E01(2012)], p. 051. DOI: 10.1088/1475-7516/2012/10/E01,10.1088/1475-7516/2011/03/051. arXiv: 1012.4515 [hep-ph].

[129] Lars Bergstrom. "Radiative Processes in Dark Matter Photino Annihilation". In: *Phys. Lett.* B225 (1989), pp. 372–380. DOI: 10.1016/0370-2693(89)90585-6.

[130] R. Flores, K. A. Olive, and S. Rudaz. "Radiative processes in LSP annihilation". In: *Physics Letters B* 232 (Dec. 1989), pp. 377–382. DOI: 10.1016/0370-2693(89)90760-0.

[131] Torsten Bringmann, Lars Bergstrom, and Joakim Edsjo. "New Gamma-Ray Contributions to Supersymmetric Dark Matter Annihilation". In: *JHEP* 01 (2008), p. 049. DOI: 10.1088/1126-6708/2008/01/049. arXiv: 0710.3169 [hep-ph].

[132] Alejandro Ibarra, Sergio Lopez Gehler, and Miguel Pato. "Dark matter constraints from box-shaped gamma-ray features". In: *JCAP* 1207 (2012), p. 043. DOI: 10.1088/1475-7516/2012/07/043. arXiv: 1205.0007 [hep-ph].

[133] Alejandro Ibarra et al. "Gamma-ray triangles: a possible signature of asymmetric dark matter in indirect searches". In: *Phys. Rev.* D94.10 (2016), p. 103003. DOI: 10.1103/PhysRevD.94.103003. arXiv: 1604.01899 [hep-ph].

[134] Camilo Garcia-Cely and Julian Heeck. "Indirect searches of dark matter via polynomial spectral features". In: *JCAP* 1608.08 (2016), p. 023. DOI: 10.1088/1475-7516/2016/08/023. arXiv: 1605.08049 [hep-ph].

[135] M. Ackermann et al. "Searching for Dark Matter Annihilation from Milky Way Dwarf Spheroidal Galaxies with Six Years of Fermi Large Area Telescope Data". In: *Phys. Rev. Lett.* 115.23 (2015), p. 231301. DOI: 10.1103/PhysRevLett.115.231301. arXiv: 1503.02641 [astro-ph.HE].

[136] M. Ackermann et al. "Updated search for spectral lines from Galactic dark matter interactions with pass 8 data from the Fermi Large Area Telescope". In: *Phys. Rev.* D91.12 (2015), p. 122002. DOI: 10.1103/PhysRevD.91.122002. arXiv: 1506.00013 [astro-ph.HE].

[137] H. E. S. S. Collaboration. "Search for Dark Matter Annihilation Signals from the Fornax Galaxy Cluster with H.E.S.S." In: 750, 123 (May 2012), p. 123. DOI: 10.1088/0004-637X/750/2/123. arXiv: 1202.5494 [astro-ph.HE].

[138] A. Abramowski et al. "Search for Photon-Linelike Signatures from Dark Matter Annihilations with H.E.S.S." In: *Phys. Rev. Lett.* 110 (2013), p. 041301. DOI: 10.1103/PhysRevLett.110.041301. arXiv: 1301.1173 [astro-ph.HE].

[139] "http://dpnc.unige.ch/dampe/". In: (Accessed 5/3/17).

[140] "https://magic.mpp.mpg.de/." In: (Accessed 5/3/17).

[141] Jamie Holder. "Latest Results from VERITAS: Gamma 2016". In: *AIP Conf. Proc.* 1792.1 (2017), p. 020013. DOI: 10.1063/1.4968898. arXiv: 1609.02881 [astro-ph.HE].

[142] A. U. Abeysekara et al. "Sensitivity of the High Altitude Water Cherenkov Detector to Sources of Multi-TeV Gamma Rays". In: *Astropart. Phys.* 50-52 (2013), pp. 26–32. DOI: 10.1016/j.astropartphys.2013.08.002. arXiv: 1306.5800 [astro-ph.HE].

[143] Torsten Bringmann and Christoph Weniger. "Gamma Ray Signals from Dark Matter: Concepts, Status and Prospects". In: *Phys. Dark Univ.* 1 (2012), pp. 194–217. DOI: 10.1016/j.dark.2012.10.005. arXiv: 1208.5481 [hep-ph].

[144] "Electron and Positron Fluxes in Primary Cosmic Rays Measured with the Alpha Magnetic Spectrometer on the International Space Station". In: *Phys. Rev. Lett.* 113 (12 2014), p. 121102. DOI: 10.1103/PhysRevLett.113.121102. URL: http://link.aps.org/doi/10.1103/PhysRevLett.113.121102.

[145] M. Ackermann et al. "Measurement of Separate Cosmic-Ray Electron and Positron Spectra with the Fermi Large Area Telescope". In: *Physical Review Letters* 108.1, 011103 (Jan. 2012), p. 011103. DOI: 10.1103/PhysRevLett.108.011103. arXiv: 1109.0521 [astro-ph.HE].

[146] O. Adriani et al. "Cosmic-Ray Positron Energy Spectrum Measured by PAMELA". In: *Phys. Rev. Lett.* 111 (2013), p. 081102. DOI: 10.1103/PhysRevLett.111.081102. arXiv: 1308.0133 [astro-ph.HE].

[147] "http://www.ams02.org/2016/12/the-first-five-years-of-the-alpha-magnetic-spectrometer-on-the-international-space-station/". In: (Dec 2016, Accessed 5/3/17).

[148] M. G. Aartsen et al. "Improved limits on dark matter annihilation in the Sun with the 79-string IceCube detector and implications for supersymmetry". In: *JCAP* 1604.04 (2016), p. 022. DOI: 10.1088/1475-7516/2016/04/022. arXiv: 1601.00653 [hep-ph].

[149] M. G. Aartsen et al. "Search for annihilating dark matter in the Sun with 3 years of IceCube data". In: (2016). arXiv: 1612.05949 [astro-ph.HE].

[150] K. Choi et al. "Search for neutrinos from annihilation of captured low-mass dark matter particles in the Sun by Super-Kamiokande". In: *Phys. Rev. Lett.* 114.14 (2015), p. 141301. DOI: 10.1103/PhysRevLett.114.141301. arXiv: 1503.04858 [hep-ex].

[151] S. Adrian-Martinez et al. "Limits on Dark Matter Annihilation in the Sun using the ANTARES Neutrino Telescope". In: *Phys. Lett.* B759 (2016), pp. 69–74. DOI: 10.1016/j.physletb.2016.05.019. arXiv: 1603.02228 [astro-ph.HE].

[152] S. Adrian-Martinez et al. "Letter of intent for KM3NeT 2.0". In: *J. Phys.* G43.8 (2016), p. 084001. DOI: 10.1088/0954-3899/43/8/084001. arXiv: 1601.07459 [astro-ph.IM].

[153] Nicole F. Bell et al. "Dark matter at the LHC: Effective field theories and gauge invariance". In: *Phys. Rev.* D92.5 (2015), p. 053008. DOI: 10.1103/PhysRevD.92.053008. arXiv: 1503.07874 [hep-ph].

[154] Sarah Malik et al. "Interplay and Characterization of Dark Matter Searches at Colliders and in Direct Detection Experiments". In: (2014). arXiv: 1409.4075 [hep-ex].

[155] Oliver Buchmueller et al. "Characterising dark matter searches at colliders and direct detection experiments: Vector mediators". In: *JHEP* 1501 (2015), p. 037. DOI: 10.1007/JHEP01(2015)037. arXiv: 1407.8257 [hep-ph].

[156] Jalal Abdallah et al. "Simplified Models for Dark Matter and Missing Energy Searches at the LHC". In: (2014). arXiv: 1409.2893 [hep-ph].

[157] Matthew R. Buckley, David Feld, and Dorival Goncalves. "Scalar Simplified Models for Dark Matter". In: *Phys.Rev.* D91 (2015), p. 015017. DOI: 10.1103/PhysRevD.91.015017. arXiv: 1410.6497 [hep-ph].

[158] Daniele Alves et al. "Simplified Models for LHC New Physics Searches". In: *J.Phys.* G39 (2012), p. 105005. DOI: 10.1088/0954-3899/39/10/105005. arXiv: 1105.2838 [hep-ph].

[159] Johan Alwall, Philip Schuster, and Natalia Toro. "Simplified Models for a First Characterization of New Physics at the LHC". In: *Phys.Rev.* D79 (2009), p. 075020. DOI: 10.1103/PhysRevD.79.075020. arXiv: 0810.3921 [hep-ph].

[160] Jonathan L. Feng et al. "Isospin-Violating Dark Matter". In: *Phys.Lett.* B703 (2011), pp. 124–127. DOI: 10.1016/j.physletb.2011.07.083. arXiv: 1102.4331 [hep-ph].

[161] Jonathan L. Feng, Jason Kumar, and David Sanford. "Xenophobic Dark Matter". In: *Phys.Rev.* D88.1 (2013), p. 015021. DOI: 10.1103/PhysRevD.88.015021. arXiv: 1306.2315 [hep-ph].

[162] Yang Bai and Tim M.P. Tait. "Searches with Mono-Leptons". In: *Phys.Lett.* B723 (2013), pp. 384–387. DOI: 10.1016/j.physletb.2013.05.057. arXiv: 1208.4361 [hep-ph].

[163] Georges Aad et al. "Search for dark matter in events with a hadronically decaying W or Z boson and missing transverse momentum in pp collisions at $\sqrt{s}$ = 8 TeV with the ATLAS detector". In: *Phys.Rev.Lett.* 112.4 (2014), p. 041802. DOI: 10.1103/PhysRevLett.112.041802. arXiv: 1309.4017 [hep-ex].

[164] Georges Aad et al. "Search for new particles in events with one lepton and missing transverse momentum in pp collisions at $\sqrt{s}$ = 8 TeV with the ATLAS detector". In: *JHEP* 1409 (2014), p. 037. DOI: 10.1007/JHEP09(2014)037. arXiv: 1407.7494 [hep-ex].

[165] CMS-Collaboration. "Search for dark matter in the mono-lepton channel with pp collision events at center-of-mass energy of 8 TeV ". In: (2013). eprint: CMS-PAS-EXO-13-004.

[166] Vardan Khachatryan et al. "Search for physics beyond the standard model in final states with a lepton and missing transverse energy in proton-proton collisions at $\sqrt{s}$ = 8 TeV". In: (2014). arXiv: 1408.2745 [hep-ex].

[167] Paolo Ciafaloni and Alfredo Urbano. "TeV scale Dark Matter and electroweak radiative corrections". In: *Phys. Rev.* D82 (2010), p. 043512. DOI: 10.1103/PhysRevD.82.043512. arXiv: 1001.3950 [hep-ph].

[168] Daniel Schmeier. "Effective Models for Dark Matter at the International Linear Collider". In: (2013). arXiv: 1308.4409 [hep-ph].

[169] Yoonseok John Chae and Maxim Perelstein. "Dark Matter Search at a Linear Collider: Effective Operator Approach". In: *JHEP* 1305 (2013), p. 138. DOI: 10.1007/JHEP05(2013)138. arXiv: 1211.4008 [hep-ph].

[170] Johan Alwall et al. "MadGraph 5 : Going Beyond". In: *JHEP* 1106 (2011), p. 128. DOI: 10.1007/JHEP06(2011)128. arXiv: 1106.0522.

[171] Anthony DiFranzo et al. "Simplified models for dark matter interacting with quarks". In: *JHEP* 1311 (2013), p. 014. DOI: 10.1007/JHEP11(2013)014,10.1007/JHEP01(2014)162. arXiv: 1308.2679 [hep-ph].

[172] Yang Bai and Joshua Berger. "Fermion portal dark matter". In: *JHEP* 1311 (2013), p. 171. DOI: 10.1007/JHEP11(2013)171. arXiv: 1308.0612 [hep-ph].

[173] Haipeng An, Lian-Tao Wang, and Hao Zhang. "Dark matter with t-channel mediator: A simple step beyond contact interaction". In: *Phys. Rev. D* 89 (2014), p. 115014. DOI: 10.1103/PhysRevD.89.115014. arXiv: 1308.0592 [hep-ph].

[174] Spencer Chang et al. "Effective WIMPs". In: *Phys. Rev. D* 89 (2014), p. 015011. DOI: 10.1103/PhysRevD.89.015011. arXiv: 1307.8120 [hep-ph].

[175] Nicole F. Bell et al. "W/Z Bremsstrahlung as the Dominant Annihilation Channel for Dark Matter". In: *Phys. Rev.* D83 (2011), p. 013001. DOI: 10.1103/PhysRevD.83.013001. arXiv: 1009.2584 [hep-ph].

[176] Mathias Garny, Alejandro Ibarra, and Stefan Vogl. "Antiproton constraints on dark matter annihilations from internal electroweak bremsstrahlung". In: *JCAP* 1107 (2011), p. 028. DOI: 10.1088/1475-7516/2011/07/028. arXiv: 1105.5367 [hep-ph].

[177] Nicole F. Bell et al. "W/Z Bremsstrahlung as the Dominant Annihilation Channel for Dark Matter, Revisited". In: *Phys. Lett.* B706 (2011), pp. 6–12. DOI: 10.1016/j.physletb.2011.10.057. arXiv: 1104.3823 [hep-ph].

[178] Paolo Ciafaloni et al. "On the Importance of Electroweak Corrections for Majorana Dark Matter Indirect Detection". In: *JCAP* 1106 (2011), p. 018. DOI: 10.1088/1475-7516/2011/06/018. arXiv: 1104.2996 [hep-ph].

[179] Andrea De Simone et al. "On the effective operators for Dark Matter annihilations". In: *JCAP* 1302 (2013), p. 039. DOI: 10.1088/1475-7516/2013/02/039. arXiv: 1301.1486 [hep-ph].

[180] Yang Bai and Joshua Berger. "Fermion Portal Dark Matter". In: *JHEP* 11 (2013), p. 171. DOI: 10.1007/JHEP11(2013)171. arXiv: 1308.0612 [hep-ph].

[181] Michele Papucci, Alessandro Vichi, and Kathryn M. Zurek. "Monojet versus the rest of the world I: t-channel models". In: *JHEP* 11 (2014), p. 024. DOI: 10.1007/JHEP11(2014)024. arXiv: 1402.2285 [hep-ph].

[182] Mathias Garny, Alejandro Ibarra, and Stefan Vogl. "Signatures of Majorana dark matter with t-channel mediators". In: *Int. J. Mod. Phys.* D24.07 (2015), p. 1530019. DOI: 10.1142/S0218271815300190. arXiv: 1503.01500 [hep-ph].

[183] Mathias Garny et al. "Majorana Dark Matter with a Coloured Mediator: Collider vs Direct and Indirect Searches". In: *JHEP* 06 (2014), p. 169. DOI: 10.1007/JHEP06(2014)169. arXiv: 1403.4634 [hep-ph].

[184] Jan Heisig et al. "Constraints on Majorana Dark Matter from the LHC and IceCube". In: (2015). arXiv: 1509.07867 [hep-ph].

[185] Dan Hooper. "Z' mediated dark matter models for the Galactic Center gamma-ray excess". In: *Phys. Rev.* D91 (2015), p. 035025. DOI: 10.1103/PhysRevD.91.035025. arXiv: 1411.4079 [hep-ph].

[186] Mattias Blennow et al. "Halo-independent tests of dark matter direct detection signals: local DM density, LHC, and thermal freeze-out". In: *JCAP* 1508.08 (2015), p. 039. DOI: 10.1088/1475-7516/2015/08/039. arXiv: 1505.05710 [hep-ph].

[187] Oleg Lebedev and Yann Mambrini. "Axial dark matter: The case for an invisible Z". In: *Phys. Lett.* B734 (2014), pp. 350–353. DOI: 10.1016/j.physletb.2014.05.025. arXiv: 1403.4837 [hep-ph].

[188] Alexandre Alves et al. "Dark Matter Complementarity and the Z' Portal". In: *Phys. Rev.* D92.8 (2015), p. 083004. DOI: 10.1103/PhysRevD.92.083004. arXiv: 1501.03490 [hep-ph].

[189] Alexandre Alves, Stefano Profumo, and Farinaldo S. Queiroz. "The dark $Z^{'}$ portal: direct, indirect and collider searches". In: *JHEP* 04 (2014), p. 063. DOI: 10.1007/JHEP04(2014)063. arXiv: 1312.5281 [hep-ph].

[190] Alexandre Alves et al. "Dirac-fermionic dark matter in $U(1)_X$ models". In: *JHEP* 10 (2015), p. 076. DOI: 10.1007/JHEP10(2015)076. arXiv: 1506.06767 [hep-ph].

[191] Haipeng An, Xiangdong Ji, and Lian-Tao Wang. "Light Dark Matter and Z' Dark Force at Colliders". In: *JHEP* 07 (2012), p. 182. DOI: 10.1007/JHEP07(2012)182. arXiv: 1202.2894 [hep-ph].

[192] Haipeng An, Ran Huo, and Lian-Tao Wang. "Searching for Low Mass Dark Portal at the LHC". In: *Phys. Dark Univ.* 2 (2013), pp. 50–57. DOI: 10.1016/j.dark.2013.03.002. arXiv: 1212.2221 [hep-ph].

[193] Mads T. Frandsen et al. "LHC and Tevatron Bounds on the Dark Matter Direct Detection Cross-Section for Vector Mediators". In: *JHEP* 07 (2012), p. 123. DOI: 10.1007/JHEP07(2012)123. arXiv: 1204.3839 [hep-ph].

[194] Giorgio Arcadi et al. "Invisible Z' and dark matter: LHC vs LUX constraints". In: *JHEP* 03 (2014), p. 134. DOI: 10.1007/JHEP03(2014)134. arXiv: 1401.0221 [hep-ph].

[195] Mads T. Frandsen et al. "Direct detection of dark matter in models with a light Z'". In: *JHEP* 09 (2011), p. 128. DOI: 10.1007/JHEP09(2011)128. arXiv: 1107.2118 [hep-ph].

[196] P. Gondolo, P. Ko, and Y. Omura. "Light dark matter in leptophobic Z' models". In: *Phys. Rev.* D85 (2012), p. 035022. DOI: 10.1103/PhysRevD.85.035022. arXiv: 1106.0885 [hep-ph].

[197] Malcolm Fairbairn and John Heal. "Complementarity of dark matter searches at resonance". In: *Phys. Rev.* D90.11 (2014), p. 115019. DOI: 10.1103/PhysRevD.90.115019. arXiv: 1406.3288 [hep-ph].

[198] Philip Harris et al. "Constraining Dark Sectors at Colliders: Beyond the Effective Theory Approach". In: *Phys. Rev.* D91 (2015), p. 055009. DOI: 10.1103/PhysRevD.91.055009. arXiv: 1411.0535 [hep-ph].

[199] Celine Degrande et al. "UFO - The Universal FeynRules Output". In: *Comput. Phys. Commun.* 183 (2012), pp. 1201–1214. DOI: 10.1016/j.cpc.2012.01.022. arXiv: 1108.2040 [hep-ph].

[200] Fabio Maltoni and Tim Stelzer. "MadEvent: Automatic event generation with MadGraph". In: *JHEP* 02 (2003), p. 027. DOI: 10.1088/1126-6708/2003/02/027. arXiv: hep-ph/0208156 [hep-ph].

[201] Torbjorn Sjostrand, Stephen Mrenna, and Peter Z. Skands. "PYTHIA 6.4 Physics and Manual". In: *JHEP* 05 (2006), p. 026. DOI: 10.1088/1126-6708/2006/05/026. arXiv: hep-ph/0603175 [hep-ph].

[202] Matteo Cacciari, Gavin P. Salam, and Gregory Soyez. "FastJet User Manual". In: *Eur. Phys. J.* C72 (2012), p. 1896. DOI: 10.1140/epjc/s10052-012-1896-2. arXiv: 1111.6097 [hep-ph].

[203] J. de Favereau et al. "DELPHES 3, A modular framework for fast simulation of a generic collider experiment". In: *JHEP* 02 (2014), p. 057. DOI: 10.1007/JHEP02(2014)057. arXiv: 1307.6346 [hep-ex].

[204] R. Brun and F. Rademakers. "ROOT: An object oriented data analysis framework". In: *Nucl. Instrum. Meth.* A389 (1997), pp. 81–86. DOI: 10.1016/S0168-9002(97)00048-X.

[205] M. Bahr et al. "Herwig++ Physics and Manual". In: *Eur. Phys. J.* C58 (2008), pp. 639–707. DOI: 10.1140/epjc/s10052-008-0798-9. arXiv: 0803.0883 [hep-ph].

[206] "A Cambridge-Aachen (C-A) based Jet Algorithm for boosted top-jet tagging". In: (2009).

[207] Matteo Cacciari, Gavin P. Salam, and Gregory Soyez. "The Anti-k(t) jet clustering algorithm". In: *JHEP* 04 (2008), p. 063. DOI: 10.1088/1126-6708/2008/04/063. arXiv: 0802.1189 [hep-ph].

[208] Mikael Chala et al. "Constraining Dark Sectors with Monojets and Dijets". In: *JHEP* 07 (2015), p. 089. DOI: 10.1007/JHEP07(2015)089. arXiv: 1503.05916 [hep-ph].

[209] Nicole F. Bell et al. "Leptophilic dark matter with Z interactions". In: *Phys. Rev.* D90.3 (2014), p. 035027. DOI: 10.1103/PhysRevD.90.035027. arXiv: 1407.3001 [hep-ph].

[210] E. Aprile et al. "Dark Matter Results from 225 Live Days of XENON100 Data". In: *Phys. Rev. Lett.* 109 (2012), p. 181301. DOI: 10.1103/PhysRevLett.109.181301. arXiv: 1207.5988 [astro-ph.CO].

[211] Qing-Hong Cao, Ernest Ma, and Gabe Shaughnessy. "Dark Matter: The Leptonic Connection". In: *Phys. Lett.* B673 (2009), pp. 152–155. DOI: 10.1016/j.physletb.2009.02.015. arXiv: 0901.1334 [hep-ph].

[212] Alejandro Ibarra et al. "Cosmic Rays from Leptophilic Dark Matter Decay via Kinetic Mixing". In: *JCAP* 0908 (2009), p. 017. DOI: 10.1088/1475-7516/2009/08/017. arXiv: 0903.3625 [hep-ph].

[213] Pedro Schwaller, Tim M. P. Tait, and Roberto Vega-Morales. "Dark Matter and Vectorlike Leptons from Gauged Lepton Number". In: *Phys. Rev.* D88.3 (2013), p. 035001. DOI: 10.1103/PhysRevD.88.035001. arXiv: 1305.1108 [hep-ph].

[214] Daniel Schmidt, Thomas Schwetz, and Takashi Toma. "Direct Detection of Leptophilic Dark Matter in a Model with Radiative Neutrino Masses". In: *Phys. Rev.* D85 (2012), p. 073009. DOI: 10.1103/PhysRevD.85.073009. arXiv: 1201.0906 [hep-ph].

[215] Patrick J. Fox and Erich Poppitz. "Leptophilic Dark Matter". In: *Phys. Rev.* D79 (2009), p. 083528. DOI: 10.1103/PhysRevD.79.083528. arXiv: 0811.0399 [hep-ph].

[216] Joachim Kopp et al. "DAMA/LIBRA and leptonically interacting Dark Matter". In: *Phys. Rev.* D80 (2009), p. 083502. DOI: 10.1103/PhysRevD.80.083502. arXiv: 0907.3159 [hep-ph].

[217] Prateek Agrawal, Zackaria Chacko, and Christopher B. Verhaaren. "Leptophilic Dark Matter and the Anomalous Magnetic Moment of the Muon". In: *JHEP* 08 (2014), p. 147. DOI: 10.1007/JHEP08(2014)147. arXiv: 1402.7369 [hep-ph].

[218] Joachim Kopp, Lisa Michaels, and Juri Smirnov. "Loopy Constraints on Leptophilic Dark Matter and Internal Bremsstrahlung". In: *JCAP* 1404 (2014), p. 022. DOI: 10.1088/1475-7516/2014/04/022. arXiv: 1401.6457 [hep-ph].

[219] Timothy Cohen and Kathryn M. Zurek. "Leptophilic Dark Matter from the Lepton Asymmetry". In: *Phys. Rev. Lett.* 104 (2010), p. 101301. DOI: 10.1103/PhysRevLett.104.101301. arXiv: 0909.2035 [hep-ph].

[220] E. A. Baltz and L. Bergstrom. "Detection of leptonic dark matter". In: *Phys. Rev.* D67 (2003), p. 043516. DOI: 10.1103/PhysRevD.67.043516. arXiv: hep-ph/0211325 [hep-ph].

[221] Chuan-Ren Chen and Fuminobu Takahashi. "Cosmic rays from Leptonic Dark Matter". In: *JCAP* 0902 (2009), p. 004. DOI: 10.1088/1475-7516/2009/02/004. arXiv: 0810.4110 [hep-ph].

[222] D. Spolyar et al. "High Energy Neutrinos As A Test of Leptophilic Dark Matter". In: *ArXiv e-prints* (May 2009). arXiv: 0905.4764 [astro-ph.CO].

[223] Pyungwon Ko and Yuji Omura. "Supersymmetric U(1)B x U(1)L model with leptophilic and leptophobic cold dark matters". In: *Phys. Lett.* B701 (2011), pp. 363–366. DOI: 10.1016/j.physletb.2011.06.009. arXiv: 1012.4679 [hep-ph].

[224] Wei Chao. "Pure Leptonic Gauge Symmetry, Neutrino Masses and Dark Matter". In: *Phys. Lett.* B695 (2011), pp. 157–161. DOI: 10.1016/j.physletb.2010.10.056. arXiv: 1005.1024 [hep-ph].

[225] Moumita Das and Subhendra Mohanty. "Leptophilic dark matter in gauged $L_\mu - L_\tau$ extension of MSSM". In: *Phys. Rev.* D89.2 (2014), p. 025004. DOI: 10.1103/PhysRevD.89.025004. arXiv: 1306.4505 [hep-ph].

[226] Xiao-Jun Bi, Xiao-Gang He, and Qiang Yuan. "Parameters in a class of leptophilic models from PAMELA, ATIC and FERMI". In: *Phys. Lett.* B678 (2009), pp. 168–173. DOI: 10.1016/j.physletb.2009.06.009. arXiv: 0903.0122 [hep-ph].

[227] Yang Bai and Joshua Berger. "Lepton Portal Dark Matter". In: *JHEP* 08 (2014), p. 153. DOI: 10.1007/JHEP08(2014)153. arXiv: 1402.6696 [hep-ph].

[228] Francesco D'Eramo, Bradley J. Kavanagh, and Paolo Panci. "Probing Leptophilic Dark Sectors with Hadronic Processes". In: (2017). arXiv: 1702.00016 [hep-ph].

[229] M. Ackermann et al. "Dark matter constraints from observations of 25 Milky Way satellite galaxies with the Fermi Large Area Telescope". In: *Phys. Rev.* D89 (2014), p. 042001. DOI: 10.1103/PhysRevD.89.042001. arXiv: 1310.0828 [astro-ph.HE].

[230] Dan Hooper, Pasquale Blasi, and Pasquale Dario Serpico. "Pulsars as the Sources of High Energy Cosmic Ray Positrons". In: *JCAP* 0901 (2009), p. 025. DOI: 10.1088/1475-7516/2009/01/025. arXiv: 0810.1527 [astro-ph].

[231] Stefano Profumo. "Dissecting cosmic-ray electron-positron data with Occam's Razor: the role of known Pulsars". In: *Central Eur. J. Phys.* 10 (2011), pp. 1–31. DOI: 10.2478/s11534-011-0099-z. arXiv: 0812.4457 [astro-ph].

[232] M. Kachelriess, P. D. Serpico, and M. Aa. Solberg. "On the role of electroweak bremsstrahlung for indirect dark matter signatures". In: *Phys. Rev.* D80 (2009), p. 123533. DOI: 10.1103/PhysRevD.80.123533. arXiv: 0911.0001 [hep-ph].

[233] Patrick J. Fox et al. "LEP Shines Light on Dark Matter". In: *Phys. Rev.* D84 (2011), p. 014028. DOI: 10.1103/PhysRevD.84.014028. arXiv: 1103.0240 [hep-ph].

[234] Serguei Chatrchyan et al. "Search for dark matter and large extra dimensions in monojet events in pp collisions at $\sqrt{s} = 7$ TeV". In: *JHEP* 09 (2012), p. 094. DOI: 10.1007/JHEP09(2012)094. arXiv: 1206.5663 [hep-ex].

[235] Georges Aad et al. "Search for dark matter candidates and large extra dimensions in events with a photon and missing transverse momentum in pp collision data at $\sqrt{s} = 7$ TeV with the ATLAS detector". In: *Phys. Rev. Lett.* 110.1 (2013), p. 011802. DOI: 10.1103/PhysRevLett.110.011802. arXiv: 1209.4625 [hep-ex].

[236] Georges Aad et al. "Search for dark matter in events with a Z boson and missing transverse momentum in pp collisions at $\sqrt{s}$=8 TeV with the ATLAS detector". In: *Phys. Rev.* D90.1 (2014), p. 012004. DOI: 10.1103/PhysRevD.90.012004. arXiv: 1404.0051 [hep-ex].

[237] ROBERT FOOT. "NEW PHYSICS FROM ELECTRIC CHARGE QUANTIZATION?" In: *Modern Physics Letters A* 06.07 (1991), pp. 527–529. DOI: 10.1142/S0217732391000543.

[238] X. G. He et al. "NEW Z-prime PHENOMENOLOGY". In: *Phys. Rev.* D43 (1991), pp. 22–24. DOI: 10.1103/PhysRevD.43.22.

[239] Xiao-Gang He et al. "Simplest Z-prime model". In: *Phys. Rev.* D44 (1991), pp. 2118–2132. DOI: 10.1103/PhysRevD.44.2118.

[240] Seungwon Baek and Pyungwon Ko. "Phenomenology of U(1)(L(mu)-L(tau)) charged dark matter at PAMELA and colliders". In: *JCAP* 0910 (2009), p. 011. DOI: 10.1088/1475-7516/2009/10/011. arXiv: 0811.1646 [hep-ph].

[241] Neil D. Christensen and Claude Duhr. "FeynRules - Feynman rules made easy". In: *Comput. Phys. Commun.* 180 (2009), pp. 1614–1641. DOI: 10.1016/j.cpc.2009.02.018. arXiv: 0806.4194 [hep-ph].

[242] G. Belanger et al. "micrOMEGAs 3: A program for calculating dark matter observables". In: *Comput. Phys. Commun.* 185 (2014), pp. 960–985. DOI: 10.1016/j.cpc.2013.10.016. arXiv: 1305.0237 [hep-ph].

[243] P. A. R. Ade et al. "Planck 2013 results. XVI. Cosmological parameters". In: *Astron. Astrophys.* 571 (2014), A16. DOI: 10.1051/0004-6361/201321591. arXiv: 1303.5076 [astro-ph.CO].

[244] Pierre Fayet. "U-boson production in e+ e- annihilations, psi and Upsilon decays, and Light Dark Matter". In: *Phys. Rev.* D75 (2007), p. 115017. DOI: 10.1103/PhysRevD.75.115017. arXiv: hep-ph/0702176 [HEP-PH].

[245] L. B. Auerbach et al. "Measurement of electron - neutrino - electron elastic scattering". In: *Phys. Rev.* D63 (2001), p. 112001. DOI: 10.1103/PhysRevD.63.112001. arXiv: hep-ex/0101039 [hep-ex].

[246] the SLD Electroweak. "A Combination of preliminary electroweak measurements and constraints on the standard model". In: (2003). arXiv: hep-ex/0312023 [hep-ex].

[247] Matthew R. Buckley et al. "Light Z' Bosons at the Tevatron". In: *Phys. Rev.* D83 (2011), p. 115013. DOI: 10.1103/PhysRevD.83.115013. arXiv: 1103.6035 [hep-ph].

[248] K. S. Babu, Christopher F. Kolda, and John March-Russell. "Implications of generalized Z - Z-prime mixing". In: *Phys. Rev.* D57 (1998), pp. 6788–6792. DOI: 10.1103/PhysRevD.57.6788. arXiv: hep-ph/9710441 [hep-ph].

[249] Anson Hook, Eder Izaguirre, and Jay G. Wacker. "Model Independent Bounds on Kinetic Mixing". In: *Adv. High Energy Phys.* 2011 (2011), p. 859762. DOI: 10.1155/2011/859762. arXiv: 1006.0973 [hep-ph].

[250] Serguei Chatrchyan et al. "Observation of Z decays to four leptons with the CMS detector at the LHC". In: *JHEP* 12 (2012), p. 034. DOI: 10.1007/JHEP12(2012)034. arXiv: 1210.3844 [hep-ex].

[251] Georges Aad et al. "Measurements of Four-Lepton Production at the Z Resonance in pp Collisions at $\sqrt{s}$ =7 and 8 TeV with ATLAS". In: *Phys. Rev. Lett.* 112.23 (2014), p. 231806. DOI: 10.1103/PhysRevLett.112.231806. arXiv: 1403.5657 [hep-ex].

[252] Wolfgang Altmannshofer et al. "Quark flavor transitions in $L_\mu - L_\tau$ models". In: *Phys. Rev.* D89 (2014), p. 095033. DOI: 10.1103/PhysRevD.89.095033. arXiv: 1403.1269 [hep-ph].

[253] Keisuke Harigaya et al. "Muon g-2 and LHC phenomenology in the $L_\mu - L_\tau$ gauge symmetric model". In: *JHEP* 03 (2014), p. 105. DOI: 10.1007/JHEP03(2014)105. arXiv: 1311.0870 [hep-ph].

[254] Torbjorn Sjostrand, Stephen Mrenna, and Peter Z. Skands. "A Brief Introduction to PYTHIA 8.1". In: *Comput. Phys. Commun.* 178 (2008), pp. 852–867. DOI: 10.1016/j.cpc.2008.01.036. arXiv: 0710.3820 [hep-ph].

[255] Eric Conte, Benjamin Fuks, and Guillaume Serret. "MadAnalysis 5, A User-Friendly Framework for Collider Phenomenology". In: *Comput. Phys. Commun.* 184 (2013), pp. 222–256. DOI: 10.1016/j.cpc.2012.09.009. arXiv: 1206.1599 [hep-ph].

[256] Georges Aad et al. "Electron performance measurements with the ATLAS detector using the 2010 LHC proton-proton collision data". In: *Eur. Phys. J.* C72 (2012), p. 1909. DOI: 10.1140/epjc/s10052-012-1909-1. arXiv: 1110.3174 [hep-ex].

[257] Nicole F. Bell, Yi Cai, and Rebecca K. Leane. "Dark Forces in the Sky: Signals from Z' and the Dark Higgs". In: *JCAP* 1608.08 (2016), p. 001. DOI: 10.1088/1475-7516/2016/08/001. arXiv: 1605.09382 [hep-ph].

[258] Patrick J. Fox et al. "Taking a Razor to Dark Matter Parameter Space at the LHC". In: *Phys. Rev.* D86 (2012), p. 015010. DOI: 10.1103/PhysRevD.86.015010. arXiv: 1203.1662 [hep-ph].

[259] Motoi Endo and Yasuhiro Yamamoto. "Unitarity Bounds on Dark Matter Effective Interactions at LHC". In: *JHEP* 06 (2014), p. 126. DOI: 10.1007/JHEP06(2014)126. arXiv: 1403.6610 [hep-ph].

[260] Sonia El Hedri, William Shepherd, and Devin G. E. Walker. "Perturbative Unitarity Constraints on Gauge Portals". In: (2014). arXiv: 1412.5660 [hep-ph].

[261] Seungwon Baek et al. "Beyond the Dark matter effective field theory and a simplified model approach at colliders". In: *Phys. Lett.* B756 (2016), pp. 289–294. DOI: 10.1016/j.physletb.2016.03.026. arXiv: 1506.06556 [hep-ph].

[262] Ulrich Haisch, Felix Kahlhoefer, and Tim M. P. Tait. "On Mono-W Signatures in Spin-1 Simplified Models". In: (2016). arXiv: 1603.01267 [hep-ph].

[263] Christoph Englert, Matthew McCullough, and Michael Spannowsky. "S-Channel Dark Matter Simplified Models and Unitarity". In: (2016). arXiv: 1604.07975 [hep-ph].

[264] Nicole Bell et al. "Unitarisation of EFT Amplitudes for Dark Matter Searches at the LHC". In: (2016). arXiv: 1606.02722 [hep-ph].

[265] James M. Cline et al. "Multimediator models for the galactic center gamma ray excess". In: *Phys. Rev.* D91.11 (2015), p. 115010. DOI: 10.1103/PhysRevD.91.115010. arXiv: 1503.08213 [hep-ph].

[266] Arghya Choudhury et al. "Less-simplified models of dark matter for direct detection and the LHC". In: (2015). arXiv: 1509.05771 [hep-ph].

[267] Karim Ghorbani and Hossein Ghorbani. "Two-portal Dark Matter". In: *Phys. Rev.* D91.12 (2015), p. 123541. DOI: 10.1103/PhysRevD.91.123541. arXiv: 1504.03610 [hep-ph].

[268] Michael Duerr et al. "How to save the WIMP: global analysis of a dark matter model with two s-channel mediators". In: *JHEP* 09 (2016), p. 042. DOI: 10.1007/JHEP09(2016)042. arXiv: 1606.07609 [hep-ph].

[269] Adam Martin, Jessie Shelton, and James Unwin. "Fitting the Galactic Center Gamma-Ray Excess with Cascade Annihilations". In: *Phys. Rev.* D90.10 (2014), p. 103513. DOI: 10.1103/PhysRevD.90.103513. arXiv: 1405.0272 [hep-ph].

[270] Mohammad Abdullah et al. "Hidden on-shell mediators for the Galactic Center γ-ray excess". In: *Phys. Rev.* D90 (2014), p. 035004. DOI: 10.1103/PhysRevD.90.035004. arXiv: 1404.6528 [hep-ph].

[271] Asher Berlin et al. "Hidden Sector Dark Matter Models for the Galactic Center Gamma-Ray Excess". In: *Phys. Rev.* D90.1 (2014), p. 015032. DOI: 10.1103/PhysRevD.90.015032. arXiv: 1405.5204 [hep-ph].

[272] Gilly Elor, Nicholas L. Rodd, and Tracy R. Slatyer. "Multistep cascade annihilations of dark matter and the Galactic Center excess". In: *Phys. Rev.* D91 (2015), p. 103531. DOI: 10.1103/PhysRevD.91.103531. arXiv: 1503.01773 [hep-ph].

[273] Gilly Elor et al. "Model-Independent Indirect Detection Constraints on Hidden Sector Dark Matter". In: (2015). arXiv: 1511.08787 [hep-ph].

[274] Wei Chao, Michael J. Ramsey-Musolf, and Jiang-Hao Yu. "Indirect Detection Imprint of a CP Violating Dark Sector". In: (2016). arXiv: 1602.05192 [hep-ph].

[275] Maxim Pospelov, Adam Ritz, and Mikhail B. Voloshin. "Secluded WIMP Dark Matter". In: *Phys. Lett.* B662 (2008), pp. 53–61. DOI: 10.1016/j.physletb.2008.02.052. arXiv: 0711.4866 [hep-ph].

[276] Maxim Pospelov and Adam Ritz. "Astrophysical Signatures of Secluded Dark Matter". In: *Phys. Lett.* B671 (2009), pp. 391–397. DOI: 10.1016/j.physletb.2008.12.012. arXiv: 0810.1502 [hep-ph].

[277] Maxim Pospelov. "Secluded U(1) below the weak scale". In: *Phys. Rev.* D80 (2009), p. 095002. DOI: 10.1103/PhysRevD.80.095002. arXiv: 0811.1030 [hep-ph].

[278] Jonathan L. Feng, Huitzu Tu, and Hai-Bo Yu. "Thermal Relics in Hidden Sectors". In: *JCAP* 0810 (2008), p. 043. DOI: 10.1088/1475-7516/2008/10/043. arXiv: 0808.2318 [hep-ph].

[279] Jonathan L. Feng and Jason Kumar. "The WIMPless Miracle: Dark-Matter Particles without Weak-Scale Masses or Weak Interactions". In: *Phys. Rev. Lett.* 101 (2008), p. 231301. DOI: 10.1103/PhysRevLett.101.231301. arXiv: 0803.4196 [hep-ph].

[280] Ira Z. Rothstein, Thomas Schwetz, and Jure Zupan. "Phenomenology of Dark Matter annihilation into a long-lived intermediate state". In: *JCAP* 0907 (2009), p. 018. DOI: 10.1088/1475-7516/2009/07/018. arXiv: 0903.3116 [astro-ph.HE].

[281] Jeremy Mardon, Yasunori Nomura, and Jesse Thaler. "Cosmic Signals from the Hidden Sector". In: *Phys. Rev.* D80 (2009), p. 035013. DOI: 10.1103/PhysRevD.80.035013. arXiv: 0905.3749 [hep-ph].

[282] Jeremy Mardon et al. "Dark Matter Signals from Cascade Annihilations". In: *JCAP* 0905 (2009), p. 016. DOI: 10.1088/1475-7516/2009/05/016. arXiv: 0901.2926 [hep-ph].

[283] Patrick Meade, Michele Papucci, and Tomer Volansky. "Dark Matter Sees The Light". In: *JHEP* 12 (2009), p. 052. DOI: 10.1088/1126-6708/2009/12/052. arXiv: 0901.2925 [hep-ph].

[284] Clifford Cheung et al. "Origins of Hidden Sector Dark Matter I: Cosmology". In: *JHEP* 03 (2011), p. 042. DOI: 10.1007/JHEP03(2011)042. arXiv: 1010.0022 [hep-ph].

[285] Hooman Davoudiasl and Ian M. Lewis. "Dark Matter from Hidden Forces". In: *Phys. Rev.* D89.5 (2014), p. 055026. DOI: 10.1103/PhysRevD.89.055026. arXiv: 1309.6640 [hep-ph].

[286] Jia Liu, Neal Weiner, and Wei Xue. "Signals of a Light Dark Force in the Galactic Center". In: *JHEP* 08 (2015), p. 050. DOI: 10.1007/JHEP08(2015)050. arXiv: 1412.1485 [hep-ph].

[287] Edward Hardy, Robert Lasenby, and James Unwin. "Annihilation Signals from Asymmetric Dark Matter". In: *JHEP* 07 (2014), p. 049. DOI: 10.1007/JHEP07(2014)049. arXiv: 1402.4500 [hep-ph].

[288] Celine Boehm, Matthew J. Dolan, and Christopher McCabe. "A weighty interpretation of the Galactic Centre excess". In: *Phys. Rev.* D90.2 (2014), p. 023531. DOI: 10.1103/PhysRevD.90.023531. arXiv: 1404.4977 [hep-ph].

[289] Samuel D. McDermott. "Lining up the Galactic Center Gamma-Ray Excess". In: *Phys. Dark Univ.* 7-8 (2014), pp. 12–15. DOI: 10.1016/j.dark.2015.05.001. arXiv: 1406.6408 [hep-ph].

[290] Zackaria Chacko et al. "Hidden dark matter sector, dark radiation, and the CMB". In: *Phys. Rev.* D92 (2015), p. 055033. DOI: 10.1103/PhysRevD.92.055033. arXiv: 1505.04192 [hep-ph].

[291] P. Ko and Yong Tang. "Dark Higgs Channel for FERMI GeV γ-ray Excess". In: *JCAP* 1602.02 (2016), p. 011. DOI: 10.1088/1475-7516/2016/02/011. arXiv: 1504.03908 [hep-ph].

[292] P. Ko, Wan-Il Park, and Yong Tang. "Higgs portal vector dark matter for GeV scale γ-ray excess from galactic center". In: *JCAP* 1409 (2014), p. 013. DOI: 10.1088/1475-7516/2014/09/013. arXiv: 1404.5257 [hep-ph].

[293] Yeong Gyun Kim et al. "Secluded singlet fermionic dark matter driven by the Fermi gamma-ray excess". In: (2016). arXiv: 1601.05089 [hep-ph].

[294] Dan Hooper, Neal Weiner, and Wei Xue. "Dark Forces and Light Dark Matter". In: *Phys. Rev.* D86 (2012), p. 056009. DOI: 10.1103/PhysRevD.86.056009. arXiv: 1206.2929 [hep-ph].

[295] Asher Berlin et al. "Pseudoscalar Portal Dark Matter". In: *Phys. Rev.* D92 (2015), p. 015005. DOI: 10.1103/PhysRevD.92.015005. arXiv: 1502.06000 [hep-ph].

[296] James M. Cline et al. "The windows for kinetically mixed Z'-mediated dark matter and the galactic center gamma ray excess". In: *JHEP* 08 (2014), p. 131. DOI: 10.1007/JHEP08(2014)131. arXiv: 1405.7691 [hep-ph].

[297] David E. Morrissey and Andrew Paul Spray. "New Limits on Light Hidden Sectors from Fixed-Target Experiments". In: *JHEP* 06 (2014), p. 083. DOI: 10.1007/JHEP06(2014)083. arXiv: 1402.4817 [hep-ph].

[298] A. Djouadi, J. Kalinowski, and M. Spira. "HDECAY: A Program for Higgs boson decays in the standard model and its supersymmetric extension". In: *Comput. Phys. Commun.* 108 (1998), pp. 56–74. DOI: 10.1016/S0010-4655(97)00123-9. arXiv: hep-ph/9704448 [hep-ph].

[299] Torbjörn Sjöstrand et al. "An Introduction to PYTHIA 8.2". In: *Comput. Phys. Commun.* 191 (2015), pp. 159–177. DOI: 10.1016/j.cpc.2015.01.024. arXiv: 1410.3012 [hep-ph].

[300] Fang Chen, James M. Cline, and Andrew R. Frey. "Nonabelian dark matter: Models and constraints". In: *Phys. Rev.* D80 (2009), p. 083516. DOI: 10.1103/PhysRevD.80.083516. arXiv: 0907.4746 [hep-ph].

[301] Nicole F. Bell, Yi Cai, and Rebecca K. Leane. "Impact of Mass Generation for Simplified Dark Matter Models". In: (2016). DOI: 10.1088/1475-7516/2017/01/039. arXiv: 1610.03063 [hep-ph].

[302] T. Kunimasa and T. Goto. "Generalization of the Stueckelberg Formalism to the Massive Yang-Mills Field". In: *Prog. Theor. Phys.* 37 (1967), pp. 452–464. DOI: 10.1143/PTP.37.452.

[303] A. A. Slavnov. "Ward Identities in Gauge Theories". In: *Theor. Math. Phys.* 10 (1972). [Teor. Mat. Fiz.10,153(1972)], pp. 99–107. DOI: 10.1007/BF01090719.

[304] M. J. G. Veltman. "Perturbation theory of massive Yang-Mills fields". In: *Nucl. Phys.* B7 (1968), pp. 637–650. DOI: 10.1016/0550-3213(68)90197-1.

[305] A. A. Slavnov and L. D. Faddeev. "Massless and massive yang-mills field. (in russian)". In: *Theor. Math. Phys.* 3 (1970). [Teor. Mat. Fiz.3,18(1970)], pp. 312–316. DOI: 10.1007/BF01031585.

[306] A. I. Vainshtein and I. B. Khriplovich. "On the zero-mass limit and renormalizability in the theory of massive yang-mills field". In: *Yad. Fiz.* 13 (1971), pp. 198–211.

[307] Ken-ichi Shizuya. "Renormalization of Two-Dimensional Massive Yang-Mills Theory and Nonrenormalizability of Its Four-Dimensional Version". In: *Nucl. Phys.* B121 (1977), pp. 125–140. DOI: 10.1016/0550-3213(77)90331-5.

[308] D. G. C. McKeon. "On using the Freedman-Townsend model to generate massive vectors". In: *Can. J. Phys.* 69 (1991), pp. 1249–1255. DOI: 10.1139/p91-187.

[309] Daniel Z. Freedman and P. K. Townsend. "Antisymmetric Tensor Gauge Theories and Nonlinear Sigma Models". In: *Nucl. Phys.* B177 (1981), pp. 282–296. DOI: 10.1016/0550-3213(81)90392-8.

[310] Yu. N. Kafiev. "Massive Yang-Mills Fields: Gauge Invariance and One Loop Counterterm". In: *Nucl. Phys.* B201 (1982), pp. 341–351. DOI: 10.1016/0550-3213(82)90436-9.

[311] Andrea De Simone and Thomas Jacques. "Simplified Models vs. Effective Field Theory Approaches in Dark Matter Searches". In: (2016). arXiv: 1603.08002 [hep-ph].

[312] Ahmed Ismail et al. "Axial Vector Z' and Anomaly Cancellation". In: (2016). arXiv: 1609.02188 [hep-ph].

[313] Steven Weinberg. "Goldstone Bosons as Fractional Cosmic Neutrinos". In: *Phys. Rev. Lett.* 110.24 (2013), p. 241301. DOI: 10.1103/PhysRevLett.110.241301. arXiv: 1305.1971 [astro-ph.CO].

[314] Gary Steigman, Basudeb Dasgupta, and John F. Beacom. "Precise Relic WIMP Abundance and its Impact on Searches for Dark Matter Annihilation". In: *Phys. Rev.* D86 (2012), p. 023506. DOI: 10.1103/PhysRevD.86.023506. arXiv: 1204.3622 [hep-ph].

[315] Nicole F. Bell et al. "Enhancing Dark Matter Annihilation Rates with Dark Bremsstrahlung". In: (2017). arXiv: 1705.01105 [hep-ph].

[316] Ricardo Flores, Keith A. Olive, and Serge Rudaz. "Radiative Processes in Lsp Annihilation". In: *Phys. Lett.* B232 (1989), pp. 377–382. DOI: 10.1016/0370-2693(89)90760-0.

[317] Lars Bergstrom, Torsten Bringmann, and Joakim Edsjo. "New Positron Spectral Features from Supersymmetric Dark Matter - a Way to Explain the PAMELA Data?" In: *Phys. Rev.* D78 (2008), p. 103520. DOI: 10.1103/PhysRevD.78.103520. arXiv: 0808.3725 [astro-ph].

[318] V. Barger et al. "Generic dark matter signature for gamma-ray telescopes". In: *Phys. Rev.* D80 (2009), p. 063537. DOI: 10.1103/PhysRevD.80.063537. arXiv: 0906.3009 [hep-ph].

[319] Nicole F. Bell et al. "Dark Matter Annihilation Signatures from Electroweak Bremsstrahlung". In: *Phys. Rev.* D84 (2011), p. 103517. DOI: 10.1103/PhysRevD.84.103517. arXiv: 1101.3357 [hep-ph].

[320] Nicole F. Bell, Amelia J. Brennan, and Thomas D. Jacques. "Neutrino signals from electroweak bremsstrahlung in solar WIMP annihilation". In: *JCAP* 1210 (2012), p. 045. DOI: 10.1088/1475-7516/2012/10/045. arXiv: 1206.2977 [hep-ph].

[321] Paolo Ciafaloni et al. "The Role of Electroweak Corrections for the Dark Matter Relic Abundance". In: *JCAP* 1310 (2013), p. 031. DOI: 10.1088/1475-7516/2013/10/031. arXiv: 1305.6391 [hep-ph].

[322] V. Berezinsky, M. Kachelriess, and S. Ostapchenko. "Electroweak jet cascading in the decay of superheavy particles". In: *Phys. Rev. Lett.* 89 (2002), p. 171802. DOI: 10.1103/PhysRevLett.89.171802. arXiv: hep-ph/0205218 [hep-ph].

[323] M. Kachelriess and P. D. Serpico. "Model-independent dark matter annihilation bound from the diffuse γ ray flux". In: *Phys. Rev.* D76 (2007), p. 063516. DOI: 10.1103/PhysRevD.76.063516. arXiv: 0707.0209 [hep-ph].

[324] Nicole F. Bell et al. "Electroweak Bremsstrahlung in Dark Matter Annihilation". In: *Phys. Rev.* D78 (2008), p. 083540. DOI: 10.1103/PhysRevD.78.083540. arXiv: 0805.3423 [hep-ph].

[325] James B. Dent, Robert J. Scherrer, and Thomas J. Weiler. "Toward a Minimum Branching Fraction for Dark Matter Annihilation into Electromagnetic Final States". In: *Phys. Rev.* D78 (2008), p. 063509. DOI: 10.1103/PhysRevD.78.063509. arXiv: 0806.0370 [astro-ph].

[326] Paolo Ciafaloni et al. "Weak Corrections are Relevant for Dark Matter Indirect Detection". In: *JCAP* 1103 (2011), p. 019. DOI: 10.1088/1475-7516/2011/03/019. arXiv: 1009.0224 [hep-ph].

[327] Vernon Barger, Wai-Yee Keung, and Danny Marfatia. "Bremsstrahlung in dark matter annihilation". In: *Phys. Lett.* B707 (2012), pp. 385–388. DOI: 10.1016/j.physletb.2012.01.001. arXiv: 1111.4523 [hep-ph].

[328] Keita Fukushima et al. "Bremsstrahlung signatures of dark matter annihilation in the Sun". In: *Phys. Rev.* D86 (2012), p. 076014. DOI: 10.1103/PhysRevD.86.076014. arXiv: 1208.1010 [hep-ph].

[329] Federica Giacchino, Laura Lopez-Honorez, and Michel H. G. Tytgat. "Scalar Dark Matter Models with Significant Internal Bremsstrahlung". In: *JCAP* 1310 (2013), p. 025. DOI: 10.1088/1475-7516/2013/10/025. arXiv: 1307.6480 [hep-ph].

[330] Mathias Garny et al. "Internal bremsstrahlung signatures in light of direct dark matter searches". In: *JCAP* 1312 (2013), p. 046. DOI: 10.1088/1475-7516/2013/12/046. arXiv: 1306.6342 [hep-ph].

[331] Torsten Bringmann and Francesca Calore. "Significant Enhancement of Neutralino Dark Matter Annihilation from Electroweak Bremsstrahlung". In: *Phys. Rev. Lett.* 112 (2014), p. 071301. DOI: 10.1103/PhysRevLett.112.071301. arXiv: 1308.1089 [hep-ph].

[332] Torsten Bringmann, Ahmad J. Galea, and Parampreet Walia. "Leading QCD Corrections for Indirect Dark Matter Searches: a Fresh Look". In: *Phys. Rev.* D93.4 (2016), p. 043529. DOI: 10.1103/PhysRevD.93.043529. arXiv: 1510.02473 [hep-ph].

[333] Gulab Bambhaniya et al. "Vector dark matter annihilation with internal bremsstrahlung". In: (2016). arXiv: 1609.05369 [hep-ph].

[334] Jason Kumar et al. "Gamma-ray Signals from Dark Matter Annihilation Via Charged Mediators". In: *Phys. Rev.* D94.1 (2016), p. 015022. DOI: 10.1103/PhysRevD.94.015022. arXiv: 1605.03224 [hep-ph].

[335] Jason Kumar, Jiajun Liao, and Danny Marfatia. "Dark matter annihilation with s-channel internal Higgsstrahlung". In: *Phys. Lett.* B759 (2016), pp. 277–281. DOI: 10.1016/j.physletb.2016.05.085. arXiv: 1605.00611 [hep-ph].

[336] Feng Luo and Tevong You. "Enhancement of Majorana Dark Matter Annihilation Through Higgs Bremsstrahlung". In: *JCAP* 1312 (2013), p. 024. DOI: 10.1088/1475-7516/2013/12/024. arXiv: 1310.5129 [hep-ph].

[337] Xue-lei Chen and Marc Kamionkowski. "Three body annihilation of neutralinos below two-body thresholds". In: *JHEP* 07 (1998), p. 001. DOI: 10.1088/1126-6708/1998/07/001. arXiv: hep-ph/9805383 [hep-ph].

[338] Paolo Ciafaloni et al. "Initial State Radiation in Majorana Dark Matter Annihilations". In: *JCAP* 1110 (2011), p. 034. DOI: 10.1088/1475-7516/2011/10/034. arXiv: 1107.4453 [hep-ph].

[339] Mathias Garny, Alejandro Ibarra, and Stefan Vogl. "Dark matter annihilations into two light fermions and one gauge boson: General analysis and antiproton constraints". In: *JCAP* 1204 (2012), p. 033. DOI: 10.1088/1475-7516/2012/04/033. arXiv: 1112.5155 [hep-ph].

[340] Paolo Ciafaloni et al. "Electroweak Bremsstrahlung for Wino-Like Dark Matter Annihilations". In: *JCAP* 1206 (2012), p. 016. DOI: 10.1088/1475-7516/2012/06/016. arXiv: 1202.0692 [hep-ph].

[341] Michael Duerr et al. "Hunting the dark Higgs". In: (2017). arXiv: 1701.08780 [hep-ph].

[342] Malte Buschmann et al. "Lepton Jets from Radiating Dark Matter". In: *JHEP* 07 (2015), p. 045. DOI: 10.1007/JHEP07(2015)045. arXiv: 1505.07459 [hep-ph].

[343] Jason Kumar and Danny Marfatia. "Matrix element analyses of dark matter scattering and annihilation". In: *Phys. Rev.* D88.1 (2013), p. 014035. DOI: 10.1103/PhysRevD.88.014035. arXiv: 1305.1611 [hep-ph].

[344] Rebecca K. Leane, Kenny C. Y. Ng, and John F. Beacom. "Powerful Solar Signatures of Long-Lived Dark Mediators". In: (2017). arXiv: 1703.04629 [astro-ph.HE].

[345] C. Amole et al. "Dark Matter Search Results from the PICO-60 C_3F_8 Bubble Chamber". In: (2017). arXiv: 1702.07666 [astro-ph.CO].

[346] W. H. Press and D. N. Spergel. "Capture by the sun of a galactic population of weakly interacting, massive particles". In: 296 (Sept. 1985), pp. 679–684. DOI: 10.1086/163485.

[347] Lawrence M. Krauss et al. "Cold dark matter candidates and the solar neutrino problem". In: *Astrophys. J.* 299 (1985), p. 1001. DOI: 10.1086/163767.

[348] Joseph Silk, Keith A. Olive, and Mark Srednicki. "The Photino, the Sun and High-Energy Neutrinos". In: *Phys. Rev. Lett.* 55 (1985), pp. 257–259. DOI: 10.1103/PhysRevLett.55.257.

[349] Annika H. G. Peter. "Dark matter in the solar system II: WIMP annihilation rates in the Sun". In: *Phys. Rev.* D79 (2009), p. 103532. DOI: 10.1103/PhysRevD.79.103532. arXiv: 0902.1347 [astro-ph.HE].

[350] I. Yu. Kobzarev, L. B. Okun, and I. Ya. Pomeranchuk. "On the possibility of experimental observation of mirror particles". In: *Sov. J. Nucl. Phys.* 3.6 (1966). [Yad. Fiz.3,1154(1966)], pp. 837–841.

[351] L. B. Okun. "LIMITS OF ELECTRODYNAMICS: PARAPHOTONS?" In: *Sov. Phys. JETP* 56 (1982). [Zh. Eksp. Teor. Fiz.83,892(1982)], p. 502.

[352] Bob Holdom. "Two U(1)'s and charge shifts". In: *Physics Letters B* 166.2 (1986), pp. 196 –198. ISSN: 0370-2693. DOI: http://dx.doi.org/10.1016/0370-2693(86)91377-8. URL: http://www.sciencedirect.com/science/article/pii/0370269386913778.

[353] Bob Holdom. "Searching for charges and a new U(1)". In: *Physics Letters B* 178.1 (1986), pp. 65 –70. ISSN: 0370-2693. DOI: http://dx.doi.org/10.1016/0370-2693(86)90470-3. URL: http://www.sciencedirect.com/science/article/pii/0370269386904703.

[354] Brian Batell et al. "Solar Gamma Rays Powered by Secluded Dark Matter". In: *Phys. Rev.* D81 (2010), p. 075004. DOI: 10.1103/PhysRevD.81.075004. arXiv: 0910.1567 [hep-ph].

[355] Stephen P. Martin. "A Supersymmetry primer". In: (1997). [Adv. Ser. Direct. High Energy Phys.18,1(1998)]. arXiv: hep-ph/9709356 [hep-ph].

[356] Matthew Reece and Lian-Tao Wang. "Searching for the light dark gauge boson in GeV-scale experiments". In: *JHEP* 07 (2009), p. 051. DOI: 10.1088/1126-6708/2009/07/051. arXiv: 0904.1743 [hep-ph].

[357] Georges Aad et al. "Search for massive, long-lived particles using multitrack displaced vertices or displaced lepton pairs in pp collisions at $\sqrt{s} = 8$ TeV with the ATLAS detector". In: *Phys. Rev.* D92.7 (2015), p. 072004. DOI: 10.1103/PhysRevD.92.072004. arXiv: 1504.05162 [hep-ex].

[358] Gerald Eigen. "Direct Searches for New Physics Particles at BABAR". In: *J. Phys. Conf. Ser.* 631.1 (2015), p. 012034. DOI: 10.1088/1742-6596/631/1/012034. arXiv: 1503.02860 [hep-ex].

[359] J. P. Lees et al. "Search for Long-Lived Particles in e^+e^- Collisions". In: *Phys. Rev. Lett.* 114.17 (2015), p. 171801. DOI: 10.1103/PhysRevLett.114.171801. arXiv: 1502.02580 [hep-ex].

[360] Sergey Alekhin et al. "A facility to Search for Hidden Particles at the CERN SPS: the SHiP physics case". In: (2015). arXiv: 1504.04855 [hep-ph].

[361] Philip Schuster, Natalia Toro, and Itay Yavin. "Terrestrial and Solar Limits on Long-Lived Particles in a Dark Sector". In: *Phys. Rev.* D81 (2010), p. 016002. DOI: 10.1103/PhysRevD.81.016002. arXiv: 0910.1602 [hep-ph].

[362] Philip Schuster et al. "High Energy Electron Signals from Dark Matter Annihilation in the Sun". In: *Phys. Rev.* D82 (2010), p. 115012. DOI: 10.1103/PhysRevD.82.115012. arXiv: 0910.1839 [hep-ph].

[363] Patrick Meade et al. "Searches for Long Lived Neutral Particles". In: *JHEP* 06 (2010), p. 029. DOI: 10.1007/JHEP06(2010)029. arXiv: 0910.4160 [hep-ph].

[364] Nicole F. Bell and Kalliopi Petraki. "Enhanced neutrino signals from dark matter annihilation in the Sun via metastable mediators". In: *JCAP* 1104 (2011), p. 003. DOI: 10.1088/1475-7516/2011/04/003. arXiv: 1102.2958 [hep-ph].

[365] Jonathan L. Feng, Jordan Smolinsky, and Philip Tanedo. "Dark Photons from the Center of the Earth: Smoking-Gun Signals of Dark Matter". In: *Phys. Rev.* D93.1 (2016), p. 015014. DOI: 10.1103/PhysRevD.93.015014. arXiv: 1509.07525 [hep-ph].

[366] Chris Kouvaris, Kasper Langaeble, and Niklas Grønlund Nielsen. "The Spectrum of Darkonium in the Sun". In: (2016). arXiv: 1607.00374 [hep-ph].

[367] Jonathan L. Feng, Jordan Smolinsky, and Philip Tanedo. "Dark Sunshine: Detecting Dark Matter through Dark Photons from the Sun". In: (2016). arXiv: 1602.01465 [hep-ph].

[368] S. Adrián-Martínez et al. "A search for Secluded Dark Matter in the Sun with the ANTARES neutrino telescope". In: *JCAP* 1605.05 (2016), p. 016. DOI: 10.1088/1475-7516/2016/05/016. arXiv: 1602.07000 [hep-ex].

[369] Rouzbeh Allahverdi et al. "Indirect Signals from Solar Dark Matter Annihilation to Long-lived Right-handed Neutrinos". In: (2016). arXiv: 1612.03110 [hep-ph].

[370] M. Ardid et al. "Constraining Secluded Dark Matter models with the public data from the 79-string IceCube search for dark matter in the Sun". In: (2017). arXiv: 1701.08863 [astro-ph.HE].

[371] A. A.m Abdo et al. "Fermi Large Area Telescope Observations of Two Gamma-Ray Emission Components from the Quiescent Sun". In: 734, 116 (June 2011), p. 116. DOI: 10.1088/0004-637X/734/2/116. arXiv: 1104.2093 [astro-ph.HE].

[372] Kenny C. Y. Ng et al. "First Observation of Time Variation in the Solar-Disk Gamma-Ray Flux with Fermi". In: *Phys. Rev.* D94.2 (2016), p. 023004. DOI: 10.1103/PhysRevD.94.023004. arXiv: 1508.06276 [astro-ph.HE].

[373] C. Zhen. "LHAASO: Science and Status". In: *Frascati Phys. Ser.* 58 (2014), p. 331.

[374] William H. Press and David N. Spergel. "Capture by the sun of a galactic population of weakly interacting massive particles". In: *Astrophys. J.* 296 (1985), pp. 679–684. DOI: 10.1086/163485.

[375] Lawrence M. Krauss, Mark Srednicki, and Frank Wilczek. "Solar System Constraints and Signatures for Dark Matter Candidates". In: *Phys. Rev.* D33 (1986), pp. 2079–2083. DOI: 10.1103/PhysRevD.33.2079.

[376] K. Griest and D. Seckel. "Cosmic Asymmetry, Neutrinos and the Sun". In: *Nucl. Phys.* B283 (1987). [Erratum: Nucl. Phys.B296,1034(1988)], pp. 681–705. DOI: 10.1016/0550-3213(87)90293-8, 10.1016/0550-3213(88)90409-9.

[377] Andrew Gould. "Direct and Indirect Capture of Wimps by the Earth". In: *Astrophys. J.* 328 (1988), pp. 919–939. DOI: 10.1086/166347.

[378] Andrew Gould. "Resonant Enhancements in WIMP Capture by the Earth". In: *Astrophys. J.* 321 (1987), p. 571. DOI: 10.1086/165653.

[379] Andrew Gould. "Cosmological density of WIMPs from solar and terrestrial annihilations". In: *Astrophys. J.* 388 (1992), pp. 338–344. DOI: 10.1086/171156.

[380] Andrew R. Zentner. "High-Energy Neutrinos From Dark Matter Particle Self-Capture Within the Sun". In: *Phys. Rev.* D80 (2009), p. 063501. DOI: 10.1103/PhysRevD.80.063501. arXiv: 0907.3448 [astro-ph.HE].

[381] Kim Griest and David Seckel. "Cosmic asymmetry, neutrinos and the sun". In: *Nuclear Physics B* 283 (1987), pp. 681 –705. ISSN: 0550-3213. DOI: http://dx.doi.org/10.1016/0550-3213(87)90293-8. URL: http://www.sciencedirect.com/science/article/pii/0550321387902938.

[382] T. K. Gaisser, G. Steigman, and S. Tilav. "Limits on cold-dark-matter candidates from deep underground detectors". In: *Phys. Rev. D* 34 (8 1986), pp. 2206–2222. DOI: 10.1103/PhysRevD.34.2206. URL: http://link.aps.org/doi/10.1103/PhysRevD.34.2206.

[383] C. Rott, T. Tanaka, and Y. Itow. "Enhanced Sensitivity to Dark Matter Self-annihilations in the Sun using Neutrino Spectral Information". In: *JCAP* 1109 (2011), p. 029. DOI: 10.1088/1475-7516/2011/09/029. arXiv: 1107.3182 [astro-ph.HE].

[384] Brian Batell, Maxim Pospelov, and Adam Ritz. "Probing a Secluded U(1) at B-factories". In: *Phys. Rev.* D79 (2009), p. 115008. DOI: 10.1103/PhysRevD.79.115008. arXiv: 0903.0363 [hep-ph].

[385] P. Gondolo et al. "DarkSUSY: Computing supersymmetric dark matter properties numerically". In: *JCAP* 0407 (2004), p. 008. DOI: 10.1088/1475-7516/2004/07/008. arXiv: astro-ph/0406204 [astro-ph].

[386] Carsten Rott, Jennifer Siegal-Gaskins, and John F. Beacom. "New Sensitivity to Solar WIMP Annihilation using Low-Energy Neutrinos". In: *Phys. Rev.* D88 (2013), p. 055005. DOI: 10.1103/PhysRevD.88.055005. arXiv: 1208.0827 [astro-ph.HE].

[387] K. Choi, Carsten Rott, and Yoshitaka Itow. "Impact of the dark matter velocity distribution on capture rates in the Sun". In: *JCAP* 1405 (2014), p. 049. DOI: 10.1088/1475-7516/2014/05/049. arXiv: 1312.0273 [astro-ph.HE].

[388] Bei Zhou et al. "TeV Solar Gamma Rays From Cosmic-Ray Interactions". In: (2016). arXiv: 1612.02420 [astro-ph.HE].

[389] Igor V. Moskalenko, Troy A. Porter, and Seth W. Digel. "Inverse Compton scattering on solar photons, heliospheric modulation, and neutrino astrophysics". In: *Astrophys. J.* 652 (2006). [Erratum: Astrophys. J.664,L143(2007)], pp. L65–L68. DOI: 10.1086/520882, 10.1086/509916. arXiv: astro-ph/0607521 [astro-ph].

[390] Elena Orlando and Andrew Strong. "Gamma-rays from halos around stars and the Sun". In: *Astrophys. Space Sci.* 309 (2007), pp. 359–363. DOI: 10.1007/s10509-007-9457-0. arXiv: astro-ph/0607563 [astro-ph].

[391] Igor V. Moskalenko and Andrew W. Strong. "Anisotropic inverse Compton scattering in the galaxy". In: *Astrophys. J.* 528 (2000), pp. 357–367. DOI: 10.1086/308138. arXiv: astro-ph/9811284 [astro-ph].

[392] Elena Orlando and Andrew Strong. "StellarICs: Stellar and solar Inverse Compton emission package". In: (2013). arXiv: 1307.6798 [astro-ph.HE].

[393] S. Sivertsson and J. Edsjö. "Accurate calculations of the WIMP halo around the Sun and prospects for its gamma-ray detection". In: 81.6, 063502 (Mar. 2010), p. 063502. DOI: 10.1103/PhysRevD.81.063502. arXiv: 0910.0017 [astro-ph.HE].

[394] J. Aalbers et al. "DARWIN: towards the ultimate dark matter detector". In: (2016). arXiv: 1606.07001 [astro-ph.IM].

[395] M. G. Aartsen et al. "Search for dark matter annihilations in the Sun with the 79-string IceCube detector". In: *Phys. Rev. Lett.* 110.13 (2013), p. 131302. DOI: 10.1103/PhysRevLett.110.131302. arXiv: 1212.4097 [astro-ph.HE].

[396] Nicolás Bernal, Justo Martín-Albo, and Sergio Palomares-Ruiz. "A novel way of constraining WIMPs annihilations in the Sun: MeV neutrinos". In: *JCAP* 1308 (2013), p. 011. DOI: 10.1088/1475-7516/2013/08/011. arXiv: 1208.0834 [hep-ph].

[397] C. Patrignani et al. "Review of Particle Physics". In: *Chin. Phys.* C40.10 (2016), p. 100001. DOI: 10.1088/1674-1137/40/10/100001.

[398] Mattias Blennow, Joakim Edsjo, and Tommy Ohlsson. "Neutrinos from WIMP annihilations using a full three-flavor Monte Carlo". In: *JCAP* 0801 (2008), p. 021. DOI: 10.1088/1475-7516/2008/01/021. arXiv: 0709.3898 [hep-ph].

[399] M. Honda et al. "Atmospheric neutrino flux calculation using the NRLMSISE-00 atmospheric model". In: *Phys. Rev.* D92.2 (2015), p. 023004. DOI: 10.1103/PhysRevD.92.023004. arXiv: 1502.03916 [astro-ph.HE].

[400] T. S. Sinegovskaya, A. D. Morozova, and S. I. Sinegovsky. "High-energy neutrino fluxes and flavor ratio in the Earths atmosphere". In: *Phys. Rev.* D91.6 (2015), p. 063011. DOI: 10.1103/PhysRevD.91.063011. arXiv: 1407.3591 [astro-ph.HE].

[401] Raj Gandhi et al. "Neutrino interactions at ultrahigh-energies". In: *Phys. Rev.* D58 (1998), p. 093009. DOI: 10.1103/PhysRevD.58.093009. arXiv: hep-ph/9807264 [hep-ph].

[402] Raj Gandhi et al. "Ultrahigh-energy neutrino interactions". In: *Astropart. Phys.* 5 (1996), pp. 81–110. DOI: 10.1016/0927-6505(96)00008-4. arXiv: hep-ph/9512364 [hep-ph].

[403] T. K. Gaisser. In: *Cambridge, UK: Univ. Pr. (1990) 279 p* (1990). URL: http://www.cambridge.org/uk/catalogue/catalogue.asp?isbn=0521326672.

[404] Matthew D. Kistler and John F. Beacom. "Guaranteed and Prospective Galactic TeV Neutrino Sources". In: *Phys. Rev.* D74 (2006), p. 063007. DOI: 10.1103/PhysRevD.74.063007. arXiv: astro-ph/0607082 [astro-ph].

[405] M. G. Aartsen et al. "Energy Reconstruction Methods in the IceCube Neutrino Telescope". In: *JINST* 9 (2014), P03009. DOI: 10.1088/1748-0221/9/03/P03009. arXiv: 1311.4767 [physics.ins-det].

[406] Matthias Danninger. PhD thesis. Stockholm U., 2013. URL: http://www.diva-portal.org/smash/record.jsf?aq2=[[]]&c=1&af=[]&searchType=SIMPLE&query=621654&language=en&pid=diva2%3A621654&aq=[[]]&jfwid=-9380&sf=all&aqe=[]&sortOrder=author_sort_asc&onlyFullText=false&noOfRows=50&dswid=7188.

[407] Jordan Smolinsky and Philip Tanedo. "Dark Photons from Captured Inelastic Dark Matter Annihilation: Charged Particle Signatures". In: (2017). arXiv: 1701.03168 [hep-ph].

[408] Arvind Rajaraman, Jordan Smolinsky, and Philip Tanedo. "On-Shell Mediators and Top-Charm Dark Matter Models for the Fermi-LAT Galactic Center Excess". In: (2015). arXiv: 1503.05919 [hep-ph].

[409] John David March-Russell and Stephen Mathew West. "WIMPonium and Boost Factors for Indirect Dark Matter Detection". In: *Phys. Lett.* B676 (2009), pp. 133–139. DOI: 10.1016/j.physletb.2009.04.010. arXiv: 0812.0559 [astro-ph].

[410] William Shepherd, Tim M. P. Tait, and Gabrijela Zaharijas. "Bound states of weakly interacting dark matter". In: *Phys. Rev.* D79 (2009), p. 055022. DOI: 10.1103/PhysRevD.79.055022. arXiv: 0901.2125 [hep-ph].

[411] Eric Braaten and H. W. Hammer. "Universal Two-body Physics in Dark Matter near an S-wave Resonance". In: *Phys. Rev.* D88 (2013), p. 063511. DOI: 10.1103/PhysRevD.88.063511. arXiv: 1303.4682 [hep-ph].

[412] Ranjan Laha and Eric Braaten. "Direct detection of dark matter in universal bound states". In: *Phys. Rev.* D89.10 (2014), p. 103510. DOI: 10.1103/PhysRevD.89.103510. arXiv: 1311.6386 [hep-ph].

[413] Mark B. Wise and Yue Zhang. "Yukawa Bound States of a Large Number of Fermions". In: *JHEP* 02 (2015). [Erratum: JHEP10,165(2015)], p. 023. DOI: 10.1007/JHEP10(2015)165, 10.1007/JHEP02(2015)023. arXiv: 1411.1772 [hep-ph].

[414] Mark B. Wise and Yue Zhang. "Stable Bound States of Asymmetric Dark Matter". In: *Phys. Rev.* D90.5 (2014). [Erratum: Phys. Rev.D91,no.3,039907(2015)], p. 055030. DOI: 10.1103/PhysRevD.90.055030, 10.1103/PhysRevD.91.039907. arXiv: 1407.4121 [hep-ph].

[415] Kalliopi Petraki, Lauren Pearce, and Alexander Kusenko. "Self-interacting asymmetric dark matter coupled to a light massive dark photon". In: *JCAP* 1407 (2014), p. 039. DOI: 10.1088/1475-7516/2014/07/039. arXiv: 1403.1077 [hep-ph].

[416] Benedict von Harling and Kalliopi Petraki. "Bound-state formation for thermal relic dark matter and unitarity". In: *JCAP* 1412 (2014), p. 033. DOI: 10.1088/1475-7516/2014/12/033. arXiv: 1407.7874 [hep-ph].

[417] Kalliopi Petraki, Marieke Postma, and Michael Wiechers. "Dark-matter bound states from Feynman diagrams". In: *JHEP* 06 (2015), p. 128. DOI: 10.1007/JHEP06(2015)128. arXiv: 1505.00109 [hep-ph].

[418] Yang Bai, Joshua Berger, and Ran Lu. "750 GeV dark pion: Cousin of a dark G -parity odd WIMP". In: *Phys. Rev.* D93.7 (2016), p. 076009. DOI: 10.1103/PhysRevD.93.076009. arXiv: 1512.05779 [hep-ph].

[419] Jennifer A. Adams, Subir Sarkar, and D. W. Sciama. "CMB anisotropy in the decaying neutrino cosmology". In: *Mon. Not. Roy. Astron. Soc.* 301 (1998), pp. 210–214. DOI: 10.1046/j.1365-8711.1998.02017.x. arXiv: astro-ph/9805108 [astro-ph].

[420] Xue-Lei Chen and Marc Kamionkowski. "Particle decays during the cosmic dark ages". In: *Phys. Rev.* D70 (2004), p. 043502. DOI: 10.1103/PhysRevD.70.043502. arXiv: astro-ph/0310473 [astro-ph].

[421] Nikhil Padmanabhan and Douglas P. Finkbeiner. "Detecting dark matter annihilation with CMB polarization: Signatures and experimental prospects". In: *Phys. Rev.* D72 (2005), p. 023508. DOI: 10.1103/PhysRevD.72.023508. arXiv: astro-ph/0503486 [astro-ph].

[422] Tracy R. Slatyer. "Indirect dark matter signatures in the cosmic dark ages. I. Generalizing the bound on s-wave dark matter annihilation from Planck results". In: *Phys. Rev.* D93.2 (2016), p. 023527. DOI: 10.1103/PhysRevD.93.023527. arXiv: 1506.03811 [hep-ph].

[423] James B. Dent, Francesc Ferrer, and Lawrence M. Krauss. "Constraints on Light Hidden Sector Gauge Bosons from Supernova Cooling". In: (2012). arXiv: 1201.2683 [astro-ph.CO].

[424] Herbert K. Dreiner et al. "Supernova constraints on MeV dark sectors from e^+e^- annihilations". In: *Phys. Rev.* D89.10 (2014), p. 105015. DOI: 10.1103/PhysRevD.89.105015. arXiv: 1310.3826 [hep-ph].

[425] Demos Kazanas et al. "Supernova Bounds on the Dark Photon Using its Electromagnetic Decay". In: *Nucl. Phys.* B890 (2014), pp. 17–29. DOI: 10.1016/j.nuclphysb.2014.11.009. arXiv: 1410.0221 [hep-ph].

[426] Ermal Rrapaj and Sanjay Reddy. "Nucleon-nucleon bremsstrahlung of dark gauge bosons and revised supernova constraints". In: (2015). arXiv: 1511.09136 [nucl-th].

[427] Yue Zhang. "Supernova Cooling in a Dark Matter Smog". In: *JCAP* 1411.11 (2014), p. 042. DOI: 10.1088/1475-7516/2014/11/042. arXiv: 1404.7172 [hep-ph].

[428] I. Jaegle. "Search for the dark photon and the dark Higgs boson at Belle". In: *Phys. Rev. Lett.* 114.21 (2015), p. 211801. DOI: 10.1103/PhysRevLett.114.211801. arXiv: 1502.00084 [hep-ex].

[429] J. P. Lees et al. "Search for a Dark Photon in e^+e^- Collisions at BaBar". In: *Phys. Rev. Lett.* 113.20 (2014), p. 201801. DOI: 10.1103/PhysRevLett.113.201801. arXiv: 1406.2980 [hep-ex].

[430] Tech. rep. ATLAS-CONF-2016-042. Geneva: CERN, 2016. URL: http://cds.cern.ch/record/2206083.

[431] Tech. rep. ATLAS-CONF-2016-103. Geneva: CERN, 2016. URL: http://cds.cern.ch/record/2219571.

[432] Vardan Khachatryan et al. "Search for long-lived charged particles in proton-proton collisions at sqrt(s) = 13 TeV". In: (2016). arXiv: 1609.08382 [hep-ex].

[433] J. D. Bjorken et al. "Search for Neutral Metastable Penetrating Particles Produced in the SLAC Beam Dump". In: *Phys. Rev.* D38 (1988), p. 3375. DOI: 10.1103/PhysRevD.38.3375.

[434] James D. Bjorken et al. "New Fixed-Target Experiments to Search for Dark Gauge Forces". In: *Phys. Rev.* D80 (2009), p. 075018. DOI: 10.1103/PhysRevD.80.075018. arXiv: 0906.0580 [hep-ph].

[435] C. Athanassopoulos et al. "Evidence for muon-neutrino —> electron-neutrino oscillations from pion decay in flight neutrinos". In: *Phys. Rev.* C58 (1998), pp. 2489–2511. DOI: 10.1103/PhysRevC.58.2489. arXiv: nucl-ex/9706006 [nucl-ex].

[436] Brian Batell, Maxim Pospelov, and Adam Ritz. "Exploring Portals to a Hidden Sector Through Fixed Targets". In: *Phys. Rev.* D80 (2009), p. 095024. DOI: 10.1103/PhysRevD.80.095024. arXiv: 0906.5614 [hep-ph].

[437] Rouven Essig et al. "Discovering New Light States at Neutrino Experiments". In: *Phys. Rev.* D82 (2010), p. 113008. DOI: 10.1103/PhysRevD.82.113008. arXiv: 1008.0636 [hep-ph].

[438] F. Bergsma et al. "A Search for Decays of Heavy Neutrinos in the Mass Range 0.5-GeV to 2.8-GeV". In: *Phys. Lett.* B166 (1986), pp. 473–478. DOI: 10.1016/0370-2693(86)91601-1.

[439] S. N. Gninenko. "Constraints on sub-GeV hidden sector gauge bosons from a search for heavy neutrino decays". In: *Phys. Lett.* B713 (2012), pp. 244–248. DOI: 10.1016/j.physletb.2012.06.002. arXiv: 1204.3583 [hep-ph].

[440] The Fermi-LAT et al. “Searching for Dark Matter Annihilation in Recently Discovered Milky Way Satellites with Fermi-LAT”. In: (2016). arXiv: 1611.03184 [astro-ph.HE].

[441] Doojin Kim, Jong-Chul Park, and Seodong Shin. “Dark Matter "Transporting" Mechanism Explaining Positron Excesses”. In: (2017). arXiv: 1702.02944 [hep-ph].

[442] M. Aguilar et al. “Antiproton Flux, Antiproton-to-Proton Flux Ratio, and Properties of Elementary Particle Fluxes in Primary Cosmic Rays Measured with the Alpha Magnetic Spectrometer on the International Space Station”. In: *Phys. Rev. Lett.* 117 (9 2016), p. 091103. DOI: 10.1103/PhysRevLett.117.091103. URL: http://link.aps.org/doi/10.1103/PhysRevLett.117.091103.

[443] M. Ajello et al. “Constraints on dark matter models from a Fermi LAT search for high-energy cosmic-ray electrons from the Sun”. In: *Phys. Rev.* D84 (2011), p. 032007. DOI: 10.1103/PhysRevD.84.032007. arXiv: 1107.4272 [astro-ph.HE].

[444] Kim Griest and Marc Kamionkowski. “Unitarity Limits on the Mass and Radius of Dark Matter Particles”. In: *Phys. Rev. Lett.* 64 (1990), p. 615. DOI: 10.1103/PhysRevLett.64.615.